Acoustic / elastic wave propagation in coupled-resonator waveguides

Tingting Wang

THESE DE DOCTORAT DE L'ETABLISSEMENT UNIVERSITE BOURGOGNE FRANCHE-COMTE

PREPAREE A L'UNIVERSITE DE FRANCHE-COMTE EN CO-TUTELLE AVEC L'UNIVERSITE BEIJING JIAOTONG (CHINE)

Ecole doctorale n°37

Sciences Pour l'Ingénieur et Microtechniques

Doctorat de Microtechniques

Par

WANG Tingting

Acoustic/Elastic Wave Propagation in Coupled-Resonator Waveguides

Propagation des ondes acousto-élastiques dans les résonateurs couplés

Thèse présentée et soutenue à Besançon, le 15 décembre 2020

Composition du Jury :

HU, Geng-Kai	Professeur, Beijing Institute of Technology	Président
BRUNET, Thomas	Maître de conférences, Université de Bordeaux	Rapporteur
CHEN, Chang-Qing	Professeur, Tsinghua University	Rapporteur
PENNEC, Yan	Professeur, Université de Lille	Examinateur
CHOLLET, Franck	Professeur, Université Bourgogne Franche-Comté	Examinateur
WANG, Yue-Sheng	Professeur, Beijing Jiaotong University	Co-directeur de thèse
LAUDE, Vincent	Directeur de recherche CNRS, Université Bourgogne Franche-Comté	Directeur de thèse
WANG, Yan-Feng	Professeur associé, Tianjin University	Examinateur

UBFC
UNIVERSITÉ
BOURGOGNE FRANCHE-COMTÉ

UFC
UNIVERSITÉ
DE FRANCHE-COMTÉ

THÈSE DE DOCTORAT DE L'ÉTABLISSEMENT UNIVERSITÉ BOURGOGNE FRANCHE-COMTÉ

PRÉPARÉE À L'UNIVERSITÉ DE FRANCHE-COMTÉ

École doctorale n°37

Sciences Pour l'Ingénieur et Microtechniques

Doctorat de Microtechniques

par

TINGTING WANG

Acoustic/Elastic Wave Propagation in Coupled-Resonator Waveguides

Thèse présentée et soutenue à Beijing, le 15 décembre 2020

Composition du Jury :

HU GENG-KAI	Professor, Beijing Institute of Technology	President
BRUNET THOMAS	Associate Professor, HDR, Université de Bordeaux	Reviewer
CHEN CHANG-QING	Professor, Tsinghua University	Reviewer
PENNEC YAN	Professor, Université de Lille	Examiner
CHOLLET FRANCK	Professor, Université Bourgogne Franche-Comté	Examiner
WANG YUE-SHENG	Professor, Beijing Jiaotong University	Co-director
LAUDE VINCENT	Research Director CNRS, Université Bourgogne Franche-Comté	Co-director
WANG YAN-FENG	Associate Professor, Tianjin University	Examinator

N° | X | X | X |

Title: Acoustic/Elastic Wave Propagation in Coupled-Resonator Waveguides

Keywords: Phononic crystal; acoustic/elastic wave; coupled-resonator waveguide; fluid-solid interaction; band gap manipulation; reconfigurability; channeled spectrum; phononic polymer

Abstract:

When a defect is introduced into a phononic crystal, states localized at the defect appear in the band gaps. They decay rapidly far away from the defect. Therefore, it is possible to localize and guide wave propagation by designing defects in the perfect phononic crystal. Coupled-resonator waveguides based on the coupling effect between a sequence of defect cavities have simultaneously strong wave confinement and low group velocity, and can be used to design rather arbitrary circuits. Furthermore, the propagation of elastic waves in a solid matrix can be controlled through changing fluid fillings based on fluid-solid interaction. Thus, they have essential applications in vibration reduction and noise isolation. In this thesis, the acoustic and elastic waves propagating in both periodic and aperiodic coupled-resonator waveguides are investigated. The fluid-solid interaction in fluid/solid phononic crystals is studied. The work is conducted by combining numerical simulations, theoretical model analysis and experimental investigations.

Titre : Propagation des ondes acousto-élastiques dans les résonateurs couplés

Mots-clés : Cristal phononique ; ondes acoustiques et élastiques ; guide d'onde à résonateurs couplés ; interaction fluide-solide ; manipulation des bandes interdites ; reconfigurabilité ; spectre cannelé ; polymère phononique

Résumé :

Lorsqu'un défaut est introduit dans un cristal phononique, des états apparaissent dans les bandes interdites et se localisent au niveau des défauts. Ils décroissent rapidement loin du défaut. Par conséquent, il est possible de localiser et de guider la propagation des ondes en concevant des défauts dans un cristal phononique parfait. Le guide d'onde à résonateurs couplés, fondé sur le couplage d'une séquence de cavités, présente simultanément un fort confinement des ondes et une faible vitesse de groupe ; il peut être utilisé pour concevoir des circuits plutôt arbitraires. En outre, la propagation des ondes élastiques dans une matrice solide peut être contrôlée en remplissant des cavités d'un fluide, sur la base des systèmes couplés fluides-solides. Ils ont des applications essentielles pour la réduction des vibrations et l'isolation acoustique. Dans cette thèse, les ondes acoustiques et élastiques se propageant dans les guides d'ondes à résonateurs couplés périodiques et apériodiques sont étudiées. L'interaction fluide-solide dans les cristaux phononiques fluide / solide est étudiée. Les travaux sont menés en combinant simulation numérique, analyse par modèles théoriques et investigation expérimentale.

UBFC UNIVERSITÉ BOURGOGNE FRANCHE-COMTÉ
Université Bourgogne Franche-Comté
32, avenue de l'Observatoire
25000 Besançon, France

ACKNOWLEDGEMENTS

First and foremost, I would like to thank the agreement for the international co-supervision between Beijing Jiaotong University (BJTU) and University of Bourgogne Franche-Comté (UBFC) that offers me an opportunity of joint doctoral degrees. The thesis was prepared under joint supervision by co-directors Prof. Vincent Laude in UBFC and Prof. Yue-Sheng Wang in BJTU as well as my supervisor associate Prof. Yan-Feng Wang.

I would like to highly acknowledge the jury members of my thesis defense, Prof. Thomas Brunet, Prof. Yan Pennec, Prof. Franck Chollet, Prof. Geng-Kai Hu, Prof. Jian-Xiang Wang, Prof. Wei-Qiu Chen, Prof. Chang-Qing Chen and Prof. Feng Xu, for reviewing my manuscript and attending my defense. Thanks for your professional remarks to improve the quality of the manuscript.

I highly appreciate my co-director Prof. Vincent Laude in UBFC. During my PhD period, I was fortunate to go to Institut FEMTO-ST in France for a joint study. His careful guidance made it come true that I completed my graduation successfully. Vincent's deep theoretical foundation, profound knowledge, and rigorous scientific research attitude deeply influenced me. During my study in France, Vincent provided a lot of suggestions and guidance for the smooth progress of my subject. His selfless help to me in life made me feel like home in a foreign country. I won't forget to enjoy the scenery of Besançon with Vincent and the fond memories in France. I would like to extend my highest respect and sincere thanks to Vincent.

I would like to express my deep gratitude towards my co-director Prof. Yue-Sheng Wang in BJTU. His profound academic attainments, rigorous academic attitude, and broad academic vision are admirable. His enthusiasm for scientific research, selflessness of work and the personality charm also deeply infected me. In scientific research, Prof. Wang leads his students to explore science, provides students with enough academic space for self-expression and opportunities for self-exercises. In life, Prof. Wang is witty, easy-going, tolerant and selfless. Thank you for teaching and enlightening my knowledge; thank you for encouraging me to get the opportunity of joint doctoral diplomas; and thank you for your patience and tolerance. Here, I would like to express my most heartfelt thanks to Prof. Wang.

I would like to offer my special thanks to my co-supervisor associate Prof. Yan-Feng Wang. His enthusiasm for scientific research, rigorous attitude to work and strict requirements for himself are the models to follow. We discussed together and researched together. He showed me the way forward and led me to grow up on the road of scientific research step by step. Not only that, but he also gave me a lot of support and help in life. I would like to extend my deepest gratitude to Yan-Feng.

Many thanks to the Phononics and Microscopy team in FEMTO for the many discussions, as well as their help. Special thanks to Sarah Benchabane, Muamer Kadic and Abdelkrim Khelif with the professional suggestions during our group meetings. I also would like to give my special thanks to Sylwester Bargiel and Franck Lardet-Vieudrin. They give me lots of scientific support to my thesis. Thank all the technical teams, in particular to the clean room team, Laurent Robert, Djaffar Belharet, Tristan Faure, Marinha Raschetti, David Raddenzati and Cyril Millon. I will also not forget the administrative teams, in particular Jocelyne Renaut, Sandrine Pyon and Joëlle Berthelot.

My grateful thanks are also extended to phononic crystal team in BJTU: Prof. Yi-Ze Wang, associate Prof. A-Li Chen, Xiao-Xing Su, Kai Yao and Huan-Yu Zhao. Thank you for your excellent and professional advises duiring the discussions. I wish to thank Prof.Ya-Fang Guo, Prof. Ying Liu, Prof. Guo-Shuang Shui, Prof. Guan-Suo Dui, Prof. Hai-Ming Huang, Prof. Jun Mao, Prof. Ming Jin, Prof. Xiao-Yan Liang, Prof. Ru-Bing Zhang, associate Prof. Xiao-Zhi Tang in BJTU and Prof. Liao-Liang Ke in TJU. Thank you all for your help and support in work and life.

I would like to thank Daniel, Aleksandr, Irma, my colleagues in FEMTO. I would never forget the D-Day time we organized together. Thanks Anurupa, Phong, Nicolas, Gautier, Raya, Asma, Khouloud, Qing-Xiang Ji and Xue-Yan Chen, my colleagues in FEMTO. Thanks for your kindly help and warm to me in France. Thanks Ju-Ma, Hao-Wen Dong, Tian-Xue Ma, Dong-Jia Yan, Sheng-Dong Zhao, Xiao-Shuang Li, Chen Liu, Jia-Jia Mao, Qun Zu, Jie Su, Li-Bo Wu, Bo Yuan, Zhi-Guo Liu, Shi-Wang Fan, Si-Min Yuan, Shu-Yan Zhang, Lin-Feng Zhu, Xuan-Bo Miao, Hong-Tao Zhou, my colleagues in BJTU and TJU with the kind support for me.

Thanks my bosom friend Lu-Yao Zhang for giving me a lot of confidence and courage in no matter work and life. Thanks my best friends Mei-Ling Yue, Si-Yu Lin, Yu-Wei Zhang, Hui-Bo Xu, Ya Wang, Li Gao and Yun-Fang Qin.

Last but not least, I wish to express my deepest gratitude to my parents Ms.Xiu-Mei Xue and Mr.Xu-Feng Wang for your continuous support and unconditional love. Special thanks should also be given to my sister and brother Yuan-Yuan Wang, Rong-Fei Ren

and Yan-Shan Wang and all my other families for your company and love. Thanks my niece Jing-Yao Ren for bring me lots of joy. Special thanks to Ms.Bao-Lian Zhang and Mr.Xu-Li Wang for your help in my life and support in spirit. I would like to give my thanks to Mr.Jia-Lu Hao for your endless love, company and courage to me.

CONTENTS

I

Context and problematic

1

INTRODUCTION

1.1/ INTRODUCTION

In 1987, Yablonovitch [8] in Bell Laboratory and John [6] in Princeton University independently proposed the concept of 'photonic crystal' when they studied the light wave/electromagnetic wave suppressing spontaneous emission and the photonic localization in disordered dielectric materials. Due to the periodic change of the material's dielectric constant, Bragg scattering is generated when light waves/electromagnetic waves propagate in the photonic crystal. The wave propagation is forbidden in some frequency ranges which are called photonic band gaps. In 1990, the researchers at the Ames Laboratory of Iowa State University in the United States, Ho et al. [9] verified the existence of the photonic band gap in diamond. On the basis of photonic crystals, some periodic structures have been found where the waves propagating in the acoustic frequency band also have such a similar effect of band gap, which is called 'phononic crystal' (PC). Phononic crystals are composed of periodic arrangements of materials with different elastic properties. In 1992, Sigalas and Economou [11] proved theoretically for the first time that a three-dimensional periodic lattice structure formed by embedding spherical scatterers into a matrix material can generate an elastic wave band gap. In 1993, Kushwaha et al. [13] clearly proposed the concept of phononic crystals for the first time by comparing the propagation of light waves in photonic crystals and the propagation of elastic waves in elastic periodic media. They also obtained the elastic wave band gap in the shear polarization direction of the periodic composite medium formed by the nickel pillars embedded in the aluminum alloy matrix, as shown in figure 1.1(a). In 1995, Martinez-Sala et al. [14] measured the acoustic properties of a sculpture "Flowing Melody" with a history of more than 200 years in Madrid, Spain, and demonstrated the existence of the phononic band gap in experiments for the first time.

Most of the phononic crystals studied before 2000 followed the Bragg scattering mecha-

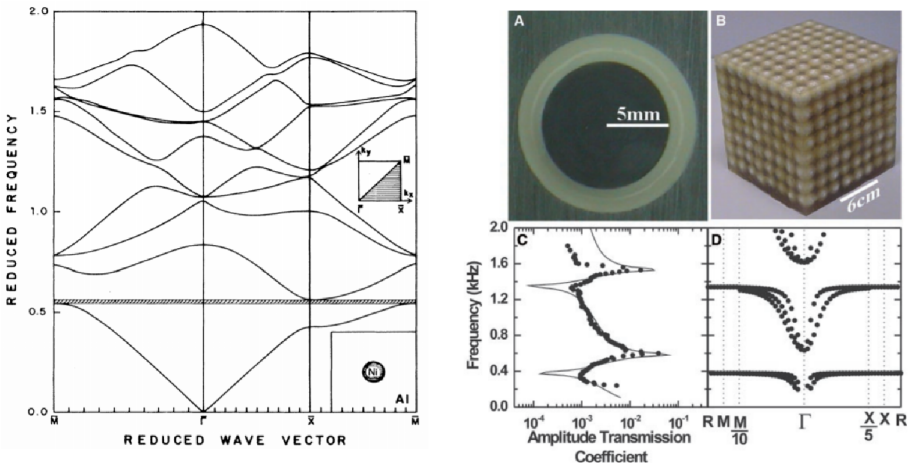

(a) (b)

Figure 1.1: (a) Band structures of the Ni/Al periodic composite [13], (b) Three-dimensional three-componment locally resonant phononic crystal and the corrsponding bandgap [29].

nism, that is, the wavelengths corresponding to the frequencies in the band gap are on the same order of magnitude as the lattice constant. Until 2000, Liu et al. [28, 29] researched the three-dimensional periodic structure of lead balls coated by silicone rubber and proposed the concept of locally resonant band gap of phononic crystals for the first time. This work proved that when the wavelength is 300 times larger than the lattice constant of the phononic crystal, a band gap can still be generated, breaking the limitation of the Bragg scattering mechanism, and successfully achieving the goal of small size controlling large wavelength, as shown in figure 1.1(b). The mechanism of local resonance they proposed opened up a new way to study the characteristics in low frequency band gaps of phononic crystals.

When one or a series of scatterers are removed or replaced in the periodic structure of phononic crystals, the original periodicity will be destroyed and point, line or planar defects are thus formed. The waves within the band gap are confined into the defects, and the waves decay rapidly when they are far away from the defects. The special characteristics of the defects [55, 43] play a huge role in the manipulation of the wave properties, which can manufacture new resonant microcavities [43], new waveguides [36, 53, 158], filters [183], sensors [48, 90], high-frequency resonators [96, 91], multiplexers [107], etc. However, the current design of waveguides is limited to linear waveguides. The researches on waveguides composed of coupled-resonator chains in crystals are limited.

We will study the propagation properties of acoustic/elastic waves in phononic crystals coupled-resonator waveguides combining with theoretical model analyses, numerical simulations and experimental measurements in this thesis. This subject has important

theoretical and practical significance and has been funded by the National Natural Science Foundation of China, China Scholarship Council, Beijing Jiaotong University, and the French National Research Agency.

1.2/ PHONONIC CRYSTALS

Phononic crystal is a new type of periodic functional composite material. The period of a phononic crystal is usually measured by the lattice constant. As an artificial crystal used for acoustic and elastic waves, it is usually composed of two or more different materials periodically and alternately. According to the different constituent materials, phononic crystals can be divided into solid/solid, solid/fluid or fluid/fluid structures. The interconnected part is called the matrix, and the unconnected part is called the scatterers. Both the marix and the scatterer can be solid, fluid or gas.

According to the spatial periodicity of phononic crystals, it can be divided into one-dimensional (1D), two-dimensional (2D) and three-dimensional (3D) structures. The distribution characteristic of one-dimensional phononic crystals is that different kinds of media are staggered and periodically arranged in a certain direction. Two-dimensional phononic crystals consist of columnar scatterers whose one direction is infinite and are arranged in two directions according to different periodic arrangements such as square lattice, rectangular lattice and triangular lattice, etc. Three-dimensional phononic crystals are granular scatterers arranged in three directions in different periodic forms such as simple cubic, face-centered cubic, body-centered cubic, and close-packed hexagons, etc. The smallest period size of phononic crystal is the lattice constant and the smallest unit is called a unit cell.

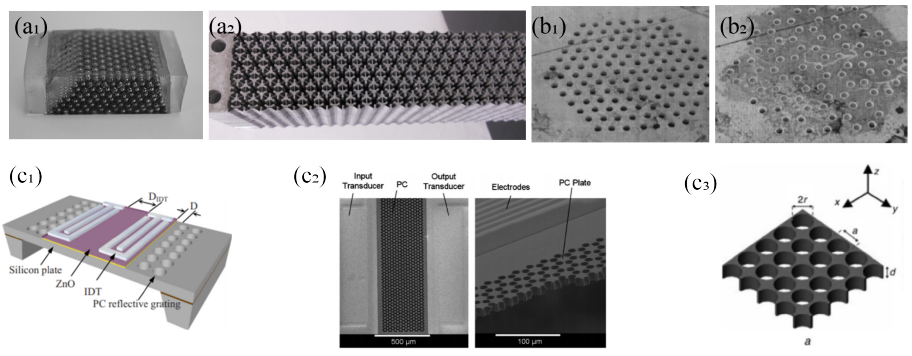

Figure 1.2: (a_1) A 3D bulk wave PC of steel spheres [102], (a_2) A 2D bulk wave PC of aluminum in air [138], (b_1) Sureface wave PC of the triangular structure [23], (b_2) Sureface wave PC of the honeycomb structure [23], (c_1) Lamb wave resonator [100], (c_2) Lamb wave transducers [81], (c_3) PC plate with holes [77].

According to different propagation modes, phononic crystals can also be divided into bulk wave phononic crystals, Lamb wave phononic crystals and surface wave phononic crystals. When the phononic crystal is infinite in non-periodic direction, or the size of the structure in non-periodic direction is much larger than the wavelength, bulk waves propagate in the periodic structure, which is called a bulk wave phononic crystal [102, 138, 19, 18, 162], as shown in figure 1.2 (a_1) and (a_2). When the phononic crystal has a certain thickness in the non-periodic direction, Lamb waves are formed during the propagation of elastic waves between the upper and lower interfaces, modulated by the periodic plane. This kind of periodic medium is called Lamb wave phononic crystal, as shown in figure 1.2 (c_1) and (c_3). When the periodic structure is set on the surface of the half-space medium, surface waves propagate along the surface of the structure, and is called a surface wave phononic crystal [23], as shown in figure 1.2 (b_1) and (b_2).

The most significant feature of phononic crystals is the existence of the band gaps. In the frequency ranges of band gaps, the propagation of acoustic or elastic waves is forbidden. For the wave in a given polarization direction, only the waves in certain directions cannot propagate in the band gap, which is called the directional band gap in this polarization direction; if the waves in all directions cannot propagate in the band gap, it is called a full band gap. If waves of all polarizations and all directions cannot propagate in the band gap, it is called a complete band gap.

1.3/ RESEARCH BACKGROUND OF PHONONIC CRYSTALS

In this section, we briefly review the generation mechanism of the band gaps, the properties and calculation methods of acoustic characteristics, and the tunable manipulation of wave propagation in phononic crystals.

1.3.1/ BAND GAPS OF THE PHONONIC CRYSTALS

According to the ratio of the lattice constant and the wavelength, there are two different generation mechanisms of band gaps in a phononic crystal, namely the Bragg scattering mechanism [46] and the locally resonant mechanism [29], as shown in figure 1.3. Generally speaking, the generation of these band gaps is affected by both the structural periodicity and Mie scattering of a single scatterer.

For Bragg phononic crystals, the interaction between the unit cells or the periodicity of the structure play a dominant role, and the incident wavelength is required to be equivalent

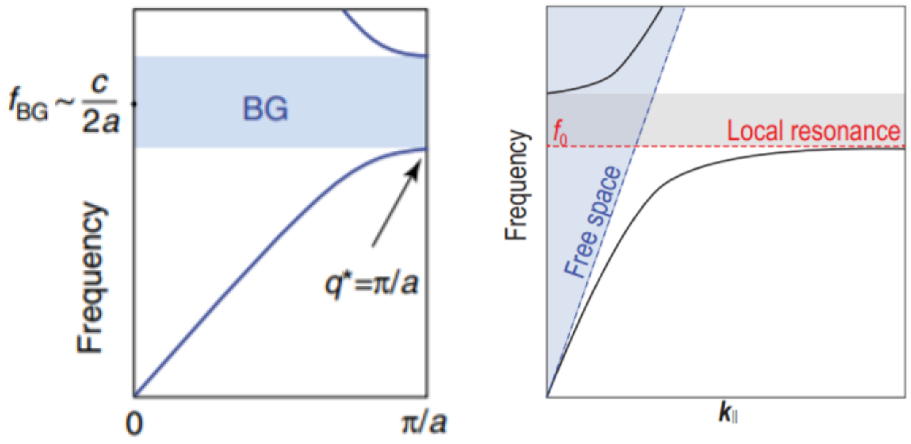

(a) (b)

Figure 1.3: (a) Bragg bandgap, (b) Local resonance bandgap.

to the lattice constant. In the audible frequency domain, the wavelength of sound waves varies from centimeter level to meter level, which requires the size magnitude of the units in phononic crystals to be similar. As a result, the size of the structure is large, which limits its applications. For locally resonant phononic crystals, the resonance characteristics of a single scatterer play a decisive role and is less sensitive to the periodicity. For a given periodicity, the phononic crystal in a smaller size can generate band gaps at lower frequencies, possibly much lower than the Bragg band gaps.

In fact, it is not rigorous that the waves do not propagate in the band gap of phononic crystal. The energy can't disappear, so there are other waves that propagate in the band gaps or waves converted from Bloch waves, namely evanescent wave. Strong localization of waves in the phononic band gap can be achieved. The complex solutions of the dispersion relations of phononic crystals can prove the existence of evanescent waves [21]. Evanescent waves can also describe all the phenomena that are important for near-field characteristics [136].

1.3.2/ Characterization and calculation methods of acoustic properties of phononic crystals

The characterization of the acoustic properties of phononic crystals is an important part of phononic crystal research. The characterization parameters commonly include the band structure, response spectrum, wave field distribution, etc.

The band structure, that is, the dispersion relation, refers to the relationship between the energy of a system and its momentum index. For light/electromagnetic waves, acous-

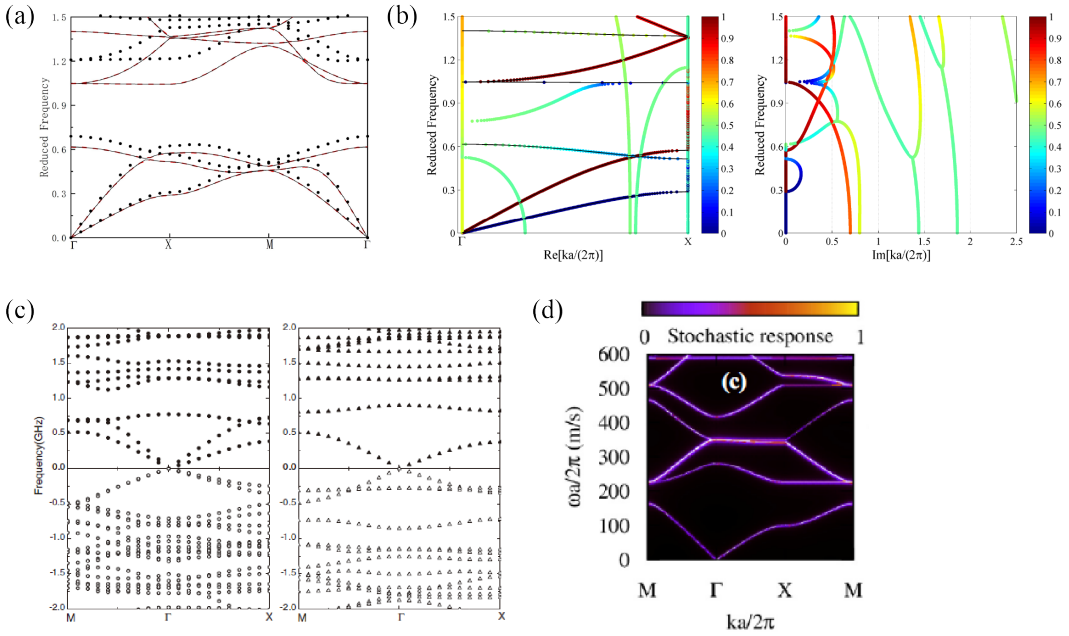

Figure 1.4: (a)Band structure [178], (b) Complex-wavevector band structure [178], (c) Complex-eigenfrequency band structure [47], (d) Resolvent band structure [201].

tic/elastic waves, their energy is proportional to the frequency of the wave ω, while momentum is proportional to the wave number k (the wavevector's modulus). Therefore, the relationship between frequency ω and wavevector $\mathbf{k}$ is the band structure of the system. Due to the translational periodicity of the structure and the symmetry of the point group, the curve of the eigenfrequencies ω with the wavevector $\mathbf{k}$, that is, the band structure, can be obtained when the wavevector $\mathbf{k}$ traversing the irreducible Brillouin zone. Generally, the eigenfrequencies ω have extreme values when the wavevector $\mathbf{k}$ locates on the irreducible boundaries of the Brillouin zone. Therefore, the wavevector $\mathbf{k}$ just needs to traverse the boundaries of the irreducible Brillouin zone if only to determine the band gaps. When the wavevector $\mathbf{k}$ is a real number, and ω is a real function of the real wavevector $\mathbf{k}$, the real band structure can be obtained by solving an eigenvalue problem.

Next we will describe four different kinds of band structures, which are real band structure (BS), complex-eigenfrequency band structure (CEBS), complex-wavevector band structure (CWBS) and resolvent band structure (RBS). Taking a two-dimensional phononic crystal with square arrangement of steel columns in epoxy matrix without viscosity as an example, both the frequency ω and the wavevector $\mathbf{k}$ are real in the band structure, which is called real band structure, as shown in figure 1.4 (a). It can be seen from the figure that a complete band gap appears in the band structure. There is no band existing within the band gap according to the concept of the real band structure. But when the frequency

of the elastic wave falls within the band gap range, the wave cannot disappear according to the conservation of energy. So in what way does the wave exist in the medium? The real band structure obviously cannot explain this phenomenon. At this time, we must use the concept of complex band structures [1, 2, 7]. In order to explore the propagation form of elastic waves when the frequency falls within the band gap, the wave number and/or frequency domain are extended to the complex domain to define the complex values $\omega(\mathbf{k})$ [55] or $\mathbf{k}(\omega)$ [43] band structure. When the wavevector $\mathbf{k}$ is a complex value, it represents the attenuation of the elastic wave in space domain [118, 113]. This kind of band structure is complex-wavevector band structure, as shown in figure 1.4 (b). The left and right parts represent the relationship between the real and imaginary parts of the wavevector and frequency, respectively. Since the imaginary part of the wavevector in the complex-wavevector band structure is not zero, the band gap represents the frequency range where only evanescent waves exist. When the frequency ω is a complex value, it represents the attenuation of the elastic wave in time domain [21, 47]. This kind of band structure is complex eigenfrequency band structure. The band gap is defined as the real frequency range where there is no band existing. Figure 1.4 (c) shows the CEBS of the phononic crystal consisting of the silica column and ice matrix, where the upper is the real part of the frequency and the lower is the imaginary part. Recently, the concept of the resolvent band structure (RBS) [201] was introduced. With the RBS, one abandons the idea of obtaining a functional relationship in the form of bands and instead proceeds to map the resolvent set over the full dual $\mathbf{k}, \omega$ space, as shown in figure 1.4 (d). The resolvent set is by defining the complement of the spectrum of eigenvalues: it is composed of the whole complex plane with the isolated eigenvalues composing the spectrum removed. In practice, the RBS can be obtained easily by considering a spatially random source distributed in the phononic crystal. Indeed, the random source will excite all modes of vibration, and it then suffices to map the response of the crystal as a function of ω and $\mathbf{k}$, which is a response function $E(\omega, \mathbf{k})$ similar to a density of states. The RBS also gives the attenuation information of the dispersion point in time domain as well as space domain. In general, when the material viscosity is considered, the real band structure cannot characterize the physical properties of the structure. In this case, CWBS, CEBS, or RBS is needed to describe the dispersion and propagation characteristics in time or/and space.

In order to further reflect the transmission properties of phononic crystals, and intuitively reflect the attenuation of the elastic wave or vibration in the high symmetry direction of the Brillouin zone, the response spectrum [65] is introduced. Since the propagation of elastic waves is forbidden in the band gap of the phononic crystal, the response spectrum can

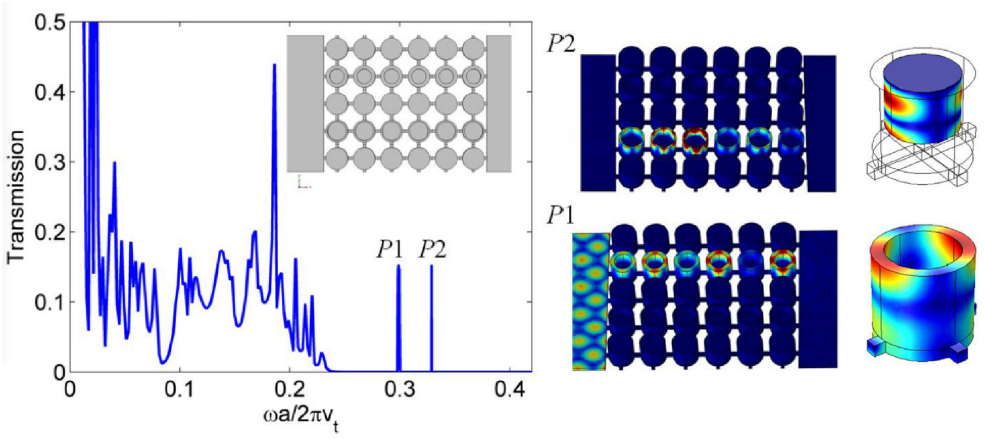

Figure 1.5: Transmission (a), displacement distribution (b) and eigenmodes [188] (c) of the line defect.

directly reflect the attenuation ability of the phononic crystal in this direction, as shown in figure 1.5 (a). In addition, the response spectrum is also easy to be tested experimentally.

The wave field distribution describe the eigenfield or response field of the phononic crystals, which can be used to describe the wave propagation in the defective system, as shown in figure 1.5 (b) and (c). The spatial or temporal distributions of the displacement, stress, pressure, etc. at a specific frequency or moment are included. It can visually display the propagation properties and local performance of the wave at a certain frequency as well. In particular, the generation mechanism of the band gaps can also be analyzed combining with the eigenfields of the band gap boundaries.

At present, a variety of mature calculation methods of acoustic characteristics have been developed. Such as plane wave expansion method (PWE) [151], multiple scattering theory (MST), Dirichlet to Neumann (DtN), boundary element method (BEM) [74], finite difference time domain (FDTD) [68] and finite element method (FEM) [70], etc. Among all of the methods for calculating band structures, the finite element method has the advantages of strong adaptability, good convergence, fast calculation speed, and high accuracy. Therefore, we use the commercial software COMSOL and the open source FreeFem++ to investigate the acoustic properties of phononic crystals in this thesis.

1.3.3/ TUNABLE MANIPULATION OF ACOUSTIC PROPERTIES OF PHONONIC CRYSTALS

Phononic crystals are artificial periodic structures, hence whether they have band gaps and in which frequency range the band gaps appear can be designed and controlled artificially. Phononic crystals can be used to control electromagnetic waves, acoustic waves and elastic waves, etc. As is well known, band gaps are found to be influenced by many factors, including the material properties [98, 131] (include anisotropy [110], viscosity [178, 101, 112, 171, 184], different number of components [190], or multifield couplings [85, 94], etc.), geometric variations [144, 145, 146, 115], and interface conditions between different components [135, 147]. The changes of the width and position of the band gaps make the phononic crystals have various applications, including vibration/noise control [124, 119, 76], acoustic focusing, energy harvesting, etc. It also provides new means for the design of new acoustic devices, such as filters, frequency dividers, couplers [65, 60, 169, 54], etc. Therefore, it is particularly important to achieve tunable manipulation of wave propagation by adjusting the band gaps. All these factors related to bandgaps are the basis of designing the tunable phononic crystals. However, the conventionally designed and fabricated structures can hardly have tunable (or reconfigurable) topologies or material parameters, which may limit their applications. Tunability of bandgaps (width, location, direction, or polarization) is extremely essential and of great importance in practical applications of PCs [109, 114, 164].

Many researchers have devoted a lot of efforts to the design, development, and demonstration of tunable PCs and MMs. A series of novel wave properties have been found, resulting in an emerging revolution for tunable, active, or even smart control of acoustic or elastic waves. In the following, we will describe tunable or active manipulation of waves either based on multifield coupling effects or by mechanical means.

1.3.3.1/ MULTIFIELD COUPLING PHONONIC CRYSTALS

Changing the geometry of PCs, adjusting the properties of the component materials by applying a biasing field is a way to tune the wave propagation. This measure usually requires multifield coupling media as the components of PCs. Such multifield coupling media include piezoelectric materials, ferroelectric materials, magnetomechanical materials, optomechanical materials, and thermomechanical materials, etc.

Piezoelectric materials exhibit the electromechanical coupling effect between the mechanical and electrical fields, which results in the change of material properties, such as

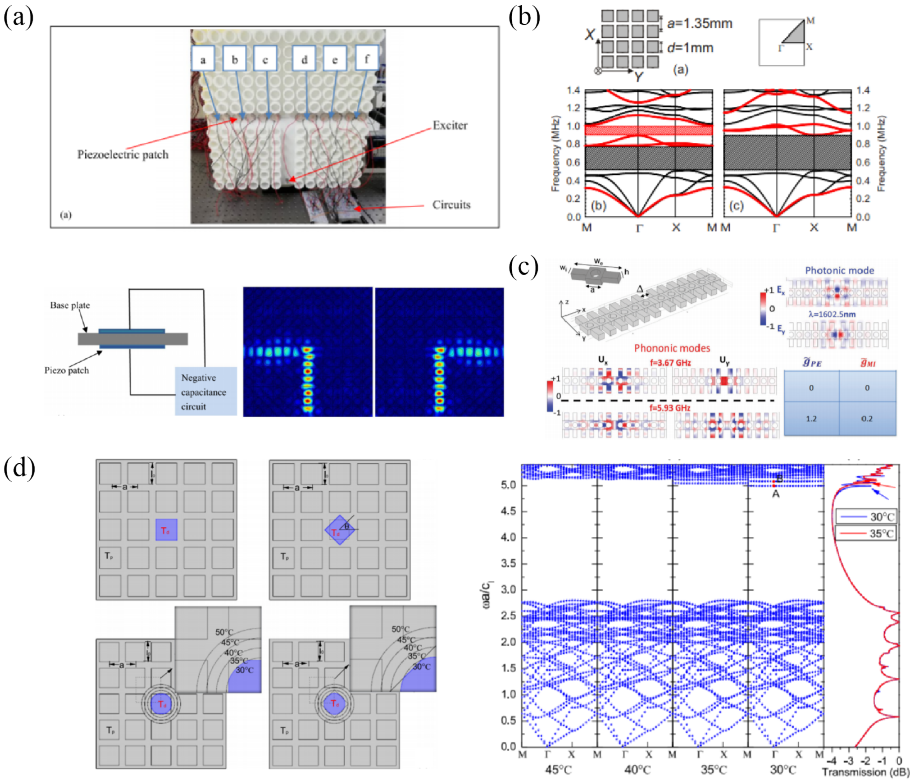

Figure 1.6: Multifield coupling structure: (a) Electromechanical coupling [203], (b) Magnetomechanical coupling [93], (c) Optomechanical coupling [163], (d) Thermomechanical coupling [157].

structural stiffness and/or acoustic parameters. Such a superior property can be considered as an effective method to tune the elastic waves in PCs [51, 66, 62, 64]. The units with piezoelectric materials are usually connected with external shunts. The wave behaviors can be controlled dynamically by modifying the external circuits through the applied voltage, inductance, and resistance. Li et al. [203] tuned the propagation direction of the fexural wave by active control system behaved as the piezoelectric patches on a plate with T-shaped waveguide, as shown in figure 1.6 (a).

Magnetostrictive materials, such as Terfenol-D, can realize the interconversion between magnetic energy and kinetic energy. Unlike control with piezoelectric materials generally bounded to the surfaces of structures, control of the behaviors of PCs with magnetostrictive materials can be realized in a noncontact measure. For PCs with magnetostrictive inclusions, their band structures can be modified by changing the magnitude and orientation of applied magnetic fields through the changes of effective elastic constants [121, 192]. Robillard et al. [93] show the contactless tunability of the absolute band gaps of a two-dimensional phononic crystal composed of an epoxy matrix and Terfenol-D inclusions by changing the external magnetic field applied to the structure, as shown in figure 1.6 (b).

Light and sound usually propagate through many materials simultaneously in the form of optical and elastic waves, respectively. They may interact with each other, especially at a micro- or nanoscale. Electrostriction and radiation pressure can generate strains inside the media as a result of the optical wave propagation. This provides us a new measure for manipulation of elastic waves. By engineering the point and linear defects, they can confine and guide sound and light waves with certain frequencies in the associated band gaps. This will strengthen the optomechanical coupling [163, 161], as shown in figure 1.6 (c). This interaction has been applied to design many devices for active modulation of light (sound) via elastic (optic) waves [15].

Thermal expansion, a kind of noncontact mode, is thus quite attractive. Both the volume and physical properties of materials can be changed due to thermal expansion. If the thermal sensitive fluids or solids are chosen as the constituents of PCs, manipulation of acoustic or elastic waves can be realized simply through temperature change. Hu et al. [157] investigated the temperature effects on the defect states by changing the temperature of the central rod of the two-dimensional ferroelectric ceramic plate and realize the manipulation of elastic waves in the band gaps, as shown in figure 1.6 (d). Many researchers have discussed the possibility to manipulate wave behaviors [86, 191], including band gaps for bulk waves [152], surface waves [152, 61] and Lamb waves [117].

1.3.3.2/ MECHANICALLY RECONFIGURABLE PHONONIC CRYSTALS

The geometric configurations of these kinds of PCs, including the shape, size, and lattice forms, can be changed through mechanical measures after fabrication, leading to the change of wave behaviors, and realizing the switch between different acoustic/elastic wave functions. The configuration of a fluid/solid system may also be changed by adding or reducing fluid fillings. Compared with other configurations, this kind of regulation is generally applicable to the unit cell level, and is more flexible.

The pre-existing state of stress, also called the “prestress,” may have a strong influence on wave propagation in elastic structures. This provides a way to tune the elastic wave characteristics through the change of the prestress [176, 189, 97]. Both experimental [123] and numerical [130, 148] investigations have already shown that in order to realize significant tunability of bandgaps for the traditional hard materials, the applied prestress should be very large. This not only makes the manipulation more difficult but also brings other problems concerning energy-consuming and structure safety. Soft materials and granular systems are good candidates for designing tunable PCs and MMs taking advantage of prestress. Soft materials and structures usually undergo reversible large deformation

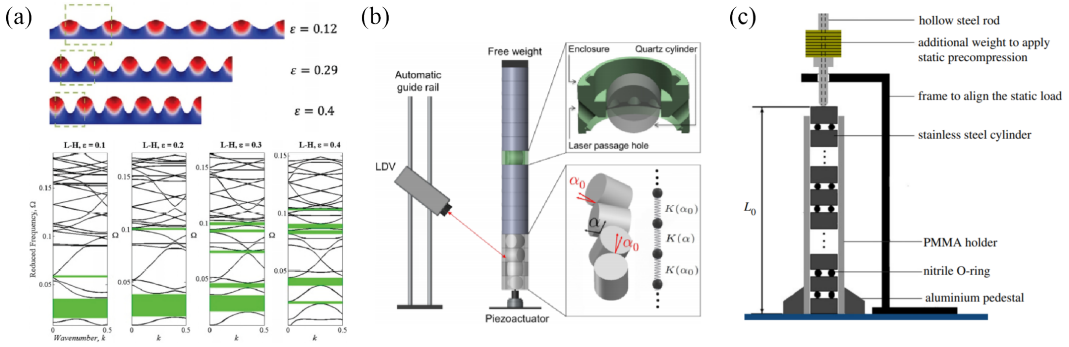

Figure 1.7: Prestressed structure: (a) Soft material system [170], (b) Change the contact angle between cylindrical particles [193], (c) Alternate arrangement of double particles with different materials [168].

without causing material damage, and can exhibit rich and complex mechanical behaviors [128, 126]. Large deformation simultaneously modifies the effective material properties and the structural geometry, and thus changes the wave propagation characteristics in soft PCs. For granular system, the wave behavior of a chain with nonspherical particles can be tuned by adjusting the particles' orientations [142]. Another way to do so is to arrange hard heavy-mass particles alternating with soft light-mass particles to exhibit localized resonances [160]. Bayat et al. [170] controlled the wave propagation by changing the distance between adjacent wrinkles using the interface layer wrinkles caused by elastic instability based on the layered medium with large deformation, as shown in figure 1.7 (a). Chaunsali et al. [193] numerically investigated and experimentally demonstrated an *insitu* topological band transition in a highly tunable mechanical system made of cylindrical granular particles by tuning its interparticle stiffness in a controllable way, simply by changing the contact angles between the cylinders. See figure 1.7 (b). Xu et al. [168] studied the propagation of short pulses with wavelength comparable to the size of a unit cell in a one-dimensional discrete metamaterial composed of steel discs alternating with toroidal nitrile O-rings under different levels of precompression using experiments, numerical simulations and theoretical analysis. This strongly nonlinear metamaterial is more tunable than granular chains composed of linear elastic spherical particles and has better potential for attenuation of dynamic loads.

As an art of paper folding, origami is an effective method to stimulate intellectual curiosity and has a lot of prospective engineering applications. Due to the geometrically programmable characteristics, an origami-based design is expected to be favorable for developing novel mechanical PCs. By combining contraction, shearing, bending, and facet-binding, radiating and focusing of acoustic waves can be controlled easily by tuning geometry forms. Harne et al. [186] realized energy focusing based on the simple topology

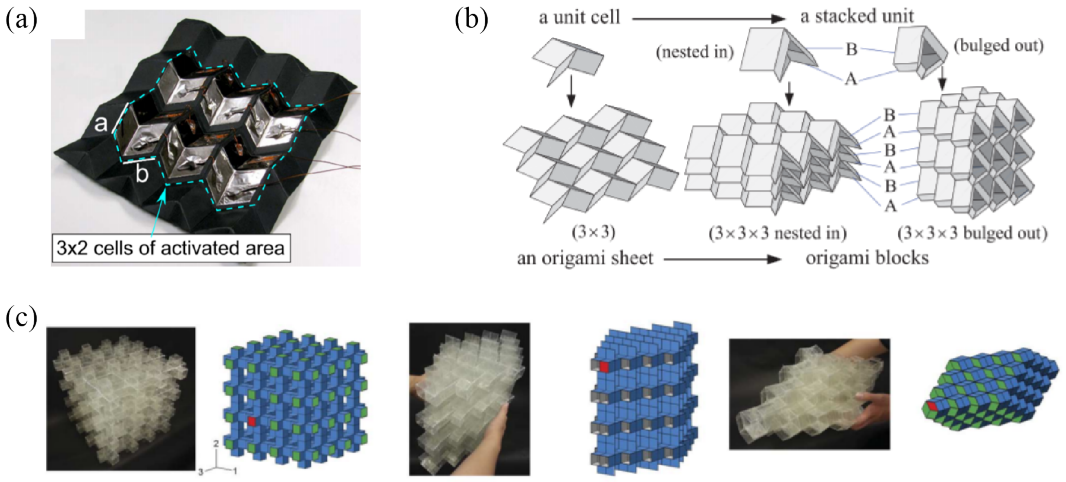

Figure 1.8: Origami structure: (a) Miura-ori-based acoustic array [186], (b) 4-vertex origami cells [181], (c) Reconfigurable origami-inspired acoustic waveguides [180].

reconfigurability of Miura-ori acoustic array, as shown in figure 1.8 (a). Fang et al. [181] discussed that the four-vertex cells are relevant to the potential application of self-locking origami structures, and offer a better design of origami-based mechanical PCs, as shown in figure 1.8 (b). Babaee et al. [180] combined numerical simulations and experiments to design a new class of reconfigurable waveguides based on three-dimensional origami-inspired metamaterials. As such, they provided an ideal platform to actively control and redirect the propagation of sound, as shown in figure 1.8 (c).

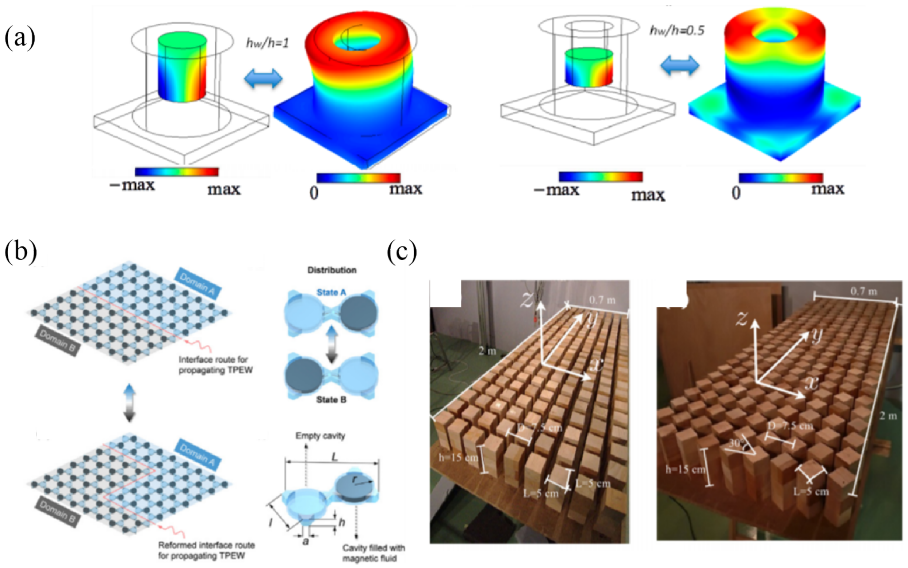

Figure 1.9: Fluid/Solid structure: (a) Change the height of the fluid in the solid matrix [187], (b) Change the magnetic fluid distribution in the solid matrix [207], (c) Rotate the solid scatter in the fluid matrix [129].

PCs composed of both solid and fluid materials have been investigated frequently, particularly in relation to experiments. The basic feature of fluids is shapeless and flowing, which makes the fluid/solid systems reconfigurable [127, 150]. Different wave equations are used for different regions of space, but they are coupled at the fluid-solid interface [127]. Acoustic waves in a fluid medium can be manipulated by changing the properties of solid inclusions. Conversely, the propagation of elastic waves in a solid matrix can be controlled through changing the properties of fluid fillings [154, 188, 52]. Pichard et al. [129] manipulated the band gaps by rotating the scatterers along the vertical axis in the audible frequency range, as shown in figure 1.9 (c). Zhang et al. [207] proposed a tunable elastic valley Hall insulator, whose unit cell consists of two cavities and magnetic fluid with the same volume as the cavity. An interface route with an arbitrary shape for propagating topologically protected edge waves can be achieved by controlling the distribution of magnetic fluid in each unit cell through a designed programmable magnet lifting array, as shown in figure 1.9 (b). Jin et al. [187] numerically tuned the solid/fluid coupling by adjusting the height of the fluid, as shown in figure 1.9 (a). There are also some works to capture surface elastic waves and acoustic waves by adding different heights of water to the grooves on the solid surface, and achieve rainbow capture [202] at the same time.

Although many related researches of tunable phononic crystals have made gratifying progress. But it is still challenging in future. At present, most researches on tunable phononic crystals are based on theoretical analysis or numerical simulation, while the experimental realization is still relatively limited, especially for active or smart control, which greatly limits the practical application of phononic crystals and the manufacture of industrial products. There is still no perfect physical mechanism to explain the characteristics of tunable phononic crystals, such as fluid-structure coupling mechanism.

1.3.4/ COUPLED-RESONATOR WAVEGUIDES

When the periodicity of a perfect phononic crystal is destroyed, i.e, when the geometry or material properties of one or several unit cells change locally, defect states will be generated in the band gaps, and the waves will be localized at the defects. The waves far away from the defects decay rapidly. The guiding of the propagation of acoustic waves or elastic waves can be realized by designing defects in the perfect phononic crystals.

According to different forms, defects include point defects [58, 44, 17, 20, 33, 37], line defects [27, 59, 39, 34] and surface defects [30], as shown in figure 1.10. Point defects refer to the defects formed by breaking the periodicity of the lattice at certain grid points of the lattice. Usually, it can be obtained by changing the size, shape, and material of the

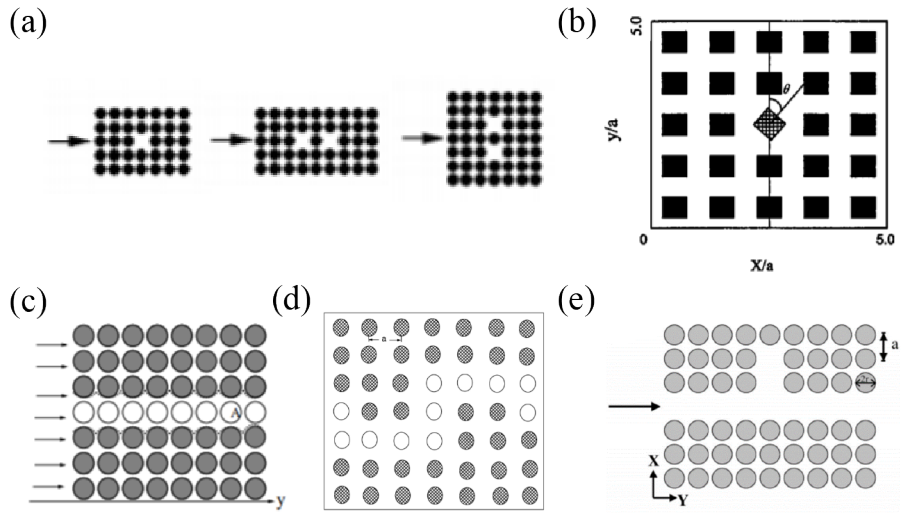

Figure 1.10: (a)-(b) Point defecte [58, 44], (c) Straight defect [27], (d) Bent defect [59], (e) Filter [39].

scatterer at the grid point. New microcavities [43] can be designed by using point defects. A line defect is formed by continuously breaking the periodicity of the lattice on the line of grid points in a two-dimensional or three-dimensional phononic crystal. It is usually obtained by changing the size, shape, and/or material of the scatterers at all grid points on the grid point line. The line defect localizes the waves at the frequencies of the defect bands into the line defect and cause them to propagate along the line defect. Therefore, it is possible to design waveguides, multiplexers and couplers [132], etc. A planar defect is like a perfect mirror. Furthermore, the combination of point defects and line defects can achieve frequency filtering, thereby designing acoustic devices such as filters, uploaders and downloaders [39].

The introduction of defects provides new ideas to realize manipulation of waves, designing and manufacturing new acoustic devices with phononic crystals, which has attracted widespread attention. Khelif et al. [52] experimentally proved the guidance and bending of acoustic waves in highly localized waveguides. Hatanaka et al. [156] developed a phonon waveguide using a one-dimensional array of suspended membranes and demonstrated that it could support and guide mechanical vibrations by nanoelectromechanical systems. Elford et al. [108] designed novel noise barriers using Matryoshka sonic crystals with different number of C-shaped shells, as shown in figure 1.11 (f). Mousavi et al. [174, 196] studied the topological phonon waveguide in an elastic plate. Ho et al. [41] proposed low-frequency sound insulation materials using the idea of local resonance. Cervera et al. [32] put forward a two-dimensional phononic crystal acoustic lens by metal rods, which can achieve focusing functions. Benchabane et al. [69] improved the performance of surface

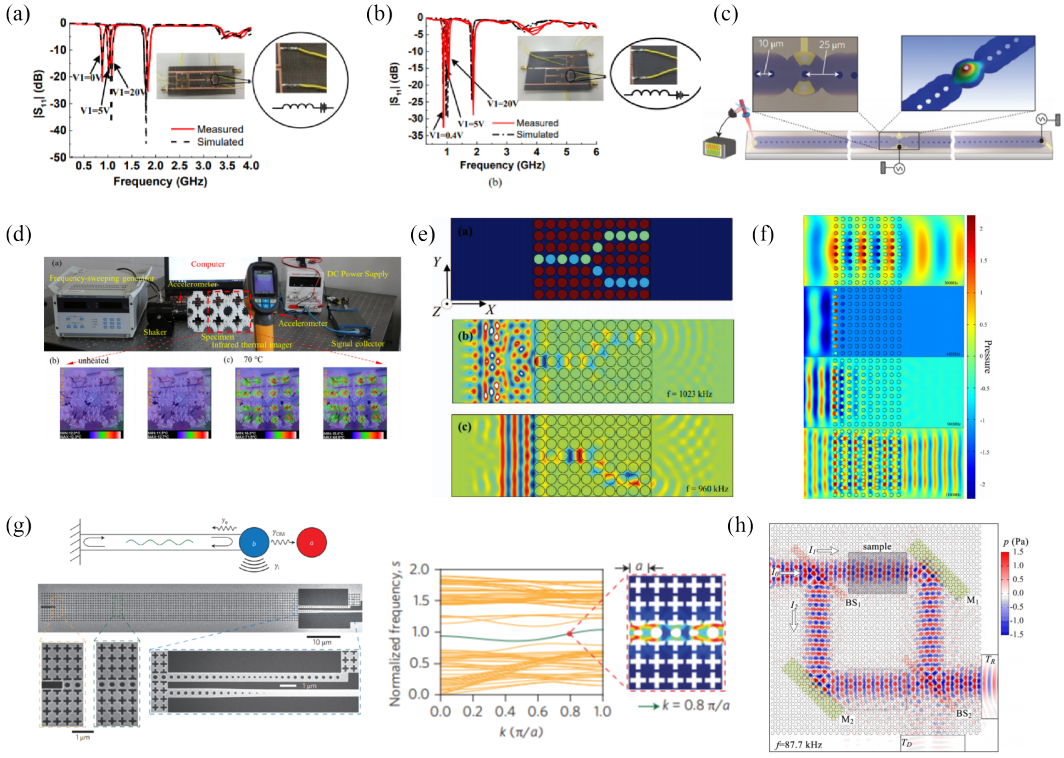

Figure 1.11: (a) Tunable dual-band filter [183], (b) Tunable diplexer [183], (c) Mechanical membrane-based phonon waveguides [156], (d) Thermally triggered tunable vibration mitigation [204], (e) Splitter [114], (f) Six concentric Matryoshka system [108], (g) Gigahertz dispersion-engineerable phonon waveguide [182], (h) Mach-Zehnder interferometer [159].

filters by studying the band gap characteristics on piezoelectric materials, researched theoretically and experimentally the resonance tunneling of acoustic waves between two parallel waveguides in water/steel phononic crystals, thereby achieved the design of the multiplexer [65] as well as the upload and download [60] of the frequencies. Kaya et al. [159] developed the Mach-Zehnder interferometer, containing two beam splitters and acoustic lenses as shown in figure 1.11 (h). Feng et al. [183] schemed tunable dual-band filter and diplexer based on folded open loop ring resonators as shown in figure 1.11 (a) and (b). Vasseur et al. [114] designed a splitter, as shown in figure 1.11 (e). Pennec et al. [54] designed the tunable filtering and demultiplexing in phononic crystals with hollow cylinders by filling water. Airoldi et al. [106] designed the acousto-electrical system characterized by an internal resonant behavior that occurs at the tuning frequency of the shunting circuits. Hsu et al. [125] demonstrated that the confined wave energy flows can be switched on/off by changing the imposed electrical boundary conditions. The methodology enabled designing PnC structures of active controlled transmission, guiding, switching, and emission for slab waves. Fang et al. [182] ealized a tight-binding

form of mechanical coupling between distant optomechanical cavities, leading to direct phonon exchange without dissipation in the waveguide, as shown in figure 1.11 (g).

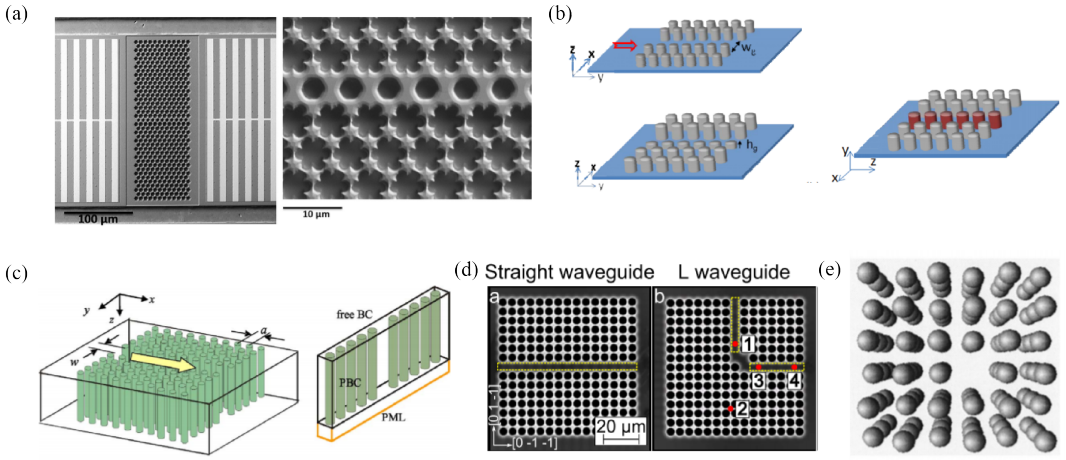

Figure 1.12: (a) Straight waveguide in 2D PnC plate with holes [200], (b) Straight waveguide in 2D PnC plate with pillars [92], (c) Straight waveguide in 2D surface wave plate [143], (d) Bent waveguide in 2D surface wave plate [73], (e) Straight waveguide in 3D PnC [50].

Linear lines of defects [185, 143, 200], as the most commonly used guidance mechanism, have received a wide attention. Many different waveguides have been formed in 2D PC slabs with holes or pillars, surface waves on semi-infinite PCs and the bulk waves in 3D PCs. For the PC slabs [57, 71], there are two common cases: one is slabs with holes [185]. Figure 1.12 (a) designed the straight waveguide by changing the shape and size of holes [200]. The other one is slabs with grafted pillars or resonators [103, 134]. Figure 1.12 (b) designed the straight waveguide by removing one row of the pillars or changing the heights and material properties of them [92]. In particular, low-frequency modes can be generated at the interface between the pillars and the plate as a resonator for a two-dimensional phononic crystal plate grafted with pillars. The other end of the pillars are free, providing it with possible deformations such as bending, torsion and compression. The pillar structures can generate both the Bragg band gaps and the locally resonant band gaps [84, 87], which aroused extensive research interests. For the surface wave PCs [143, 73, 149], the straight and bent waveguides are designed by removing one row of unit cells, respectively, as shown in figure 1.12 (c) and (d). For bluk wave PCs [50], the bulk waveguides are designed by removing the planar unit cells.

Based on linear waveguides, waveguides composed of linear chains of coupled-resonators in a crystal were first proposed in the field of photonics, called the coupled-resonator optical waveguide (CROW) [26, 82]. These CROWs can have applications in slow light [80], light storage [79], sensing [165], and light capture [83], etc. Coupled-

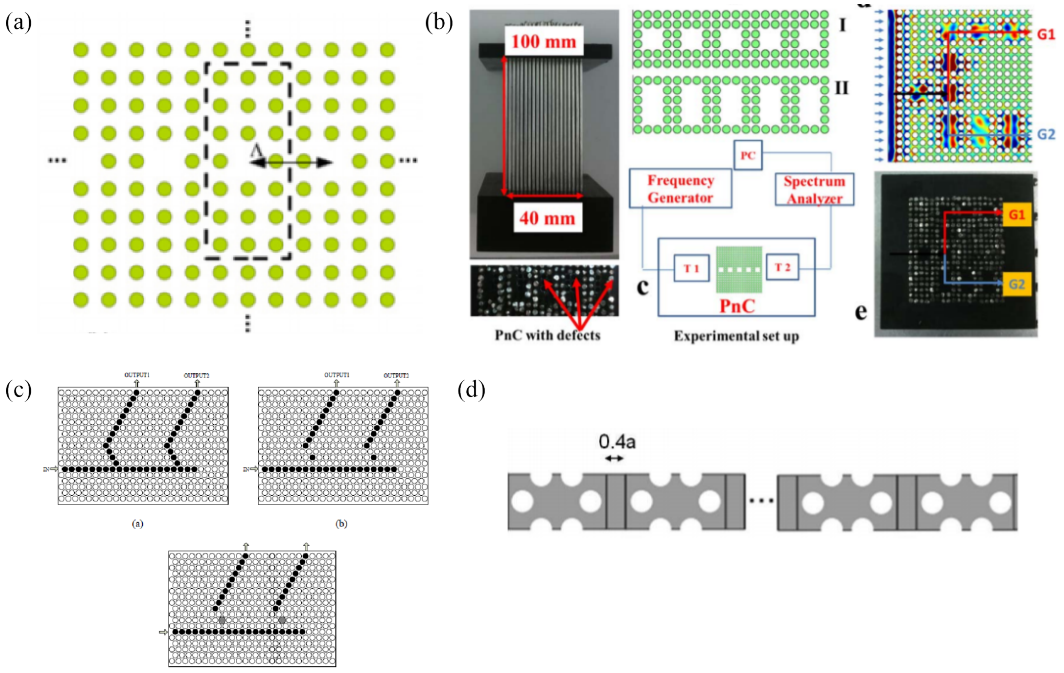

Figure 1.13: (a) CREW [137]; (b) CRAW [205]; (c) Filter based on CREW; (d) VHF Phononic Band Gap Band Pass Filters using CRAW [111].

resonator waveguides have been extended to the field of phononic crystals, because the propagation of waves in evanescent coupled optical waveguides is simple and efficient among various physical mechanisms of guiding light waves in photonic crystals. In contrast to linear waveguides, the coupled-resonator waveguide is based on the coupling mechanism of evanescent wave caused by defect cavities or resonators [42, 198, 166], realizing the design of rather arbitrary acoustic circuits [72, 137].

The coupling between the neighboring defect cavities or resonators causes a band with a smaller slope near the flat band generated by point defect, that is, a defect band. The eigenmodes entering the band gap are called defect states. Since the frequency of the defect state is in the band gap of the perfect structure, the defect state is completely localized in the defect. The field beyond the defect is evanescent, decaying exponentially as it moves away from the defect. Waveguides based on linear chains of coupled cavities have been shown theoretically to allow simultaneously for very strong wave confinement [25, 104, 40] and for low group velocity transmission [137]. It is conducive to design new and efficient acoustic devices. The coupled-resonator waveguide is extremely sensitive to local changes in the defect cavities or resonators, so its dispersion relationship is ultimately determined by the coupling strength between the defect cavities or resonators.

In fact, as long as the distance between the resonators in the coupled-resonator waveg-

uide is not too far and they have the same initial resonance frequencies, any defect chain that acts as defect cavities or resonators can form a waveguide [43]. This is the basic idea of a coupled-resonator waveguide. Coupled-resonator waveguides can't only manipulate the wave propagation by changing the length of the waveguides, but also regulate the dispersion relationship by changing the distance between the resonators, the numbers of resonators on the circuits, and adjusting the coupling coefficient between the resonators. Li et al. proved that the design of a coupled-resonator elastic waveguide (CREW) by introducing a resonator unit into the splitter can improve its separation performance, as shown in figure 1.13 (c). Mohammadi et al. [111] realized an effective band-pass filter for wireless communication based on a coupled-resonator acoustic waveguide (CRAW) designed in a phononic crystal plate, as shown in figure 1.13 (d). For two-phase phononic crystals composed of two materials, the coupled resonant waveguide can also be realized by the coupling between different materials on the path, especially the coupling of solid and fluid materials. The coupled-resonator acoustoelastic waveguide (CRAEW) can tune the band gaps of the phononic crystal by changing the physical and geometric properties of the material, such as the material properties of the solid matrix, the density and height of the fluid fillings, etc. Active or smart control of wave propagation is achieved. Due to the diversity of wave control in the coupled resonant waveguide and the flexibility in the design of the dispersion relationship, it can also excite more propagating modes. However, the existing works are mainly focused on CRAWs, as shown in figure 1.13 (b). There are few studies on CREWs and further CRAEWs, while the corresponding experimental verifications are lacking.

So far, the existing studies have only analyzed the different intervals between resonators in the coupled resonant waveguide which will generate different transmission characteristics. There has been no corresponding physical mechanism being proposed to explain the influence of the coupling coefficient between the resonators on wave propagation. Moreover, there are great limitations in the design of the circuit, which is limited by the periodic coupled-resonator waveguide, and the wave propagation along the aperiodic waveguide has not been realized. The circuit design of the periodic coupled-resonator waveguide is also very simple, and the influences of the circuit length and the numbers of bends on the wave propagation has not been studied. Most importantly, there is almost no research on the CRAEWs, which is the acoustoelastic waveguide by the coupling of acoustic and elastic waves. Fluid-solid coupling is the easiest way for a phononic crystal to realize the reconfigurability. It is also easier to achieve the active and smart control of acoustic/elastic waves. How to realize reconfigurability in the coupled resonant waveguide is still an urgent problem to be solved. In general, almost all the works of coupled reso-

nant waveguides are limited to numerical simulations and a small amount of theoretical analysis, and lack experimental verification.

1.4/ OBJECTIVES AND PLAN OF THE THESIS

1.4.1/ OBJECTIVES OF THE THESIS

In the past decade, some achievements have been realized in the related researches on the wave manipulation of phononic crystals. But there are still many problems that need to be solved urgently. For example, the wave propagation properties in coupled-resonator waveguides have not been fully developed. The corresponding theoretical model has not yet been proposed. The reconfigurability of fluid-solid phononic crystals need to be further studied and lack of experimental verifications. This thesis will focus on the following four aspects:

(1) For the periodic coupled-resonator waveguides in phononic crystals, how to express the functional relationship between the transmission oscillations and frequencies? What effects do the length and distribution of the coupled-resonator waveguides have on wave propagation? There is no experimental verification for the propagation of Lamb waves in coupled-resonator straight waveguides and bent waveguides. We will design different types of periodic coupled-resonator waveguides, develop corresponding theoretical models, and study the transmission properties of acoustic/elastic waves in periodic coupled-resonator waveguides combined with the experimental measurements in this thesis.

(2) So far, the research on coupled resonant waveguides is limited to periodic waveguides. How to break the limitation of periodicity and realize the wave propagation along an aperiodic waveguide? How to achieve collective resonances at ultrasonic frequencies? We will design an aperiodic coupled-resonator waveguide, develop an approximate theoretical model, and study the vibration characteristics of the resonators combined with the experimental measurements in this thesis.

(3) The coupled resonant acoustic waveguide has very rich physical properties. There have been studies to manipulate the locally resonant band gaps in phononic crystals by changing the geometric parameters of the solid resonators. However, this kind of structure cannot be changed once it is fabricated, and the frequency range is fixed, which brings large limitations to the control of wave propagation. Therefore,

how to accurately realize the tunable control of wave propagation without changing the topology and material parameters of the structure and the characteristics of the resonators? We will design a one-dimensional tunable resonant waveguide, and realize the manipulation of the band gaps by filling the matrix with fluid without changing the properties of the resonators with experimental verifications in this thesis.

(4) Reconfigurability is easier to realize in the coupled resonant acoustoelastic waveguide. Therefore, in addition to adjusting the characteristics of the matrix, how to achieve the tunable manipulation of waves by changing the properties of the resonators without changing the structural size and material properties of the existing processing? We will design different kinds of coupled resonant acoustoelastic waveguides and study their transmission properties based on the fluid-solid phononic crystals in this thesis. Based on the one-dimensional phononic metastrip and the two-dimensional phononic metaplate, different kinds of reconfigurable waveguides are designed by filling the resonators with fluid without changing the characteristics of the matrix. We will investigate the wave propagation properties along them combined with experimental measurements.

1.4.2/ PLAN OF THE THESIS

In this thesis, several problems of acoustic/elastic wave propagation in coupled-resonator waveguides are studied numerically, theoretically and experimentally. The main work contains the following parts:

In chapter 1, we introduce the concept, basic characteristics, application prospects, and calculation methods of phononic crystals, summarize the wave tunable manipulations of phononic crystals, introduce the concept of coupled-resonator waveguides and the related characteristics, and finally point out the main research purposes and research contents of this thesis.

In chapter 2, we introduce the methods of calculating the band structure using finite element methods, develop the calculation methods of the complex-wavevector band structure, complex-eigenfrequency band structure and resolvent band structure of viscoelastic phononic crystals. The method of solving the fluid-solid coupling problem is introduced by the finite element method.

In chapter 3, we develop the theoretical model of the channeled spectrum and predict the shape and field distribution of the channeled spectrum in the periodic coupled-resonator

waveguides. The influences of material parameters on the band structures of the coupled-resonator waveguide are analyzed. The propagation of acoustic/elastic waves in different types of periodical coupled-resonator waveguides is studied and verified by experiments.

In Chapter 4, the concept of the phononic polymer is proposed. The corresponding approximate theoretical model is developed to describe the number of resonance frequencies and calculate the band structures. An aperiodic coupled-resonator waveguide is designed and processed in a micro-scale phononic crystal plate, and its vibration properties are studied and measured.

In chapter 5, we design a one-dimensional tunable resonant waveguide and discuss the influences of material viscosity and lattice constant on different band structures. By filling the fluid into the matrix without changing the characteristics of the resonators and adjusting the height of the fluid, the tunable manipulation of the band structures and transmission spectra of the phononic crystal is realized, which is verified by the experiments.

In Chapter 6, we design the coupled resonant acoustoelastic waveguides with different lengths and bends based on the fluid-solid phononic crystal. The transmission properties are studied and the influence of the distance between neighboring resonators on the band structure is discussed. The phononic metastrip and metaplate are designed. The band structure is manipulated by filling fluid into the resonators without changing the characteristics of the matrix. Different reconfigurable waveguides are designed and their transmission properties are studied and measured with the corresponding experiments.

In chapter 7, we summarize the whole work and propose prospects for further works.

1.5/ LIST OF PAPERS

1. Ting-Ting Wang, Sylwester Bargiel, Franck Lardet-Vieudrin, Yan-Feng Wang, Yue-Sheng Wang, and Vincent Laude, Phononic Coupled-resonator waveguide microcavities, Applied Sciences, 2020, 10: 6751.

2. Ting-Ting Wang, Sylwester Bargiel, Franck Lardet-Vieudrin, Yan-Feng Wang, Yue-Sheng Wang, and Vincent Laude, Collective resonances of a chain of coupled phononic microresonators, Physical Review Applied, 2020, 13: 014022.

3. Ting-Ting Wang, Vincent Laude, Muamer Kadic, Yan-Feng Wang and Yue-Sheng Wang, Complex-eigenfrequency band structure of viscoelastic phononic crystals, Applied Sciences, 2019, 9: 2825.

4. Ting-Ting Wang, Yan-Feng Wang, Yue-Sheng Wang, and Vincent Laude, Evanescent-wave tuning of a locally resonant sonic crystal, Applied Physics Letters, 2018, 113: 231901.

5. Ting-Ting Wang, Yan-Feng Wang, Yue-Sheng Wang, and Vincent Laude, Tunable fluid-filled phononic metastrip, Applied Physics Letters, 2017, 111: 041906.

6. Yan-Feng Wang, Ting-Ting Wang, Jin-Ping Liu, Yue-Sheng Wang, and Vincent Laude, Guiding and splitting Lamb waves in coupled-resonator elastic waveguides, Composite Structures, 2018, 206: 588-593.

7. Yan-Feng Wang, Ting-Ting Wang, Jun-Wei Liang, Yue-Sheng Wang, and Vincent Laude, Channeled spectrum in the transmission of phononic crystal waveguides, Journal of Sound and Vibration, 2018, 437: 410-421.

8. Yan-Feng Wang, Ting-Ting Wang, Yue-Sheng Wang, and Vincent Laude, Reconfigurable phononic-crystal circuits formed by coupled acoustoelastic resonators, Physical Review Applied , 2017, 8: 014006.

2

COMPUTATION OF WAVE PROPERTIES BASED ON FEM

2.1/ INTRODUCTION

The manipulation of band gaps plays an important role in the application of phononic crystals. The energy band structure is the most direct and effective way to characterize band gap characteristics. Due to its wide application range, fast calculation speed, good convergence, etc., the finite element method has been widely used in various fields. Currently, kinds of commercial software have been developed, such as ABAQUS, ANSYS, NASTRAN, or COMSOL. Free software such as FreeFem++ is available as well. COMSOL and FreeFem++ can directly perform complex number operations. They can solve complex coefficient eigenvalue equations, which improves the efficiency of modeling and solving. Another feature of COMSOL is that it can conduct multiphysics coupling analysis, especially in fluid-solid coupling problems.

In this chapter, we introduce the calculation of band structures of phononic crystals based on the commercial software COMSOL. Particularly, we develop the calculation of complex-wavevector band structures, complex-eigenfrequency band structure and resolvent band structure of viscoelastic phononic crystals.

2.2/ ACOUSTIC/ELASTIC WAVE EQUATION

In solid media that are linear elastic with small deformation, anisotropic, non-damping and passive non-uniform, the elastic wave equation is [10]

$$\nabla \cdot [\mathbf{C}(\mathbf{r}) : \nabla \mathbf{u}(\mathbf{r}, t)] = \rho(\mathbf{r}) \frac{\partial^2 \mathbf{u}(\mathbf{r}, t)}{\partial t^2}, \tag{2.1}$$

where $\mathbf{u} = (u_x, u_y, u_z)$ presents the displacement vector; $\mathbf{r} = (x, y, z)$ is the position vector; $\nabla = (\partial/\partial x, \partial/\partial y, \partial/\partial z)$ is the differential operator; ":" represents the double dot product and t is the time variable. $\mathbf{C}(\mathbf{r})$ and $\rho(\mathbf{r})$ are the material elastic tensor and the mass density, respectively. Eq. (2.1) can also be written as the following component form:

$$\nabla_{iJ} T_J = \rho(\mathbf{r}) \frac{\partial^2 u_i}{\partial t^2}, \tag{2.2}$$

where T_J is the element of stress tensor $\mathbf{T} = [\sigma_{xx}, \sigma_{yy}, \sigma_{zz}, \sigma_{yz}, \sigma_{xz}, \sigma_{xy}]^T$, and

$$T_I = C_{IJ} S_J, \tag{2.3}$$

where S_J is the element of strain tensor $\mathbf{S} = [\varepsilon_{xx}, \varepsilon_{yy}, \varepsilon_{zz}, \varepsilon_{yz}, \varepsilon_{xz}, \varepsilon_{xy}]^T$; C_{IJ} is the concise notation of C_{ijkl}, $I, J = 1, 2, 3, 4, 5, 6$, and meet the following correspondence:

$$1 \leftrightarrow xx, 2 \leftrightarrow yy, 3 \leftrightarrow zz, 4 \leftrightarrow yz, zy, 5 \leftrightarrow xz, zx, 6 \leftrightarrow xy, yx, \tag{2.4}$$

The differential operator ∇_{iJ} is

$$\nabla_{iJ} = \begin{bmatrix} \partial/\partial x & 0 & 0 & 0 & \partial/\partial z & \partial/\partial y \\ 0 & \partial/\partial y & 0 & \partial/\partial z & 0 & \partial/\partial x \\ 0 & 0 & \partial/\partial z & \partial/\partial y & \partial/\partial x & 0 \end{bmatrix}. \tag{2.5}$$

For two-dimensional non-uniform media, we assume that elastic waves propagate in the $x - y$ plane and that all displacement vectors are independent of z. Elastic waves can be decoupled into plane mixed mode and anti-plane shear mode. When the frequency is ω, their wave equations are [10]:

$$\nabla_T \cdot [\mu(\mathbf{r}) \nabla_T u_i] + \nabla_T \cdot [\mu(\mathbf{r}) \frac{\partial}{\partial x_i} \mathbf{u}_T] + \frac{\partial}{\partial x_i} [\lambda(\mathbf{r}) \nabla_T \cdot \mathbf{u}_T] = -\rho(\mathbf{r}) \omega^2 u_i, i = x, y \tag{2.6}$$

and

$$\nabla_T \cdot [\mu(\mathbf{r})\nabla_T u_z] = -\rho(\mathbf{r})\omega^2 u_z, \tag{2.7}$$

where $\nabla_T = (\partial/\partial x, \partial/\partial y)$; $\mathbf{u}_T = (u_x, u_y)$; and λ and μ are the Lamé coefficients of the material.

When the medium is a gas or a liquid, only longitudinal wave exists. If the viscosity is not considered, the wave equation is [45]:

$$\nabla \cdot \left(\frac{1}{\rho(\mathbf{r})}\nabla p\right) = -\frac{1}{\rho(\mathbf{r})c_0^2(\mathbf{r})}\omega^2 p, \tag{2.8}$$

where p presents the pressure; and c_0 is the velocity of acoustic waves.

Comparing the Eq. (2.7) and Eq. (2.8), it can be inferred that these two equations are equivalent if p , $1/\rho$ and $1/(\rho c_l^2)$ correspond to u_z, μ and ρ, respectively. Hence, we can calculate the band structures of anti-plane shear modes by solving the plane acoustic wave equation.

2.3/ BAND STRUCTURES OF PHONONIC CRYSTALS

2.3.1/ REAL BAND STRUCTURE

In this subsection, we will introduce the commonly used finite element method (FEM) to calculate the real band structures of the considered phononic crystal. The basis is to solve the wave equation. Based on Bloch's theorem, we apply the Bloch-Floquet periodic condition to the structures. Due to the periodicity of phononic crystals, the calculation can be implemented in a representative unit cell, as shown in figure 2.1. After the finite mesh of the unit cell is created adaptively, it is divided into finite elements connected by nodes. The discrete form of the eigenvalue equation in the unit cell can be written as

$$(\mathbf{K} - \omega^2\mathbf{M})\mathbf{U} = 0, \tag{2.9}$$

where $\mathbf{K}$ is the stiffness matrix of the unit cell:

$$\mathbf{K} = \int \mathbf{B}^T\mathbf{C}(\mathbf{r})\mathbf{B}\mathrm{d}Ve. \tag{2.10}$$

$\mathbf{M}$ is the mass matrix of the unit cell,

$$\mathbf{M} = \int \rho(\mathbf{r})\mathbf{N}^T\mathbf{N}\mathrm{d}Ve. \tag{2.11}$$

In the equation, $\mathbf{B}$ is strain matrix; $\mathbf{N}$ is shape function matrix and V_e presents the whole area of the unit cell. What's more, $\mathbf{U}$ is the displacement matrix,

$$\mathbf{U} = \begin{bmatrix} \mathbf{U}_1 & \mathbf{U}_2 & \cdots & \mathbf{U}_n \end{bmatrix}^T, \tag{2.12}$$

where $\mathbf{U_i}$ is the displacement at the nodes,

$$\mathbf{U}_i = \begin{bmatrix} u_i & v_i & w_i \end{bmatrix}^T (i = 1, 2, \cdots, n). \tag{2.13}$$

Suppose that elastic waves propagate along the periodic plane (i.e.the x–y plane), $\Psi(\mathbf{r})$ is the elastic displacement vector. According to Bloch's theorem, the displacement field can be expressed as

$$\Psi(\mathbf{r}) = e^{i(\mathbf{k}\cdot\mathbf{r})}\Psi_{\mathbf{k}}(\mathbf{r}), \tag{2.14}$$

where $\Psi = u_x, u_y$; $\mathbf{k} = (k_x, k_y)$ is the wavevector; $\Psi_{\mathbf{k}}(\mathbf{r})$ is a periodical vector function with the same periodicity as the crystal lattice. Bloch's theorem is applied on the boundaries of the unit cell in the direction where periodicity applies, yielding the following relation between displacements $\mathbf{U}(\mathbf{r})$ at the nodes on the boundary of the unit cell:

$$\mathbf{U}(\mathbf{r} + \mathbf{a}) = e^{i(\mathbf{k}\cdot\mathbf{a})}\mathbf{U}(\mathbf{r}), \tag{2.15}$$

where $\mathbf{r}$ is located at the boundary nodes and $\mathbf{a}$ is the lattice constant vector. We solve directly the eigenvalue problem Eq. (2.9) given the wavevector $\mathbf{k}$ under the complex boundary condition Eq. (2.15). We can get the whole band structure when the wavevector $\mathbf{k}$ sweep the irreducible Brillouin zone. If only the band gaps are needed, we simply sweep the edges of the irreducible Brillouin zone. It is called the $\omega(k)$ method that fixes the wavevector $\mathbf{k}$ and solves the eigenfrequencies ω.

In our work, COMSOL Multiphysics 5.4 is utilized to calculate directly the real band structure of the unit cells. It can also solve a given problem in the complex domain directly without dividing it into the real and imaginary parts, thus we can impose the Bloch boundary conditions on the boundaries of a single unit cell directly. In addition, COMSOL can also perform multi-field coupling calculations to study the solid-fluid coupling problem in phononic crystal structures. Next, we use the different modules of the COMSOL and give

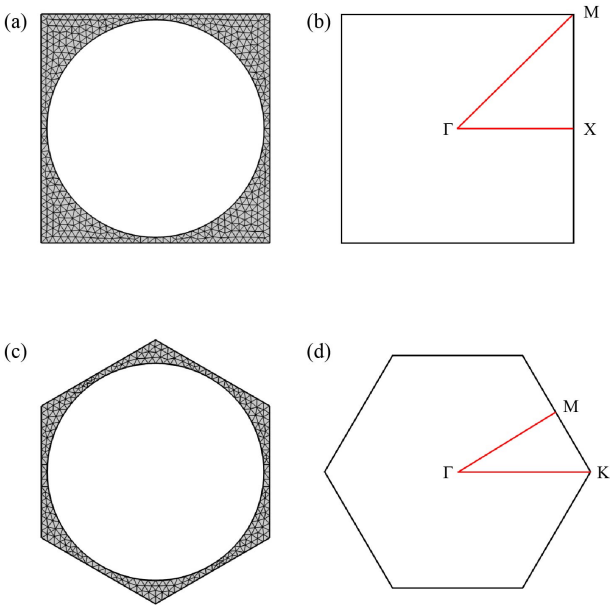

Figure 2.1: Finite element model of the unit cells and the corresponding irreducible Brillouin zones of PC with a square or triangular Bravais lattice.

the examples of the square lattice and hexagonal lattice to present the calculation process and results of the real band structures. Figure 2.1 gives the geometric shape of the unit cells of different lattice and the corresponding Brillouin zones. The triangle parts are the boundaries of the irreducible Brillouin zone where the wavevector $\mathbf{k}$ only needs to be swept during the calculation process of the band structure.

The Solid Mechanics Module can directly solve the mixed modes. In this module, the frequency is analysed as the eigenvalue. The periodic condition 'Floquet periodicity' in COMSOL Multiphysics 5.4 implements the Bloch-Floquet periodic boundary condition. As a matter of fact, there is no specific module to calculate directly the 2D anti-plane shear waves. Considering this, we use the Pressure Acoustic Module to solve the problem in the light of the similarity of Eq. (2.7) and Eq. (2.8).

2.3.1.1/ TWO DIMENSIONAL PHONONIC CRYSTAL

In this subsection, we consider a 2D phononic crystal with a circular hole in the unit cell as an example. The diameter of the hole is $d = 0.95a$ and the lattice constant is a. Steel is chosen as the solid material. The material parameters are shown in Table 2.1. The band structures of 2D steel PC in square and hexagonal lattice with the mixed mode (a) and the shear mode (b) are shown in figures 2.2 and 2.3, respectively. The insets are the lower (A) and upper (B) edge modes of the band gap respectively in figures 2.2(a)

Table 2.1: Material parameters

material	ρ (kg/m^3)	c_l (m/s)	c_t (m/s)
Steel	7780	5940	3240
Water	1000	1490	

and 2.3(a).

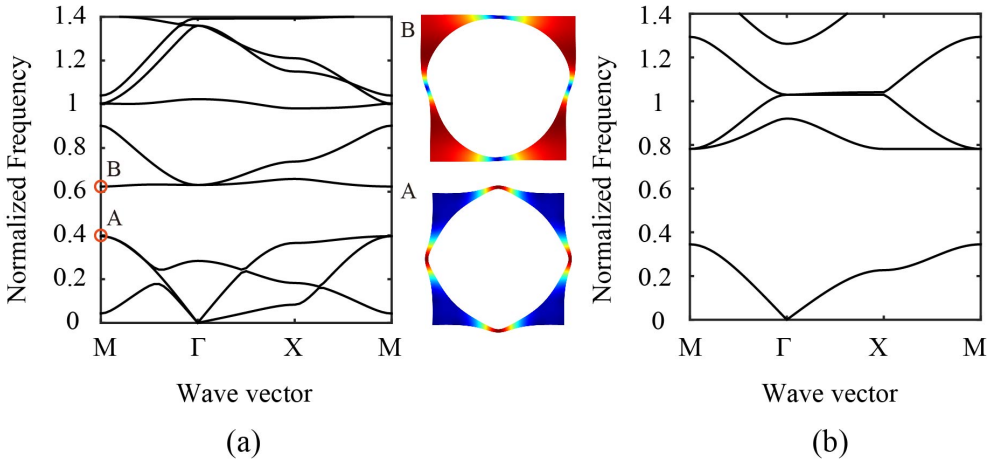

Figure 2.2: Band structures of two-dimensional hole/steel PC in a square lattice: (a) the mixed mode, (b) the shear mode.

The y-axis of the band structure presents the normalized frequency $\Omega = \omega a/(2\pi c_t)$, where $c_t = \sqrt{\mu/\rho}$ is the shear velocity of the steel matrix. The triangle elements are used for meshing the unit cell. For the square lattice, the degrees of freedom to solve the mixed mode and shear mode are 946 and 522, respectively. For the hexagonal lattice, the degrees of freedom to solve the mixed mode and shear mode are 646 and 364, respectively.

2.3.1.2/ TWO DIMENSIONAL PHONONIC CRYSTAL SLAB

We can extend the 2D phononic crystal to a 2D phononic slab and investigate the real band structure. The diameter and height of the unit cell are $d = 0.95a$ and $h = 0.4a$ where a is the lattice constant. Generally, the free boundary condition is imposed on the top and bottom surface and on the inner wall of the hole of the unit cell as shown in figure 2.4. Bloch boundary conditions are applied on the two opposite surface of the unit cell. The top surface of the unit cell is first meshed by using the default triangular elements then the mesh is swept along the z-axis. The swept meshing can largely reduce the number of degrees of freedom which is 6382 to shorten the calculation time.

The band structure of the 2D phononic crystal slab is illustrated in figure 2.5. It can be

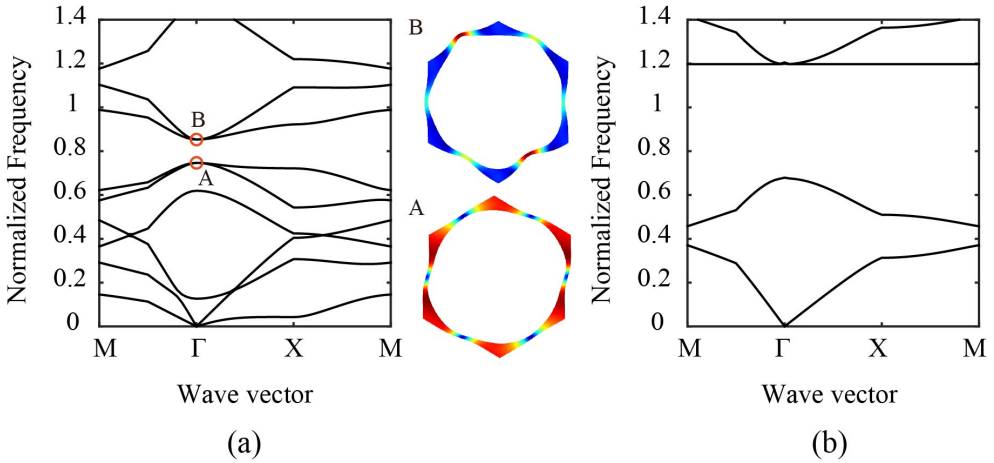

Figure 2.3: Band structures of two-dimensional hole/steel PC in a hexagonal lattice: (a) the mixed mode, (b) the shear mode.

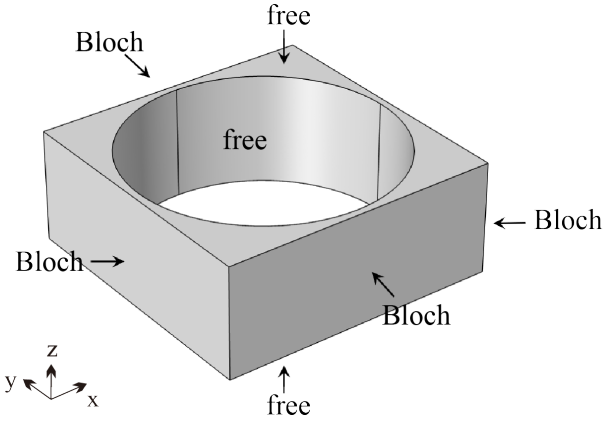

Figure 2.4: Schematic diagram of unit cell of the two-dimensional steel PC slab with hole in a square lattice.

seen from the figure that there is one band gap between the sixth and the seventh bands, where the normalized frequency range is 0.48-0.60.

2.3.1.3/ TWO DIMENSIONAL FLUID/SOLID PHONONIC CRYSTAL

Acoustic waves satisfy the wave equation Eq. (2.8) during wave propagation in inhomogeneous media, which in homogeneous media can be converted to

$$\frac{\partial^2 p}{\partial x^2} + \frac{\partial^2 p}{\partial y^2} + \frac{\partial^2 p}{\partial z^2} - \frac{1}{c_0{}^2}\frac{\partial^2 p}{\partial t^2} = 0. \tag{2.16}$$

For the fluid-solid coupling cases, there are three main types of fluid boundaries: The first

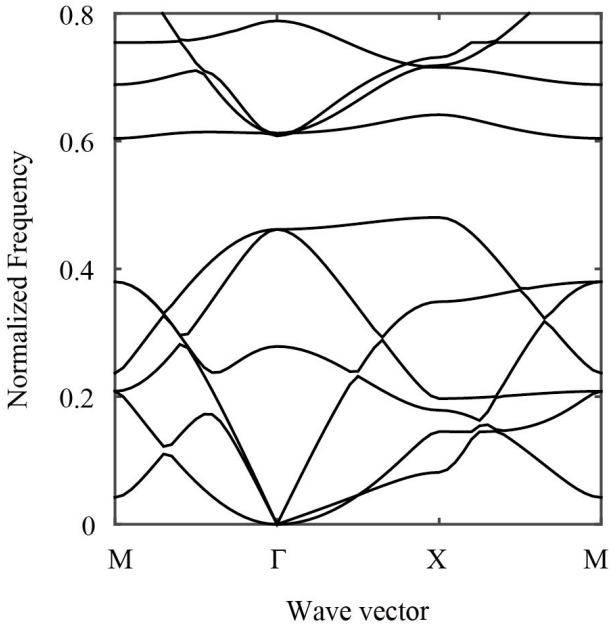

Figure 2.5: Band structure of a two-dimensional steel PC plate with a hole in a square lattice.

one is the fluid boundary with known pressure, for which the boundary condition is

$$p = p_0, \tag{2.17}$$

where p_0 is the value of the acoustic pressure. This kind of fluid boundary changes to a free boundary when $p_0 = 0$.

The second boundary is the fluid-solid coupled interface where the normal velocity is continuous. The equation of the boundary condition is

$$\frac{\partial p}{\partial \mathbf{n}} = \rho \frac{\partial^2 u_n}{\partial t^2} \mathbf{n}, \tag{2.18}$$

where u_n is the normal displacement of the solid boundary, and $\mathbf{n}$ is the normal unit vector.

The third one is called the fixed boundary condition where the normal displacement is zero. The boundary condition

$$p_{,n} = 0 \tag{2.19}$$

can be used as a sound hard boundary where the incident acoustic wave can be totally reflected.

Considering the fluid-solid interaction, the discrete form of the eigenvalue equations can

be written as

$$\begin{pmatrix} \mathbf{K}_s & \mathbf{S}_{fs}^T \\ \mathbf{0} & \mathbf{K}_f \end{pmatrix} \begin{pmatrix} \mathbf{u} \\ \mathbf{p} \end{pmatrix} = \omega^2 \begin{pmatrix} \mathbf{M}_s & \mathbf{0} \\ -\mathbf{S}_{fs} & \mathbf{M}_f \end{pmatrix} \begin{pmatrix} \mathbf{u} \\ \mathbf{p} \end{pmatrix}, \tag{2.20}$$

where $\mathbf{u}$ and $\mathbf{p}$ present the displacement at the unit node of the solid field and the pressure at the unit node of the fluid field, respectively; $\mathbf{K}_s$ and $\mathbf{K}_f$ are the stiffness matrices of the solid and fluid; $\mathbf{M}_s$ and $\mathbf{M}_f$ are the mass matrices of the solid and fluid; $\mathbf{S}_{fs}$ represents the fluid-solid coupling matrix and $\mathbf{S}_{fs}^T$ is its transpose matrix. According to the dynamic equilibrium equation Eq. (2.20) under the coupling between fluid and solid, we can calculate the pressure in the fluid field and the displacement and the velocity in the solid field.

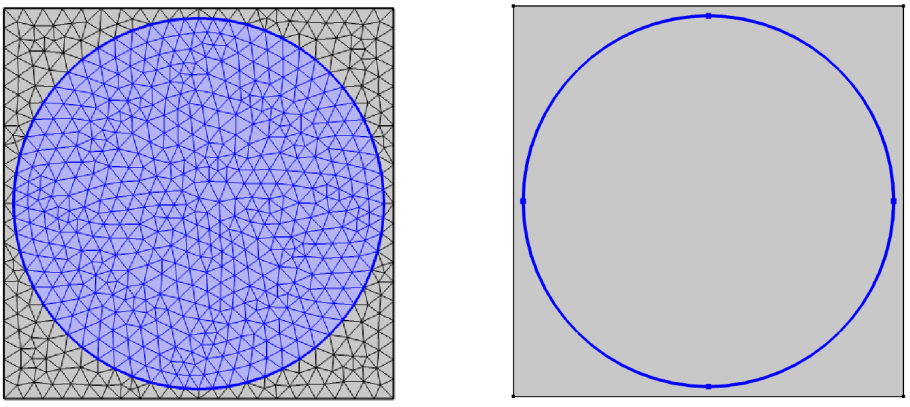

Figure 2.6: The element mesh (a) and acoustic structure boundary condition (b) in the unit cell of the two-dimensional water/steel PC in a square lattice.

COMSOL Multiphysics 5.4 can be used to solve the fluid-solid coupling problem by building the corresponding finite element model according to the above theory. The Pressure Acoustic Module is chosen to compute the band structure. The fluid-solid boundary condition is applied at the interface between the fluid and solid and is the 'Acoustic-Structure Boundary' in COMSOL as shown in figure 2.6 (b).

Here we take the model of filling water into the steel hole in a square lattice for the example shown in figure 2.6 (a). The diameter of the hole is $d = 0.95a$. For meshing, the number of degrees of freedom is 3136. The material parameters are presented in table 2.1.

Then we get the band structure of the fluid-solid structure. From figure 2.7 (a), we can infer that there is a full band gap existing between the fifth and sixth bands where the

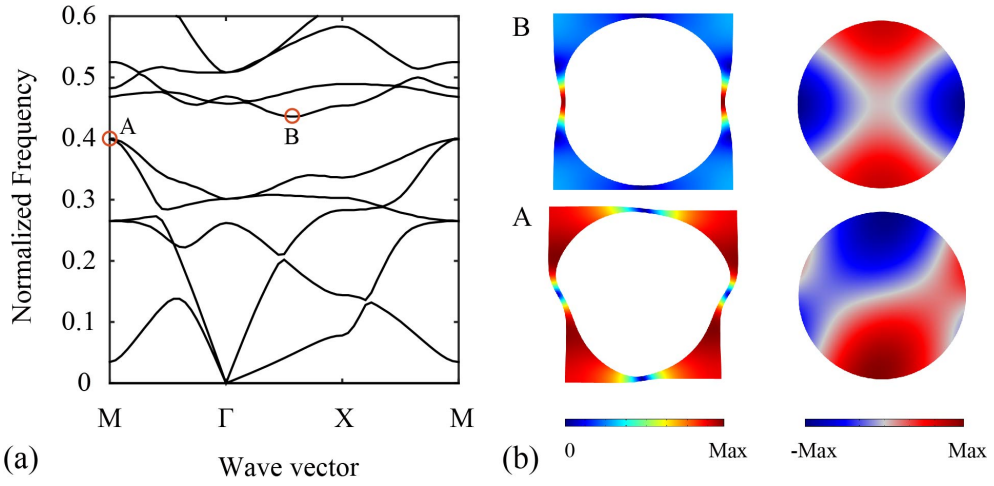

Figure 2.7: (a) Band structures of two-dimensional water/steel PC in a square lattice. (b) The displacement distribution of the solid field and the pressure distribution of the fluid field at the lower edge (A) and upper edge (B) of the band gap.

normalized frequencies range is 0.399-0.436. The displacement distribution of the solid field and the pressure distribution of the fluid field at the lower edge (A) and upper edge (B) of the band gap are presented in figure 2.7 (b). It can be inferred that the displacement and pressure distribution are totally associated.

2.3.2/ COMPLEX-WAVEVECTOR BAND STRUCTURE

The consideration of material losses in phononic crystals leads naturally to the introduction of complex-valued eigenwavevectors representing the attenuation of elastic waves in space. When the frequency ω is a real-valued dependent variable, then a complex-wavevector will be obtained to describe the mode attenuation with space. In this way, a complex-wavevector band structure can be obtained, in which the relationship between the real part of the wavevector and the frequency is characterized as the dispersion relationship, while the relationship between the imaginary part and the frequency presents the attenuation characteristics. Therefore, it is necessary to use the wavevector $\mathbf{k}$ as the eigenvalue to solve the problem when using the finite element software to solve the problem. This method is called $\mathbf{k}(\omega)$ method. This subsection gives the calculation method of the complex-wavevector band structure based on the Partial Differential Equation (PDE) module in COMSOL.

The governing equation in coefficient form in the PDE module is

$$\mathbf{e}_a\Lambda^2\mathbf{U} - \mathbf{d}_a\Lambda\mathbf{U} - \nabla\cdot(\mathbf{c}:\nabla\mathbf{U} + \boldsymbol{\alpha}\mathbf{U} - \boldsymbol{\gamma}) + \mathbf{b}\mathbf{U} + \boldsymbol{\beta}\cdot\nabla\mathbf{U} = \mathbf{f}. \tag{2.21}$$

There are two kinds of boundary conditions, namely Neumann boundary condition:

$$\mathbf{n} \cdot (\mathbf{c} : \nabla \mathbf{U} + \boldsymbol{\alpha} \mathbf{U} - \boldsymbol{\gamma}) + \mathbf{q}\mathbf{U} = \mathbf{g} - \mathbf{h}^T \boldsymbol{\vartheta} \tag{2.22}$$

and Dirichlet boundary condition:

$$\mathbf{h}\mathbf{U} = \mathbf{r}, \tag{2.23}$$

where Λ is the eigenvalue; $\mathbf{e}_a$ is the mass coefficient; $\mathbf{d}_a$ is the damping coefficient; $\mathbf{c}$ is the diffusion coefficient; $\boldsymbol{\alpha}$ is the conservative flux convection coefficient; $\boldsymbol{\beta}$ is the convection coefficient; γ is the conservative flux source term; $\mathbf{b}$ is the absorption coefficient and $\mathbf{f}$ is the source term. What's more, $\mathbf{h}$, $\mathbf{g}$, $\mathbf{q}$ and $\mathbf{r}$ are undetermined coefficients or coefficient matrices; $\mathbf{n}$ is the outer normal unit vector of the boundary; an unknown quantity $\boldsymbol{\vartheta}$ is called the Lagrange multiplier, which is only defined on the boundary; $\mathbf{h}^T$ is the transpose of $\mathbf{h}$ in Neumann boundary condition of equation Eq. (2.22) and $\mathbf{h}^T = \mathbf{h}$ if $\mathbf{h}$ is a scalar.

When $\mathbf{e}_a$ or $\mathbf{d}_a$ is zero, Eq. (2.22) is a linear eigenvalue equation. And if both $\mathbf{e}_a$ and $\mathbf{d}_a$ are not zero, then Eq. (2.22) is a quadratic eigenvalue equation. COMSOL converts it into a linear eigenvalue equation by introducing variables. After the constraints are processed, an equation set of the form $\mathbf{A}x = \Lambda \mathbf{B}x$ can be obtained. Then we can use ARPACK to solve the eigenvalue of the matrix

$$\mathbb{C} = \mathbf{A}^{-1}\mathbf{B} \tag{2.24}$$

to get the eigenvalues of the problem.

Then, sweeping in the frequency range of interest to obtain the complex-wavevector gives the complex band structure of the phononic crystal.

Another system that has been often considered for microsonic applications is the case of holes in a crystal matrix [67]. In the case of silicon phononic crystal, cylindrical holes can be obtained by etching at the microscale. We take a 2D phononic crystal with circle hole in the unit cell as an example. The diameter of the hole is $0.833a$ and the lattice constant is a=1μm. The complex-wavevector band structures are shown in figure 2.8. Panels (a)

Table 2.2: Independent material constants

Silicon	$\rho = 2331$ kg/m^3		
(cubic)	$c_{11} = 165.7$ GPa	$c_{66} = 79.62$ GPa	$c_{12} = 63.9$ GPa
	$\eta_{11} = 1.505$ mPa.s	$\eta_{66} = 0.553$ mPa.s	$\eta_{12} = -0.532$ mPa.s

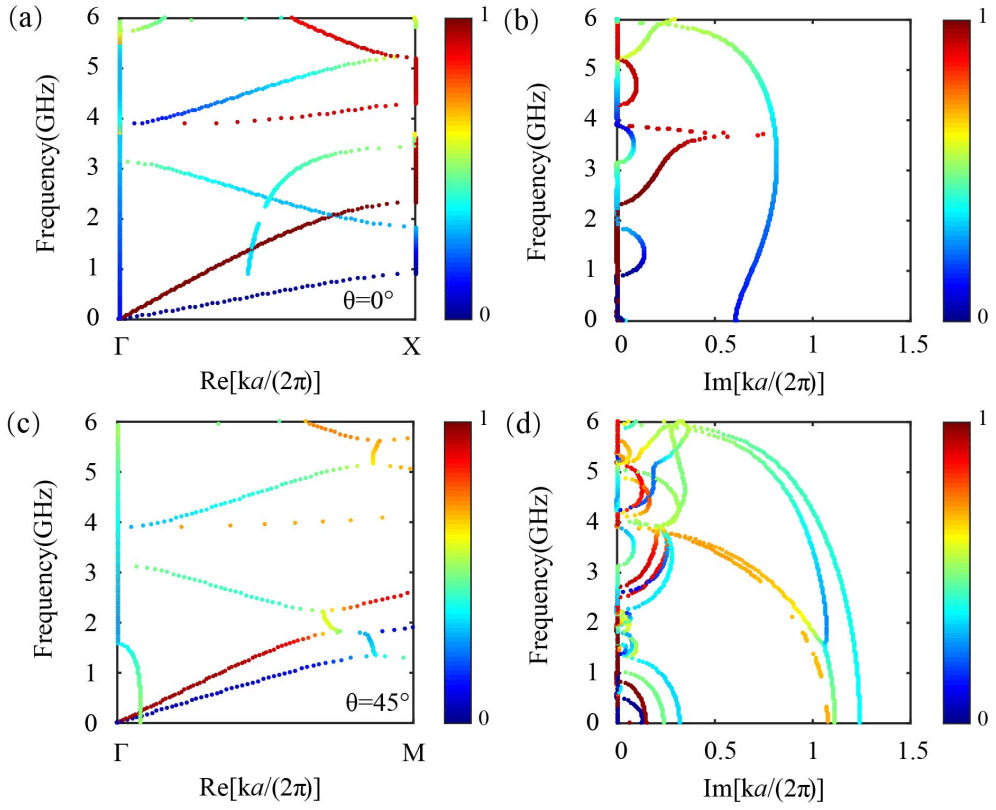

Figure 2.8: Complex-wavevector band structures for square lattice phononic crystal composed of holes in silicon: (a)-(b) $\theta = 0°$, (c)-(d) $\theta = 45°$

and (b) illustrate the variation of the frequency with the real and imaginary parts of the wavevector for the direction $\theta = 0°$ (ΓX), respectively. On the other side, panels (c) and (d) present the real and imaginary part of the wavevector for the direction ΓM, which correspond to $45°$ for square lattice. The imaginary part here has no periodicity and only shows the part within a limited range ($|\mathrm{Im}(ka/(2\pi))| \leq 1.5$), but there are other complex bands outside this range. It can be seen from the figure that a Bragg band gap appears in the frequency range 3.15-3.89 GHz between the third and fourth bands. There are other wave modes with a different dispersion besides the propagating Bloch waves existing in the real part of the complex-wavevector band structure, namely evanescent waves, which cannot be revealed by the real band structure. The wavevectors of these modes have a non-zero imaginary part. The magnitude of their spatial attenuation is determined by the value of the imaginary part of the wavevector.

It is worth noting that from the imaginary part of the complex-wavevector band structure in figure 2.8, the band gap in a strict sense is not that there is no band, but is indicated by the characteristics of the evanescent wave: All Bloch waves must be evanescent in the band gap. In the real band structure, the number of bands at a given frequency

varies. There are as many bands as degrees of freedom at low frequencies. There is no band in the band gap, and the number of bands increases with the frequency. On the contrary, the complex-wavevector band structure is always continuous and will not appear or disappear, since the number of eigenvalues of the wavevector is equivalent to the size of the matrix. Under this mechanism, the number of bands at any frequency remains unchanged. It can also be seen from the imaginary part of the figure that there is a vertical connection between the bands at the high symmetry points of the Brillouin zone, which indicates that the infinite group velocity is related to the exponential decay of the evanescent wave propagation [99].

Due to the periodicity of the system, Bloch waves can be expanded into a series of harmonic waves, each of which corresponds to the real part of the wavevector $\mathbf{k}$. Since the imaginary part of $\mathbf{k}$ is unique for each Bloch wave, its attenuation at a given frequency can be determined. In general, the complex-wavevector band structure gives the possible complex value range of the wavevector $\mathbf{k}$ as a function of frequency. Since the modes of evanescent waves do not satisfy discrete translational symmetry and diverge [35] when they reach infinity along the propagation direction, there is currently no corresponding physical method that can excite the evanescent state in perfect phononic crystals. However, the evanescent waves can still be used to explain the physical properties of modes within the band gap.

2.3.3/ COMPLEX-EIGENFREQUENCY BAND STRUCTURE

The complex-wavevector band structure gives the complex-valued Bloch wavevector as a function of real frequency [89, 31, 105]. It is in essence well suited to the description of the attenuation in space of monochromatic waves originating from a source of finite extent excited at a given frequency [139]. It is the purpose of this subsection to propose a complex-eigenfrequency band structure method that is suited for viscoelastic materials. When the wavevector $\mathbf{k}$ is a real-valued variable, the complex frequency can be obtained by $\omega = \omega' + \mathrm{i}\omega''$. The imaginary part of the frequency, ω'', represents the attenuation of the mode with time. We call the method of solving the frequency as the eigenvalue the $\omega(\mathbf{k})$ method, so that the complex-eigenfrequency band structure is obtained. In particular, the complex-eigenfrequency band structure $\omega(\mathbf{k})$ does not capture any spatial propagation information but provides one with information complementary to the complex band structure $\mathbf{k}(\omega)$.

Elastic Bloch waves have a displacement vector of the form $\mathbf{U}(\mathbf{r}, t) = \mathbf{u}(\mathbf{r}) \exp(\mathrm{i}(\omega t - \mathbf{k} \cdot \mathbf{r}))$ where $\mathbf{u}(\mathbf{r})$ is the periodic part of the Bloch wave, ω is the angular frequency, t is the time

variable, and $\mathbf{k}$ is the Bloch wavevector. In elastic solids, the stress and strain tensors are related by Hooke's law via the order-4 elastic tensor c_{ijkl}. Bloch waves of phononic crystals are obtained by solving an eigenfrequency problem under periodic boundary conditions. In viscoelastic solids, Hooke's law is generalized to a complex-valued elastic tensor $c_{ijkl}+\mathrm{i}\omega\eta_{ijkl}$, with η_{ijkl} being the order-4 phonon viscosity tensor. The imaginary part is thus explicitly proportional to the angular frequency. A complex eigenfrequency band structure can anyway be obtained using the method described in the following and with the assumption that viscoelastic losses are proportional to ω. We start with the formal eigenproblem with a viscoelastic term:

$$(\mathbf{K}(\mathbf{k}) + \mathrm{i}\omega\mathbf{V}(\mathbf{k}) - \omega^2\mathbf{M})\mathbf{u} = \mathbf{0}, \tag{2.25}$$

with $\mathbf{u}$ being a vector of the degrees of freedom (d.o.f), $\mathbf{K}$ a stiffness matrix, $\mathbf{M}$ a mass matrix, and $\mathbf{V}$ a viscosity matrix. Note that both the stiffness matrix and the viscosity matrix are functions of the Bloch wavevector $\mathbf{k}$; we omit the dependence on $\mathbf{k}$ in the rest of this sub-section for simplicity of the presentation. The mass matrix generally has constant coefficients. All matrices are square, and the number of lines equals the number of degree of freedom (d.o.f) of the system. We set $\lambda = \mathrm{i}\omega$ and rewrite Eq. (2.25) as

$$(\mathbf{K} + \lambda\mathbf{V} + \lambda^2\mathbf{M})\mathbf{u} = \mathbf{0}. \tag{2.26}$$

This second-degree polynomial eigen-equation is equivalent to the first-degree system of equations:

$$\mathbf{v} = \lambda\mathbf{u}, \tag{2.27}$$

$$\mathbf{K}\mathbf{u} + \lambda\mathbf{V}\mathbf{u} + \lambda\mathbf{M}\mathbf{v} = \mathbf{0}, \tag{2.28}$$

or finally equivalent to the double-size eigenvalue problem:

$$\begin{pmatrix} \mathbf{K} & \mathbf{0} \\ \mathbf{0} & \mathbf{I} \end{pmatrix} \begin{pmatrix} \mathbf{u} \\ \mathbf{v} \end{pmatrix} = \lambda \begin{pmatrix} -\mathbf{V} & -\mathbf{M} \\ \mathbf{I} & \mathbf{0} \end{pmatrix} \begin{pmatrix} \mathbf{u} \\ \mathbf{v} \end{pmatrix}. \tag{2.29}$$

This asymmetric eigenvalue problem yields complex eigenvalues, and hence the complex-eigenfrequency band structure. The wavevector $\mathbf{k}$ enters via the dependence of matrices $\mathbf{K}$ and $\mathbf{V}$. Note that the eigensystem can be written in an Hermitian symmetric form, providing the mass matrix can be inverted and is symmetric, and both K and V

are Hermitian symmetric, e.g.

$$\begin{pmatrix} \mathbf{K} & \mathbf{0} \\ \mathbf{0} & -\mathbf{M}^{-1} \end{pmatrix} \begin{pmatrix} \mathbf{u} \\ -\mathbf{M}\mathbf{v} \end{pmatrix} = \lambda \begin{pmatrix} -\mathbf{V} & \mathbf{I} \\ \mathbf{I} & \mathbf{0} \end{pmatrix} \begin{pmatrix} \mathbf{u} \\ -\mathbf{M}\mathbf{v} \end{pmatrix}. \tag{2.30}$$

As a result, eigenvalues come in complex conjugate pairs (λ, λ^*). Each pair of eigenfrequencies have the same real part (and hence propagation constant) but opposite imaginary part. The eigenfrequency with positive imaginary part is a mode of vibration that attenuates in time, whereas the eigenfrequency with negative imaginary part is a mode of vibration that amplifies in time. Note that their respective excitation is dictated by initial boundary conditions. For instance, specifying that the energy in the mode cannot grow to infinity with increasing time disqualifies the amplifying mode of vibration.

For elastic waves in solids, the elastodynamic equation for the displacement vector components U_i can be written as the partial differential equation [172]:

$$-[(c_{ijkl}(\mathbf{r}) + \mathrm{i}\omega\eta_{ijkl}(\mathbf{r}))U_{k,l}(\mathbf{r})]_{,j} = \omega^2\rho(\mathbf{r})U_i(\mathbf{r}). \tag{2.31}$$

A variational formulation of the problem of Bloch wave propagation allows one to write the eigenvalue problem in the form Eq. (2.25). Note that we consider the periodic part of the elastic Bloch waves as the variables for the variational formulation. A weak form suitable for finite element implementation can be obtained directly by considering a mixed finite element space with variables $(\mathbf{u}, \mathbf{v})$ and test functions $(\mathbf{u}', \mathbf{v}')$ and reads (where the dependence of functions on the space coordinates is implicit)

$$\int_\Omega \begin{pmatrix} \mathbf{u}' \\ \mathbf{v}' \end{pmatrix}^T \begin{pmatrix} (\nabla + \mathrm{i}\mathbf{k})c(\nabla - \mathrm{i}\mathbf{k}) & \mathbf{0} \\ \mathbf{0} & \mathbf{I} \end{pmatrix} \begin{pmatrix} \mathbf{u} \\ \mathbf{v} \end{pmatrix} \mathrm{d}\Omega = \lambda \int_\Omega \begin{pmatrix} \mathbf{u}' \\ \mathbf{v}' \end{pmatrix}^T \begin{pmatrix} -(\nabla + \mathrm{i}\mathbf{k})\eta(\nabla - \mathrm{i}\mathbf{k}) & -\rho\mathbf{I} \\ \mathbf{I} & \mathbf{0} \end{pmatrix} \begin{pmatrix} \mathbf{u} \\ \mathbf{v} \end{pmatrix} \mathrm{d}\Omega \tag{2.32}$$

under periodic boundary conditions. This is the formulation we use for implementation of the complex-eigenfrequency band structures in this subsection. The different matrices thus have the following formal expressions

$$K(\mathbf{k}) = \int_\Omega (u'_{i,j} + \mathrm{i}k_j u'_i)c_{ijkl}(u_{k,l} - \mathrm{i}k_l u_k)\mathrm{d}\Omega, \tag{2.33}$$

$$V(\mathbf{k}) = \int_\Omega (u'_{i,j} + \mathrm{i}k_j u'_i)\eta_{ijkl}(u_{k,l} - \mathrm{i}k_l u_k)\mathrm{d}\Omega, \tag{2.34}$$

$$M = \int_\Omega u'_i \rho v_i \mathrm{d}\Omega. \tag{2.35}$$

Acoustic Bloch waves have a pressure field of the form $P(\mathbf{r},t) = p(\mathbf{r})\exp(\mathrm{i}(\omega t - \mathbf{k}\cdot\mathbf{r}))$ with $p(\mathbf{r})$ being the periodic part of the pressure field. Wave propagation in a sonic crystal can be written as the partial differential equation

$$-[(\rho(\mathbf{r}))^{-1}P_{,j}(\mathbf{r})]_{,j} = \omega^2(B(\mathbf{r}) + \mathrm{i}\omega\eta(\mathbf{r}))^{-1}P(\mathbf{r}). \tag{2.36}$$

Here the elastic modulus B and the viscosity η are scalar functions of position. Generally speaking, we have a problem to obtain an equation of the form Eq. (2.25) since the kinetic part of the equation involves the inverse function $[B(\mathbf{r})+\imath\omega\eta(\mathbf{r})]^{-1}$. Restricting the problem to a single homogeneous viscous fluid, however, the material constants are independent of space coordinates and Eq. (2.36) can be multiplied by $1+\mathrm{i}\omega\eta/B$ to get

$$-\left[\frac{1}{\rho}P_{,j}(\mathbf{r})\right]_{,j} - \left[\frac{\mathrm{i}\omega\eta}{\rho B}P_{,j}(\mathbf{r})\right]_{,j} = \omega^2\frac{1}{B}P(\mathbf{r}). \tag{2.37}$$

As a result, we can introduce $q=\lambda p$ and the test functions (p',q') to obtain the following variational formulation

$$\int_\Omega \begin{pmatrix} p' \\ q' \end{pmatrix}^T \begin{pmatrix} (\nabla+\mathrm{i}\mathbf{k})\frac{1}{\rho}(\nabla-\mathrm{i}\mathbf{k}) & \mathbf{0} \\ \mathbf{0} & \mathbf{I} \end{pmatrix}\begin{pmatrix} p \\ q \end{pmatrix}\mathrm{d}\Omega = \lambda\int_\Omega \begin{pmatrix} p' \\ q' \end{pmatrix}^T \begin{pmatrix} -(\nabla+\mathrm{i}\mathbf{k})\frac{\eta}{\rho B}(\nabla-\mathrm{i}\mathbf{k}) & -\frac{1}{B}\mathbf{I} \\ \mathbf{I} & \mathbf{0} \end{pmatrix}\begin{pmatrix} p \\ q \end{pmatrix}\mathrm{d}\Omega \tag{2.38}$$

under periodic boundary conditions. The different matrices thus have the following formal expressions

$$K(\mathbf{k}) = \int_\Omega (\nabla q + \mathrm{i}\mathbf{k}q)\frac{1}{\rho}(\nabla p - \mathrm{i}\mathbf{k}p)\mathrm{d}\Omega, \tag{2.39}$$

$$V(\mathbf{k}) = \int_\Omega (\nabla q + \mathrm{i}\mathbf{k}q)\frac{\eta}{\rho B}(\nabla p - \mathrm{i}\mathbf{k}p)\mathrm{d}\Omega, \tag{2.40}$$

$$M = \int_\Omega p'\frac{1}{B}q\mathrm{d}\Omega. \tag{2.41}$$

In the following, we take the two-dimensional silicon PC with circle holes in square lattice where the lattice constant a=1μm and the diameter of the hole is 0.833a. Their unit cells are represented on a finite element mesh enclosed by boundaries. Periodic boundary conditions are applied on the external boundaries. Lagrange finite elements of degree 2 are used for the approximation of all unknown and test functions. For the m-th band of the

crystal, the quality factor is estimated from the complex eigenfrequencies as

$$Q_m(\mathbf{k}) = \frac{\mathrm{Re}[\omega_m(\mathbf{k})]}{2\mathrm{Im}[\omega_m(\mathbf{k})]}. \tag{2.42}$$

Figure 2.9 shows the complex-eigenfrequency band structures of the systems.

More significantly, it is again observed that the complex-eigenfrequency band structure adds information about time decay in the band, and the quality factor varies as the inverse of frequency, which means that the larger the frequency, the smaller the quality factor, and the larger the attenuation. There are different damping rates for the different bands. This variability is anisotropic in nature, and the quality factor depends on the vector polarization of Bloch waves.

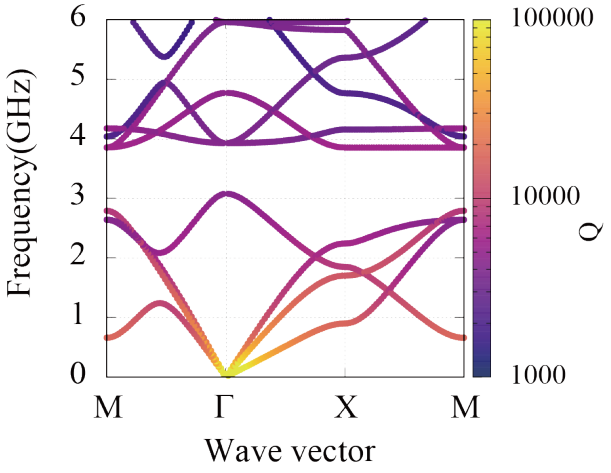

Figure 2.9: Complex-eigenfrequency band structure of two-dimensional square lattice PC composed of holes in silicon. The color scale of the band diagrams corresponds to the quality factor Q of each Bloch eigenstate.

In all numerical results presented in this subsection, the imaginary parts of the viscoelastic constants were much smaller than their real parts. These results are thus mainly relevant to the case where one is interested in engineering wave propagation properties through a sonic or phononic crystal with small damping. Of course, the equations defining the complex-eigenfrequency band structure also apply beyond this small attenuation regime, as could be interesting for applications to the mitigation of sound or vibrations. In the small damping limit, the first-order perturbation theory of Ref. [140] applies. The main result of this theory in our context is that the relative variation of the frequency of a band at a fixed value of the Bloch wavevector is given by

$$\frac{\delta\omega|_{\mathbf{k}}}{\omega} = \frac{\mathrm{i}}{2}\omega\frac{\langle\nabla_{\mathbf{k}}\mathbf{u}|\eta|\nabla_{\mathbf{k}}\mathbf{u}\rangle}{\langle\nabla_{\mathbf{k}}\mathbf{u}|c|\nabla_{\mathbf{k}}\mathbf{u}\rangle}, \tag{2.43}$$

where

$$\langle \nabla_{\mathbf{k}} \mathbf{u} | c | \nabla_{\mathbf{k}} \mathbf{u} \rangle = \int_{\Omega} (u^*_{i,j} + \mathrm{i} k_j u^*_i) c_{ijkl} (u_{k,l} - \mathrm{i} k_l u_k) \mathrm{d}\Omega, \tag{2.44}$$

$$\langle \nabla_{\mathbf{k}} \mathbf{u} | \eta | \nabla_{\mathbf{k}} \mathbf{u} \rangle = \int_{\Omega} (u^*_{i,j} + \mathrm{i} k_j u^*_i) \eta_{ijkl} (u_{k,l} - \mathrm{i} k_l u_k) \mathrm{d}\Omega. \tag{2.45}$$

The latter equations are the spatial averages of the real and imaginary part of the viscoelastic tensor taken with respect to the particular Bloch wave considered. They include all the influence of the details of the crystal on the appearance of an imaginary part for the eigenfrequency. The quality factor for band m can then be estimed as

$$Q_m(\mathbf{k}) = \frac{\langle \nabla_{\mathbf{k}} \mathbf{u} | c | \nabla_{\mathbf{k}} \mathbf{u} \rangle}{\omega_m(\mathbf{k}) \langle \nabla_{\mathbf{k}} \mathbf{u} | \eta | \nabla_{\mathbf{k}} \mathbf{u} \rangle}. \tag{2.46}$$

A practical algorithm and an alternative to the theory in the limit of small viscoelasticity are to solve for the lossless band structure first, thus obtaining the real eigenvalues $\omega_m(\mathbf{k})$ and their corresponding Bloch waves. Eq. (2.46) then gives a first-order perturbation theory estimate of the quality factor for any band.

When there is a single homogeneous material in a sonic crystal, the relative frequency variation simplifies to

$$\frac{\delta\omega|_{\mathbf{k}}}{\omega} = \frac{\mathrm{i}}{2} \omega \frac{\eta}{B}, \tag{2.47}$$

i.e. the distribution of the Bloch wave has no incidence on the result, and the quality factor has the same expression as for a plane wave in an homogeneous medium:

$$Q = \frac{B}{\omega \eta}, \tag{2.48}$$

where B is the bulk modulus of the material. Note that the quality factor is independent of the filling fraction of the crystal in this scalar homogeneous case. When there is a single homogeneous but anisotropic material in a phononic crystal, as is the case for the holey silicon crystal of figure 2.9, similar conclusions can be drawn. But the quality factor is dependent of the filling fraction and it further depends on the direction of propagation and on the polarization of the particular Bloch wave, i.e. the ratio of the material averages $\langle c \rangle / \langle \eta \rangle$ is different for quasi longitudinal and quasi shear Bloch waves.

Compared with the complex-wavevector band structure, the complex-eigenfrequency band structure does not reflect the spatial attenuation characteristics of the Bloch wave

as the wave propagates, but essentially explains the instantaneous attenuation of the Bloch wave in the phononic crystal. And it has nothing to do with the local group velocity. In the case of a defect cavity embedded in a very large crystal, the method would give the quality factor of the resonance, if combined with a super-cell technique. Beyond time-harmonic excitations, transient or short pulse excitations are equally important for experiments.

2.3.4/ RESOLVENT BAND STRUCTURE

When adding material loss, we can still use the same formulation as before because Bloch's theorem remains valid for coefficients that depend on frequency. However, the eigenvalue problem becomes nonlinear. So we apply the stochastic excitation method to the calculation. A Bloch-Floquet excitation with a stochastic periodic part is added to the acoustic equation. We then explore the resolvent set as a function of $\mathbf{k}$ and ω and obtain the resolvent band structures. Generaly, in contrast to eigenvalue-based methods, we don't need to look for an explicit $\omega(\mathbf{k})$ or $\mathbf{k}(\omega)$ functional dispersion relation. Instead, an implicit response $E(\omega, \mathbf{k})$ is obtained that is similar to a local density of states. The resolvent band structure also gives the basic information of the attenuation of the dispersion point in the time domain and the space domain. When the material viscosity being condisered, linear wave equations, including those for acoustic, elastic, and optical waves, can generally be written for time-harmonic waves as [201]

$$(\mathbf{K}(\mathbf{k}) - \omega^2\mathbf{M})\mathbf{u}(\omega, \mathbf{k}) = \mathbf{f}(\omega, \mathbf{k}), \tag{2.49}$$

where $\mathbf{K}$ is a stiffness operator; $\mathbf{M}$ is a mass operator; $\mathbf{u}(\omega, \mathbf{k})$ is a function describing the solution in reciprocal space; and $\mathbf{f}(\omega, \mathbf{k})$ is a forcing term at a particular frequency and wavevector. Eq. (2.49) is obtained from a Fourier transform of the original wave equation over the time coordinate.

Eq. (2.49) can be viewed as the dynamical equation obtained from the Euler-Lagrange principle with a Laplacian combining potential elastic energy, kinetic energy, and the work of the forcing term. A Hamiltonian operator can then be defined as

$$\mathbf{H} = \frac{1}{2}(\mathbf{K} + \omega^2\mathbf{M}), \tag{2.50}$$

and we evaluate the response as the self-energy of the solution, or

$$\mathbf{E} = \langle \mathbf{H}\mathbf{u}, \mathbf{u} \rangle. \tag{2.51}$$

As in the previous subsection, taking the circle hole/silicon phononic crystal arranged in a two-dimensional square lattice as an example, the total energy [201, 172, 88] of the elastic wave in the structure is

$$\langle \mathbf{Hu}, \mathbf{u} \rangle = \frac{1}{2} \int_{\Omega} S_I(\mathbf{u})^* c_{(I_J)} S_J(\mathbf{u}) \mathrm{d}\Omega + \frac{1}{2} \omega^2 \int_{\Omega} \mathbf{u}^* \cdot \rho \mathbf{u} \mathrm{d}\Omega. \tag{2.52}$$

Due to the large amount of calculation in the complex-wavevector space, only the resolvent band structure in the real wavevector space is given here as shown in figure 2.10. It can be seen from the figure that the energy attenuation increases as the frequency increases, which is the same as the result of the complex eigenfrequency band structure in figure 2.9.

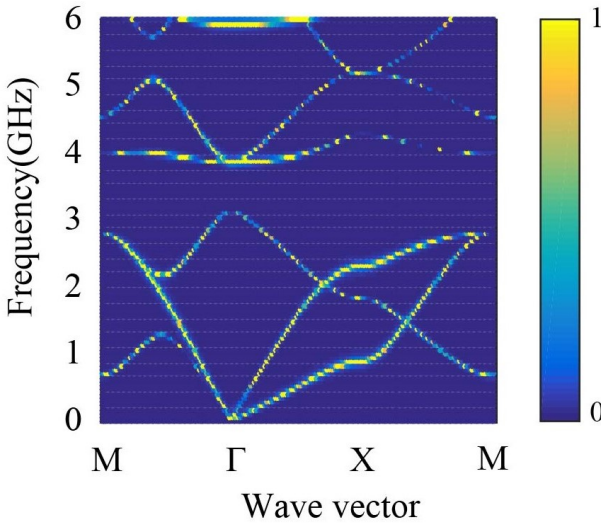

Figure 2.10: Resolvent band structure of two-dimensional square lattice PC composed of holes in silicon. The color scale of the band diagrams corresponds to the normalized stochastic response throughout the $(\omega, \mathbf{k})$ dispersion plane. The color represents the normalized total energy.

The frequency-dependent attenuation can also be reflected by the cross section of the band structure for a fixed wavevector. Figure 2.11 shows the response cross section at high symmetry point X in the first Brillouin zone. The attenuation of the Lorentz function can be clearly observed from the figure. The Lorentz function, namely Cauchy distribution function, can describe the solution of the forced resonance differential equation, and its probability density function can also describe the attenuation information. It can be seen from figure 2.11 that the width of the Lorentz response in the vertical cross section reveals the time decay of each frequency eigenvalue at a fixed wavevector. Figure 2.12 shows the response cross-section along the wavevector direction, where the frequencies of 1.5 GHz and 4.5 GHz are in the passing band, and 3.5 GHz is in the band gap. It can be

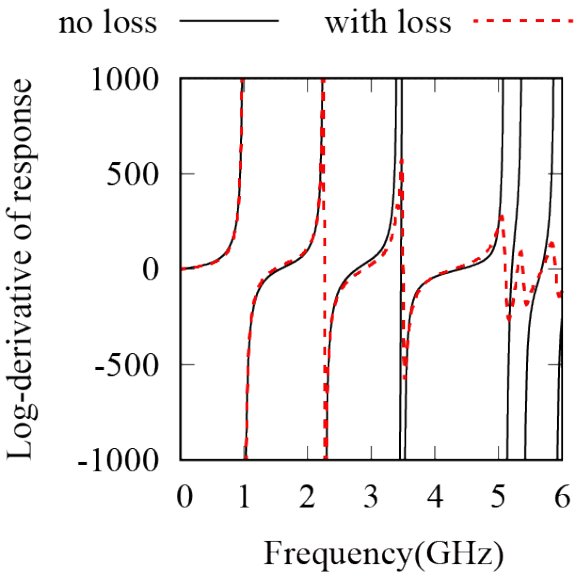

Figure 2.11: Vertical cross section of the resolvent band structure of figure 2.10, taken at the X point of the first Brillouin zone.

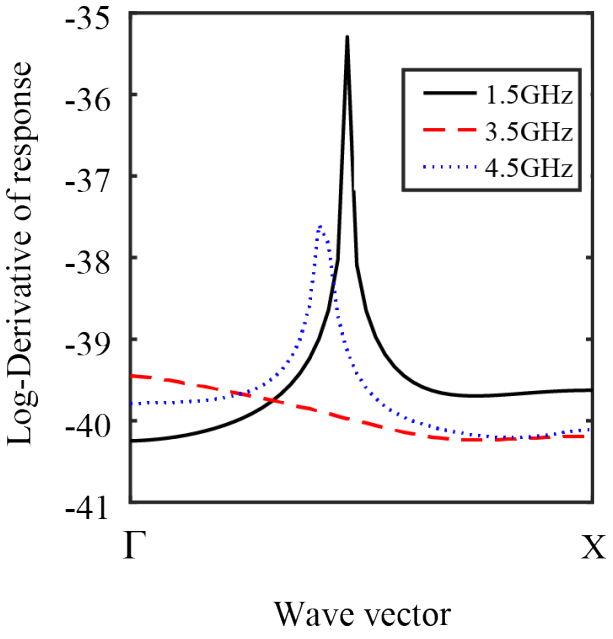

Figure 2.12: Horizontal cross section of the resolvent band structure of figure 2.10, taken at different frequencies along the direction ΓX.

seen from the figure that the width of the Lorentz response of the horizontal cross-section reveals the spatial attenuation of each wavevector eigenvalue at a fixed frequency.

In general, there are no other bands in the complete band gap of the classical real band structure. According to the conservation of energy, waves will not disappear, so the real

band structure cannot explain this phenomenon. The complex-wavevector band structure, as shown in figure 2.8, contains all the bands of the classical real band structure. In the frequency range of band gap, all the imaginary parts of the wavevector are not zero, that is to say, there are only evanescent waves. In the passband range, there are not only propagating waves with zero imaginary part, but also evanescent waves with nonzero imaginary part, which explains the existence of waves in both band gaps and passing bands. Furthermore, the value of the imaginary part in the complex-wavevector band structure also represents the spatial attenuation capacity of the wave. On the other hand, the complex eigenfrequency band structure represents the wave attenuation information in frequency or time domain, as shown in figure 2.9. It can be observed from the figure that the larger the frequency is, the smaller the quality factor is, and the larger the attenuation is. Different bands have different attenuation rates. Finally, the width of the Lorentz function in the vertical cross-section of the resolvent band structure shown in figure 2.10 reveals the attenuation of the relevant frequency. The higher the frequency is, the larger the attenuation is. The width of the Lorentz function in the horizontal cross-section of the resolvent band structure reveals the spatial attenuation at the same eigenvalue. In general, both CEBS and RBS can reflect the attenuation of the wave in frequency or time domain; on the other hand, both CWBS and RBS can reflect the attenuation of the wave with the wavevector.

2.4/ DEFECTS IN PHONONIC CRYSTALS

When periodicity of the ideal periodic structure is broken by introducing perturbations, defect modes are generated. The perturbation, for instance, are changing the geometry of the unit cell or the material properties, removing or adding the scatterers. Based on the different forms, the defects include the point defect, line defect and planar defect. The point defect is generated by breaking the periodicity on the grid of the lattice. In addition, when the periodicity is broken along a series of straight or bent grids continuously, a line defect is formed. Defect states are produced in the band gaps of the phononic crystals in case that defects exist where wave states are localized in the defects. This limits the waves transmitting inside phononic crystals. Currently, a lot of applications of phononic crystals have applied the properties of defect states such as resonant cavities formed by point defects and waveguides formed by line defects. In this section, we calculate the band structure of the supercell with a point or a line defect by FEM. The supercell is generated by a periodic extension of the unit cell, of course with defects inside. By doing this, we can retain the periodicity of the structure and use the Bloch boundary condition.

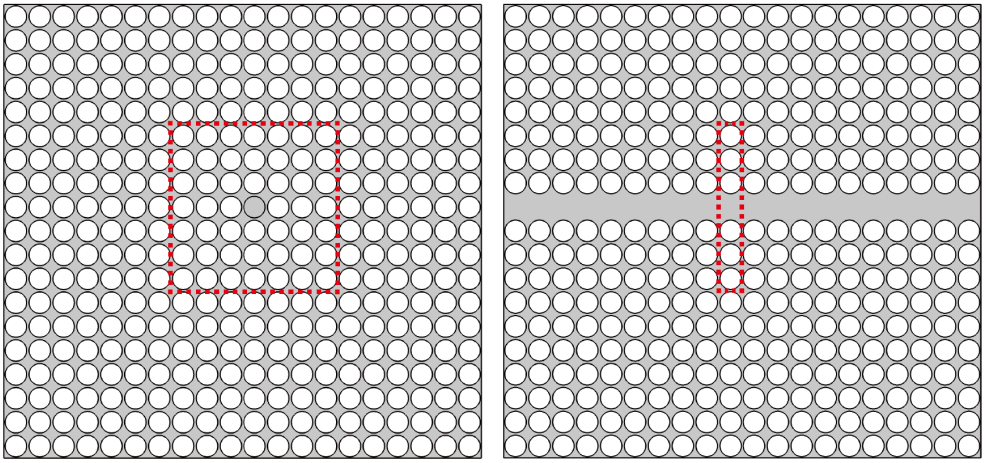

Figure 2.13: Phononic crystals supercells with a point defect (a) and a line defect (b).

Then we introduce the point defect and line defect inside a perfect phononic crystal with a square lattice, as shown in figure 2.13. The point defect is formed by removing the hole located in the center of the supercell with 7×7 unit cells. A 1×7 supercell is used to calculate the band structure with the line defect by removing the hole in center, which represents the situation of waves propagating along the ΓX direction. In the calculation of the band structure by FEM, periodic conditions are applied on both sides (x and y directions) of the supercell with defects. The band structure of the phononic crystal with a point defect around the frequency range of the band gap and the displacement field distributions for different defect modes is shown in figure 2.14 (a) and (b), respectively. The white area represents the complete band gap of the corresponding perfect phononic crystal. It can be inferred that there are six additional flat bands A-E' appearing inside the band gap. The corresponding frequencies are 1478.1Hz, 1541.7Hz, 1839.9Hz, 1898.6Hz, 1900.6Hz and 1900.8Hz, respectively. From the displacement field distribution of the different defect modes A-E', the vibrations are all concentrated on the point defect and present strong local properties. The modes E and E' at 1900.6Hz and 1900.8Hz are degenerate modes, while the modes C and D are not, though their frequencies are close.

Next, we discuss the band structure of phononic crystal with line defect around the frequency range of the band gap. Figure 2.15 illustrates the band structure (a) and the displacement field distributions for different line defect modes (b). There are also several extra defect bands produced inside the band gap. Different bands correspond to different waveguide states in the phononic crystal. We notice that there exists a single mode or multiple guide modes at one frequency. For the frequencies with multiple guided modes,

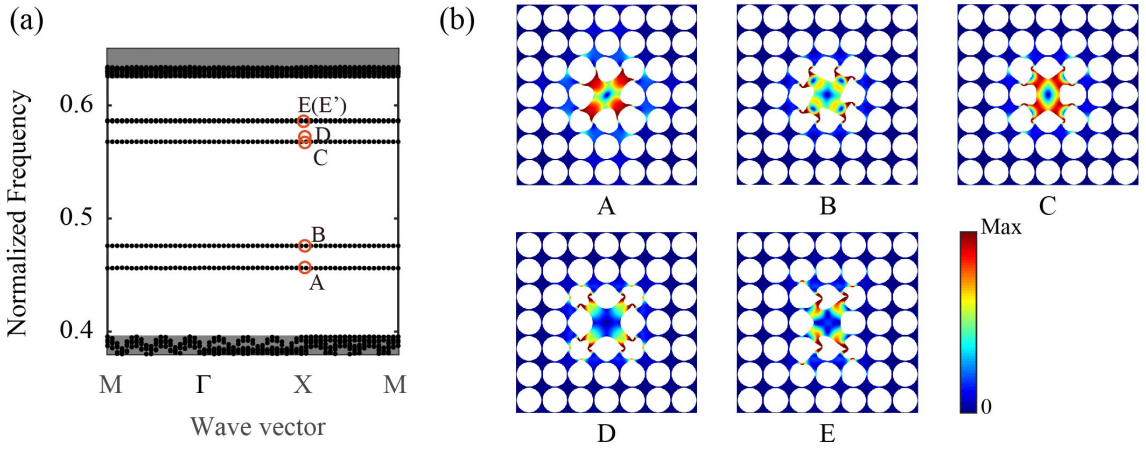

Figure 2.14: Phononic band structures of the 2D phononic crystal with a point defect (a) and displacement field distributions for different defect modes (b).

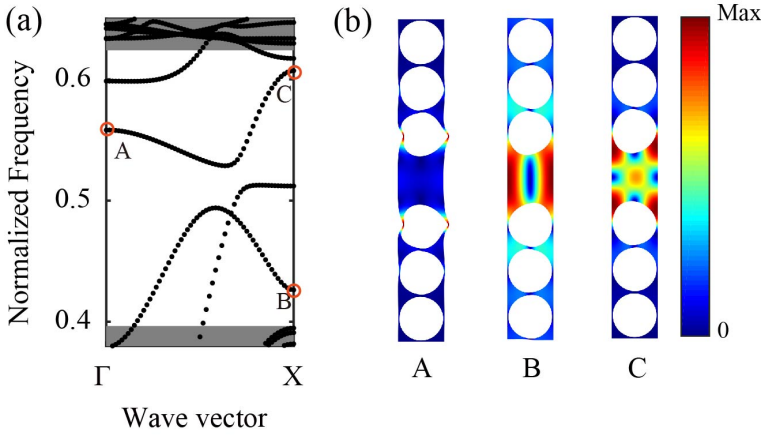

Figure 2.15: Phononic band structures of the 2D phononic crystal with a line defect (a) and displacement field distributions for different defect modes (b).

the modes may convert to other guide modes by coupling. According to the transmission and polarization direction, the guided modes can be clarified to longitudinal mode (A), shear mode (B) and mixed mode (C). The vibrations are highly concentrated around the line defects.

2.5/ RESPONSE SPECTRUM OF PHONONIC CRYSTALS

In finite structures of phononic crystals, the response spectrum is another characteristic to describe the properties of the band gaps. At the same time, the response spectrum may value the attenuation of the elastic wave or vibration in the finite structures. In this section, we will show the calculation of the response spectrum of a two-dimensional phononic

crystal by the finite element method software COMSOL.

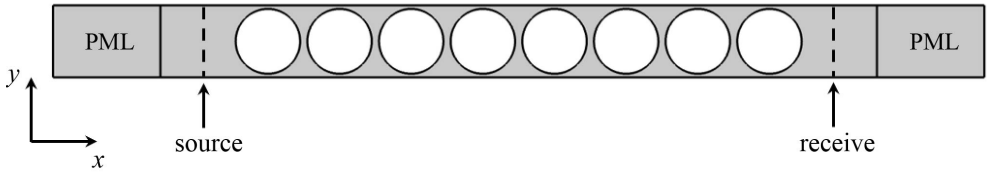

Figure 2.16: Model of calculating the transmission spectra of two-dimensional perfect PC along the ΓX direction.

Figure 2.16 is a schematic diagram for calculating the transmission spectra of 2D PCs along the ΓX direction. There are 8 periodic unit cells in the transmission direction (x derection), sandwiched between an ingoing and an outgoing homogeneous medium. We assume it is infinitely periodic perpendicular to the direction of wave propagation (y direction). The periodic conditions are applied to both sides of the PCs in the y direction so that only one periodic structure can represent the whole calculation area. The amount of calculation is deeply reduced. Perfectly matched layers (PMLs) or radiation boundary conditions are added to both ends of the PCs. PML is a kind of absorbing boundary layer, which can absorb the elastic disturbance gradually to avoid reflection of the elastic wave at the boundary of the structures.

A line source of elastic waves with unit amplitude is positioned along segment S_l at the left side of the structure. Transmission displacements are collected at the right side S_r. The amplitude of the displacement at the line source is noted U_0. By sweeping the reduced frequency, we evaluate the transmission $T(fa)$ in decibels units by

$$T(fa) = 20\log_{10}\left(\frac{\int_{S_r} U\mathrm{d}s}{\int_{S_l} U_0\mathrm{d}s}\right), \tag{2.53}$$

where U is the total displacement along S_r, a receiver segment placed at the right exit of the waveguide.

Figure 2.17 shows the transmission spectra of the structure shown in figure 2.16. The black line and red line present the transmission of x polarized and y polarized waves. It can be noticed that there are some directional band gaps appearing excited by the x polarized and y polarized vibrations. In these band gaps, only x polarized waves (longitudinal waves) or y polarized waves (shear waves) exist, which leads to the waves with orthogonal polarization not able to transmit in the structures. Generally, the band gaps in the ΓX direction only correspond to frequency ranges of simultaneous attenuation for

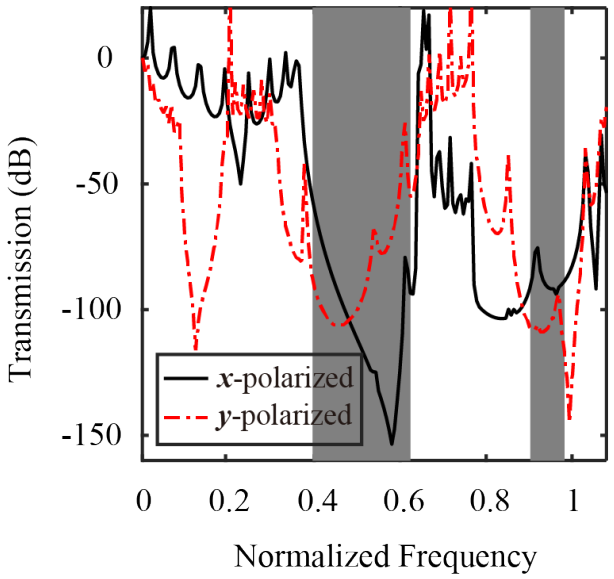

Figure 2.17: In-plane mode transmission spectra of 2D phononic crystal along the ΓX direction.

both polarization. We find that the position of the band gap in transmission spectra is consistent with the result of the band structure shown in figure 2.2.

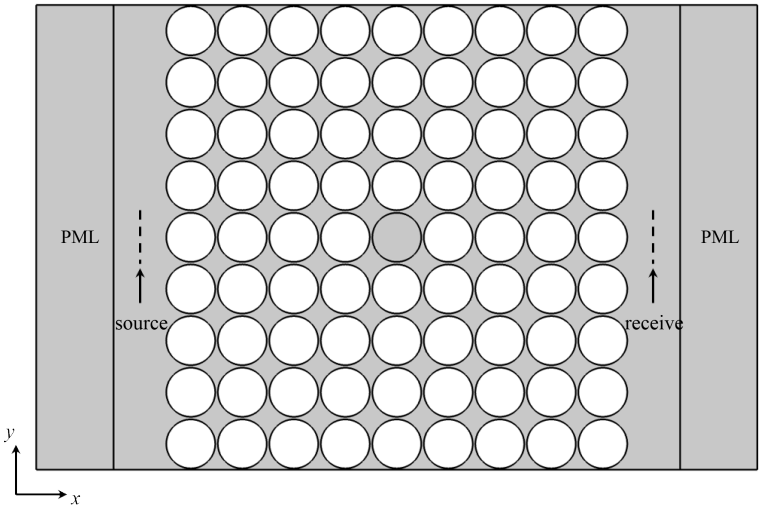

Figure 2.18: Model for calculating the transmission spectra of two-dimensional PC with point defect along the ΓX direction.

Next, the transmission spectrum of the structure with a point defect is calculated. Here, a supercell formed by a periodic arrangement of 9×9 unit cells is selected, and a point defect is introduced by removing the central scatterer, as shown in figure 2.18. The supercell is also sandwiched with two homogeneous mediums for input and output of waves, and periodic boundary conditions are imposed on both sides along the y direction.

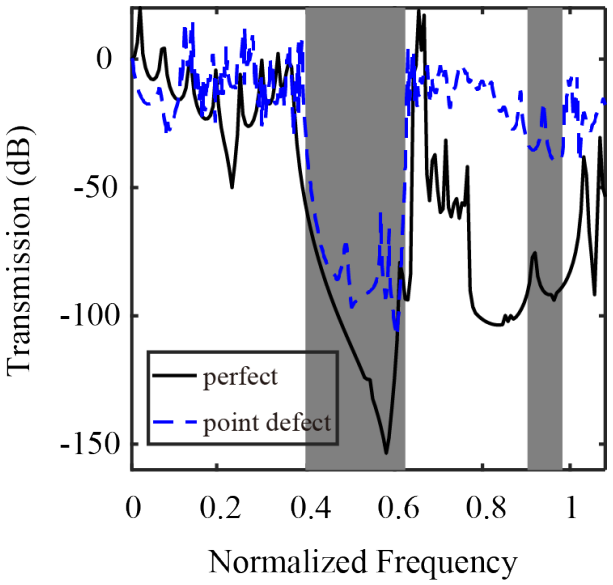

Figure 2.19: The in-plane mode transmission spectra of two-dimensional PC with point defect along the ΓX direction.

The black and blue solid lines in figure 2.19 represent the response spectra of the perfect phononic crystal and of the phononic crystal with a point defect, respectively. It can be seen from the figure that some sharp points appear in the band gap of the transmission spectrum with point defects, and their positions are consistent with the position of the local resonance flat band in the band gap in figure 2.14(a).

2.6/ CONCLUSIONS

The main contents of this chapter are summarized as follows:

(1) The method of calculating the real band structures of phononic crystal based on the COMSOL finite element software is introduced (include fluid-solid system). Considering the viscosity of materials, we propose the methods of calculating the complex-wavevector band structures, complex-eigenfrequency band structure and resolvent band structure of phononic crystals based on finite element method. The calculations for typical examples show that the finite element method can accurately give the band structures of phononic crystals with different information. The introduction of viscosity generally enhances the attenuation of the structure.

(2) The method of calculating the phononic crystal with point and line defects is introduced.

(3) The calculation of frequency response function of phononic crystal based on COMSOL finite element software is introduced.

II

CONTRIBUTION

3

WAVE PROPAGATION IN PERIODIC COUPLED-RESONATOR ACOUSTIC/ELASTIC WAVEGUIDES

3.1/ INTRODUCTION

When the periodicity of a perfect phononic crystal is destroyed, i.e, when the geometry or material properties of one or several unit cells change locally, defect states are generated in the band gaps, and the waves will be localized at the defect. Waves far away from the defect decay rapidly. In particular, waveguides created by line defects can achieve perfect localization and guidance of waves. Previous research works mainly focused on linear waveguides [5, 12] formed by linear defects. The coupled-resonator waveguide formed by a series of defect cavities or resonators can realize strong localization and low group velocity transmission [137].

It has been recognized from the beginning that the transmission of a PC waveguide shows oscillation of the transmission as a function of frequency, which is called the channeled spectrum [12]. The channeled spectrum has long been known in guided-wave optics and is a classical technique for the characterization of dispersion properties and group delay dispersion [38]. The channeled spectrum in a homogeneous waveguide results from the interference of forward propagating guided wave with the backward propagating wave generated by internal reflections, especially at the ends of the waveguide. However, the nature of these oscillations [24] in phononic waveguides has remained mostly unexplained.

In addition, the propagation of Lamb waves in a phononic crystal plate [116, 155, 173] has attracted widespread attention. The phononic crystal plate is periodic and infinite

in two directions, but it is limited in the third direction, so there is almost no leakage of energy. Although Lamb waves are strictly restricted between the two free surfaces, they can still be manipulated in the periodic plane, providing a broad platform for the design of acoustic circuits.

In this chapter, we take the phononic crystal composed of mercury matrix and water column as an example. A theoretical model is developed that predicts accurately the distribution of frequencies at which maxima and minima of transmission occur, together with the pressure distribution at those frequencies. Linear waveguides and periodic coupled-resonator acoustic waveguides with different lengths and defect distributions are designed. The transmission characteristics of acoustic waves in these different waveguides are studied. Then, taking the stainless steel phononic crystal plate as an example, periodic coupled-resonator straight and bifurcated elastic waveguides are designed. The highly localized transmission characteristics of Lamb waves in these elastic waveguide are studied and experimentally verified. Finally, the influence of the geometrical parameters of the structure on the band structure is discussed.

3.2/ WAVE PROPAGATION IN CRAWS

In this section, a two-dimensional phononic crystal composed of water column and mercury matrix is build. A theoretical model of the channeled spectrum is developed. The linear waveguides and periodic CRAWs are designed. The transmission characteristics of waves propagating in waveguides with different lengths and defect distributions are studied. The influence of material viscosity on the channeled spectrum is discussed.

3.2.1/ THEORETICAL MODEL

In this subsection, a theoretical model is proposed to provide a physical explanation for the appearance of frequencies at which transmission maxima and minima occur, similar to the channeled spectrum in optics. For a single-mode PC waveguide in the considered frequency range, the fundamental guided mode is a propagation channel for waves traveling to the right or to the left, as depicted in figure 3.1(a).

The time-harmonic pressure field inside the waveguide can then be written as the superposition of a left-traveling Bloch wave, $p_l(x,y)$, with a right-traveling Bloch wave, $p_r(x,y)$,

$$p(\omega;x,y) = \alpha p_r(x,y)e^{-ik(\omega)x} + \beta p_l(x,y)e^{+ik(\omega)x}. \tag{3.1}$$

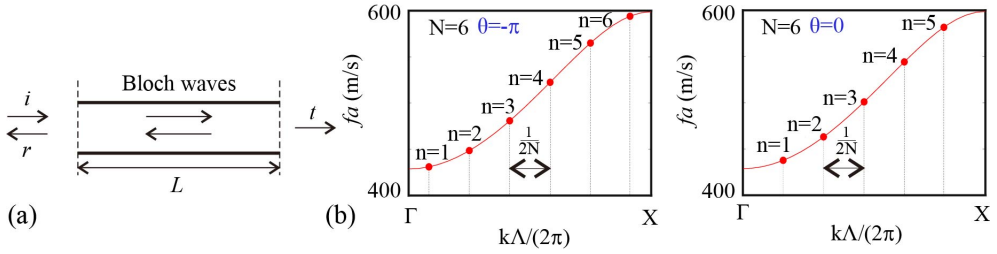

Figure 3.1: (a) Simplified model of transmission through a single-mode periodic waveguide at a single frequency. (b) Graphical construction of the channeled spectrum from the dispersion relation of the infinite waveguide for the particular cases $\theta = -\pi$ and $\theta = 0$.

In this equation, x is a curvilinear coordinate along the waveguide axis and y is a transverse coordinate. The functions $p_l(x, y)$ and $p_r(x, y)$ have periodicity Λ along x and satisfy $p_l(\Lambda - x, y) = p_r^*(x, y)$. They depend in principle on frequency, though we don't explicit this dependence here. The complex coefficients α and β are to be determined. $k(\omega)$ is the Bloch wavenumber along the waveguide axis. Since we consider periodic waveguides with one direction of periodicity, the Bloch wavevector indeed reduces to a single wavenumber. Note that $k(\omega)$ can be obtained by inverting the dispersion relation $\omega(k)$ of the waveguide, with k being considered as a continuous variable. It is also important to note that the two guided Bloch waves propagate unperturbed and that they only convert to one another at the ends of the waveguide. Hence, the model only considers a waveguide of finite length L, and periodicity is not directly apparent because it is already embedded in the guided Bloch waves.

By continuity of pressure, the transmission in amplitude at the exit of the waveguide can be determined as $t(\omega) = p(\omega; L, 0)$, or

$$t(\omega) = \alpha p_r(L, 0)e^{-\mathrm{i}k(\omega)L} + \beta p_l(L, 0)e^{+\mathrm{i}k(\omega)L}, \tag{3.2}$$

where $L = N\Lambda$ is the length of the waveguide; and N is the number of the periodic unit cells. We further assume that the x-periodic functions $p_l(x, y)$ and $p_r(x, y)$ are normalized such that $|p_l(0, 0)| = |p_l(\Lambda, 0)| = 1$ and $|p_r(0, 0)| = |p_r(\Lambda, 0)| = 1$. Any residual phase can then be absorbed in the coefficients α and β, and we finally have without loss of generality

$$t(\omega) = \alpha e^{-\mathrm{i}k(\omega)L} + \beta e^{+\mathrm{i}k(\omega)L}. \tag{3.3}$$

The transmission in intensity is then

$$|t(\omega)|^2 = |\alpha|^2 + |\beta|^2 + 2|\alpha\beta| \cos(2k(\omega)L - \theta), \tag{3.4}$$

with $\theta = \mathrm{Arg}(\alpha\beta^*)$ being a phase angle dependent on the particular superposition of guided Bloch waves.

Transmission maxima and minima are obtained when

$$\frac{\mathrm{d}|t(\omega)|^2}{\mathrm{d}\omega} = 0. \tag{3.5}$$

By neglecting the possible dependence of α and β on frequency, maxima are obtained when $2k(\omega)L = \theta$ modulo 2π, or for a discrete sequence of frequencies and wavenumbers such that

$$k(\omega_n)\Lambda = \frac{\theta}{2N} + \frac{n}{N}\pi. \tag{3.6}$$

As a result, frequencies at which transmission is maximum can be directly inferred from the dispersion relation of the waveguide, as depicted in figure 3.1(b). It is noted that there are N maxima given by Eq. (3.6) between points Γ and X of the first Brillouin zone when $\theta \neq 0$. However, when $\theta = 0$, there are $N - 1$ maxima since the Bloch waves at high symmetry points Γ and X can hardly be excited. Similarly, frequencies at which transmission is minimum are obtained for

$$k(\omega_{n+1/2})\Lambda = \frac{\theta}{2N} + \frac{n + 1/2}{N}\pi. \tag{3.7}$$

Following from Eqs. (3.6-3.7), transmission maxima and minima are sampled uniformly along the k-axis with the step $\delta k = \frac{\pi}{N\Lambda}$ so that their density increases in proportion to the length of the waveguide. The frequencies of transmission maxima and minima have a variable distribution, or free spectral range. Indeed, their local separation is proportional to the group velocity, according to

$$\delta\omega \approx v_g(k)\ \delta k = v_g(k)\frac{\pi}{N\Lambda}, \tag{3.8}$$

where the group velocity can be directly obtained from the dispersion relation as

$$v_g(k) = \frac{\mathrm{d}\omega}{\mathrm{d}k}. \tag{3.9}$$

When k is close to the high symmetry points Γ and X, the group velocity tends to zero and the frequency spacing of transmission maxima and minima reduces. The present model is valid for any monomodal phononic crystal waveguide, as we illustrate next.

3.2.2/ LINEAR ACOUSTIC WAVEGUIDES

In this subsection, we investigate the transmission properties in periodic linear waveguides. We select a 2D square PC composed of water cylinders embedded in mercury matrix. Material parameters used here are ρ=1025 kg/m^3, c=1531 m/s for water, and ρ=13600 kg/m^3, c=1450 m/s for mercury. The filling fraction is 0.4. The finite element method is used for all numerical simulations. In the absence of frequency-dependent loss, the PC can be scaled arbitrarily, and its dispersion relation can be represented as reduced frequency fa versus reduced wavenumber ka, with f being the frequency, k the wavenumber, and a the lattice constant. The perfectly periodic PC possesses a complete bandgap for 398 m/s $< fa <$ 1095 m/s, as shown by the white area in figure 3.2(a).

A linear waveguide is formed by introducing a line defect. Within the line defect, the radius of the water cylinders is changed to r/a=0.1. Figure 3.2(a) illustrates the dispersion relation of the periodic linear waveguide in the ΓX direction of the irreducible Brillouin zone. Three guided modes are generated within the complete bandgap, in the frequency range of 429 m/s $< fa <$ 599 m/s for Bloch wave A, 886 m/s $< fa <$ 1005 m/s for Bloch wave B and 983 m/s $< fa <$ 1086 m/s for Bloch wave C. Their pressure distributions at the point X, labeled a,b and c, are displayed in figure 3.2(b). Each guided mode has a special pattern of pressure distribution. The pressure amplitudes at points a and b decay rapidly away from the linear defect in the transverse direction, owing to the existence of the complete band gap, so guided modes are well confined to the linear defect. Point c is strongly influenced by the passing bands right above the band gap, and its confinement is weak.

The appearance of channeled transmission spectra is intimately linked to the finite length of a waveguide and to the termination conditions. Here, we consider linear waveguides with different length and number of turns, as depicted in figure 3.3. The finite structures have 11×11 unit cells in figure 3.3(a) and (b), and 13×11 unit cells in figure 3.3(c). Three different linear waveguides are considered: (a) a straight waveguide with length $L = 11a$, (b) a waveguide with length $L = 13a$ and 2 turns, and (c) a straight waveguide with length $L = 13a$. In the following, they are referred to as the LW1, the LW2 and the LW3 waveguides, respectively.

One characteristic of waveguides is their transmission for acoustic waves, which can be evaluated as follows. The finite PC is placed in a homogeneous mercury region. A radiation boundary condition is set on the outer boundary, closing the computation domain and minimizing reflections. A line source for acoustic waves with unit amplitude $p_0 = 1$ is positioned at the left end S_l of the waveguide. The width of the source segment is exactly

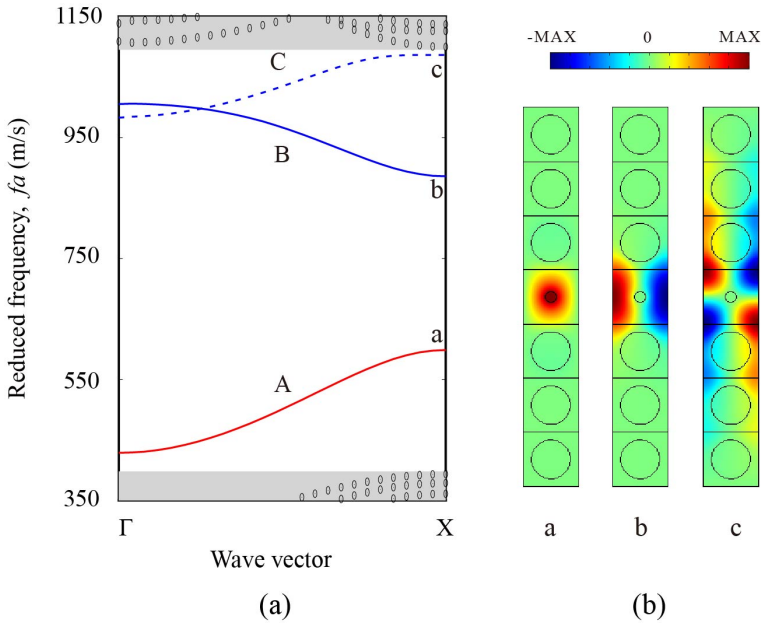

Figure 3.2: Dispersion relation of an infinitely linear waveguide with cavity radius r/a=0.1. (a) Band structure for a 7×1 super-cell of the square PC of water cylinders in mercury is presented in the ΓX direction of the first Brillouin zone. The gray areas indicate the passing frequency ranges. Three guided modes exist inside the complete band gap and are labelled A, B and C. (b) Pressure distributions at the X point of the first Brillouin zone are presented for the three guided modes. The color scale represents the amplitude from blue for negative to red for positive values.

one lattice constant a. By sweeping the reduced frequency in the frequency range of interest, the transmission $T(fa)$ in decibels units can be estimated as

$$T(fa) = 20 \log_{10} \left(\frac{\int_{S_r} |p| \mathrm{d}s}{\int_{S_l} |p_0| \mathrm{d}s} \right), \tag{3.10}$$

where p is the pressure along the right end S_r of the waveguide.

Figure 3.3(d) shows transmissions for the different waveguides as a function of reduced frequency. For comparison, transmission for the perfect PC, i.e. with no defect, are also plotted. Two passing frequency ranges come up clearly inside the complete bandgap. They coincide with the dispersion relations of the waveguides in figure 3.2(a), except for Bloch wave C in the frequency range of 1005 m/s $< fa <$ 1086 m/s. Bloch wave C is actually a deaf mode, since the pressure distribution at point C shown in figure 3.2(b) is anti-symmetric with respect to the direction of the wavevector (the horizontal axis). Such a mode can thus not be excited by an incident plane wave. However, evanescent Bloch waves with the right symmetry can still be excited, and result in a small transmission. The

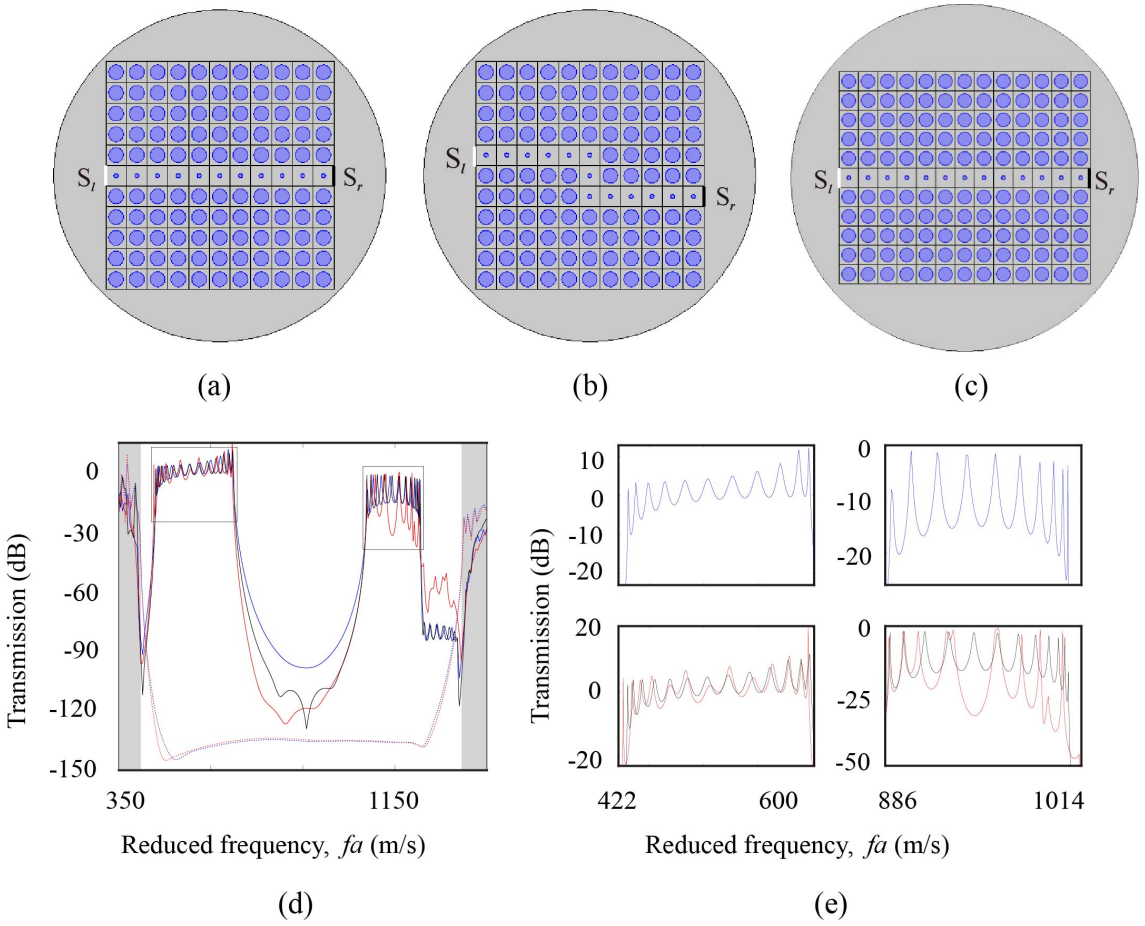

Figure 3.3: Cross-sections of linear waveguides arranged in three different circuits inside finite square PCs and the related transmission. The length L of a waveguide is an integer multiple of the lattice constant a. We consider (a) a straight waveguide with $L = 11a$ (LW1), (b) a waveguide with 2 turns and $L = 13a$ (LW2), and (c) a straight waveguide with $L = 13a$ (LW3). The wave sources used for transmission computation are marked by white lines. The transmitted wave is detected along the black lines on the other side of the waveguides. (d) Transmission through waveguides LW1, LW2 and LW3 are shown with blue, red, and black solid lines, respectively. The dashed lines represent the transmission through the perfect PC, with source and detector placed as in the case of waveguides LW1 and LW2. (e) For clarity, transmissions around $fa = 500$m/s and $fa = 1000$m/s are zoomed.

upper passing range is thus identified with Bloch wave B. The lower one corresponds to Bloch wave A. In the extent of passing frequency ranges, only small differences in transmission exist for the different circuits. This indicates that the wave can propagate along the waveguides with an arbitrary number of turns. Transmission is generally very low for frequencies in-between passing bands and is then dominated by the total length of the waveguide as shown in figure 3.3(d). The smaller transmission is thus found for the longer waveguide.

For comparison, transmissions for bare PCs are also calculated and plotted in figure 3.3.

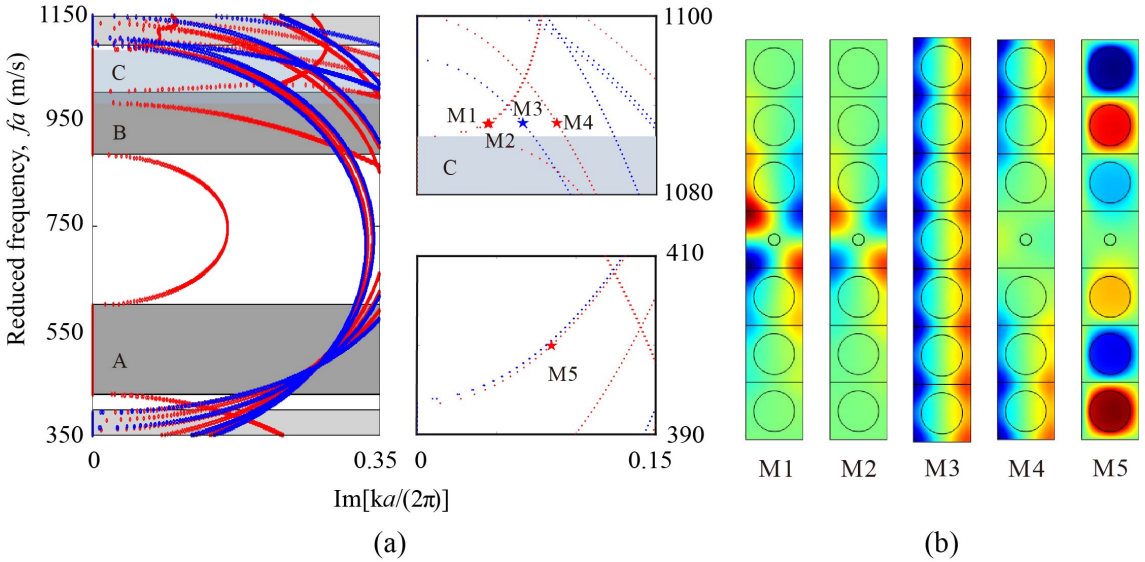

Figure 3.4: Imaginary part of the complex band structure of the linear waveguide (red dots). The dark-gray and slate gray regions in panel (a) correspond to the frequency ranges of the three guided waves in figure 3.2(a). The blue dots represent the results for the bare PC computed by a 7×1 super-cell. For clarity, band structures around $fa = 400$m/s and $fa = 1090$m/s are zoomed. The pressure distributions in the linear waveguide and in the bare PC at the marked points in panel (a) are illustrated in panel (b).

It is observed that the transmission through the waveguides can be smaller than through the perfect PC. This is owing to the reconstruction of the complex band structure, especially the imaginary part of the Bloch wavenumber shown in figure 3.4. It is known that the minimum imaginary part value of the Bloch wavenumber dominates the transmission. For the bare PC, the minimum imaginary part value is always non-zero in the bandgap. When a linear defect is introduced, its value changes a lot. There are even some frequency ranges where it is larger than for the bare PC (see the zoomed panels). The pressure distributions of evanescent Bloch waves at the marked points in figure 3.4(a) are shown in figure 3.4(b). For the linear waveguide, the modes at points M1 and M2 of the imaginary bands are asymmetric with respect to the x-axis. So they cannot be excited in the simulation, similarly to Bloch wave C. Mode M3 for the bare PC, and modes M4 and M5 for the linear waveguide can be excited. Clearly, the latter two modes have larger imaginary part values and so they decay faster than mode M3. A smaller transmission for the waveguides is then expected, in coincidence with the results in figure 3.3(d).

The lower and the upper passing frequency ranges support single mode propagation and large maximum transmission. Figure 3.3(e) shows a close-up view at transmission within the lower and upper passing frequency ranges. A pattern of successive maxima and minima appears in the transmission spectra. Table 3.1 reports the frequencies with

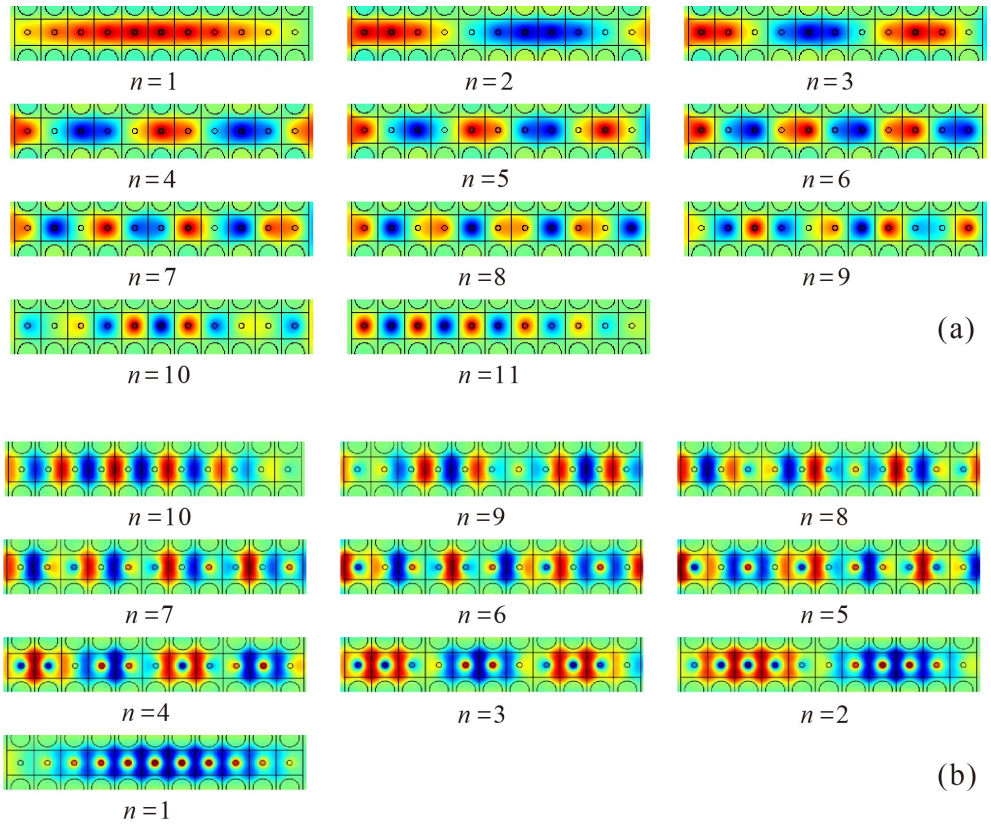

Figure 3.5: Pressure distribution of the straight waveguide (LW1, $L = 11a$) at the resonant peaks of the (a) lower or (b) upper passing frequencies listed in Table 3.1. The number of pressure oscillations are shown below the field maps.

Table 3.1: Frequencies at which transmission is maximum for different waveguides in the lower or upper passing frequencies of figure 3.3(d). The units of reduced frequency, fa, are m/s.

order	1	2	3	4	5	6	7	8	9	10	11	12	13
LW1	431.2	438.2	449.4	464.6	483.2	504.2	526.8	549.8	571	587.8	597.4		
	1005.2	1002	996	987	974	958	939.4	920.2	902.8	890.4			
LW2	426.4	434.6	442.2	452.8	469.6	484	506.4	524.2	546	563.8	579.2	590.4	596.6
	1012.4	1001.8	992.4	987.2	975.2	959.2	958.4	930.4	926.2	907.6	897.8	888.6	
LW3	430.6	435.6	444	455.4	469.4	485.6	503.8	523	542.6	561.4	578	590.8	597.8
	1005.6	1003.2	999	982.8	984.2	973	959.4	943.8	927.6	911.8	898.4	889.2	

maximum transmissions for the three considered waveguides. Waveguides with the same length but different number of turns, such as LW2 and LW3, have the same number and positions of extremal frequencies, though there are slight differences in amplitudes. Bloch wave A has a doubly symmetric shape but is slightly 'compressed' by periodicity towards the left and the right. Then the coupling between adjacent defects is slightly asymmetric along the x-axis (left/right) compared to the y-axis (up/down). The number of maxima is

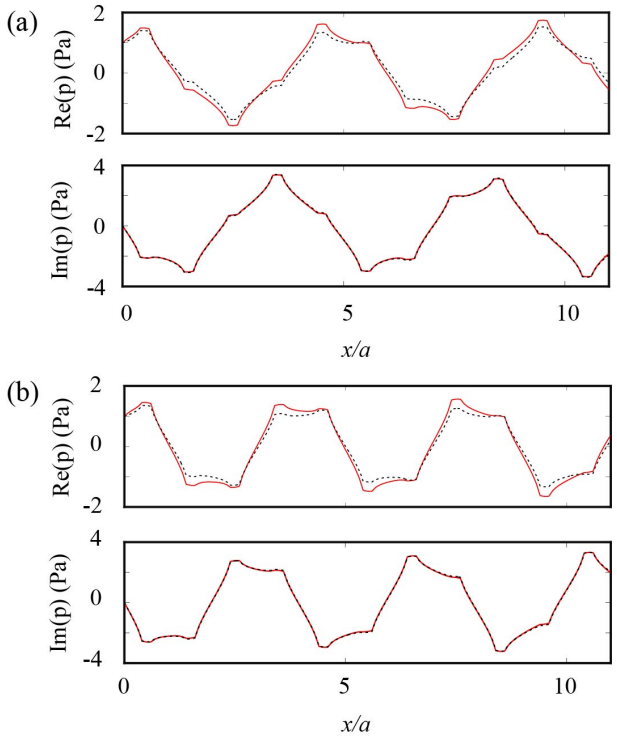

Figure 3.6: Numerical (solid line) and predicted (dashed line) pressure distribution along the central line of the straight linear waveguide LW1 in figure 3.5(a) for (a) n=5 ($\alpha = -1.40 + 1.37$i, $\beta = 2.38 + 1.76$i) and (b) n=6 ($\alpha = -1.08 + 1.60$i, $\beta = 2.18 + 1.94$i)

inferred to be N for the lower passing frequency and $N-1$ for the upper frequency range, though in both cases the length of the waveguide is $L = Na$. We have checked that this apparent discrepancy is not owing to the frequency resolution in the computation, but can rather be attributed to the value of the phase angle θ in Eq. (3.6). There are indeed generally N positive values of $k(\omega_n)\Lambda$ for $\theta \neq 0$ and $N+1$ possible values if $\theta = 0$. However, when a particular value falls close to 0 or π, the group velocity tends to zero: the Bloch wave will not be efficiently excited and hence will not appear in the transmission. As a result, there can be either N or $N-1$ transmission peaks.

Pressure fields at the observed maxima of the straight waveguide LW1 with $L = 11a$ are shown in figure 3.5(a) for the lower passing frequency and figure 3.5(b) for the upper passing frequency. As n increases, the number of spatial oscillations along the waveguide is seen to increase, in accordance with Eq. (3.6). In general, the envelopes of the guided wave fields indeed show sinusoidal variations, as described by Eq. (3.1).

The model of Eq. (3.1) can only be approximate since evanescent Bloch waves are not taken into account. Evanescent Bloch waves are expected to be excited at the two ends of the waveguide and to decay rapidly with distance. Figures 3.6 and 3.7 show the real and imaginary parts of the pressure distribution for the lower or upper frequency range,

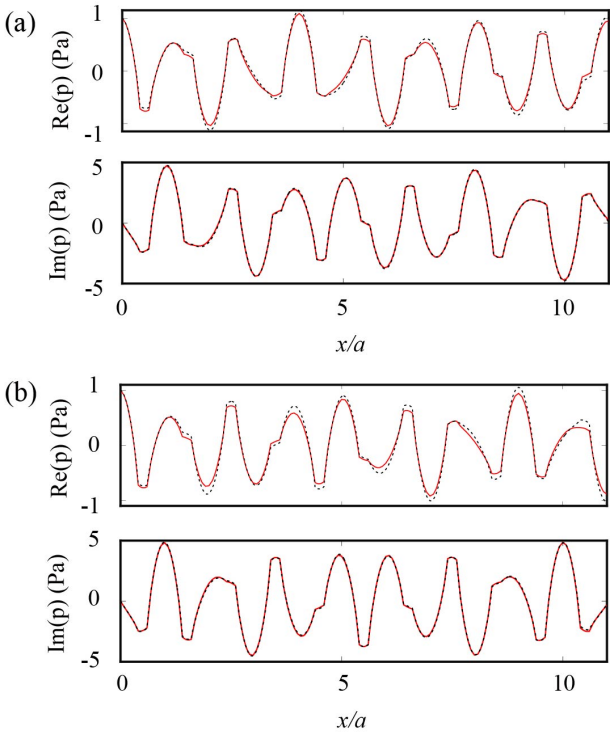

Figure 3.7: Numerical (solid line) and predicted (dashed line) pressure distribution along the central line of the straight linear waveguide LW1 in figure 3.5(b) for (a) n=5 ($\alpha = 1.37 - 0.91$i, $\beta = -0.43 - 0.50$i) and (b) n=6 ($\alpha = 1.20 - 1.08$i, $\beta = -0.35 - 0.51$i).

along the central line of the straight waveguide for maxima $n = 5$ and $n = 6$. In the lower passing frequency, 5 or 6 oscillations are clearly observed in the envelopes of the pressure distribution. While for the upper frequency range, the oscillations are too faint to be distinguished. The pressure distributions obtained by using Eq. (3.1) after fitting α and β are also given in figures 3.6 and 3.7. There is a good overall agreement between computed and fitted pressure distributions.

3.2.3/ PERIODIC COUPLED-RESONATOR ACOUSTIC WAVEGUIDES

In this section, we consider periodic coupled-resonator acoustic waveguides formed by sequences of defect cavities. The separation between adjacent cavities is Λ, which is an integral number of lattice constants. We select $\Lambda = 2a$ in this subsection, and the supercell is shown in figure 3.8(a). A cavity is introduced by replacing one cylinder of water with mercury. By sweeping the wavevector in the ΓX direction of the first Brillouin zone, the dispersion relation of the CRAW is obtained and illustrated in figure 3.8(b). The reduced wavenumber, $k\Lambda/(2\pi)$, is used in the band structure. Three guided modes are formed within the complete band gap. Their pressure distributions at the Γ point corresponding to points d, e and f are displayed in figure 3.8(c). The pressure distributions of the guided

Bloch waves have the same symmetries as those in figure 3.2(b). Bloch wave F is a deaf mode, although it has a better confinement than Bloch wave C.

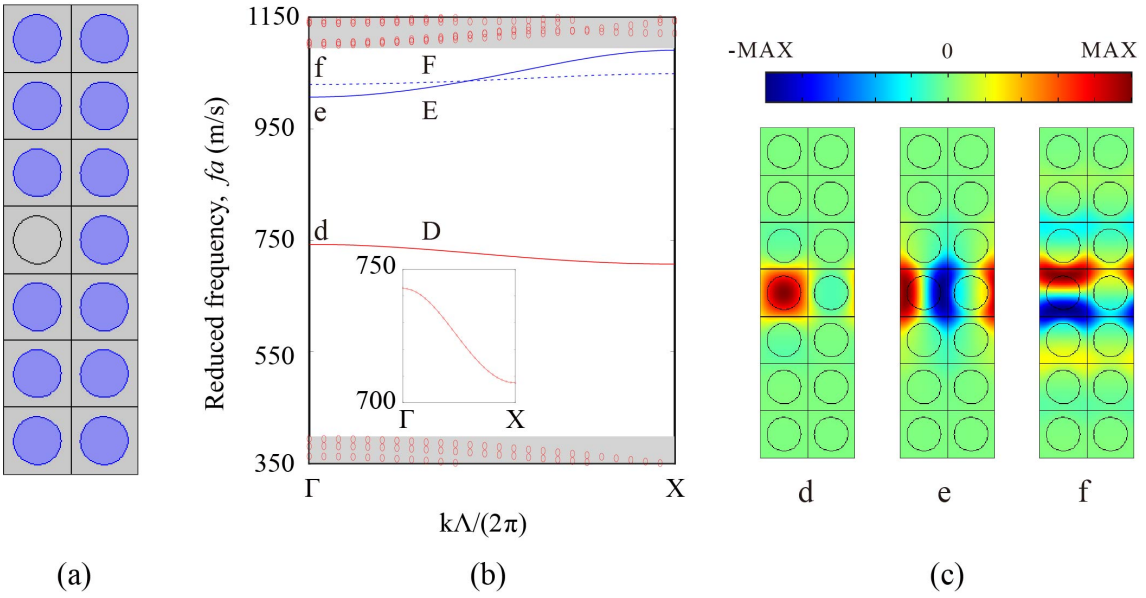

Figure 3.8: Band structure of a CRAWs with cavity separation Λ=2a. (a) A 7×2 supercell of the square PC of water cylinders in mercury. (b) The dispersion relation is presented in the ΓX direction of the first Brillouin zone. The gray areas indicate the passing frequency ranges. Scatterers and lines represent the numerical and fitted results, respectively. (c) Pressure distributions for the three guided modes are presented at dispersion points d, e and f. The color scale extends symmetrically from blue for negative values to red for positive values.

Next, we consider periodic CRAWs with different lengths and number of turns defined in finite PCs, as shown in figure 3.9(a)-(d). Four different variations on the theme of CRAWs are considered: (a) a straight chain of 10 cavities, (b) a chain of 13 cavities and 2 turns, (c) a chain of 17 cavities and 8 turns, and (d) the same as (b) but for a straight chain. For simplicity, they are named CW1, CW2, CW3, and CW4, respectively.

Figure 3.9(e) shows transmissions for different circuits. For comparison, transmission for the perfect PC is also presented. Two passing frequency ranges appear clearly inside the complete bandgap, coinciding with the CRAW dispersion bands in figure 3.8(b). Transmissions for different circuits have slight differences in the extent of passing frequency ranges. This indicates that the CRAW principle can be applied to design rather arbitrary waveguides, i.e. waveguides with an arbitrary number of turns. In the upper passing frequency range, the transmissions for different circuits have large variations that strongly depend on the considered waveguide. Indeed, the more turns along the waveguide appear, the larger the variations are. We do not attribute these complications to the presence of two guided modes in this frequency range, since Bloch wave F is deaf, but

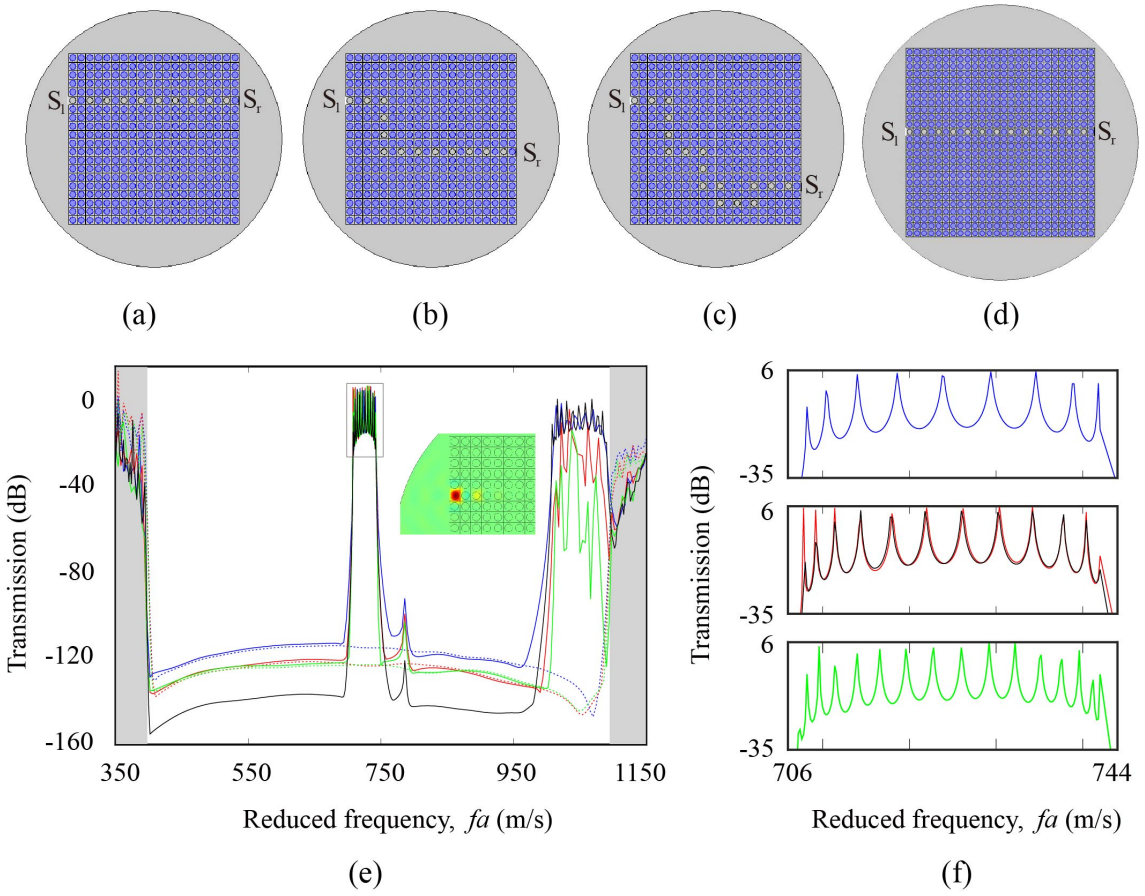

Figure 3.9: Cross-sections of CRAWs arranged in different circuits inside finite PCs and the related transmission. The length L of a waveguide is an integer multiple of the cavity separation $\Lambda = 2a$. We consider (a) a straight waveguide with $L = 10\Lambda$ (CW1), (b) a waveguide with 2 turns and $L = 13\Lambda$ (CW2), (c) a waveguide with 8 turns and $L = 17\Lambda$ (CW3), and (d) a straight waveguide with $L = 13\Lambda$ (CW4). The wave sources used for transmission computation are marked by white lines. Transmitted waves are detected at the black lines. (e) Transmissions for CW1, CW2, CW3 and CW4 are shown by the blue, red, green and black lines, respectively. The dashed lines represent transmission through the perfect PC, with source and detector placed as in the case of waveguides. The inset shows the pressure distribution at $fa = 786$m/s for the straight waveguide. (f) For clarity, transmission around $fa = 725$m/s is zoomed.

rather to the modal shape of Bloch wave E (shown in figure 3.8(c)) that is not as compatible with turns as the modal shape of Bloch wave D. Bloch waves D and A have a similar doubly symmetric shape, so they can almost couple equally to 4 different directions. The only difference is that Bloch wave A is slightly more 'compressed' by periodicity, as we noted before, so its coupling is slightly asymmetric along the horizontal and vertical directions. This is further proved by the comparison of the transmission for waveguides with the same length but different turns in figures 3.3(e) and 3.9(f).

In the following, we will correspondingly focus our attention on the lower passing fre-

Table 3.2: Frequencies at which transmission is maximum for different CRAWs in the lower passing frequency of figure 3.9(e). The units of reduced frequency, fa, are m/s.

order	1	2	3	4	5	6	7	8	9	10	11	12	13	14	15	16
CW1	741.8	738.8	734.6	729.4	723.8	718.6	714	710.4	708.2							
CW2	742	740.4	737.8	734.2	730.4	726.2	722	718	714.4	711.4	709.2	707.8				
CW3	742	741.2	739.6	737.4	735.2	732.2	729.2	726	722.8	719.6	716.6	714	711.4	709.6	708.2	707.4
CW4	742	740.4	737.8	734.2	730.2	726	721.8	717.8	714.4	711.4	709.2	707.8				

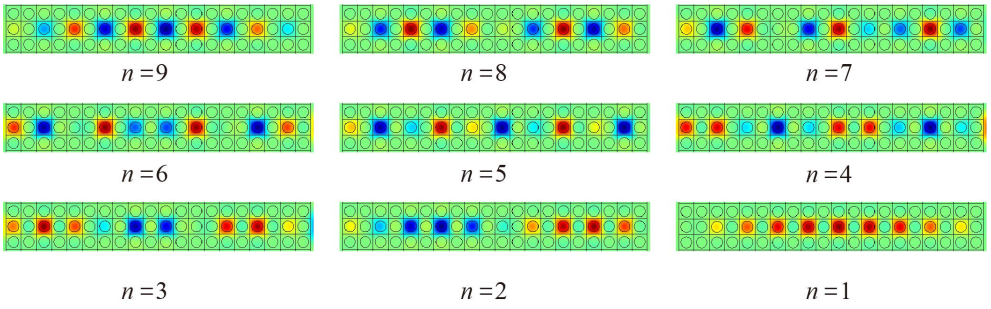

Figure 3.10: Pressure distribution of the straight CRAW (CW1, $L = 10\Lambda$) at the resonant peaks listed in Table 3.2. The number of pressure oscillations are shown below the field maps.

quency range that supports single mode propagation and large maximum transmission. Low transmissions are observed at frequencies in-between passing bands, similar to those in figure 3.3. They are generally determined by the total length of the waveguide. Longer CRAWs generally have smaller transmission. It is also noted that there is a spurious resonance appearing above the lower passing frequency range. Its generation is directly related to the excitation of a localized resonance close to the line source, as the pressure distribution shown in the inset of figure 3.9(e) shows. Given the very low transmission at this local resonance, it can be safely ignored.

Figure 3.9(f) shows a close-up view at transmission within the lower passing frequency range. A pattern of successive maxima and minima appears in the transmission spectra. Table 3.2 reports the frequencies with maximum transmissions for the four considered waveguides, presented in decreasing order in accordance with the dispersion relation of Bloch wave D in figure 3.8(b). It is observed that the waveguides with the same length (CW2 and CW4) have the same number and positions of maxima of transmission, similar to the results for linear waveguides. Moreover, the effect of the turns is lower compared to that for the linear waveguides, owing to the higher confinement of the CRAWs. The number of maxima is inferred to be $N - 1$ if the length of the waveguide is $L = N\Lambda$, in accordance with Eq. (3.6) when $\theta = 0$. Indeed, for $n = 0$ (Γ point) and $n = N$ (X point), the guided Bloch waves have zero group velocity and are not excited by a source placed outside the waveguide.

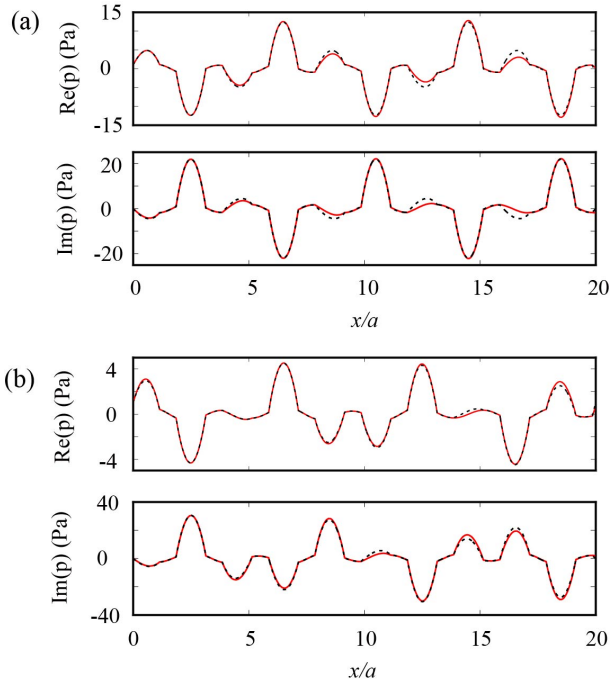

Figure 3.11: Numerical (solid line) and predicted (dashed line) pressure distribution along the central line of the straight CRAW CW1 in figure 3.10 for (a) n=5 ($\alpha = -0.81 - 0.72$i, $\beta = 1.20 + 0.42$i) and (b) n=6 ($\alpha = -1.24 - 0.35$i, $\beta = 1.50 - 0.02$i). Real and imaginary parts of the pressure are both illustrated in the upper or lower part, respectively.

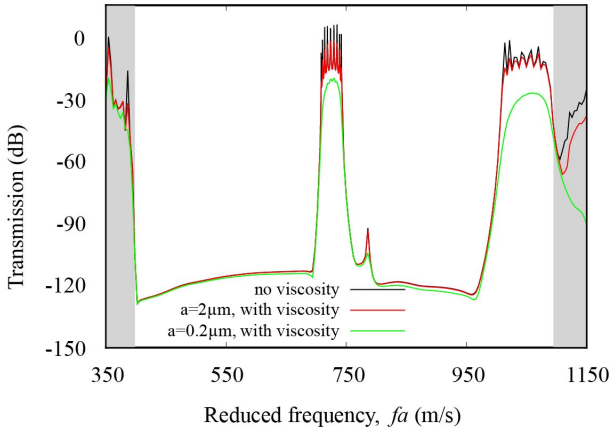

Figure 3.12: Influence of viscous damping in fluids on the transmissions of the straight CRAW CW1 for different lattice constants.

Pressure fields in the straight CRAW CW1 with $L = 10\Lambda$ are shown in figure 3.10 for the 9 observed maxima. Similar to the linear waveguides, the number of spatial oscillations along the waveguide is seen to increase with the increase in n. Figure 3.11 shows the real and imaginary parts of the pressure distribution along the central line of the straight waveguide for maxima $n = 5$ and $n = 6$, as well as the results predicted by using Eq. (3.1) after fitting α and β. A good overall agreement between computed and fitted pressure distributions is again observed. In general, it can be concluded that the channeled

transmission spectrum is well explained by the simple model presented in the theoretical model part.

In practice, acoustic wave damping has distinct effects on the transmission through a waveguide. The frequency-dependent viscosity [22] of water and mercury can be taken into account by using a viscous fluid model [4]. Viscous losses effectively increase with the square of frequency in this model. The effects of damping on the transmission spectrum for different lattice constants a are shown in figure 3.12, in the case of the straight waveguide. Changing the lattice constant amounts to tuning the operating frequency range. It is observed that the influence of viscosity remains limited if the lattice constant is larger than 2 μm, i.e. for operating frequencies lower than about 300 MHz. The effect of viscosity however increases rapidly for smaller lattice constants. Viscous effect in passing frequency ranges is more apparent as compared to their outside, because guided waves have small group velocities, and the spatial decay on propagation is known to vary inversely with the group velocity. In the limit of large viscous damping, the spectral oscillations in the channeled spectrum tend to be washed out, indicating a quenching of the interference of forward and backward guided Bloch waves.

3.3/ WAVE PROPAGATION IN CREWS

The previous section studied the propagation of acoustic waves in periodic coupled resonator waveguides. In this section, we extend the concept to elastic waves. It is easier for cross holes to produce a wider band gap than circle holes [115] in a solid plate. We investigate numerically and experimentally Lamb wave propagation in the periodic coupled-resonator elastic waveguides formed by a chain of cavities in a two-dimensional phononic crystal slab with cross holes. The influence on the dispersion of guided waves of the slab thickness and of the hole length is also investigated.

3.3.1/ EXPERIMENTAL MEASUREMENTS AND NUMERICAL METHODS

Figure 3.13 presents a photograph of the experimental setup used for measuring Lamb wave propagation in a PC slab. An asymmetric wave source is formed by sticking a piezoelectric patch to one side of the slab, in order to generate Lamb waves. Two kinds of temporal signals are used. A periodic chirp is used to measure the transmission properties. A harmonic signal with given frequency is further used to measure the distribution of the out-of-plane displacement over the surface of the slab. Displacements are mea-

sured using the Polytec PSV-500 scanning vibrometer. Such a technique is often used to detect Lamb wave [56, 63]. Transmissions are estimated by detecting out-of-plane displacements around designated points and are averaged over the surface of one unit cell of the PC slab.

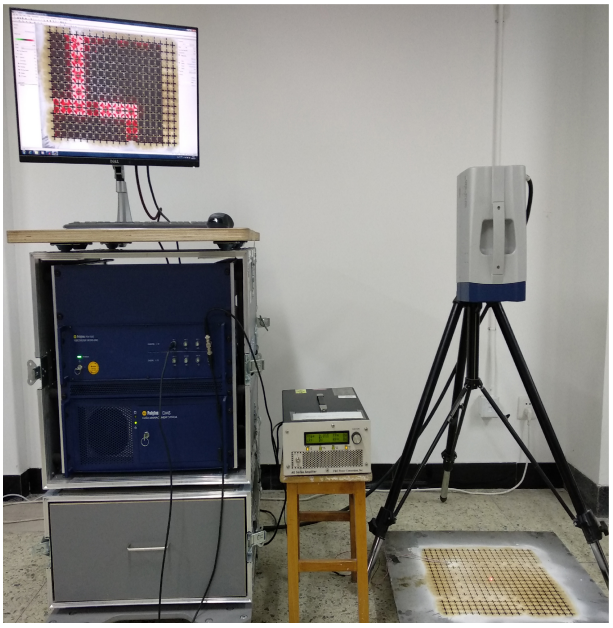

Figure 3.13: Photograph of the experimental setup illustrating the measurement of vertical displacements of Lamb waves excited in a PC slab sample.

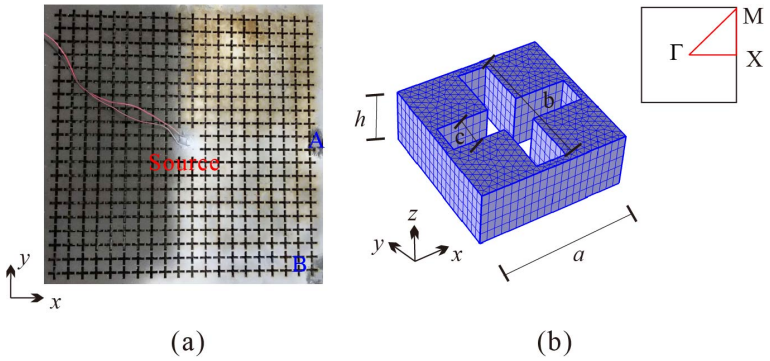

(a) (b)

Figure 3.14: PC slab sample manufactured in a stainless steel plate. (a) The Lamb wave source in the center is a piezoelectric patch. Transmitted waves are measured along the ΓX direction (at point A) and the ΓM direction (at point B). (b) The primitive unit cell is schematized, including geometrical dimensions and the first Brillouin zone for the square lattice.

Numerical simulations are conducted using the finite element method. A primitive unit cell, as sketched in figure 3.14(b), is chosen to determine the dispersion relation of the perfect PC slab. Due to the large impedance ratio between steel and air, air is treated as a vacuum in the numerical model. A supercell technique is used to investigate the

dispersion relation and eigenmodes of CREWs. Traction-free boundary conditions are set on the top and bottom surfaces and inside the holes, and periodic Bloch boundary conditions are applied on the other boundaries. The mesh spacing in the plane of the slab is smaller than $a/20$, with a being the lattice constant. There are 5 elements in the depth of the plate. Second degree polynomial elements of the Lagrange type are used to approximate the displacement vector considered as the unknown. A sparse eigenvalue solver is used to search for eigenfrequencies. Band structures are obtained by letting the wavevector sweep the selected directions of the first Brillouin zone. The displacement distribution for selected eigenmodes is obtained by selecting the relevant frequency and wavevector.

Numerical transmissions are further calculated by considering a time-harmonic 3D model of the finite slab. A z-polarization displacement wave source with unit amplitude ($|U_{z0}|$=1) is applied to the central part of the slab. Transmitted displacements are collected at the ends of the waveguide and of the splitter circuit, similarly to the experimental arrangement. The transmission, $T(f)$, is evaluated as the ratio of the vertical displacement amplitude ($|U_z|$) integrated over two identical homogeneous parts around the excitation ($S_i = a^2$) and detection areas ($S_d = a^2$), i.e.,

$$T(f) = 20\log_{10}\left(\frac{\int_{S_d}|U_z|\,\mathrm{d}s}{\int_{S_i}|U_{z0}|\,\mathrm{d}s}\right). \tag{3.11}$$

It should be noted that the transmission thus defined can be larger than zero without violating energy conservation.

3.3.2/ Analysis and discussions

We first consider a 2D square lattice PC slab with cross holes, as shown in figure 3.14(a). The sample is composed of an array of 20×20 unit cells with a central defect where the source is attached. The unit cell including mesh elements and the geometrical dimensions of the perfect PC is shown in figure 3.14(b). The geometrical parameters are chosen as b/a=0.9, c/a=0.2 and h/a=0.4, with the lattice constant a=20 mm. The solid matrix is isotropic steel with mass density $\rho = 7850$ kg/m^3, Poisson's ratio $\nu = 0.3$, and Young's modulus $E = 206$ GPa.

The phononic band structure of the perfect PC slab is shown in figure 3.15(a). The dispersion bands are classified as in-plane or out-of-plane by evaluating the displacement

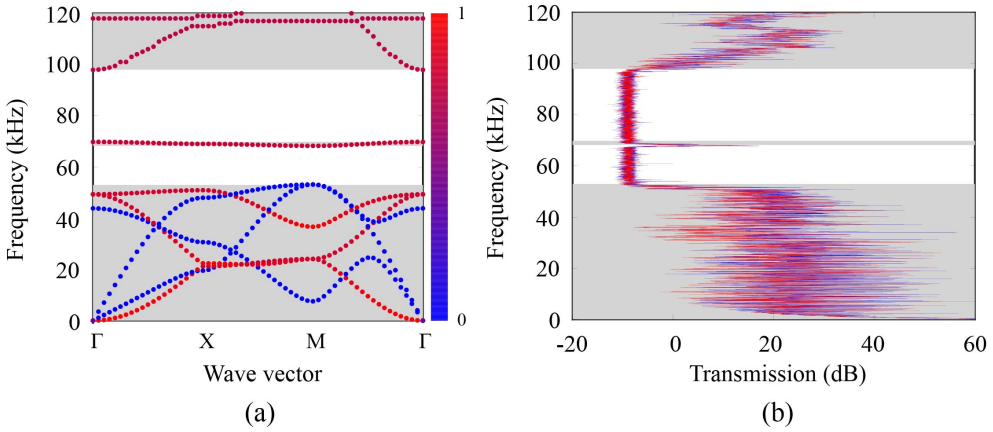

Figure 3.15: (a) Phononic band structure and (b) experimental transmission of the perfect PC slab with cross holes. The color scale in panel (a) measures the polarization and varies from in-plane modes (blue) to out-of-plane modes (red). The gray areas indicate the passing frequency ranges. The blue and red lines in panel (b) show measurements along the ΓX and ΓM directions, respectively.

vector of each Bloch wave. Two complete band gaps extend in the frequency ranges 53.15 kHz $< f <$ 68.25 kHz and 69.8 kHz $< f <$ 87.9 kHz. Experimental transmissions along the ΓX and ΓM directions are shown in figure 3.15(b). Excellent agreement is observed between numerical simulation and experiments, without any parametric adjustment. As a remark, the excitation is asymmetric with respect to the mid-plane of the slab and favors the excitation of out-of-plane modes. In-plane modes can, however, be excited as well as a result of the finite lateral extent of the source. The wide complete bandgaps are suitable for the design of highly confined coupled-resonator waveguides, as we discuss next.

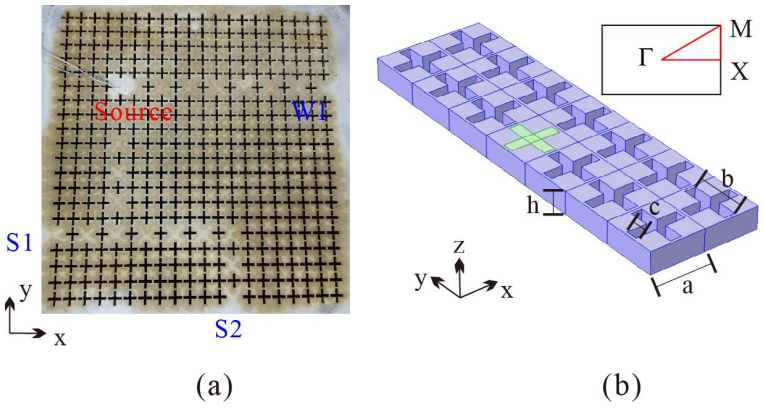

Figure 3.16: Coupled-resonator elastic waveguides. (a) The experimental sample includes a linear chain of defect cavities defining a straight waveguide (W1), and a wave splitter circuit with 90° bends and two output ports (S1 and S2). The Lamb wave source is a piezoelectric patch. (b) The supercell of the coupled-resonator elastic waveguide is used to obtain the dispersion of guided waves.

The periodic CREWs are formed in the perfect PC slab by filling certain cross holes to

form defect cavities. The sample fabricated in stainless steel is shown in figure 3.16(a). CREWs are formed by considering a chain of defect cavities separated by 2 lattice constants. Both a straight waveguide and a wave splitter are fabricated on the same sample. The straight waveguide (W1) is a sequence of 7 cavities. The wave splitter is composed of one straight part and of two asymmetric parts (labeled S1 and S2), including sharp corners with 90° bends.

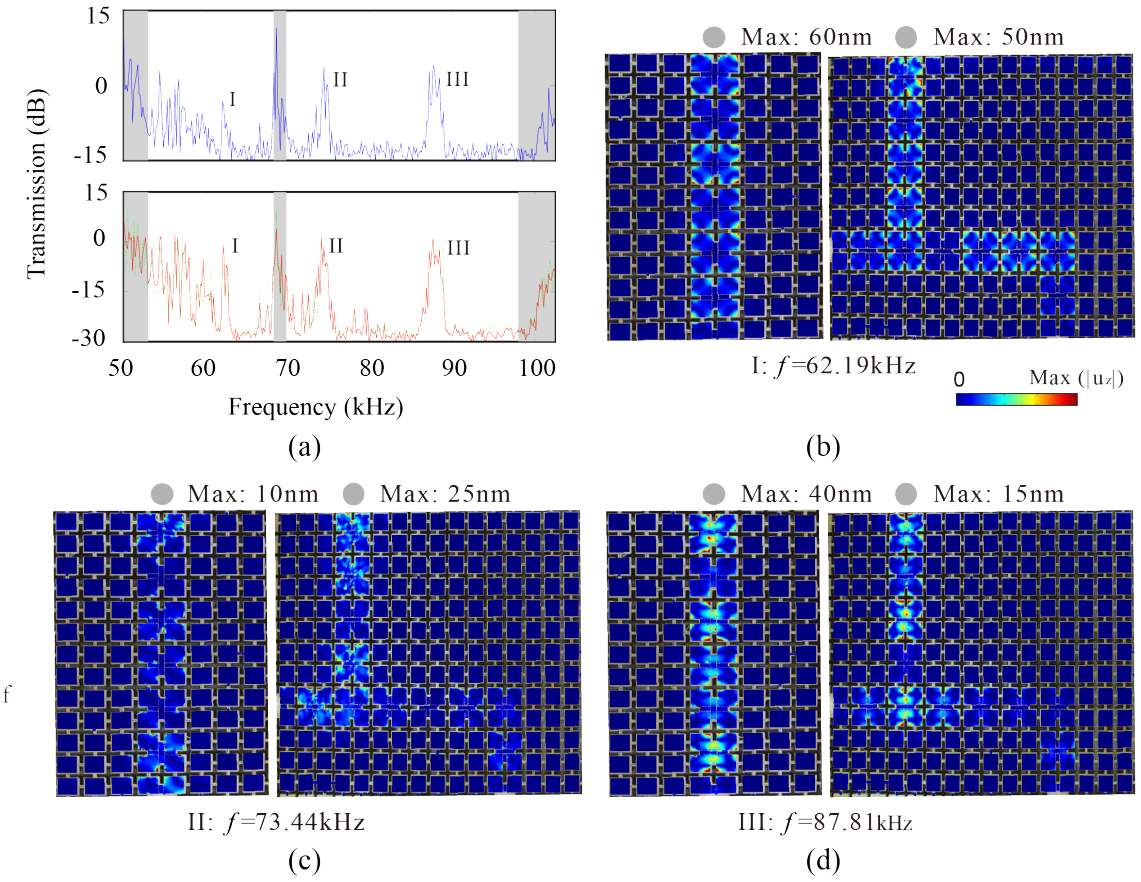

Figure 3.17: Experimental observation of Lamb wave propagation in the sample of figure 3.16(a). (a) The transmission through the waveguide (blue line: W1) and through the splitter (red line: S1, green line: S2) is shown as a function of frequency. Transmission is measured for the vertical component of displacement $|u_z|$ and is normalized to its value at low frequency. The gray areas indicate the passing bands for perfect PC slab. Panels (b)-(d) show field distributions of displacement measured at chosen frequencies of the three passing frequency ranges labeled I-III in (a). In each panel, the left and right subplots are for the straight waveguide or the wave splitter, respectively. The wave source position is indicated by the gray disk. The color scale is for amplitude of z-displacement normalized with respect to the maximum amplitude (Max).

Experimental transmissions are shown in figure 3.17(a). They are normalized by the transmission for the straight waveguide measured at a low passing frequency. Three distinct guidance frequency ranges, labeled I-III, are clearly observed inside the complete

bandgap. In the case of the wave splitter, the transmissions measured at the two ends present only slight differences, especially in the logarithmic scale, although their total lengths are quite different. This observation is consistent with the high degree of confinement of guided waves. Experimental displacement fields at the chosen frequencies for each of the three passing frequency ranges are presented in figure 3.17(b)-(d). Lamb waves are found to be strongly confined as they are guided along the waveguides and to turn efficiently at the 90° bends. They are furthermore split rather evenly at the T-junction of the wave splitter. Away from the defect cavities, Lamb waves decay very fast in all directions. This is a further confirmation of the complete bandgap of the PC slab.

The phononic band structure shown in figure 3.18(a) is obtained considering a supercell of size $2a \times 7a \times h$, as depicted in figure 3.16(b). It indicates the existence of a total of 9 guided Bloch waves. Each of them emerges around a resonance frequency of the isolated defect cavity. The lowest 3 guided Bloch waves are mixed together and are thus left out of the following analysis, though they clearly lead to transmission both experimentally and theoretically. Eigenmodes at the X point are shown in figure 3.18(b). Guided Bloch waves 1, 5, and 6 are polarized mostly out-of-plane. In contrast, guided Bloch waves 2, 3, and 4 are polarized mostly in-plane.

The numerical transmissions through the waveguide and the wave splitter shown in figure 3.18(c) are in quite good agreement with the experimental results. Bloch waves 4 and 6 have a flat dispersion and thus can hardly be excited; hence they do not contribute to the transmission. Since the wave source is vertical and symmetrical with respect to the xz plane, longitudinal modes can be excited. The distribution of x-displacement for Bloch wave 2 shown in figure 3.19(a) is symmetric with respect to the xz plane. This mode can thus be excited, and results in a relatively high transmission. In contrast, the x-displacement distribution of Bloch wave 3 is asymmetric with respect to the xz plane. Such a mode can then hardly be excited, and a quite low transmission is observed in both simulation and experiment. Summarizing, passing frequency ranges I, II and III can be attributed to Bloch waves 1, 2 and 5, respectively. In each of these frequency ranges, guidance is single-mode. Taking range III for example, guiding and splitting of Lamb waves in figure 3.18(d) are clearly observed owing to the excitation of the eigenmode at X5 for Bloch wave 5.

3.3.3/ INFLUENCE OF GEOMETRY PARAMETERS

Some previous researches have demonstrated that the dispersion of Lamb waves is strongly dependent on the geometry. Accordingly, we investigate the influence of geo-

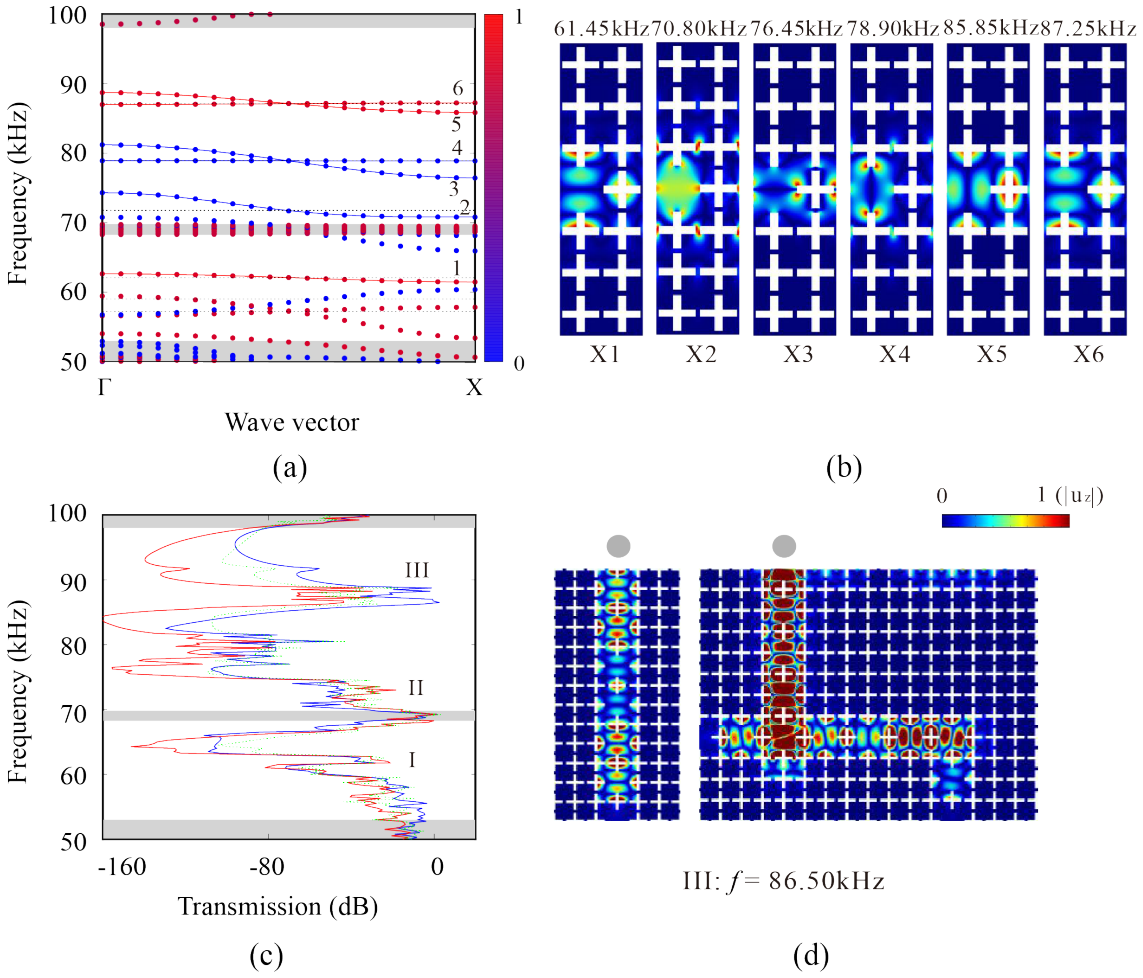

Figure 3.18: Finite element analysis of dispersion and transmission for CREWs. (a) The band structure is obtained from a supercell model of the periodic waveguide. Points are for finite element results. Solid lines are obtained by fitting to a theoretical model (see text). The horizontal dashed lines mark the resonant frequencies for an isolated cavity in the PC slab. The color scale represents from the in-plane modes (blue) to out-of-plane modes (red). The gray areas indicate the passing bands for the perfect PC slab. (b) The displacement distributions at the X point of the 6 Bloch waves labeled in (a) are shown. (c) The numerical transmission through the straight waveguide and the wave splitter is plotted as a function of frequency. Panel (d) shows the displacement distributions at a chosen frequency inside passing range III. The color scale in panels (b) and (d) is for amplitude of z-displacement normalized with respect to the maximum amplitude (Max).

metric parameters, including slab thickness and size of the hole, on the dispersion of guided waves in this subsection. The variation of the phononic band structure with the slab thickness is shown in figure 3.20. For a small thickness ($h/a = 0.15$), only passing bands appear below 94.5 kHz. In the absence of a band gap, guided modes cannot form between adjacent defect cavities. When $h/a = 0.3$, guided modes are formed owing to the appearance of complete bandgaps. As the slab thickness is varied continuously, it is expected that bands shift continuously in dispersion space. Bands can then be la-

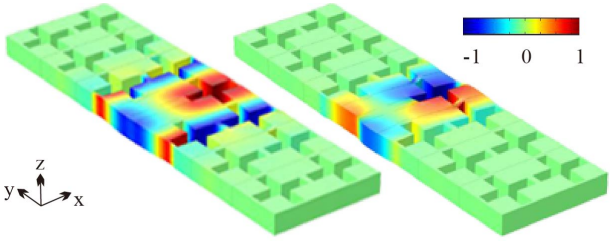

Figure 3.19: Distribution of the x-displacement at the X point for Bloch waves 2 and 3 in figure 3.18(a). The color scale varies from negative (blue) and positive (red) normalized values.

beled by comparing eigenmodes with those of figure 3.18(b). With h/a increasing to 0.4, the frequencies of Bloch waves 1, 5 and 6 generally increase. Since these modes are mostly out-of-plane, their eigenfrequencies are to the first order proportional to the slab thickness. In contrast, the frequencies of Bloch waves 2, 3 and 4 do almost not change, since these modes are mostly in-plane. When $h/a = 0.55$, Bloch waves 5 and 6 move to even higher frequencies, and Bloch wave 1 is mixed with the in-plane guided modes. When $h/a = 0.9$, higher order vibration modes with cutoff frequencies [146] appear, and are mixed with Bloch waves 3 and 4. With a further increase of the slab thickness, these modes will close the bandgap, causing the disappearance of the guided modes.

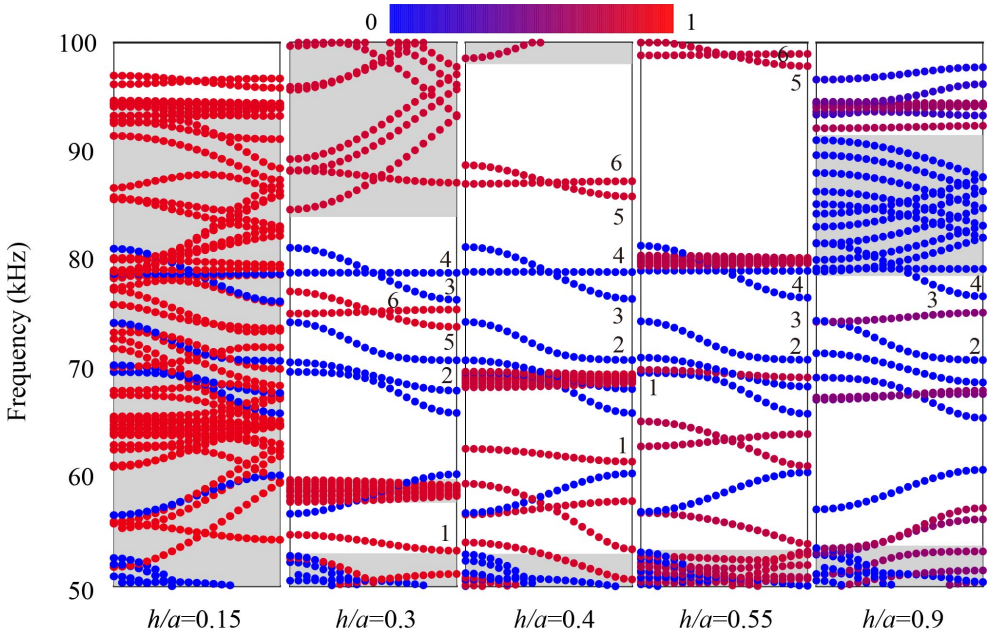

Figure 3.20: Band structures of CREWs with different relative thicknesses ($b/a = 0.9$, $c/a = 0.2$). The color scale measures the polarization and varies from in-plane modes (blue) to out-of-plane modes (red). The gray areas indicate the passing bands for the corresponding perfect PC slab.

We further consider the effect of the hole length, b/a, on the guided modes. The results

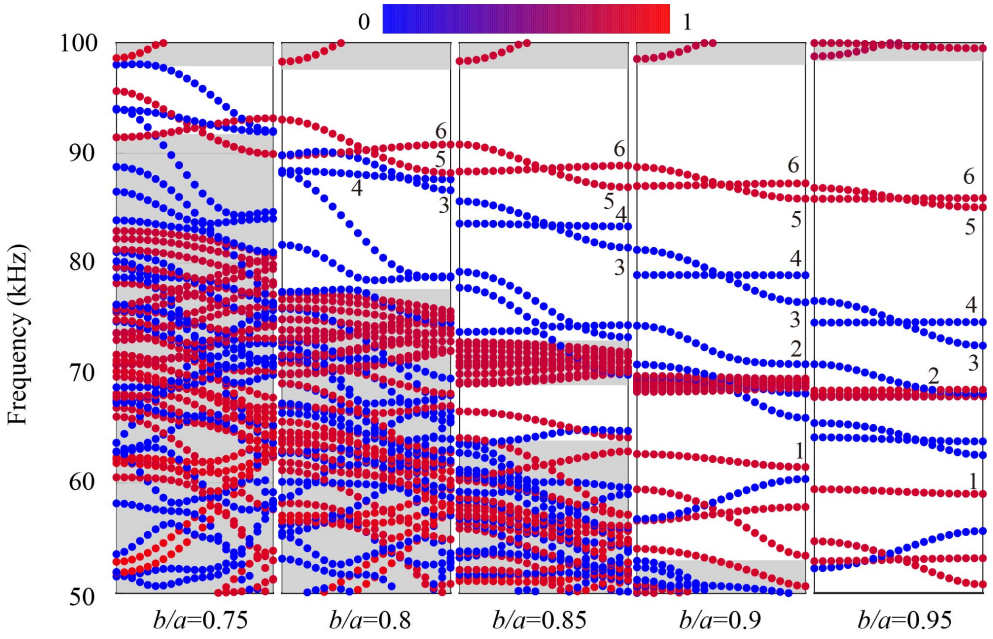

Figure 3.21: Band structures of CREWs with different relative hole lengths ($c/a = 0.2$, $h/a = 0.4$). The color scale measures the polarization and varies from in-plane modes (blue) to out-of-plane modes (red). The gray areas indicate the passing bands for the corresponding perfect PC slab.

Table 3.3: Fitted expansion coefficients, $\Gamma_m/(2\pi)$ (kHz), used for the prediction of CREW dispersion according to the theoretical model of Ref. [137].

	Mode	$n = 1$	$n = 2$	$n = 3$	$n = 4$	$n = 5$	$n = 6$
h/a=0.3	$\Gamma_0/(2\pi)$	54.04	72.12	78.78	78.83	75.38	75.27
b/a=0.9	$\Gamma_1/(2\pi)$	0.37	0.88	1.19	0.005	0.81	-0.09
	$\Gamma_2/(2\pi)$	-0.02	0.21	-0.019	-0.001	0.054	-0.001
	$\Gamma_3/(2\pi)$	-0.002	-0.06	0.003	-0.0002	0.006	-0.00009
h/a=0.4	$\Gamma_0/(2\pi)$	62.05	72.15	78.85	78.9	87.2	87.1
b/a=0.9	$\Gamma_1/(2\pi)$	0.30	0.90	1.19	0.005	0.72	-0.06
	$\Gamma_2/(2\pi)$	-0.01	0.20	-0.019	-0.001	0.035	-0.00048
	$\Gamma_3/(2\pi)$	-0.001	-0.06	0.004	-0.0002	0.003	-0.00003
h/a=0.4	$\Gamma_0/(2\pi)$	59.23	69.31	74.59	74.61	85.92	85.87
b/a=0.95	$\Gamma_1/(2\pi)$	0.11	0.67	1.01	-0.010	0.44	-0.02
	$\Gamma_2/(2\pi)$	-0.0008	0.08	-0.031	-0.002	0.015	-0.00012
	$\Gamma_3/(2\pi)$	-0.000	-0.002	0.003	-0.0003	0.0008	-0.0000

are illustrated in figure 3.21. When $b/a = 0.75$, a narrow complete bandgap exists in the considered frequency range and guided modes are mixed with passing bands. This

mixture disappears when $b/a = 0.8$, but the in-plane and the out-of-plane guided modes remain mixed. With a further increase of the hole length, Bloch waves 3 and 4 separate from Bloch waves 5 and 6. When $b/a = 0.9$, Bloch waves 1 and 2 come up. When $b/a = 0.95$, Bloch wave 2 interferes with the passing bands around 70 kHz. As a rule, the frequencies of guided modes generally decrease with an increase in the hole length. Furthermore, the frequencies of in-plane Bloch waves decrease faster than those of the out-of-plane Bloch waves.

The dispersion of guided Bloch waves in a linear chain of coupled cavities can be fitted against the theoretical model of Ref. [137]. The corresponding dispersion relation can be expressed by Fourier series [75]

$$\omega = \Gamma_0 + \sum_{m=1}^{\infty} 2\Gamma_m \cos(km\Lambda), \tag{3.12}$$

where $\omega = 2\pi f$ is the angular frequency and k is the wavenumber. The Fourier coefficients Γ_m can be interpreted as representing the coupling strength between defects separated by a distance $m\Lambda$.

The fitting parameters are listed in Table 3.3 for the six Bloch waves and for different geometrical parameters. As a note, parameter $\Gamma_0/(2\pi)$ is the resonance frequency of the isolated cavity. The predicted dispersion relations are further shown in figure 3.18, 3.20 and 3.21 with solid lines. It can be seen that the fit of dispersion with the numerical results is excellent. Significantly, it is observed that the coupling coefficients hardly change with the slab thickness for the in-plane Bloch waves 2, 3 and 4. This is a direct evidence that the dispersion of the in-plane guided Bloch waves is almost independent of the slab thickness. In contrast, coupling coefficients clearly vary with the hole length, especially for in-plane Bloch waves.

3.4/ CONCLUSIONS

In this chapter, we have discussed the appearance of channeled transmission spectra in phononic crystal waveguides and investigated periodic coupled-resonator elastic waveguides designed in a PC slab with cross holes. The conclusions are as follows:

(1) For the water/mercury 2D phononic crystal with circle holes, we have proposed a model and predicted the pressure distribution in the waveguide and the shape of the channeled spectrum. The influence of fluid viscosity on transmission at different lattice constants is discussed. The results show that the channeled spectra are

dependent on the length of the waveguide but are almost independent of the circuit details, including the number of turns. Theoretical results agree well with numerical transmissions and pressure distributions. The smaller the lattice constant is, the larger the effect of viscosity on transmission is; as the viscosity of the material increases, the oscillations in the channeled spectrum gradually disappear.

(2) For the 2D phononic crystal plate with cross holes, coupled-resonator elastic waveguides formed with chains of coupled cavities are then designed and fabricated. The transmission characteristics of the wave propagating along different waveguides are numerically studied and experimentally verified. The influence of the geometrical parameters of the system on the band structures is discussed. The results show that the transmission of strongly confined Lamb waves along a straight waveguide and in a wave splitter circuit is observed. Guidance and splitting of Lamb waves at 90° bends were clearly observed in the experiments. Numerical simulations successfully explain the experimental transmission results and allow us to identify the guided Bloch waves responsible for guidance. The slab thickness is found to have little influence on the dispersion of in-plane guided Bloch waves, contrary to the usual case of Lamb waves of an homogeneous plate.

The conclusions in this chapter could be extended and applied to multimode PC waveguides, though the shape of the channeled spectrum would obviously be less simple. If one wants to remove the occurrence of maxima and minima in the transmission spectrum, care should be taken to engineer the terminations of the waveguide to minimize reflections, for instance by using tapering techniques similar to electromagnetic and optical waveguides. They can be used for the practical design of elastic wave devices based on coupled defect cavities at ultrasonic frequencies, and could be used to design more complicated phononic circuits.

4

WAVE PROPAGATION IN APERIODIC COUPLED-RESONATOR ELASTIC WAVEGUIDES

4.1/ INTRODUCTION

The evanescent wave [172] existing in the band gap of the perfect phononic crystal provides a coupling mechanism [166] for the coupled resonant waveguide. Strong confinement and localization [25, 104, 40] within the band gap of the entire phononic crystal are achieved. In previous researches, the coupled resonant waveguide was limited to the periodic array of resonator chains. We remark that coupling between adjacent resonators were limited to straight lines or to privileged crystallographic directions [72, 137]. Instead, evanescent coupling inside a complete band gap is omnidirectional and decreases exponentially away from a resonator. Therefore, evanescent waves can realize the coupling of adjacent resonators in an aperiodic coupled-resonator chain, i.e, a rather arbitrary path with finite length. On the other hand, the current works on coupled-resonator waveguides have focused on large scale phononic crystal structures, not micro-nano structures. Micro-nano phononic crystals can produce wide band gaps in the high frequency range. They have potential applications in vibration control [199], heat treatment [133], MEMS [206], SAW [195] and the development of new acoustic equipments [194].

The propagation of acoustic and elastic waves in periodical coupled-resonator waveguides was studied in the previous chapter. This chapter breaks the limitation of periodicity and extends to aperiodic coupled-resonator waveguides with near-field coupled discrete resonators which are designed and processed in a fused silica plate at the micrometer scale. The transmission characteristics of elastic waves in the waveguide are studied.

The collective resonances at ultrasonic frequencies (MHz) are observed. Actually, interaction between adjacent resonators is reminiscent of the chemical bonds of molecular polymers. The concept of 'phonon polymer' is proposed. An approximate theoretical model of phononic polymer is developed to explain the frequency response and to predict the discrete spectrum of resonance frequencies.

4.2/ PROCESSING OF EXPERIMENTAL SAMPLE

We introduce the method of processing of the two-dimensional phononic crystal sample with aperiodic coupled-resonator waveguide at the micrometer scale. Femtosecond laser-assisted wet etching has been demonstrated as a powerful mask-free micromachining method, allowing fabrication of various 3D microstructures [49] in fused silica (a-SiO_2) and other glass materials with high spatial precision. This method is well suited for the fabrication of phononic crystals resonators due to the high selectivity of etching of glass materials in KOH (> 200), resulting in high aspect ratio structures with well-defined and smooth vertical sidewalls. In this research, the process parameters are adjusted to produce a significant increase in the etch rate of irradiated silica (> 200 times in KOH). Increased etch rate can be explained by laser-induced stress generation that is responsible for weakened chemical bonds (and hence bond angle variations [122]) in the SiO_2 matrix. Moreover, with increasing number of laser pulses, stress builds up and a porous structure is created that can be penetrated much faster by the etchant.

The chain of coupled-resonators shown in figure 4.1 was manufactured in a fused silica plate. We designed the chain of resonators by omitting the etching of selected holes. The sample size is 26 $\mathrm{mm}\times$ 20 $\mathrm{mm}\times$ 500 $\mu\mathrm{m}$. A square lattice of cross holes, with lattice constant $a = 714$ $\mu\mathrm{m}$, was etched in the plate by using a 3D laser system (FEMTOprint model f100 aHEAD Enhanced), equipped with a 5 W femtosecond laser operating at $\lambda = 1030$ nm. The overall fabrication process is a direct writing method (i.e., without mask) and is composed of three main steps. The process flow is shown in figure 4.1(a). First, a laser machining process is programmed in 3D by use of a dedicated software (Alphacam) that results in the generation of a machining code file. Next, the fused silica substrate is scanned by the focused laser beam, according to the program, and the material is exposed to low-energy femtosecond pulses that accelerate locally the etching rate. Only a very thin contour (2-2.5 $\mu\mathrm{m}$ wide) of each cross-hole is exposed through the whole substrate thickness in sequential order. In the final step, the thin walls of exposed silica (aspect ratio ≈ 80) are double-side etched in a 10M KOH solution at 80°C. The

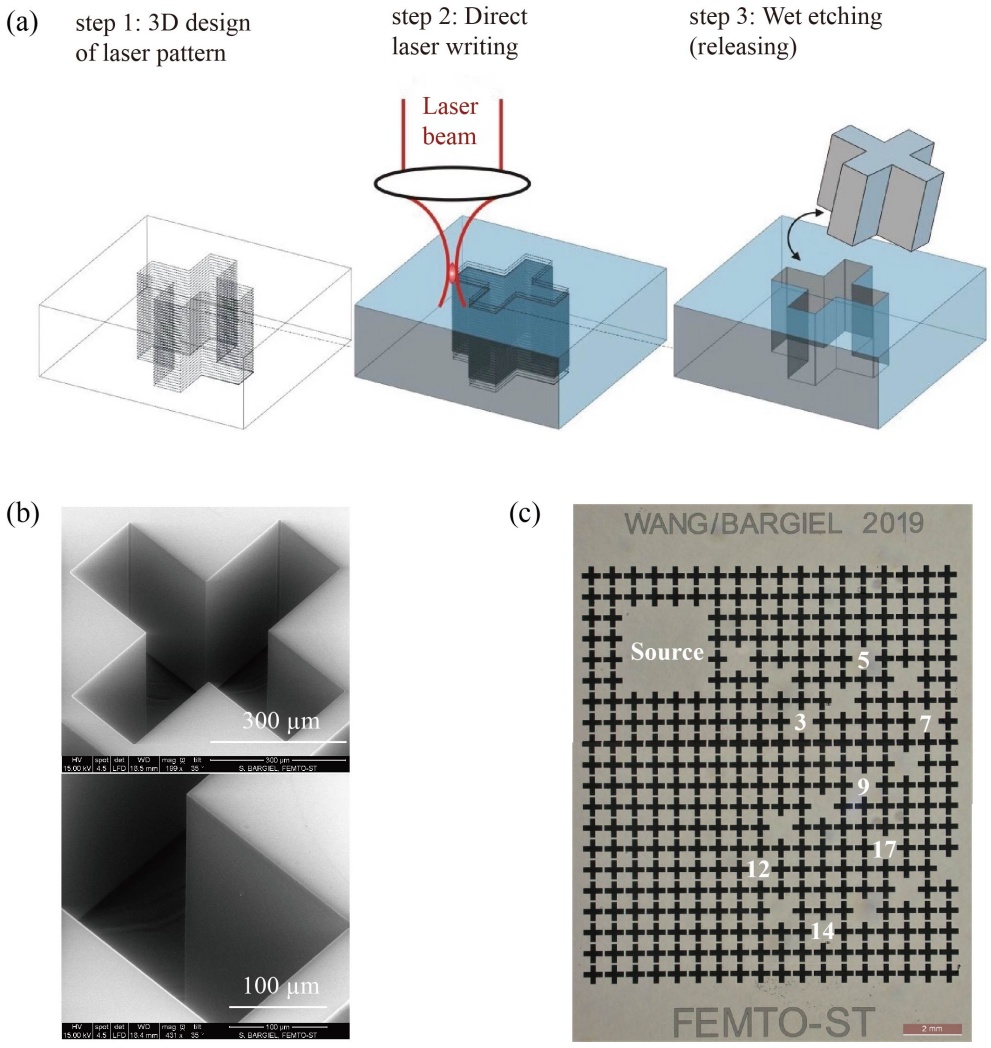

Figure 4.1: Experimental setup for excitation and imaging of the vibrations of a chain of coupled-resonators in a phononic crystal slab. (a) A array of cross holes forming a square lattice is etched in a fused silica plate by femtosecond laser-assisted wet etching. (b) A scanning electron microscope image of a single cross hole and a zoomed view at a sidewall, illustrating the fabrication roughness, are shown. (c) An optical microscope image of the sample shows the chain of 18 coupled-resonators embedded in a 20×18 phononic crystal of cross holes and the position of the source of vibrations.

total etching time was 3h (etch rate $\approx 2.2\ \mu\text{m/min}$) resulting in releasing of silica cross blocks into the etchant. Ultrasonic vibrations were activated periodically during etching to enhance penetration of KOH through the high aspect structure and to stabilize the etching rate. The scanning electron microscope image of a cross hole (measured with SEM Quanta 450W) in figure 4.1(b) allows to verify the smoothness of the walls after etching. Fabrication errors are estimated to be less than $\pm 1\ \mu\text{m}$. To verify the precision of the fabrication, an optical microscope (Leica model DM8000) is used to check the dimensions of the fabricated structures as shown in figure 4.1(c). The resonators along the chain are

numbered in sequence.

4.3/ EXPERIMENTAL MEASUREMENTS AND NUMERICAL METHODS

The experimental sample is a finite fused silica plate formed by 20×18 unit cells as shown in figure 4.1(c). There are 18 resonators in the path. We purposely chose the sequence of defects to follow a rather arbitrary path in the plane of the surface, with the intent of showing that the coupling of resonators allows to tunnel elastic waves without creating straight channels. Adjacent resonators are separated by $(\pm 2, \pm 1)$ or $(\pm 1, \pm 2)$ lattice shifts, i.e. their absolute separation distance is fixed by the direction of the chain jumps from resonator to resonator. The source region is placed inside the phononic crystal. For frequencies inside the complete phononic band gap, this ensures that the source region is isolated from the frame surrounding the phononic crystal structure. Evanescent coupling decreases very fast with distance, resulting effectively in near-neighbor coupling along the chain. Since the first resonator is the only one close to the source region, it is the only resonator that is significantly coupled with it.

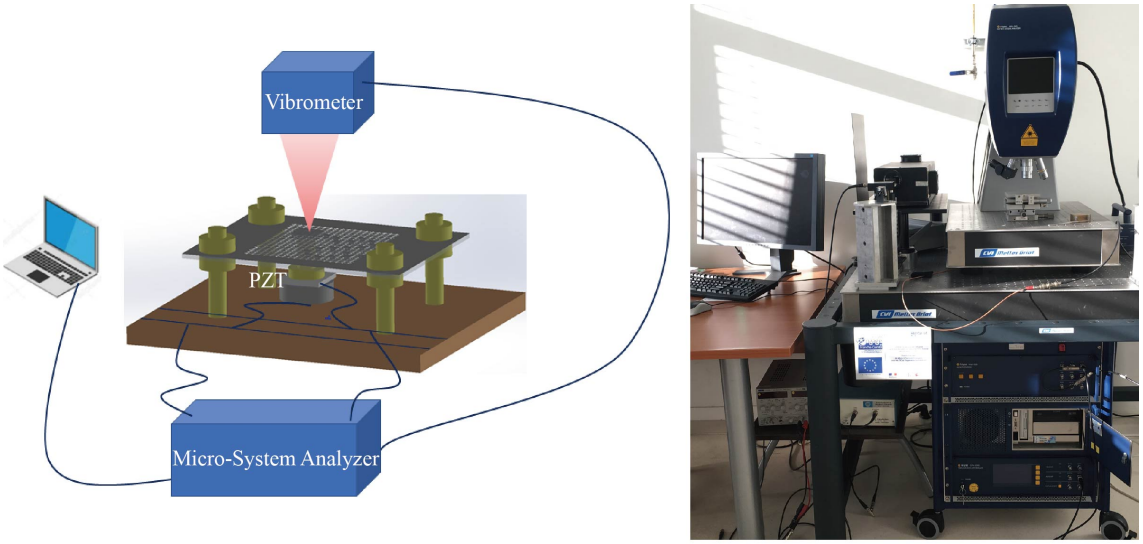

(a) (b)

Figure 4.2: (a) A sketch of the experimental setup shows the fused silica sample attached to a PCB by screws and nuts. The bottom surface is in contact with a piezoelectric patch (PZT) acting as a source of vibrations. Out-of-plane vibrations are detected at the top surface with a laser micro-system analyzer. (b) Photography of the experimental setup.

Figure 4.2(a) shows a sketch of the experimental setup, presented with the photography of the setup in figure 4.2(b). The sample is held over a printed circuit board (PCB) by using screws and nuts. Its bottom surface is in contact with a piezoelectric ceramic trans-

ducer (PZT) that acts as a source of vibrations. We use a MEGGIT Pz27 (Navy II) soft relaxor type PZT whose fundamental resonant frequency is 5 MHz to cover the whole frequency range of interest. Pz27 is an all-round soft PZT material with good coupling factor, good charge coefficients, high Curie temperature, and low mechanical quality factor. We avoid resonance effects in the transducer by working below its fundamental resonance frequency. A periodic chirp is chosen as the source waveform in order to cover the frequency range of interest. The electric signal is transformed to a displacement vibration signal via the PZT transducer. The transformed vertical displacement vibration signal is transmitted to the sample through a contacting screw. The vertical, or out-of-plane, displacement signal is recorded by the vibrometer at the top surface of the sample. Measurements of vibrations of the chain are conducted by using a laser Doppler vibrometer (Polytec Microsystem Analyzer MSA-500, equipped with analog displacement decoder model DD-300; 0.03-24 MHz frequency response with 50 nm/V sensitivity).

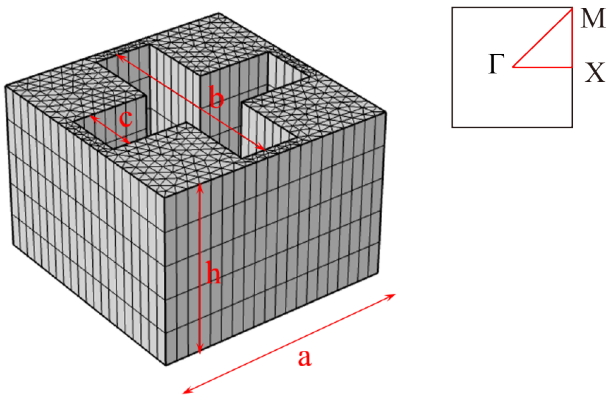

Figure 4.3: The primitive unit cell including geometrical dimensions and the first Brillouin zone for the square lattice.

All numerical simulations in this section are implemented using the finite element method in three dimensions. A 3D finite element model of the unit cell is set in figure 4.3. The mechanical material parameters used for isotropic fused silica are mass density $\rho = 2201$ $\mathrm{kg/m^3}$, Poisson's ratio $\nu = 0.17$, and Young's modulus $E = 72.5$ GPa. The geometric parameters here are $h = 0.7a$, $b = 0.9a$ and $c = 0.25a$, where a is the lattice constant. In order to obtain high transmission, it would be necessary to take care of the coupling of the source with the entrance of the waveguide, but also to reduce the reflection coefficient at the exit of the chain considered as a waveguide. The mesh encompasses the full 20×18 phononic crystal of cross holes, the chain of resonators, and the source. To minimize wave reflections at the lateral boundaries of the mesh, radiation boundary conditions are applied. To allow for a direct comparison with experiment, a time-harmonic and spatially random wave source of vertical polarization is applied at the source region. With this

setting, all possible modes of vibration are excited as the frequency is swept though the band gap range. The frequency response function (FRF) can be recorded at any position along the sample surface. Dispersion relations are obtained by solving an eigenvalue problem with periodic boundary conditions applied at the external boundaries of the unit cell or supercell.

The perfect phononic crystal has a complete band gap extending from 1.5 to 4 MHz. Material loss can be estimated with the Qf factor (product of quality factor by operating frequency in Hertz). $Qf \approx 5 \times 10^{12}$ for fused silica. With the largest frequency considered being 4 MHz, we then have in principle $Q > 1.25 \times 10^{6}$ for the material loss limit. Given our experimental resolution, such fine line width cannot be resolved in practice. As a result, material damping is not added to numerical simulations. Note, however, that radiation damping, resulting from the finite number of phononic crystal rows around the resonator chain, is taken into account through the use of radiation boundary conditions.

4.4/ ANALYSIS AND DISCUSSIONS

The experimental measurement of the frequency response function (FRF) is presented in figure 4.4(a). The line colors represent the FRF measured at different numbered resonators. The FRF shows a series of sharp resonances within the complete phononic band gap, corresponding to vibration modes of the sample. We consider particularly in the following frequency regions around 2.26 MHz, 2.53 MHz, and 3.55 MHz, where the clearest signals are observed. When looking closer, it is observed that each main response actually subdivides in a series of closely spaced sharp resonances, as shown in figure 4.4(c). The number of sub-peaks is of the order of 18 in each case, i.e. a number related to the number of coupled-resonators in the chain. A similar observation was made in the previous chapter regarding the channeled spectrum of the waveguides. The maximum amplitude of the vertical displacement of each resonance peak varies notably, indicating that vibration modes are variously matched to the excitation source. The vertical motion at the source location is shown in figure 4.4(e) for comparison. It can be observed that the resonance peaks measured at the source location do not match those measured inside the chain of resonators. This is expected, since at the source location thickness resonances[1] of the fused silica plate should be excited and these have a different dispersion spectrum compared to the resonators. Interestingly, even when the source region vibrates very faintly, the vibrations of the chain of resonators can still be excited

[1] Thickness resonances are standing Lamb waves of the homogeneous plate, having a zero lateral wavenumber.

until the very last resonator.

The numerical results are shown in figure 4.4(b). In the three frequency ranges extending around 2.26 MHz, 2.53 MHz, and 3.55 MHz, series of sharp resonances are obtained with a frequency spacing in fair agreement with experimental results, as illustrated in the zoomed figure 4.4(d). Note that the experimental frequency resolution is limited to 1.56 kHz, due to a limitation on the number of sample points, while numerical computations are presented with a resolution of 0.2 kHz to ensure that each peak is resolved. Generally, numerical and experimental results agree fairly well, except for frequencies around 3 MHz, where a significant FRF is only observed in the numerical simulation. We attribute this small discrepancy to the actual experimental environment that differs from the numerical excitation source: the experimental excitation is not truly spatially random as is assumed in the numerical simulation. Furthermore, it may be that the excited vibrations have too small amplitude to be observed over the experimental noise floor.

The numerical and experimental vertical displacement distribution at frequencies 2.2625 MHz, 2.5234 MHz, and 3.5578 MHz are further shown in figure 4.5(a) and (b). It is verified that all resonators oscillate collectively at the same frequency. In all cases, vibrations are mainly concentrated at the four corners of the resonators. A clear modal shape repeats for every resonator, in correspondence with the initial vibration mode of the resonator. The collective vibrations are for the whole chain of resonators, without apparent spatial attenuation along the chain, and are only limited by the size of the array.

To compare the acoustic transmission rate between the phononic polymer and conventional phononic waveguides, we designed three additional and more traditional coupled-resonator waveguides with a different number of bends as shown in figure 4.6(b). The inputting and outgoing positions keep the same with the aperiodic path. The periodic coupled resonator waveguides designed here are mainly to observe the collective resonance of the resonator, not to prove the propagation along the waveguide. Figure 4.6(a) shows the simulated transmission spectra. The main observation that we make is that transmission spectra are similar for all waveguides and for the phononic polymer, though the details of the spectra (separation between resonances) depend on the total length of each chain. Compared to conventional coupled-resonator phononic waveguides, a distinctive advantage of the phononic polymer is that guided waves can propagate along a rather arbitrary path and not only along principal directions of the crystal.

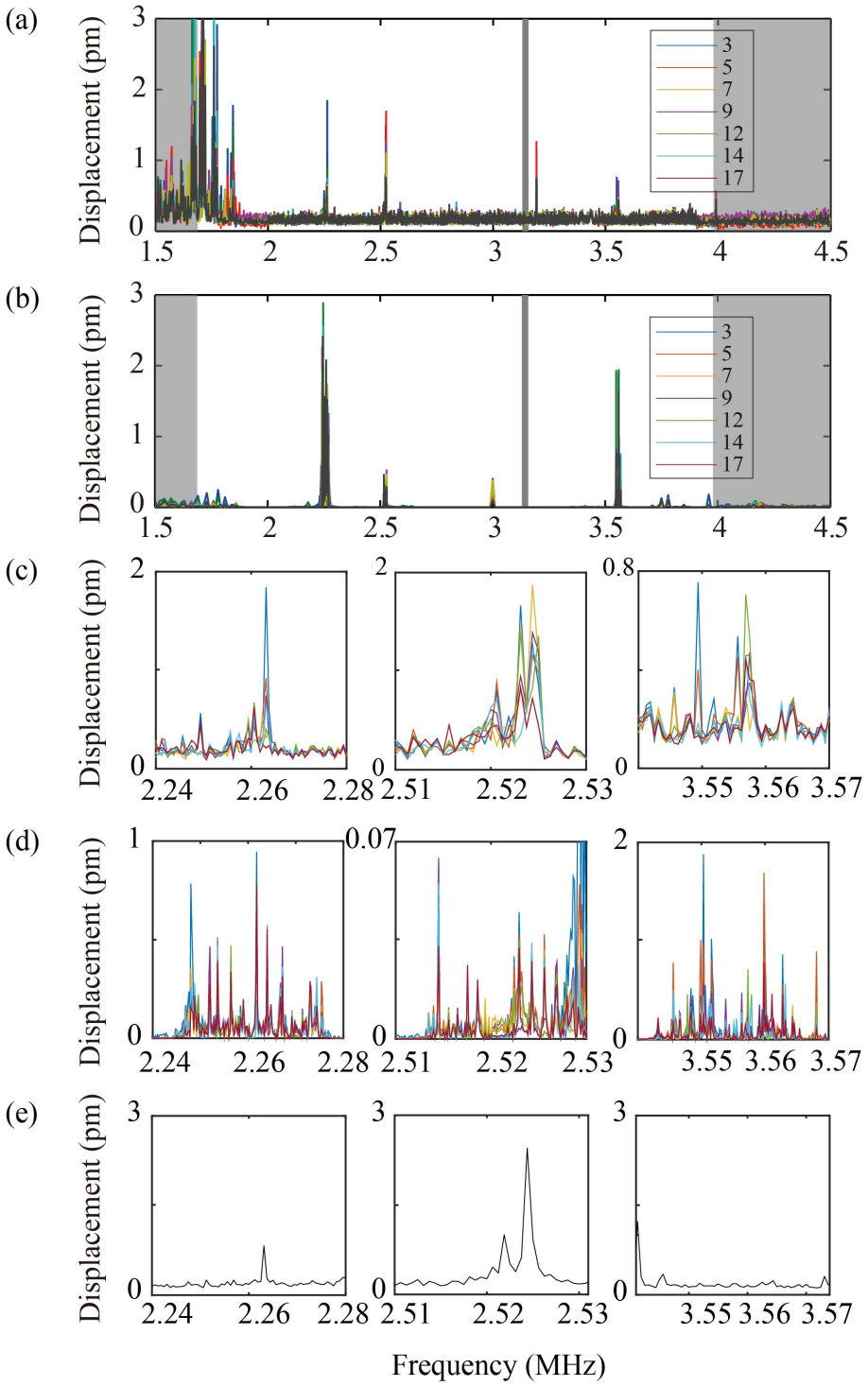

Figure 4.4: (a) Experimental and (b) numerical absolute vertical displacements at the position of the resonators. Each line color is for a particular resonator as labeled in figure 4.1 (c). The complete band gap of the perfect PC extends over the white region. (c)-(d) Enlarged views around selected frequencies. (e) Absolute experimental vertical displacements at the location of the source of vibrations are shown for comparison.

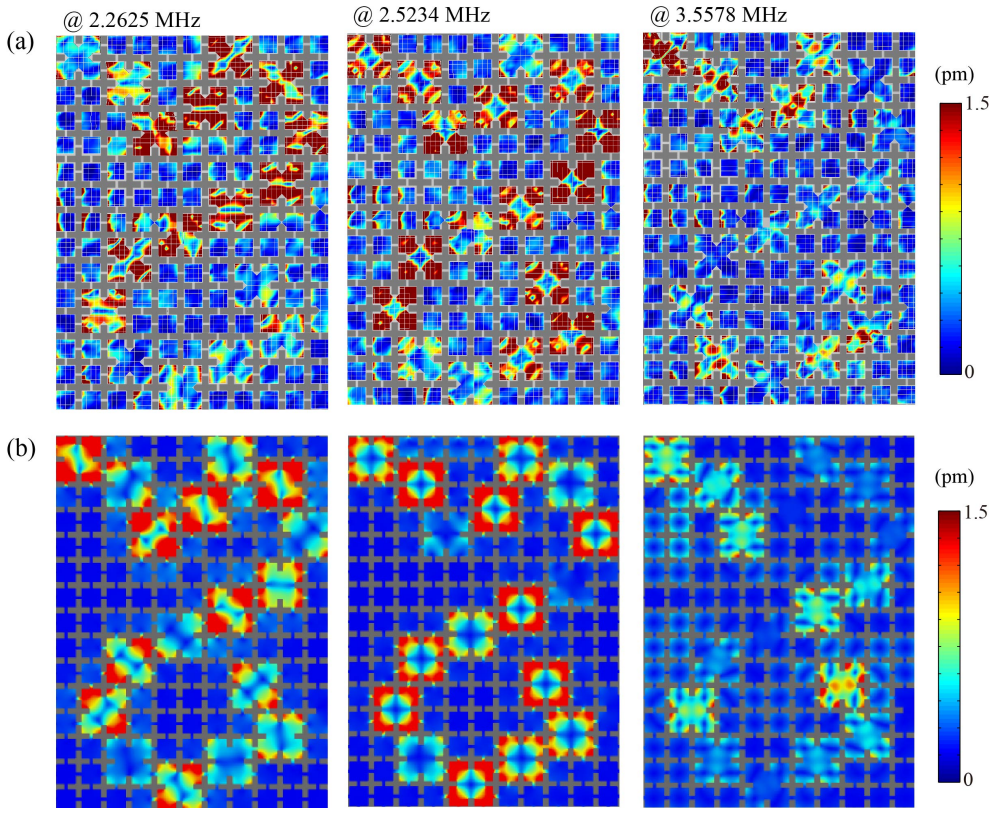

Figure 4.5: Vertical-displacement maps at frequencies of 2.2625, 2.5234, and 3.5578 MHz in the experiment (a) and the numerical simulation (b), respectively. The color scale is for the amplitude of the vertical displacement from 0 (blue) to maximum (red). Numerical values are globally scaled to experimental values.

4.5/ APPROXIMATE THEORETICAL MODEL OF PHONONIC POLYMER

In aperiodic coupled-resonator waveguide, the interaction between the adjacent resonators is similar to the chemical bond of polymer molecules. The concept of 'phononic polymer' is proposed in this section. The approximate theoretical model of phononic polymer is developed. The approximate dispersion relationship of the aperiodic coupled-resonator waveguide is given in theory and simulations.

The chain of coupled-resonators forming a phononic polymer can be analyzed with various discrete models. Hamiltonian models [177, 175] have been proposed, especially in the context of topological phononics. Following the Su-Schrieffer–Heeger (SSH) models [3] of polyacetylene, a coupling Hamiltonian can be constructed for eigenstates combining the degrees of freedom describing each resonator. Solving for the Schrödinger equation with the coupling Hamiltonian gives the sequence of eigenfrequencies. Such a technique parallels the dynamical matrix approach used to describe the dispersion of phonons in atomic lattices. Here, we consider a classical version of such quantum tech-

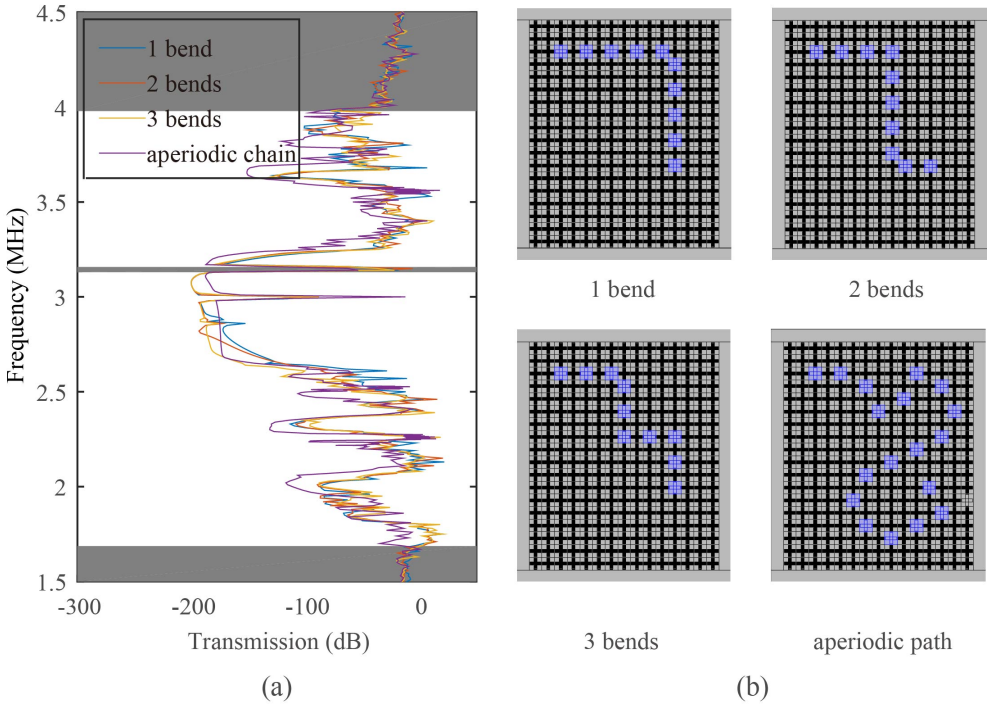

Figure 4.6: (a) Transmission spectra for three circuits with a different number of bends and for the aperiodic chain. The circuits are shown in (b).

niques where the state of the phononic polymer is described by one macroscopic degree of freedom per resonator, U_n. All resonators are identical except for a spatial shift in the crystal and have the same isolated resonance frequency ω_0. By isolated resonator, we mean a resonator embedded in the infinite crystal and placed very far from any other resonator.

The dynamical equation for coupled-resonators [179] is written as

$$-\ddot{U}_m = \sum_{n=1}^{N} D_{m,n} U_n, \tag{4.1}$$

with a element of symmetric dynamical matrix $D_{m,n}$ such that $D_{m,m} = \omega_0^2$. The symmetry of the dynamical matrix is a consequence of reciprocity. Considering time-harmonic vibrations at a frequency ω, the dynamical equation leads to eigenfrequencies that are eigenvalues of the dynamical matrix:

$$\omega^2 U_m = \sum_{n=1}^{N} D_{m,n} U_n. \tag{4.2}$$

As a result, there are exactly N eigenstates of vibration of the phononic polymer. The symmetry of the dynamical matrix implies that the eigenfrequencies $(\omega_i, i = 1 \cdots N)$ are

real. This is the most general form we can obtain without making further simplifying assumptions.

If the resonators are distributed evenly along the chain, it can be assumed that the dynamical matrix is banded, i.e. $D_{m,n} = \gamma_{|m-n|}$, reflecting the idea of a translationally invariant chain [35]. The coefficients $\gamma_{|m-n|}$ account for nearest-neighbor coupling. This particular assumption was made for coupled-resonator waveguides formed of infinite chains of coupled-resonators[2]. The dispersion relation for Bloch waves of the infinite periodic chain was then obtained as

$$\omega^2 = 2\sum_{m=0}^{\infty} \gamma_m \cos(km\Delta). \tag{4.3}$$

We stress that this formula applies to the phononic polymer only in the limit $N \to \infty$.

If we further assume that only nearest-neighbor coupling occurs, then the dynamical matrix simplifies to

$$\mathbf{D} = \begin{pmatrix} \omega_0^2 & \gamma & 0 & \cdots & 0 \\ \gamma & \ddots & \ddots & \ddots & \vdots \\ 0 & \ddots & \ddots & \ddots & 0 \\ \vdots & \ddots & \ddots & \ddots & \gamma \\ 0 & \dots & 0 & \gamma & \omega_0^2 \end{pmatrix}. \tag{4.4}$$

For this particular case, the eigenfrequencies can be obtained analytically and are

$$\omega_{N,m}^2 = \omega_0^2 + 2\gamma \cos\left(\frac{\pi m}{N+1}\right), m = 1 \cdots N. \tag{4.5}$$

Let us consider a finite chain of N discrete resonators described by Eq.(4.5). The dynamical matrix has the form $\mathbf{D}_N = \omega_0 \mathbf{I}_N + \gamma \mathbf{C}_N$, where $\mathbf{I}_N$ is the identity matrix of size N and

$$\mathbf{C}_N = \begin{pmatrix} 0 & 1 & 0 & \cdots & 0 \\ 1 & \ddots & \ddots & \ddots & \vdots \\ 0 & \ddots & \ddots & \ddots & 0 \\ \vdots & \ddots & \ddots & \ddots & 1 \\ 0 & \dots & 0 & 1 & 0 \end{pmatrix}. \tag{4.6}$$

[2]For a finite chain of coupled-resonators, there are in principle end effects that break the banded matrix assumption: resonators at either ends do not see the same environment as resonators in the middle of the chain.

The eigenvalues of the latter matrix are roots of the characteristic polynomial $P_N(X = \lambda) = \det(\mathbf{C}_N - \lambda \mathbf{I}_N)$. It is easy to check that the set of polynomials P_N thus defined satisfy the recurrence relation:

$$P_{N+2} + XP_{N+1} + P_N = 0, N \geq 0, \tag{4.7}$$

with the first two polynomials being $P_0 = 1$ and $P_1 = -X$. The next polynomials are $P_2 = X^2 - 1$, $P_3 = -X^3 + 2X$, $P_4 = X^4 - 3X^2 + 1$, and so on.

The existence of the recurrence relation Eq. (4.7) implies that the set of the real polynomials P_N is orthogonal. As a consequence, their roots are all real and are interleaved. The recurrence relation actually resembles the one for Tchebychev polynomials [16]

$$T_{N+2} - 2XT_{N+1} + T_N = 0. \tag{4.8}$$

Tchebychev polynomials are characterized by the relation $T_N(\cos\theta) = \cos(N\theta)$ for $0 \leq \theta \leq \pi$, but are not the only set of orthogonal polynomials determined by this recurrence relation. In particular, their derivatives $U_N = \frac{1}{N}T'_N$ also do. Those polynomials satisfy $U_N(\cos\theta) = \sin(N\theta)/\sin(\theta)$ and are $U_1 = 1$, $U_2 = 2X$, $U_3 = 4X^2 - 1$, $U_4 = 8X^3 - 4X$ and so on. It is easily checked that $P_N(X) = U_{N+1}(-2X)$. The zeros of U_{N+1} are given by condition $\sin((N+1)\theta)/\sin(\theta) = 0$, or $\theta_m = \frac{m\pi}{N+1}, m = 1 \cdots N$. As a result, the zeros of P_N are $\lambda_m = -2\cos(\theta_m) = -2\cos(\frac{m\pi}{N+1}), m = 1 \cdots N$ and are all in interval $[-2, 2]$.

It is further obtained that they distribute on the continuous dispersion relation for the infinite polymer

$$\omega^2 = \omega_0^2 + 2\gamma\cos(k\Delta), \tag{4.9}$$

where Δ is the period of the chain and with the wavenumber being sampled according to $k\Delta = \frac{\pi m}{N+1}, m = 1 \cdots N$. This condition is equivalent to the phase-matching condition introduced to describe the channeled spectrum of the transmission of phononic crystal waveguides. As a generalization, we infer that if the dispersion relation $\omega^2(k\Delta)$ is known, then the resonance frequencies will be given by $\omega^2(\frac{\pi m}{N+1}), m = 1 \cdots N$. This distribution explains the sequence of sub-peaks in figure 4.4 around each initial defect resonance.

As we know, the direct computation of the band structure of phononic polymer is impossible in the case of the aperiodicity. Also, direct comparison of the discrete phononic polymer model with a coupled-resonator waveguide is not strictly possible since the former is aperiodic while the latter is periodic. Anyway, in order to enable comparison to some extent, we consider a simplified periodic version of the phononic polymer, as depicted by

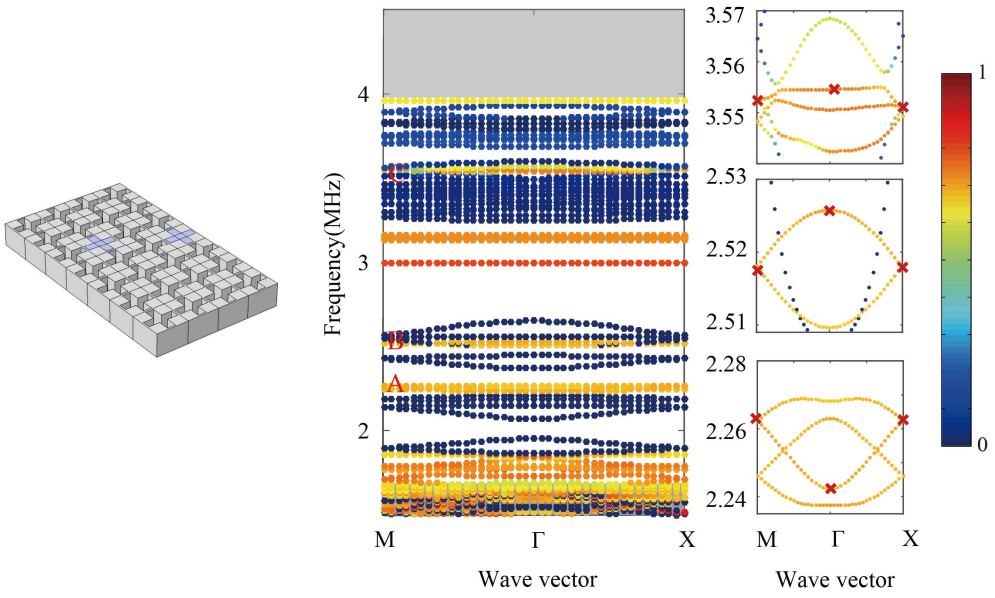

Figure 4.7: Dispersion of an approximate coupled-resonator elastic waveguide: (a) Supercell, (b) Band structure, (c) Zoomed band structures around 2.26 MHz, 2.52 MHz, and 3.55 MHz, corresponding to range A, B and C, respectively. Blue (red) corresponds to zero (maximum) amplitude for the out-of-plane displacement field. The gray areas indicate the passing frequency ranges of the perfect PC.

the supercell in figure 4.7(a). Compared to the actual chain of coupled-resonators considered in experiments, the coupled-resonator waveguide of figure 4.7(a) implements a sequence of lattice translations $(2,-1)$ and $(2,+1)$ so that the spatial period along axis x is $4a$ (four crosses along axis x in the supercell). The coupled-resonator waveguide thus defined could be obtained by a continuous deformation of the chain of resonators.

Figure 4.7(b) shows the phononic band structure for the coupled-resonator waveguide whose supercell is presented in figure 4.7(a). The color bar measures the polarization amount of the vertical component of displacement. Compared to the phononic band structure of the perfect crystal, additional bands appear inside the complete band gap. Figure 4.7(c) shows close-up views of the band structure around 2.26 MHz, 2.52 MHz, and 3.555 MHz, corresponding to labels A, B, and C inserted in panel (a). As a note, the $4a$ period causes spurious foldings at the X and M points of the first Brillouin zone, since two periods of the chain are actually included in the supercell. As a result, there are 2 bands in spectral ranges A and B, and presumably more in spectral range C. These bands have different polarization contents and thus couple differently with the source of vibrations. In particular, the mostly vertically polarized band in spectral range B has the cosine shape of Eq. (4.3), in correspondence with the single coupling coefficient of the dynamical matrix in Eq. (4.4). The other bands do not have this simple cosine shape and

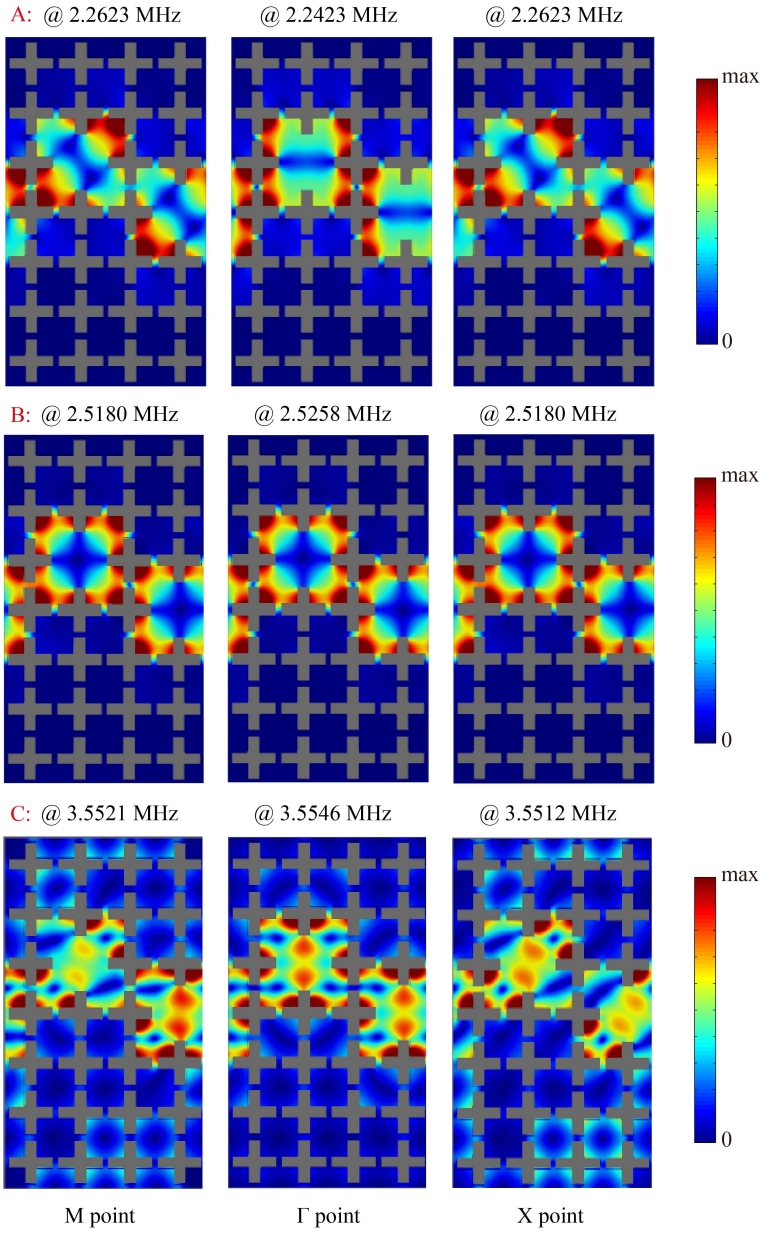

Figure 4.8: Eigenmodes of the supercell shown at the M point, Γ point and X point of the first Brillouin zone at the passing bands corresponding to A, B and C labeled in figure 4.7(B). Blue (red) corresponds to zero (maximum) amplitude for the displacement field.

more coupling coefficients should be included to describe them. Significantly, all bands extend almost symmetrically toward the X and the M points, indicating that the coupling coefficients are here mostly independent of the direction of the coupling, as we have implicitly assumed in the discrete model.

Eigenmodes at the high symmetry points of the Brillouin zone on three selected bands of spectral ranges A, B, and C are illustrated in figure 4.8. We further verify that they

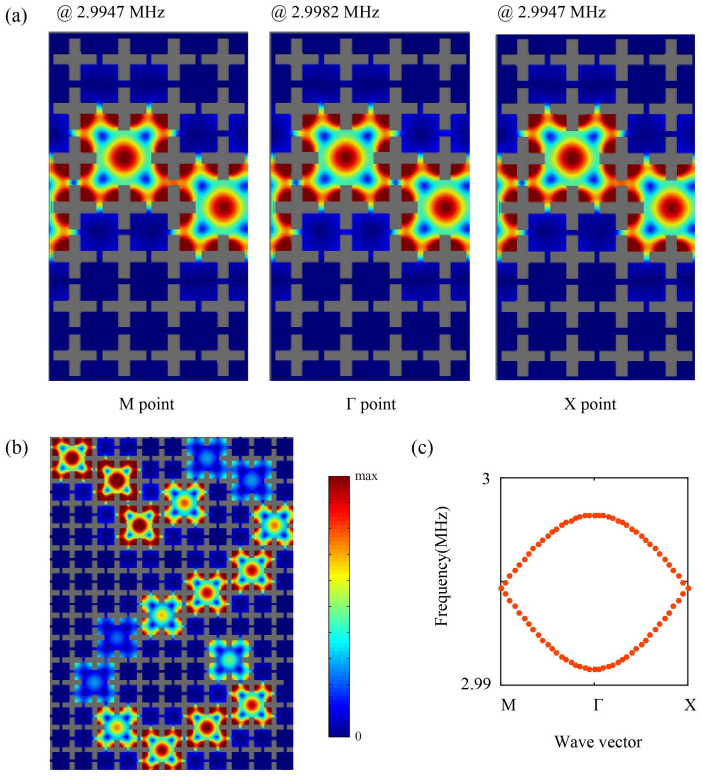

Figure 4.9: Characteristics of the band appearing around 3 MHz. (a) Eigenmodes are shown at the M point, the Γ point and the X point of the first Brillouin zone. (b) Numerical vertical displacement map at 2.9947 MHz for the chain of resonators. (c) Band structure of the equivalent coupled-resonator elastic waveguide.

are identical with the defect mode of the isolated resonator. More significantly, the modal shapes are clearly identical with those of figure 4.5, supporting the conclusion that the collective vibrations of the chain result from evanescent coupling of the individual resonators. It can be seen that the eigenmodes in spectral range B are identical for all high symmetry points. In spectral range A, the situation is a bit more intricate, as two degenerate isolated defect modes co-exist. They form two separate bands when unfolded, with a dispersion involving more than one Fourier harmonic, i.e. corresponding to the general form Eq. (4.3) rather to the simpler Eq. (4.9). In spectral range C, the bands do not have a pure out-of-plane vibration character, and the discrete model of the phononic polymer should be enriched with up to three degrees of freedom per resonator, which we leave as a perspective.

Finally, based on the approximate periodic model of the phononic polymer, the special case of aperiodic coupled resonant waveguide near 3MHz is discussed. As remarked, the band appearing around 3 MHz in the numerical simulation is not observed in the experiment. For completeness, however, we discuss briefly its characteristics. The eigenmodes at the M point, the Γ point and the X point of the first Brillouin zone are shown

in figure 4.9(a). These eigenmodes are identical for all three high symmetry points. Figure 4.9(b) further displays the numerical displacement distribution in the chain of resonators at 3 MHz. It can be seen that each resonators in the chain undergoes collective resonance with the eigenmode at this frequency. The band in figure 4.9(c) has a cosine shape similar to the out-of-plane band in range B, indicating the dominance of nearest-neighbor coupling. Overall, the vibration characteristics at 3 MHz should be mostly similar to those at 2.5 MHz.

4.6/ CONCLUSIONS

In this chapter, coupled elastic vibrations of a chain of coupled-resonators in a square lattice phononic crystal slab have been studied. We get some conclusions as follows:

(1) The aperiodic coupled-resonator waveguide on a fused silica plate with periodic cross holes is designed and fabricated. The corresponding frequency response functions are calculated by picking up the vibrations on the different resonators. Finally, the comparison between the periodic and the aperiodic CREWs are discussed. The results show that the coupling of resonators is evanescent within the wide complete band gap obtained with cross holes, resulting in nearest-neighbor coupling. The resonators oscillate collectively at the same frequency. The numerical simulation and experimental measurement results are in good agreement. Compared with the periodic coupled-resonator waveguides, the aperiodic one breaks the limitation of the period and can realize the transmission of elastic waves in arbitrary direction.

(2) An approximate theoretical model of phononic polymer is proposed. The vibration characteristics of aperiodic coupled-resonator waveguide is studied. The results show that the number of resonances is as a rule equal to the number of resonators in the chain, in the first approximation. The approximate model of phononic polymer provides a theoretical foundation for the design of rather arbitrary acoustic circuit.

This work provides a foreground for the consideration of phononic polymers, where resonators with equal free resonance frequency are arranged in an arbitrary chain and coupled evanescently. Active or even smart manipulation of localized resonators is thus expected. Such phononic polymers could be used for fusion sensing purposes, with each resonator functionalized to the same or different analytes. It is expected that the collective vibrations should be highly sensitive to a local change in one of the resonators. Phononic

polymers could also be employed in optomechanics, using light forces such as radiation pressure to excite and detect collective resonances without any mechanical contact. Furthermore, by tuning the coupling coefficients between resonators, it should be possible to implement topological phononic models inspired for instance by the Su-Schrieffer–Heeger (SSH) model of the molecule of polyacetylene. The fabrication process we employed relies on the locally-selective etching of fused silica. Other microfabrication techniques could obviously be alternatively selected, in view of different material platforms or to adjust the frequency range of the ultrasonic resonances.

5

WAVE PROPAGATION IN 1D TUNABLE RESONANT ACOUSTIC WAVEGUIDE

5.1/ INTRODUCTION

As is well known, band gaps can be produced because of two different mechanisms, Bragg interference and local resonances of substructures in the unit cell. Based on the advantage that the local resonance band gaps appear lower than the Bragg band gaps, researchers have designed, processed and studied many local resonant structures with rich characteristics in recent years. However, the topology and material parameters of these structures were difficult to tune. In comparison, reconfigurability is easier to achieve in two-phase phononic crystals composed of solid and fluid materials. Elford et al. [108] designed novel noise barriers by using Matryoshka sonic crystals with different number of C-shaped shells. Wang et al. [197] investigated longitudinal near-field coupling between acoustic resonators grafted along a waveguide through altering the length of resonators. Arguably, the structures proposed in the above studies are hardly continuously tunable.

In this chapter, we will take the tunable resonant acoustic waveguide formed by the periodically arranged acoustic resonators grafted on a tubular waveguide as an example. Then we explore the dependence of the locally resonant band gap on the lattice constant and the influence of the viscosity of the material on the local resonance band gap. Without changing the characteristics of the resonators, the locally resonant band gaps are manipulated by tuning the dispersion of the evanescent wave in the transmission medium at the resonators by filling the waveguide with a fluid and changing the amount of the filled fluid. This method can easily achieve reconfigurability.

5.2/ CALCULATIONS AND ANALYSIS OF BAND STRUCTURES

Figure 5.1 shows a schematic diagram of a one-dimensional tunable resonant acoustic waveguide, which is composed of a tubular waveguide and grafted resonators in a periodical arrangement. In this section, the influence of the viscosity of air and the lattice constant of the unit cell on different band structures is discussed by calculating the real band structure, complex-wavevector band structure, complex-eigenfrequency band structure and resolvent band structure.

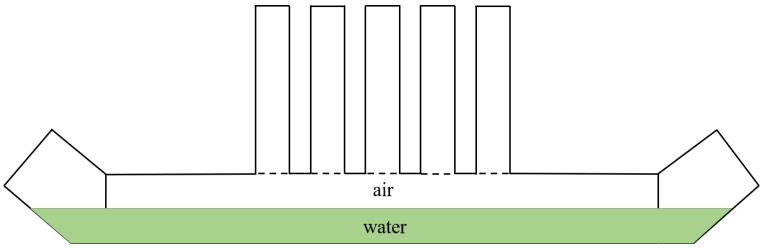

Figure 5.1: Schematic diagram of the 1D tunable resonant waveguide.

5.2.1/ INFLUENCE OF VISCOSITY

The meshing elements in the finite element model (a) and the field distribution of the random excitation signal (b) are shown in figure 5.2. The lattice constant is a=25cm. The diameters of the tubular waveguide and of the grafted resonators are d_1=10cm and d_2=5cm, respectively. The real band structure of the resonant acoustic waveguide without viscosity is first calculated, as illustrated in figure 5.3. It can be observed that several locally resonant band gaps appear in the frequency range below 2500 Hz.

Since the locally resonant sonic crystal is made of air, in practical applications, the viscosity of the material will affect the acoustic properties of the sonic crystal. Viscosity is usually frequency-dependent. Here we introduce viscosity through complex elastic modulus $B' = B + \mathrm{i}\omega\eta$, where η represents the viscosity of air and B is the bulk modulus of air. To investigate the effect of material viscosity on the acoustic properties of the structure, we consider two arbitrary values of viscous damping, either $\mu/Ba = 10^{-9}$m/s or $\mu/Ba = 10^{-6}$m/s, and we calculate the different kinds of band structures in the following.

Figures 5.4 and 5.5 show the real part and imaginary part for small loss $\mu/Ba = 10^{-9}$m/s and larger loss $\mu/Ba = 10^{-6}$m/s in the complex-wavevector band structures. It can be deduced from the figure that the introduction of material loss makes all bands in the complex-wavevector band structures contain nonzero imaginary part values. That is to

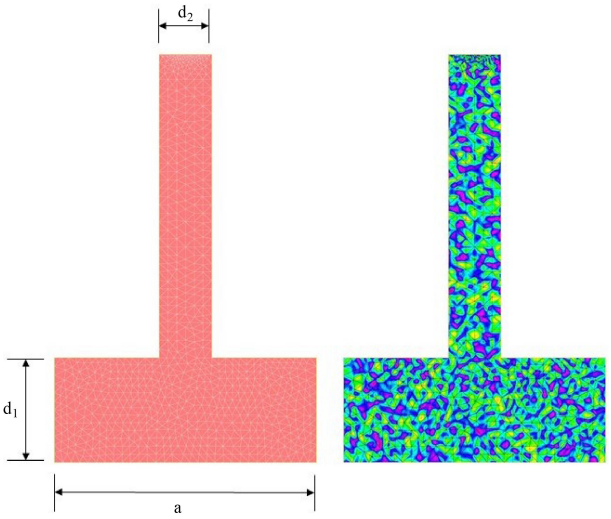

Figure 5.2: The finite element mesh applied in the unit cell and the stochastic excitation applied as a random periodic field when the lattice constant is a=25cm.

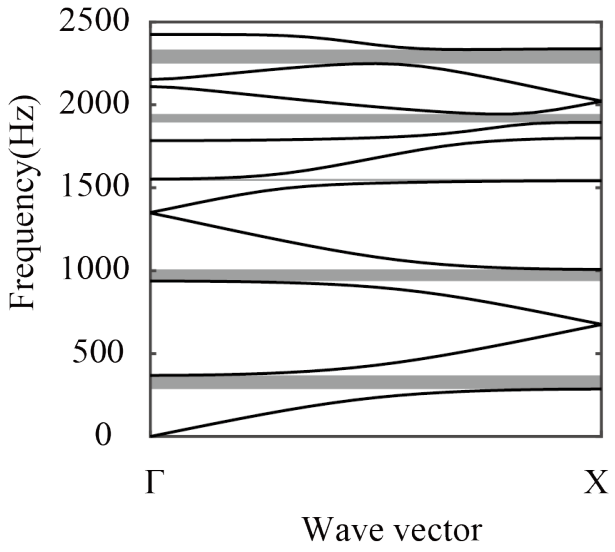

Figure 5.3: Band structure of the 1D resonant waveguide with the lattice constant a=25cm.

say, there are only evanescent waves in viscous sonic crystals. Different from the Bragg band gap in figure 2.8, the upper and lower boundaries of the locally resonant band gap appear at different high symmetry points of the irreducible Brillouin zone. The imaginary parts of the bands connecting them are composed of two intersecting bands, which lead to the sharp angles in the imaginary part of the wavevector corresponding to the locally resonant band gaps. That means the corresponding imaginary part values are large, indicating the large wave attenuation in the locally resonant band gaps.

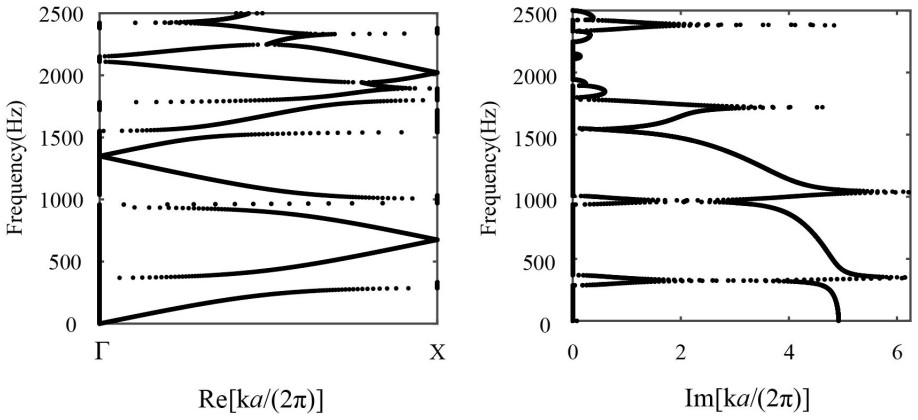

Figure 5.4: Complex-wavevector band structures of the 1D resonant waveguide for lattice constant $a = 25$ cm and loss $\mu/Ba = 10^{-9}$m/s.

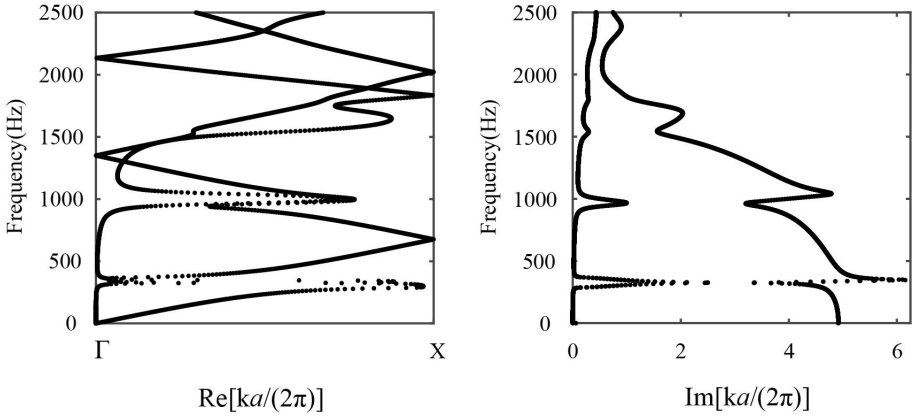

Figure 5.5: Complex-wavevector band structures of the 1D resonant waveguide for lattice constant $a = 25$ cm and loss $\mu/Ba = 10^{-6}$m/s.

Comparing figures 5.4 and 5.5, it is observed that the complex-wavevector band structures, especially the real part values of the wavevector, are significantly affected when material loss is added. The influence is mainly focused on the sharp corners at high symmetry points Γ and X in Brillouin zone where the real bands become smooth. With an increase of the material loss, the above effections are further strengthened, and the imaginary part values of the wavevector are also remarkably affected. Furthermore, we find that the real part values of the complex band structure do not occupy all the first Brillouin zone. According to that observation, the conception "wavevector bandgap [178]" within a certain wavevector range is introduced, namely, the propagation of waves is forbidden in the particular wavevector range. Moreover, the range of the wavevector in the wavevector bandgap gradually increases with the increasing of the material loss. From figure 5.5, we find that the minimum non-zero imaginary part value increases with frequency as viscos-

ity increases, such that the corresponding evanescent wave attenuation is strengthened. However, it cannot be ignored that the second non-zero imaginary part value decreases as the frequency increases. Especially near the frequency of 1000 Hz, an increase of the viscosity causes the two complex bands to separate at the intersection, forming two new complex bands, which contribute to the weak attenuation. Physically, viscosity damps local resonance.

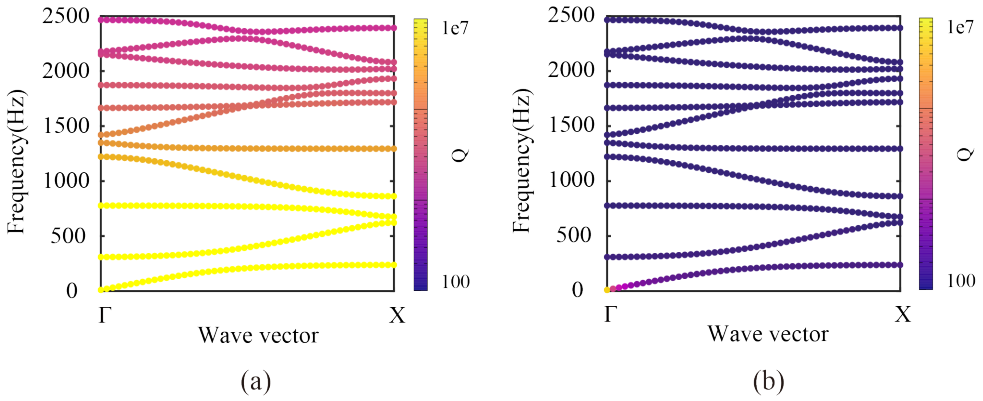

Figure 5.6: Complex-eigenfrequency band structure of the 1D resonant waveguide for lattice constant $a = 25$ cm when the loss of the material $\mu/Ba = 10^{-9}$m/s (a) and $\mu/Ba = 10^{-6}$m/s (b).

Next, the complex-eigenfrequency band structures for small loss $\mu/Ba = 10^{-9}$m/s (a) and larger loss $\mu/Ba = 10^{-6}$m/s (b) are calculated in figure 5.6. The color presents the quality factor describing the attenuation:

$$Q_m(\mathbf{k}) = \frac{\mathrm{Re}[\omega_m(\mathbf{k})]}{2\mathrm{Im}[\omega_m(\mathbf{k})]}. \tag{5.1}$$

It can be inferred from figure 5.6 with the same viscosity that the Q values are very large, that is to say, the real part values of the frequency are much larger than the imaginary part values. As the frequency increases, the Q values gradually decrease, and the differences between the real and imaginary part values gradually become smaller. The higher the frequency is, the more obvious the influence of the imaginary part values is, and finally the greater the attenuation is. Furthermore, we found that the Q value decreases as the viscosity increases at the same frequencies, which means that the imaginary part value is larger. This explains that the attenuation of energy is larger when the wave propagates in the sonic crystal with larger material loss.

Finally, we calculate the resolvent band structures for two viscous damping $\mu/Ba = 10^{-9}$m/s (a) and $\mu/Ba = 10^{-6}$m/s (b) in figure 5.7. For the smaller value of material loss $\mu/Ba = 10^{-9}$m/s, the resolvent band structure is visible with about the same intensity.

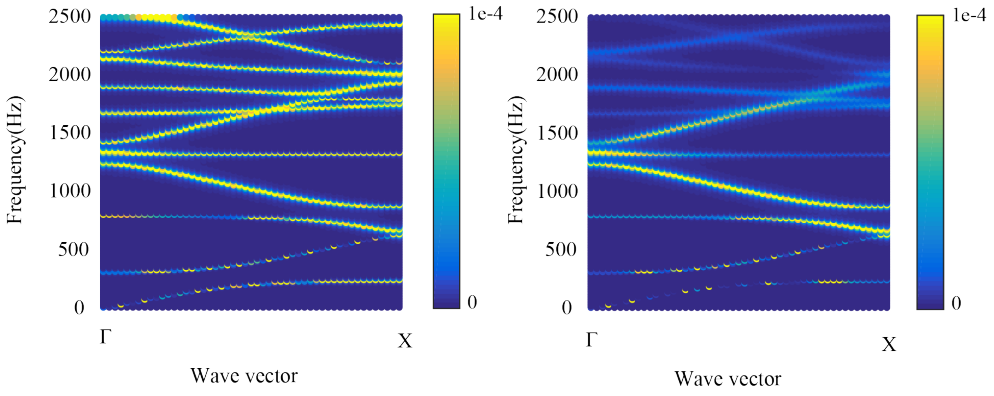

Figure 5.7: Resolvent band structures for response with the stochastic excitation method of the 1D resonant waveguide for lattice constant $a = 25$ cm when the loss of the material $\mu/Ba = 10^{-9}$m/s (a) and $\mu/Ba = 10^{-6}$m/s (b).

For the larger value of viscous damping, the resolvent bands become less visible as the frequency increases. The higher the frequency is, the larger the energy attenuation is. Therefore, for the same frequency, the larger the material viscosity is, the larger the attenuation is. This is consistent with the conclusion of the complex-eigenfrequency band structures.

5.2.2/ INFLUENCE OF LATTICE CONSTANT

Next, we introduce a sub-wavelength structure, a tunable resonant sonic waveguide with a lattice constant of a=8 cm. The influence of different lattice constants on the band structure is discussed. Figure 5.8 shows the element mesh of the unit cell (a) and the stochastic excitation applied as a random periodic field while the lattice constant a=8cm.

Then we calculate the real band structure of the 1D resonant waveguide. It can be inferred that the first locally resonant band gap produces a small frequency offset when the lattice constant a changes from 25 cm to 8 cm. This change is in respect that the lattice constant $a = 8$ cm is more than 3 times smaller than the wavelength, which leads to the interaction between propagating waves reflected at the grafted resonators. For further information, we find that the third locally resonant band gap disappears when a diminishes to 8 cm. Because of the decrease of the lattice constant, the mutual influence between the resonators becomes very significant, even making the local resonance band gap disappear.

In order to further discuss the influence of the lattice constant on other band structures, a small viscosity is introduced into the material $\mu/Ba = 10^{-9}$m/s. The complex-wavevector

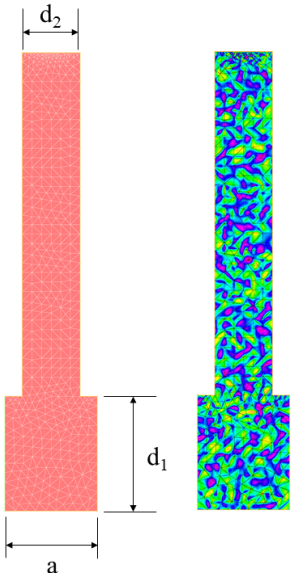

Figure 5.8: The element mesh applied in the unit cell and the stochastic excitation applied as a random periodic field when the lattice constant a=8cm.

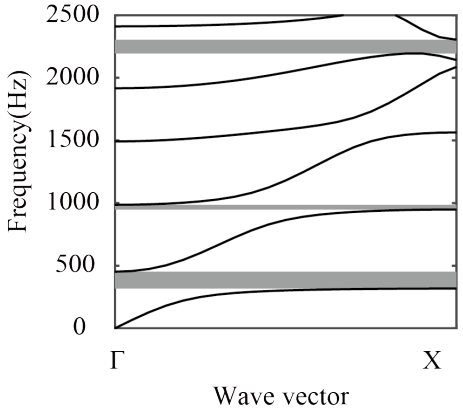

Figure 5.9: Band structure of the 1D resonant waveguide when the lattice constant a=8cm.

band structures are first calculated. Figure 5.10 displays the real part and imaginary part for a=8cm. We observe that the imaginary part value when a=8cm is not zero, and that evanescent waves exsit. Comparing with the results when a=25cm, the same offset of the first locally resonant band gap and the disappearance of the third band gap are observed in the CWBS. This is consistent with the real band structures. It is worth noting that the absolute imaginary part value of the complex-wavevector band structure is smaller when the lattice constant is 8 cm near the third band gap, causing the attenuation in the local resonance band gap to reduce, until the band gap disappears. This is consistent with the conclusion of the real band structure as well.

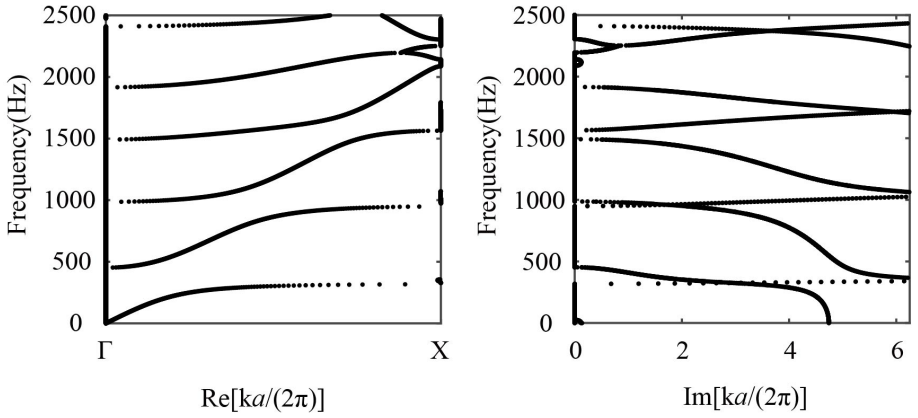

Figure 5.10: Complex-wavevector band structures of the 1D resonant waveguide for a=8cm and loss $\mu/Ba = 10^{-9}$m/s.

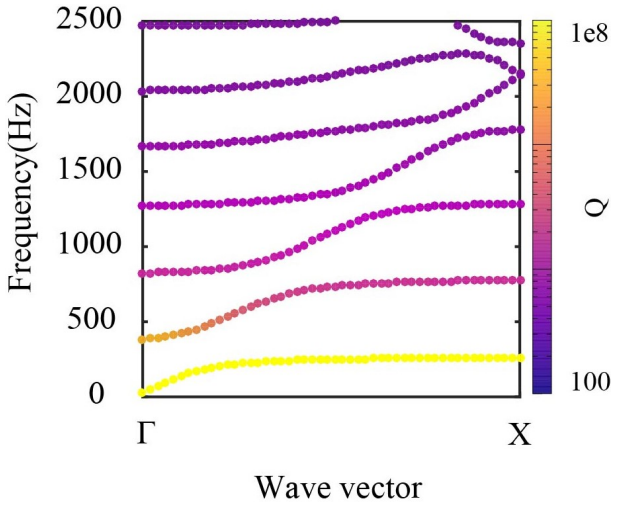

Figure 5.11: Complex-eigenfrequency band structure of the 1D resonant waveguide when the lattice constant a=8cm and loss $\mu/Ba = 10^{-9}$m/s.

Then the complex-eigenfrequency band structure when a=8cm is calculated and shown in figure 5.11. The color represents the quality factor Q which represents the attenuation in time. As the frequency increases, the quality factor Q becomes smaller, leading to a larger attenuation. By comparing the color scales at the same frequencies for the lattice constant a=25cm in figure 5.6(a), the imaginary part values at a=8cm are smaller, resulting in smaller attenuation. This result is consistent with that of real band structures.

Finally, the resolvent band structure for the lattice constant a=8cm is calculated and shown in figure 5.12. Comparing with the result for the lattice constant a=25cm, the resolvent bands are all visible with roughly the same intensity in the frequency range. We find that the change of the lattice constant almost has no influence on the visibility

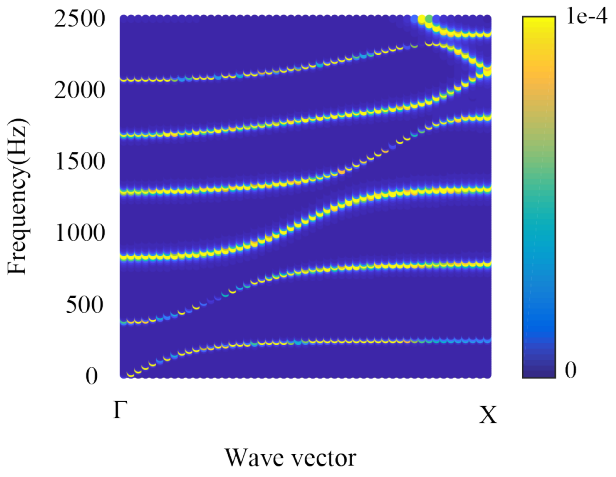

Figure 5.12: Resolvent band structure of the 1D resonant waveguide when the lattice constant a=8cm and loss $\mu/Ba = 10^{-9}$m/s.

of the resolvent band structures, which makes it difficult to intuitively judge the influence of the lattice constant on the wave propagation characteristics from the resolvent band structures.

Based on the above analysis, it can be clarified that the lattice constant and material viscosity both have influence on the wave propagation in one-dimensional tunable resonant waveguides. The small lattice constant, that is, the small distance between the resonators grafted on the waveguide, leads to an enhanced interaction between the reflected guided waves at the resonators. The energy attenuation in the locally resonant band gap at higher frequencies is weakened, even resulting disappearance of the band gap disappearing. The viscosity of the material has a significant effect on the real and imaginary parts of the complex-wavevector band structure. The large viscosity obviously effects the band at high frequencies and strengthens the energy attenuation.

5.3/ NUMERICAL ANALYSIS OF TRANSMISSION

In this section, we consider a locally resonant sonic crystal built by using a tubular waveguide grafted with periodic acoustic resonators. Tunability is realized by filling the waveguide with water up to a controlled level, without acting on the properties of the resonators. We first investigate numerically the local resonance mechanism for a single grafted resonator as a function of water height. Dispersion relations and transmission properties are obtained with a three-dimensional time-harmonic finite element model of wave propagation. The sound velocity inside the tube, $c = 333$ m/s, is determined experimentally and

is used without any adjustment in numerical simulations. The surface separating water and air is considered as imposing a perfectly rigid boundary condition, i.e. acoustic wave propagation in water is neglected.

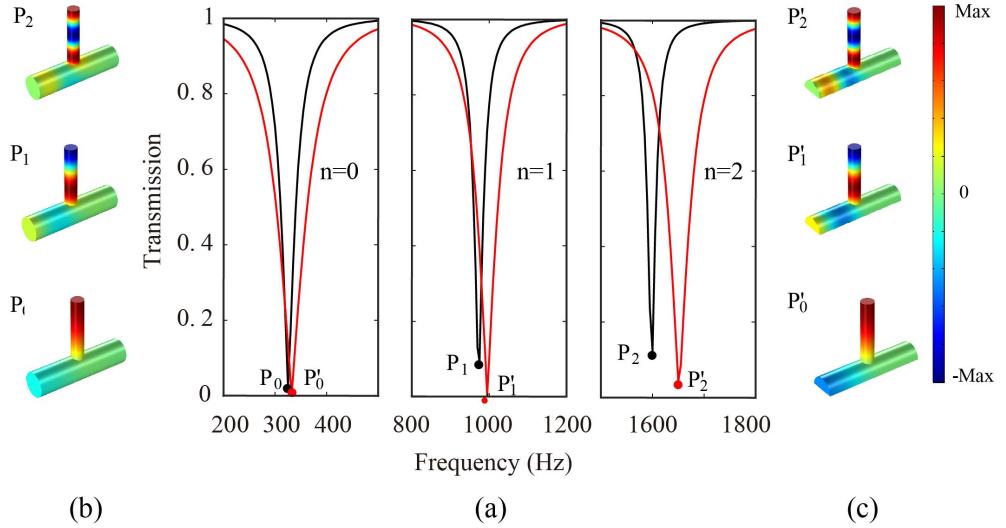

Figure 5.13: Case of a single resonator. (a) Numerical transmission is plotted around the 0th, 1st, and 2nd acoustic resonances of a single resonator grafted onto the waveguide. The black and red lines are for no water ($h_w = 0$) and half-water ($h_w = d/2$), respectively. (b-c) Vibration modes at resonant frequencies are shown. The color scale represents the amplitude of the pressure normalized to the maximum (Max).

Figure 5.13 shows the transmission around the three resonances that appear below 1800 Hz. When the waveguide is empty ($h_w = 0$), the transmission dips appear around 327.3, 975.4 and 1601.3 Hz. When the waveguide is half filled ($h_w = d/2$), the dips are moved upward to 332.4, 995.2, and 1651.7 Hz. Figure. 5.13(b) and (c) show that the pressure distributions inside the resonator at the frequencies of the dips are unaffected by the water level and correspond to the first three natural vibration modes of the resonator. The main change for the pressure distribution occurs inside the waveguide as the water level is changed.

The transmission dips appear near a resonance frequency by the coupling between evanescent guided waves originating from the grafting point and propagating guided waves. In particular, in case frequencies remain below the cutoff of the second guided mode, the center frequency of the dip is approximated by

$$\omega_0^2 = \Omega^2 + \frac{\kappa_{22}}{2\alpha}, \tag{5.2}$$

where Ω is the natural frequency of the resonator; α is the imaginary part value of the wavenumber for the least evanescent guided mode (the wave with the smallest imaginary

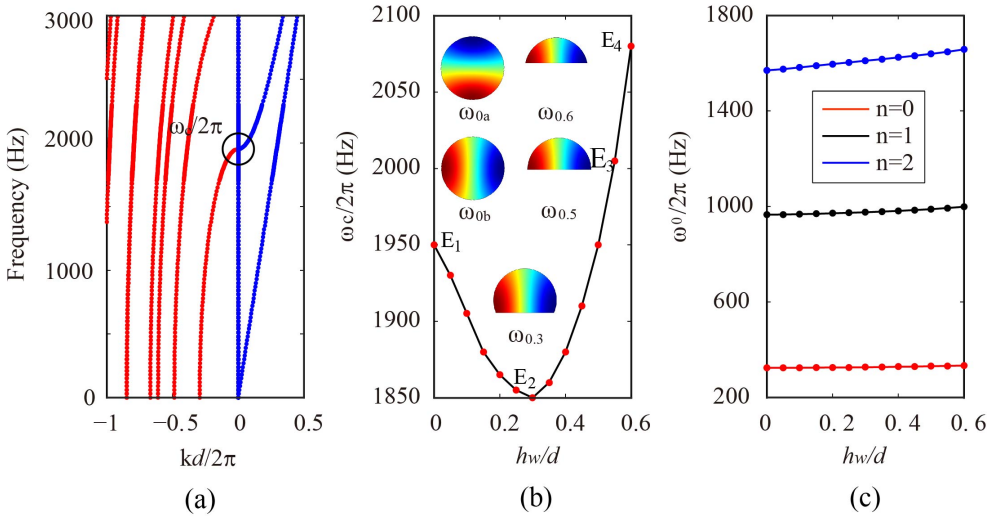

Figure 5.14: Band structure of the 1D resonant waveguide: (a) The complex band structure for guided modes is shown for half-water ($h_w = d/2$). Both the real (blue) and imaginary (red) parts of the complex dispersion relation are presented. The cutoff frequency $\omega_c/(2\pi)$ of the least evanescent wave is marked by the black circle. (b) $\omega_c/(2\pi)$ is depicted as a function of the normalized height of water h_w/d. The insets show the pressure distribution of the least evanescent wave at cutoff for $h_w = 0$ (E$_1$), $0.3d$ (E$_2$), $0.5d$ (E$_3$) and $0.6d$ (E$_4$). (c) The first three locally resonant frequencies for a single resonator are presented as a function of the normalized height of water.

part value of the propagation constant); and κ_{22} is a coupling coefficient proportional to the overlap integral of the modal distributions of the least evanescent guided wave and the fundamental propagating guided wave. Loosely speaking, Eq. (5.2) implies that energy at resonance is the sum of the energy in the resonator plus the energy of the evanescent wave. As the local resonance frequency increases, the energy in the evanescent wave must increase, since Ω remains fixed.

These observations point at the change of the dispersion relation for guided waves as the water level changes. Figure 5.14 (a) shows the complex dispersion relation in the case of $h_w = d/2$. At low frequencies, there is a single propagating guided wave with linear dispersion and speed of sound c. All other guided waves are evanescent, as indicated by their pure imaginary wavenumbers. The least evanescent of these waves reaches a cutoff at $\omega_c/(2\pi)$, above which the waves become propagating and thus propagation is not monomodal anymore. As a note, the dispersion relation is

$$\omega^2 = c^2k^2 + \omega_c^2, \tag{5.3}$$

for all waves, where k is the complex wavenumber; and only the value of ω_c is different between different waves. Figure 5.14 (b) shows the variation of the cutoff frequency of

the least evanescent guided wave as a function of the height of water. As the height of water increases, ω_c first decreases until $h_w = 0.3d$ and then increases again. Given that $\alpha = \sqrt{|\omega^2 - \omega_c^2|}/c$, this number at a fixed frequency first decreases then increases following ω_c. The value of the coupling coefficient κ_{22} also changes with the water height. Indeed, the pressure distributions shown as insets of figure 5.14 (b) indicate that the modal shape remains relatively stable though the cross-section of the waveguide changes significantly. Owing to the circular symmetry of the waveguide for $h_w = 0$, the two independent modes ω_{0a} and ω_{0b} are degenerate. In contrast, the symmetry of the waveguide is broken as soon as $h_w \neq 0$, leaving a single mode defining the least evanescent guided wave. Overall, it is obtained numerically that both changes in α and κ_{22} combine to lead to a steady increase in the first three locally resonant frequencies $\omega_0/(2\pi)$ as a function of water level, as shown by figure 5.14 (c). The locally resonant frequencies can thus be tuned continuously by adjusting the water level in the waveguide.

Next, we consider a sonic crystal composed of a periodic sequence of five grafted tubes, and observe the changes in locally resonant band gaps as the water level is increased. The lattice constant is a=8cm.

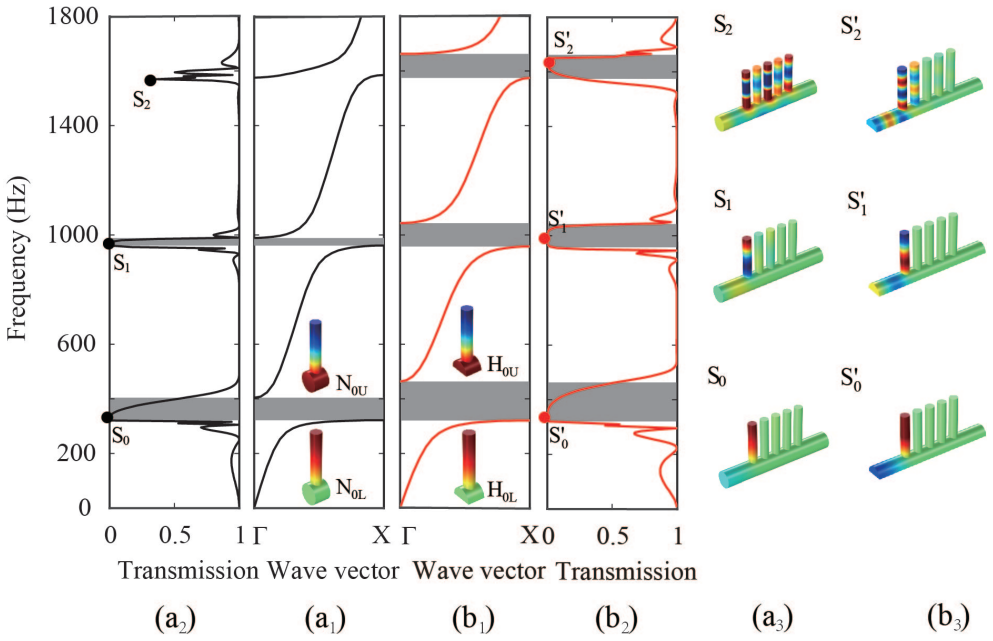

Figure 5.15: Band structure and transmission through the sonic crystal. Band structures are shown (a_1) without ($h_w = 0$) and (b_1) with half-water ($h_w = d/2$). The insets show the pressure distributions of the eigenmodes at the edges of the lowest bandgap. Numerical transmission spectra are shown in (a_2) and (b_2), respectively. (a_3 - b_3) Pressure distributions at the 0th, 1st, and 2nd local resonance frequencies are depicted. The color scale represents the amplitude of the pressure.

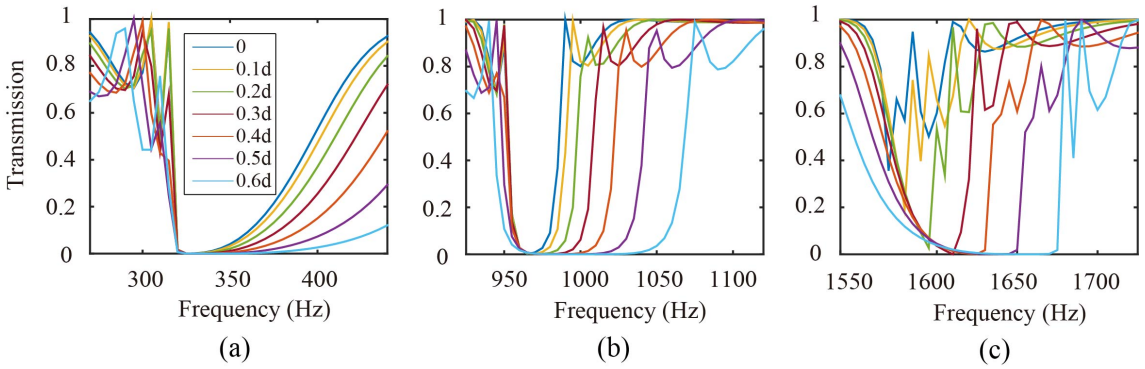

Figure 5.16: Numerical transmission as a function of water level. (a-c) Numerical transmission spectra around the 0th, 1st and 2nd locally resonant band gaps are shown as a function of the height of water.

We first compare the band structures and transmission spectra for $h_w = 0$ and $h_w = d/2$ obtained numerically as shown in figure 5.15. Normalized pressure distribution at labeled points taken at the 0th, 1st, and 2nd locally resonant frequencies respectively are shown in figure 5.15 (a_3 - b_3). Locally resonant band gaps are expected to appear around the resonant frequencies for the single resonator, and their width is known to depend on the reflection coefficient on a single resonator. The insets in figures 5.15 (a_1) and (b_1) show the eigenmodes at the frequencies of the lower edge (L) and the upper edge (U) of the 0-th locally resonant band gap. It is seen that the pressure distributions at the upper edge extend both in the resonator and in the waveguide. In contrast, the pressure distributions at the lower edge only concentrate inside the resonator. It was checked that the situation is similar for the other two band gaps. As a result, the lower edges of the band gaps remain almost unchanged, since they are not affected by the waveguide characteristics, while the upper edges shift to higher frequencies as water is filled into the waveguide. Overall, band gaps become wider. The corresponding transmission spectra shown in figures 5.15 (a_2) and (b_2) are consistent with the band structures. In general, the water level changes the waveguide cross-section and as a result tunes the dispersion of evanescent guided waves, which contribute to the continuous manipulation of band gaps.

Then we changed the heights of water continuously and explore the transmission spectra. Numerical transmissions obtained as a function of water level are reported in figure 5.16. For all 3 band gaps, the lower frequency edge remains almost constant while the upper edge increases continuously which is presented intuitively in figure 5.17 by computing the different band structures. As a result, band gaps become gradually wider as the cross-section of the waveguide decreases with increasing water level. Moreover, the transmission generally gets smaller.

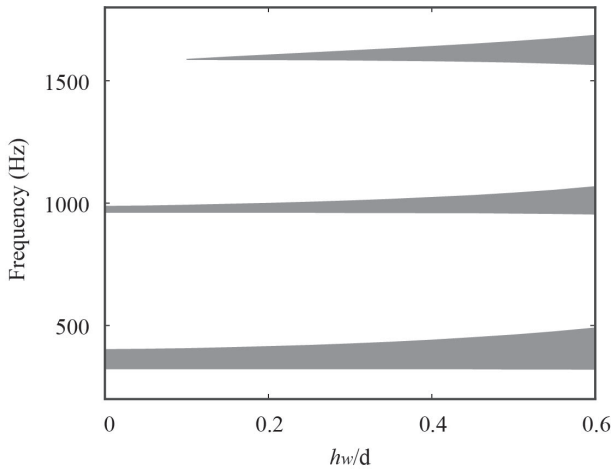

Figure 5.17: The variation of the 0th, 1st and 2nd band gap edges is plotted as a function of the normalized height of water numerically.

5.4/ EXPERIMENTAL MEASUREMENTS OF TRANSMISSION

In this section, the experimental measurements of wave propagation in a tunable sonic waveguide are presented. Figure 5.18 shows a sketch of the experiment. The sonic crystal sample is constructed on a cylindrical polyvinyl chloride (PVC) tube used as a waveguide for acoustic waves in air with a sequence of five tubes grafted on it. The white and green parts in the system represent air and water, respectively. The lattice constant is a. Dimensions in the experiment are L=2m, a=8cm, d_1=10cm, d_2=2.5cm, and h= 24cm. Two bent tubes are glued at the ends of the waveguide in order to hold water inside. The height of water, h_w, can be continuously adjusted by filling or removing water. A periodic array of resonators is introduced in the form of PVC tubes closed at one extremity and grafted onto the waveguide with a period a=8cm. A source and a receiver for sound in the audible range are used to measure acoustic transmission through the locally resonant sonic crystal.

Figure 5.19 presents the zoomed transmissions around the locally resonant frequencies in figure 5.15 (a_2) and (b_2). Experimental transmission curves (dashed lines) appear more rounded than those obtained from numerical simulations (solid lines), which we attribute to losses that are present in the experiment but are not taken into account numerically. Overall, both numerical and experimental transmissions are consistent and indicate that locally resonant band gaps enlarge when h_w is changed from 0 to $d/2$. The third band gap that was hardly opened for $h_w = 0$ especially deepens for $h_w = d/2$. This could be attributed to the dispersion shift of certain evanescent bands with changing water level, which were initially closing the third band gap. The experimental and numerical results

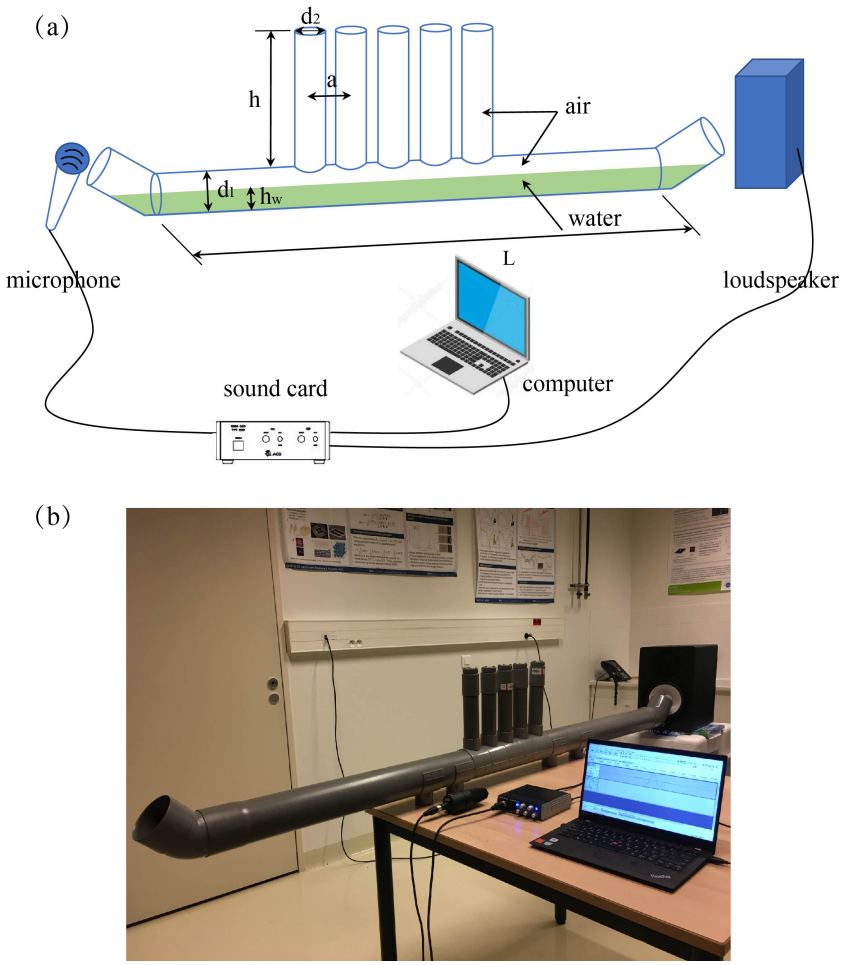

Figure 5.18: (a)Schematic drawing of the experimental setup. Transmission of sound through the sonic crystal sample is obtained using a microphone on the one side and a loudspeaker on the other side. (b) Photography of the experimental setup.

are well consistent .

Experimental transmissions obtained as a function of water level are reported in figure 5.20. It is inferred that the three band gaps become gradually wider with increasing water level which is well consistent with numerical results. Since the level of water in the waveguide can be changed continuously, the continuous tunability of the locally resonant band gaps is realized.

5.5/ CONCLUSION

The main work of this chapter is summarized as follows:

(1) The real band structure, complex-wavevector band structure, complex-

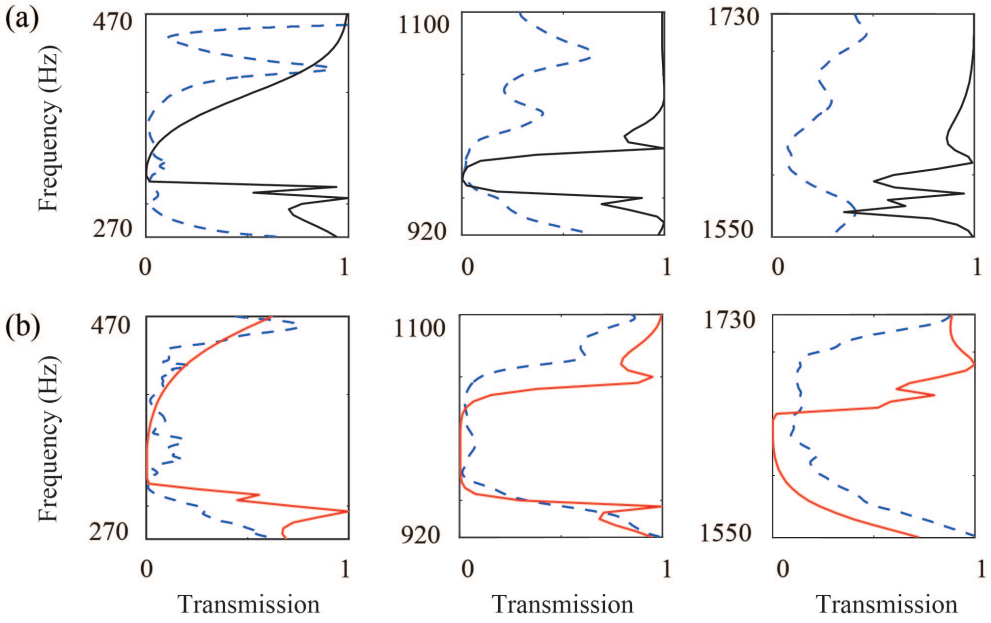

Figure 5.19: Close-up views of the numerical (solid line) and of the experimental transmission (blue dash line) around the locally resonant frequencies filling without water (a) and with half water (b), respectively.

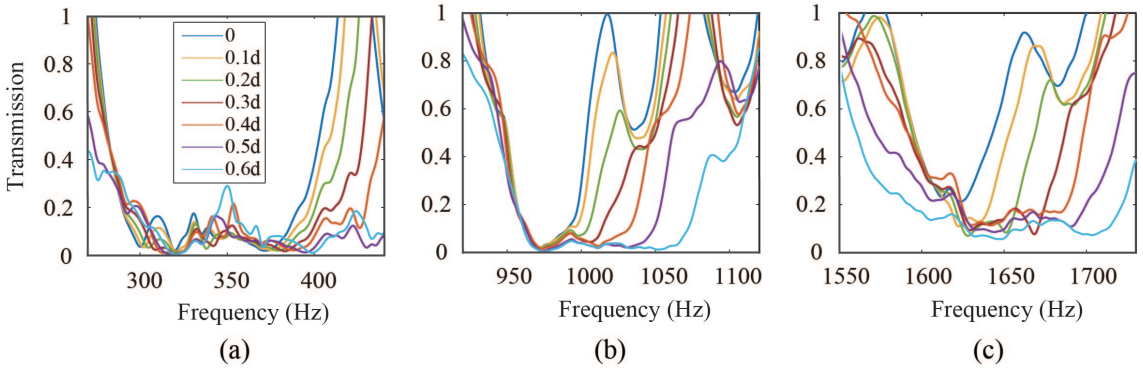

Figure 5.20: Experimental transmission spectra as a function of water level. (a-c) Experimental transmission spectra around the 0th, 1st and 2nd locally resonant band gaps are shown as a function of the height of water.

eigenfrequency band structure and resolvent band structure of the one-dimensional tunable resonant waveguide are calculated using the finite element method. The influence of material viscosity and lattice constant on the band structures is discussed. The results show that the lattice constant and material viscosity of the two-dimensional sonic crystal both have an influence on the wave propagation characteristics. The introduction of material viscosity significantly affects the real and imaginary parts of the complex-wavevector band structure, the complex-eigenfrequency band structure and the resolvent band structure, resulting in

changes of the energy attenuation. The change in the lattice constant causes the interaction between the guided waves reflected at the grafting point to change, which has a great influence on the attenuation of energy and on the position of the locally resonant band gaps.

(2) A locally resonant sonic crystal composed of a waveguide and grafted periodically arranged resonators is designed. The band structure and transmission spectrum of the structure when different levels of water are filled into the waveguide are discussed. The processed samples are experimentally measured. The results show that band gaps can be tuned continuously by changing the level of water inside the waveguide, effectively changing the cross-section and thereby the dispersion of evanescent guided waves. Tunability thus does not rely on changing any parameter of the resonators, and neither on changing the propagation velocity of the supporting medium, but instead works by playing with the grafting conditions of the resonators to the propagation matrix. Both the central resonant frequency and the width of the band gaps are shown to depend on the water level. The experimental and numerical results are in good agreement.

The present work gives insights for the practical design of tunable acoustic devices. The ideas in this chapter can be directly extended to 2D acoustic systems, as well as to the tuning of acoustic metamaterials. An application could be the acoustic monitoring of fluid level inside tubes and pipes.

6

WAVE PROPAGATION IN COUPLED-RESONATOR ACOUSTOELASTIC WAVEGUIDES

6.1/ INTRODUCTION

Recently, the tunable manipulation of acoustic or elastic waves has become a fast-developing topic. Many works have realized acoustic/elastic waves propagation along different acoustic circuits in a single-phase phononic crystal. However, topology or material parameters of the fabricated structures can hardly be changed [95], or made tunable or reconfigurable [141], largely restricting their applications. It is thus highly expected to manipulate waves in real-time flexibly and actively. Therefore, many researchers have focused on tunable phononic crystals. For instance, changing the geometry of the phononic crystals and adjusting the properties of the component materials by applying a biasing field [114] is a way to tune wave propagation. However, this measure usually requires multifield coupling media as the components of PCs. Reconfigurability can, in principle, be achieved rather easily by using solid-fluid phononic crystals [153]. A basic feature of a fluid is that it is shapeless though flowing. This feature makes fluid-solid systems potentially reconfigurable. In other words, acoustic waves in a fluid medium can be manipulated by changing the properties of elastic waves in solid inclusions. Conversely, the propagation of elastic waves in a solid matrix can be controlled through changing the properties of fluid fillings. Compared with solid inclusions, the tuning of geometric parameters and material properties of fluid inclusions is more flexible, providing more possibilities for the realization of reconfigurability. However, researches on adjusting fluid properties to manipulate the elastic waves are limited, and often without corresponding experimental verification.

This chapter focuses on wave propagation in tunable coupled-resonator acoustoelastic waveguides. Based on a two-dimensional phononic crystal with periodically arranged holes, different coupled-resonator acoustoelastic waveguides are designed by selectively filling fluid in a solid matrix. The transmission properties along different circuits are discussed. Then we extend the consideration to phononic crystal plates including the 1D phononic metastrip and 2D phononic metaplates with periodically arranged hollow pillars. The influence of fluid-solid interaction on transmission properties is investigated as well as the influence of fluid filling on band gaps. Furthermore, different reconfigurable waveguides are designed and fabricated to realize the flexible control of elastic waves.

6.2/ WAVE PROPAGATION IN TUNABLE FLUID-FILLED PHONONIC CRYSTAL

In this section, wave propagation in a 2D phononic crystal with periodic fluid-filled holes is investigated. Reconfigurable phononic circuits can be created by selectively filling fluid in the holes of a solid phononic crystal. The dispersion relation and the transmission properties of coupled-resonator acoustoelastic waveguides are investigated. Furthermore, the effects of the polarization of the wave source on transmission are also discussed. As a whole, rather arbitrary phononic circuits can be created, such as multiply-bent waveguides or wave splitters.

6.2.1/ COUPLED-RESONATOR ACOUSTOELASTIC WAVEGUIDE

In this section, the coupled-resonator acoustoelastic waveguide is designed by selectively filling fluid into a solid matrix. The solid matrix and fluid filling are isotropic aluminum and water, respectively. Periodic holes are arranged in an infinite aluminum plate with lattice constant a. A series of defect cavities are formed by selectively filling water in the circular holes, thus forming the coupled-resonator acoustoelastic waveguide as shown in figure 6.1. The distance between neighboring defect cavities, Λ, is an integer multiple of the lattice constant, which is $\Lambda = 2a$ here.

6.2.2/ BAND STRUCTURES OF CRAEWS

In this section, we discuss the dispersion relation of the coupled-resonator acoustoelastic waveguides (CRAEWs). The derivation follows the equivalent purely elastic structures

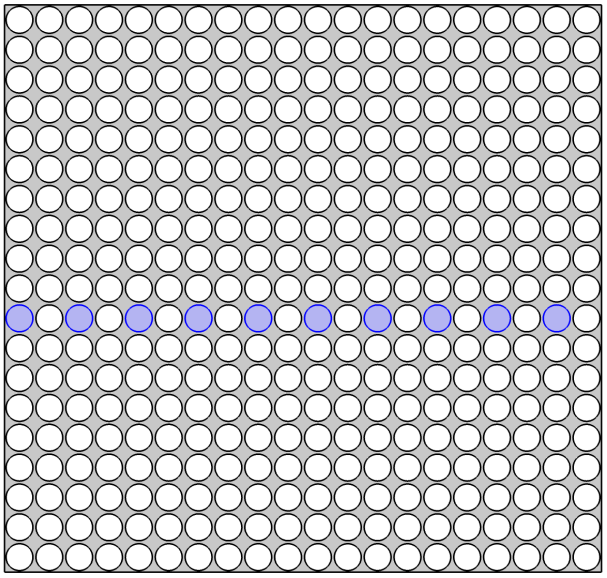

Figure 6.1: Schematic representation of coupled-resonator acoustoelastic waveguide.

but extends to coupled acoustoelastic wave propagation. Numerical simulations are performed with the finite-element method, taking explicitly into account fluid-solid interaction. The supercells used in the case of an isolated cavity and in the case of a CRAEW are depicted in figure 6.2. Periodic boundary conditions are applied on pairs of opposite boundaries of the supercell. Phononic band structures are shown in figure 6.3, and some remarkable Bloch waves are displayed in figure 6.4.

For concreteness, we consider isotropic aluminum as the solid matrix (mass density $\rho_s = 2700$ kg/m^3, Poisson's ratio $\nu = 0.33$, and Young's modulus $E = 68.9$ GPa) and water as the fluid that can fill certain holes (mass density $\rho_f = 1000$ kg/m^3 and sound velocity $c = 1490$ m/s). A two-dimensional square lattice phononic crystal is chosen for the following examples. The radius r of the hole is set by $r/a = 0.45$, with a being the lattice constant.

The defect modes created by locally filling one hole with water are the basic building blocks of a CRAEW. They can be analyzed with the supercell consisting of 7×7 circular holes depicted in figure 6.2(a). The size of the supercell is large enough to guarantee that coupling between adjacent defects can be neglected. The resonant frequencies of the six defect modes are listed in Tab. 6.1. Figure 6.4 shows the acoustic and elastic polarization of those six defect modes, noted as S_n, with $n = 1, 2, \cdots, 6$. It can be infered that each defect mode has a unique pattern for the distribution of the displacement fields in the solid matrix and of the pressure in the fluid. The displacement fields are such that the amplitude of the vibration decays exponentially away from the defect, thanks to the presence of the complete bandgap. Deformations mainly locate at the lumps for modes S_1 and S_2, and at the thin connectors for modes S_3 to S_6. Modes S_4 and S_5 are actually

frequency degenerate. The different symmetries of the defect modes with respect to the vertical and horizontal axes are listed in Tab. 6.1. These symmetries are important for understanding the coupling of defect modes with waves incident from the solid matrix.

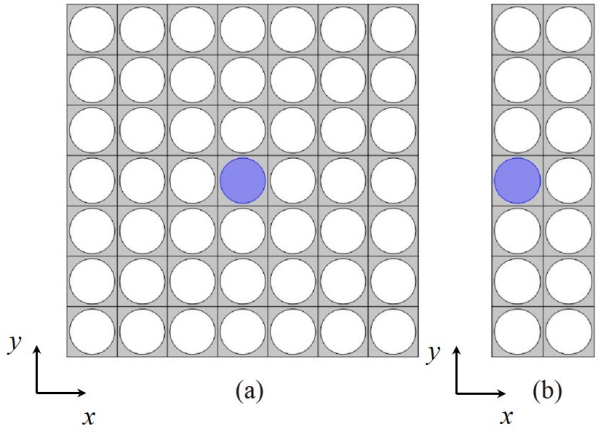

Figure 6.2: Supercells used for the calculation of the band structures for (a) a cavity formed by a single point defect and (b) a coupled-resonator acoustoelastic waveguide (CRAEW) created in the same PC. The blue, gray and white parts represent water, aluminum and vacuum, respectively.

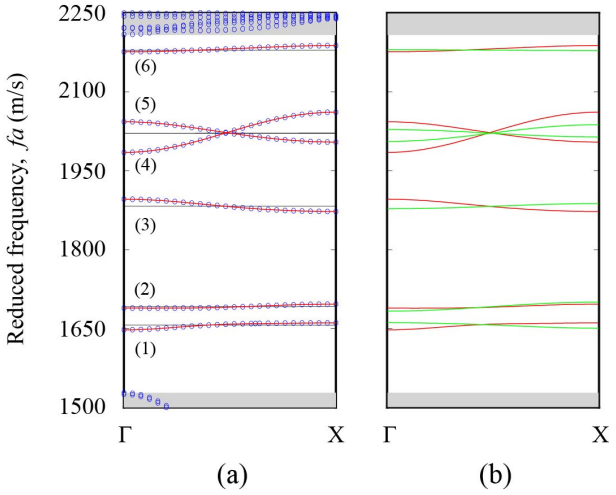

Figure 6.3: Band structures of the 2D phononic crystal with CRAEW: (a) Dispersion for cavity separation $\Lambda = 2a$. The result of finite element computation with the supercell of figure 6.2(b) is shown with blue circles. Horizontal black lines mark the resonant frequencies for the isolated cavity. Red lines show the CRAEW dispersion relation as obtained with the model of Eq. (6.1). The gray areas indicates the passing bands for the perfect phononic crystal. Dispersion curves are numbered with respect to each defect mode. (b) Comparison of the CRAEW dispersion relation for cavity separation Λ=2a (red lines) and Λ=3a (green lines).

A CRAEW is formed by a sequence of defect cavities separated by a distance Λ that is an integral number of lattice constants. When Λ is not too large, as shown in figure 6.2(b) in

the case of $\Lambda = 2a$, the defect modes can couple with each other though the evanescent fields emanating from them. A channel for guided waves can thus be created for frequencies within the complete bandgap. The phononic band structure of the CRAEW along the $\Gamma - X$ direction of the first Brillouin zone is shown in figure 6.3 for the cases $\Lambda = 2a$ and $\Lambda = 3a$. Guided modes are formed around the resonances of the isolated defect with smooth dispersions, labeled as 1,2,3,4,5 and 6, respectively. The polarizations of those guided Bloch waves at the Γ point in the case of the isolated cavity (S_n) and $\Lambda = 2a$ (C_n, $n = 1, 2, \cdots, 6$) are shown in figure 6.4. When the distance between the cavities is $\Lambda = 2a$, the modes are in good correspondence with the corresponding modes of the isolated defect. In other words, wave guidance in CRAEW is owing to the excitation and coupling of isolated defect modes.

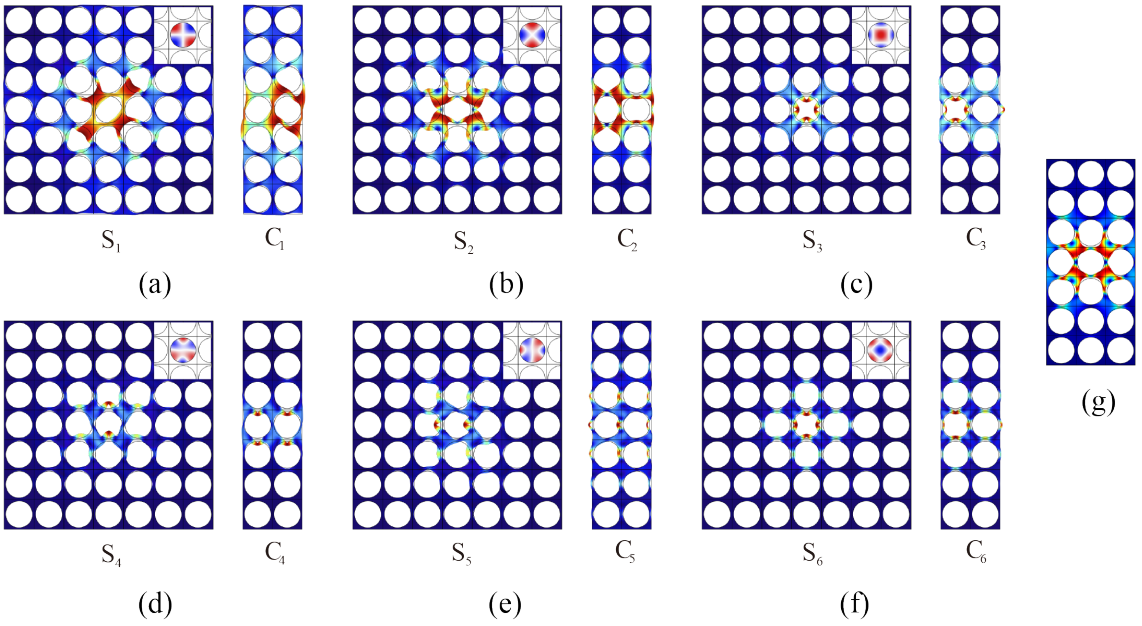

Figure 6.4: Displacement and pressure fields of the six defect modes of the supercells, shown at the Γ point of the first Brillouin zone. (a-f) Letters S_n and C_n are for the n-th defect mode for the isolated cavity and coupled-resonator waveguides with cavity separation $\Lambda = 2a$, respectively. The pressure distribution in water is shown as a inset in the isolated cavity case. (g) Displacement field of mode C_2 for cavity separation $\Lambda = 3a$.

The dispersion relation of CRAEW modes is very smooth. This property can actually be associated with the rapid decrease with distance of the coupling strength between adjacent cavities, as described by the theoretical model of a linear chain of coupled cavities [137]. The Hamiltonian of the CRAW is a sum of the Hamiltonians of isolated cavities plus an interaction Hamiltonian describing the interaction of coupled cavities in a quantum

Table 6.1: Parameters of the dispersion model for linear chains of coupled acoustoelastic cavities. Symmetry (S) or antisymmetry (A) with respect to the vertical and horizontal axes are given in that order for each of the 6 defect modes. The third row shows the resonant frequencies of the isolated cavity. Reduced frequencies, fa, and expansion coefficients, $\Gamma_m a/(2\pi)$, are given in units of m/s. Expansion coefficients were determined for $\Lambda = 2a$ and $\Lambda = 3a$, and are obtained by fitting the computed dispersion with the model in Eq. (6.1).

	Mode Symmetry	$n=1$ AA	$n=2$ SS	$n=3$ SS	$n=4$ SA	$n=5$ AS	$n=6$ SS
Isolated cavity	fa	1656.77	1691.85	1882.55	2021.08	2021.17	2179.24
$\Lambda = 2a$	$\Gamma_0 a/(2\pi)$	1656.27	1691.68	1882.95	2023.70	2022.68	2181.91
	$\Gamma_1 a/(2\pi)$	-2.95	-1.96	5.80	-19.15	9.57	-2.93
	$\Gamma_2 a/(2\pi)$	-1.06	0.49	0.64	-0.29	0.58	0.072
	$\Gamma_3 a/(2\pi)$	-0.34	0.02	0.04	0.01	0.10	-0.05
$\Lambda = 3a$	$\Gamma_0 a/(2\pi)$	1656.31	1691.74	1882.58	2021.78	2021.26	2179.29
	$\Gamma_1 a/(2\pi)$	2.58	-4.29	-2.46	-7.96	3.51	0.41
	$\Gamma_2 a/(2\pi)$	-0.20	-0.03	0.07	-0.07	0.05	0.00
	$\Gamma_3 a/(2\pi)$	0.02	0.00	-0.00	-0.00	0.00	-0.00

treatment. The dispersion can be expressed directly as the Fourier series

$$\omega = \Gamma_0 + \sum_{m=1}^{\infty} 2\Gamma_m \cos(km\Lambda), \tag{6.1}$$

where $\omega = 2\pi f$ is the angular frequency and k is the wavevnumber. The Fourier coefficients Γ_m can be interpreted as representing the coupling strength between defects separated by a distance $m\Lambda$.

Tab. 6.1 lists the numerical values obtained by fitting the computed CRAEW dispersion relations with Eq. (6.1). The different symmetries of the defect modes with respect to the vertical and horizontal axes are listed in Tab. 6.1. These symmetries are important in order to understand the coupling of defect modes with waves incident from the solid matrix. The Fourier series are found to converge very quickly. When compared to the coupling of neighboring cavities for the case of pure shear waves, coupling of fluid cavities in solid PCs remains relatively small. Figure 6.3(a) compares the dispersion of CRAEW for $\Lambda = 2a$ obtained numerically with the fit in Eq. (6.1). Numerical and theoretical results match very well with only the first 4 Fourier coefficients considered, meaning that couplings need only be considered up to the third nearest neighboring cavity. If the separation between cavities is increased to $\Lambda = 3a$, the dispersion generally gets even smaller, as shown in figure 6.3(b). The fitted Fourier coefficients are also listed in Tab. 6.1 in this

case. Except for the particular case of mode S_2, the Fourier coefficients are generally smaller compared to the case $\Lambda = 2a$. The polarization of mode C_2 at the Γ point is shown in figure 6.4(g) for $\Lambda = 3a$ for completeness.

The results in this section suggest the possibility of creating reconfigurable phononic circuits based on CRAEWs. Indeed, different CRAEWs can be designed based on the coefficients listed in Table 6.1. In the following, we will specifically consider the case $\Lambda = 2a$ for the design of phononic circuits. Similar results and conclusions will be obtained for larger separations, such as $\Lambda = 3a$. It should be noted that for line-defect waveguides formed when $\Lambda = a$, the guiding mechanism is different. In particular, the interaction between different guiding bands will be much stronger and lead to their interference and the opening of mini-band gaps for guided waves. The guided bands considered in this section are isolated, so that the circuits support single-mode guided propagation.

6.2.3/ TRANSMISSION SPECTRA OF CRAEWS

In this section, we consider phononic circuits created by filling with a fluid certain holes of a solid phononic crystal. Computations are performed for a finite phononic crystal with 19×19 primitive cells, as shown in figure 6.5. Phononic circuits are characterized by the transmission of waves through them. We first consider different variations on the theme of the coupled-resonator acoustoelastic waveguide, with or without bends, before moving on to a simple wave splitter.

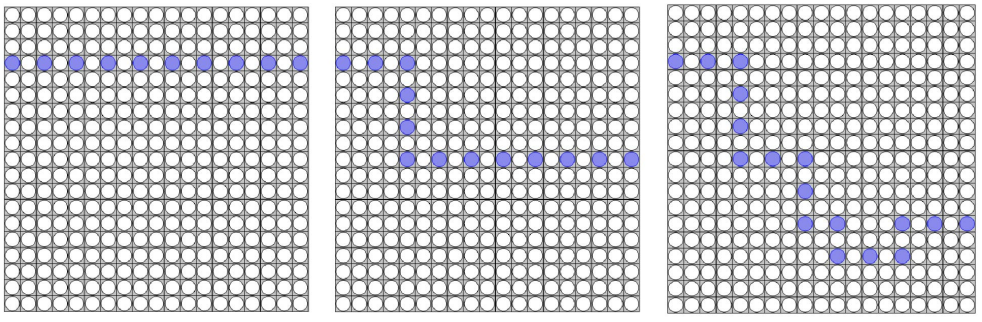

(a) (b) (c)

Figure 6.5: Cross-sections of coupled-resonator acoustoelastic waveguides formed by filling holes with water in different circuits on a finite phononic crystal with 19×19 cells: (a) straight waveguide, (b) 2-bend waveguide, and (c) 8-bend waveguide.

Figure 6.5 depicts three different waveguides for which fluid-filled cavities are separated by distance $\Lambda = 2a$. The fluid cavities are distributed in three different circuits: (a) a straight circuit formed by a sequence of 10 cavities, (b) a circuit formed by a sequence of 13 cavities with two bends, and (c) a circuit formed by a sequence of 17 cavities with eight

bends. In the following, we refer to them as the straight waveguide, the 2-bend waveguide and the 8-bend waveguide, respectively.

Transmission through a circuit is estimated as follows. A line source for elastic waves polarized along either the x axis (longitudinal excitation) or the y axis (shear excitation) is positioned along segment S_l at the left side of the waveguide. Excitation along the z axis is not considered, as vertical shear waves in the solid do not couple to pressure waves in the fluid for the two-dimensional case considered here. The length of the source segment S_l is exactly one lattice constant a. The amplitude of the displacement at the line source is noted U_0. Low reflection boundary conditions are applied on all other external boundaries of the computation domain. By sweeping the reduced frequency, we evaluate the transmission $T(fa)$ in decibels units by

$$T(fa) = 20\log_{10}\left(\frac{\int_{S_r} U\mathrm{d}s}{\int_{S_l} U_0\mathrm{d}s}\right), \tag{6.2}$$

where U is the total displacement along S_r, a receiver segment placed at the right exit of the waveguide. Instead of displacement, it would be perfectly possible to compute the flux of the Poynting vector at input and exit boundaries. This flux, however, would be a superposition of right-traveling and left-traveling guided waves, owing to the remaining small reflections at the boundaries, so the result would not simply represent directional energy flux propagation. Nevertheless, all transmissions in this section respect the principle of conservation of energy.

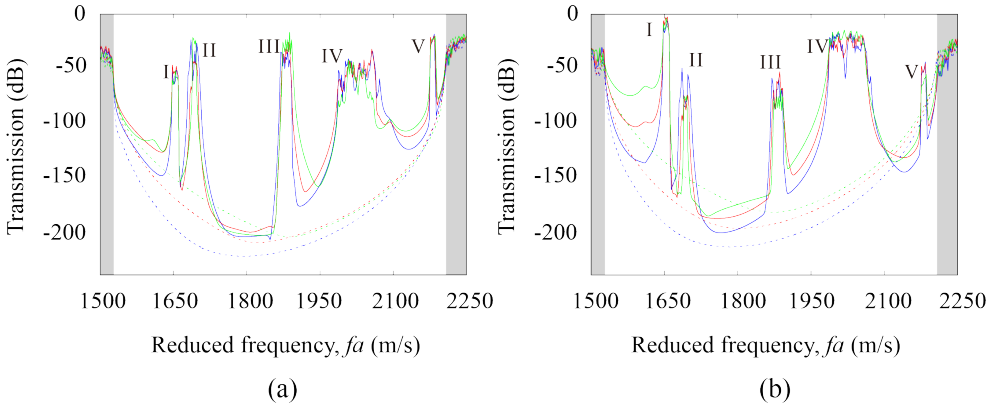

Figure 6.6: Transmission as a function of frequency through the CRAEWs of figure 6.5 for (a) a longitudinal wave source and (b) a shear wave source. Transmission is shown for the straight waveguide (green line), the 2-bend waveguide (red line), and the 8-bend waveguide (blue line). Numbers I-V are for the 5 passing frequency ranges. For comparison, transmission through the bare phononic crystal is also plotted with dashed lines, with source and receiver positioned as in the case of waveguides.

The transmissions for the different waveguides are shown in figure 6.6 as a function of reduced frequency. Five passing frequency ranges, labeled from I to V in the figure, are clearly observed inside the complete bandgap. These passing frequency ranges coincide with the CRAEW dispersion bands in figure 6.3(a): range I can be identified with the band for Bloch wave C_1, II with C_2, III with C_3, and V with C_6. Range IV can be identified with a mixture of Bloch waves C_4 and C_5, as we will argue later. It is apparent that there are no significant differences in the extent of passing frequency ranges for different circuits, though the precise oscillations inside the passing bands are characteristic of each circuit. These oscillations are caused by interferences of waves traveling along the waveguide and depend on its total length. For frequencies in-between passing bands, transmission is generally very low but again depends on the total length of the waveguide: the longer the coupled-resonator waveguide is, the smaller the transmission is. These results indicate that rather arbitrary waveguides can be defined based on the CRAEW principle, i.e. waveguides with arbitrary bends.

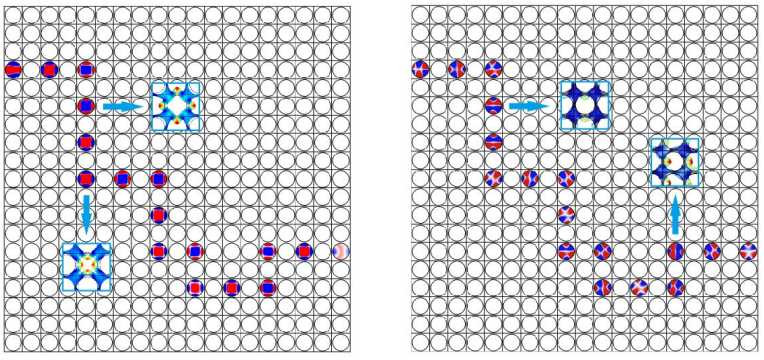

(a) (b)

Figure 6.7: Normalized pressure distribution for (a) a longitudinal wave source at reduced frequency $fa = 1882$ m/s and (b) a shear wave source at $fa = 2004$ m/s. The color scale goes from negative (blue) to positive (red). Insets show displacements around selected cavities.

Comparing transmissions in figure 6.6, we find that passing frequency ranges II, III and V are dominantly excited by the wave source of longitudinal polarization, while ranges I and IV are dominantly excited by the wave source of shear polarization. The pressure distribution along the 8-bend waveguide is shown in Figure 6.7(a) at $fa = 1882$ m/s (range III) for longitudinal excitation and in figure 6.7(b) at $fa = 2004$ m/s (range IV) for shear excitation. Pressure patterns similar to Bloch wave S_3, and to a mixture of Bloch waves S_4 and S_5, respectively, are clearly observed. Because of the Bloch waves S_4 and S_5 being of orthogonal polarization, there is a superposition of two independent transmission channels in the common frequency range of bands C_4 and C_5 in figure 6.3(a). These

results suggest that the different defect modes can be independently generated and controlled by selecting excitation frequencies and polarization. As a perspective, it seems also likely that wave sources perfectly adapted to each defect mode could be defined. In the case of perfect adaptation, unit transmission from the source to the last cavity might be achievable. Obviously, the wave sources that we considered, having uniform displacement amplitude along the straight boundary S_l, are not optimal in this respect.

Transmission for the bare phononic crystal, i.e. without any filled cavity, is added to figure 6.6 for comparison. It is found that the transmission for waveguides can be smaller than for the bare crystal, especially in the case of the shear wave source. This can be explained using the complex band structure in comparison with the transmission in the third chapter. We verified that the complex band structure is significantly modified for certain frequencies when some hollow cavities are filled with water. In particular, the smallest imaginary part value, which plays a dominant role in the determination of the attenuation inside a Bragg band gap, undergoes fast changes as a function of frequency and polarization.

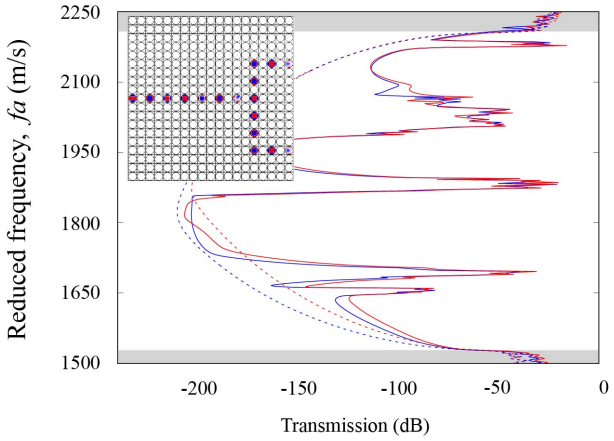

Figure 6.8: Transmission as a function of frequency through a wave splitter composed of a straight waveguide separating into two bent waveguides, for a longitudinal wave source. Transmissions at the end of the upper (red line) and lower (blue line) bent waveguides are displayed. The normalized pressure distribution at reduced frequency fa=1882 m/s is shown in an inset. The color scale goes from negative (blue) to positive (red). For comparison, transmission through the bare phononic crystal is also plotted with dashed lines, with source and receiver positioned as in the case of the splitter circuit.

When different defects are combined, it is known that various acoustic devices can be designed, such as the acoustic wave splitter [54]. Here, based on the CRAEW principle, the design of the elastic wave splitter illustrated in figure 6.8 is discussed. The phononic circuit is composed of one straight part and two asymmetric bent parts with different lengths. A wave source of longitudinal vibrations is placed at the left side of the waveguide. Elas-

tic waves first propagate along the straight part, and are then evenly split into the two bent waveguides. The wave splitting function is illustrated in the inset of figure 6.8 by the pressure distribution at reduced frequency $fa = 1882$ m/s. Similar to the results obtained for different circuits in figure 6.6, the transmissions measured at the two ends of the splitter are almost the same in the passing frequency ranges, and slightly different outside them owing to different circuit lengths. The splitter circuit ensures that wave amplitude is equally split at the junction. However, the outputs at the two ends may differ slightly in amplitude because the lengths of the two waveguides following the splitter are unequal: reflections at the ends hence interfere with incoming waves with different phases. It is worthwhile noting that this difference would disappear if there were no reflection at the ends. Reciprocally, it can be noted that if different signals of the same frequency were sent from the ends of the splitter, they would be combined into the straight waveguide.

We have observed that damping in water introduces a frequency dependence that becomes relevant at the small scale, typically when $a < 20$ μm for fluid-solid phononic crystals. This implies that the phononic circuits we have described could operate from small frequencies up to about 100 MHz, covering the typical range of ultrasonic applications such as medical ultrasound, non-destructive evaluation, etc. Selective fluid-filling of holes is a technical problem that can be tackled in different mechanical or chemical ways, depending on the hole size. Spotting machines can, for instance, be used to form pL-volume droplets and infiltrate them in individual holes with diameters of the order of 10 μm. Furthermore, techniques that have been developed in the field of optofluidics to infiltrate sub-micron holes in photonic crystal devices [78, 120] could also be applied for reconfiguring phononic circuits.

6.3/ WAVE PROPAGATION IN A TUNABLE FLUID-FILLED PHONONIC METASTRIP

We investigate wave propagation in a 1D tunable fluid-filled phononic metastrip in this section. We study the propagation of Lamb waves in a one-dimensional tunable phononic metastrip composed of a periodic sequence of hollow pillars grafted onto a strip perforated with periodic rectangular holes that can be selectively filled with water.

6.3.1/ WAVE PROPAGATION IN A PERFECT METASTRIP

The manipulation of bandgaps by filling water or not into the phononic crystals is discussed in this subsection. The manufactured sample is shown in figure 6.9(a). The chosen solid and fluid materials are isotropic aluminum 6061 (mass density ρ_s = 2700 kg/m^3, Poisson's ratio υ = 0.33, and Young's modulus E =68.9 GPa) and water (mass density ρ_f = 1000 kg/m^3 and sound velocity c = 1490 m/s), respectively. The unit cell is composed of one pillar grafted onto a perforated plate forming a strip, as depicted in figure 6.9(b). This phononic strip generates complete bandgaps in the relatively low frequency range.

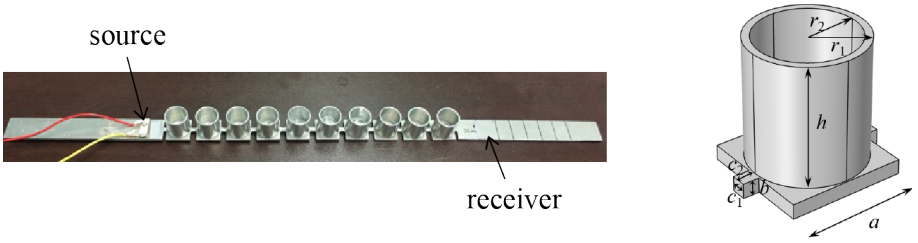

Figure 6.9: (a) A finite 1D phononic metastrip aluminum sample consisting of ten hollow pillars bonded on a strip. (b) Schematic of the PC unit cell. Geometrical parameters used in this paper are $a = 2$ cm, $h = 0.8a$, $b = c_1 = 0.1a$, $r_1 = 0.38a$, $r_2 = 0.33a$, and $c_2 = 0.11a$, respectively.

Measurements were conducted by using a Polytec-PSV-500 scanning vibrometer. The locations of the source and receiver are labeled in figure 6.9(a). To evaluate numerically the transmission properties, we built a 3D finite element model. Acoustic-structure boundary conditions are applied at the interface between fluid and solid, and a sound-soft boundary condition is applied on the top surface of the fluid column when fluid is filled. Dispersion curves are calculated by using Bloch-Floquet periodic boundary conditions. Numerical transmission is further calculated by considering a finite metastrip with ten unit cells, sandwiched between an ingoing and an outgoing homogeneous medium. Perfectly matched layers (PMLs) are added to both ends of the metastrip to avoid reflections. A wave source of z-polarization with the displacement amplitude U_{z0} is applied on the left homogeneous part of the metastrip. The transmitted displacements are recorded on the right homogeneous part. We then evaluate the transmission by considering the ratio of the z-component of the displacements integrated over the two homogeneous parts.

$$T(f) = 20\log_{10}\left(\frac{\int_{S_r} U_z \mathrm{d}s}{\int_{S_l} U_{z0}\mathrm{d}s}\right). \tag{6.3}$$

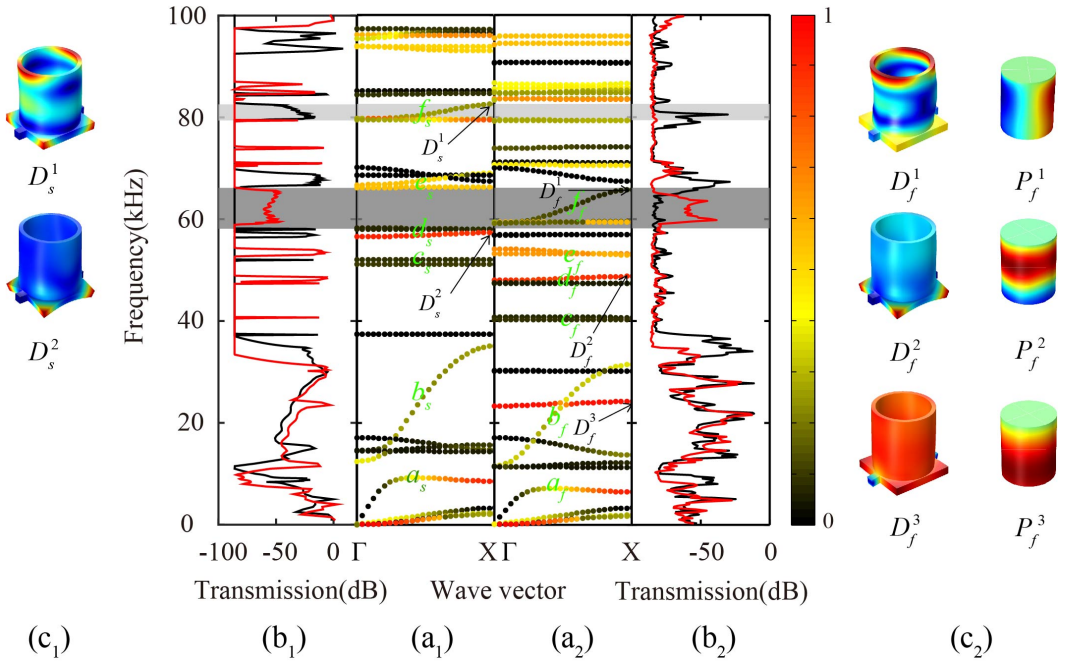

Figure 6.10: Phononic band structure of a metastrip (a_1) without and (a_2) with water filling the hollow pillars. (b_1) Numerical and (b_2) experimental transmission spectra for a finite metastrip with 10 pillars without (black line) or with (red line) water. The gray and light gray frequency ranges highlight particular bandgaps and passbands discussed in the text. The color scale is for the polarization amount of the z-component of displacement. Eigenmodes at selected points are shown (c_1) without and (c_2) with water filling. The total displacement is shown in both case and pressure is added in the case of water filling. Blue (red) corresponds to zero (maximum) amplitude for the displacement field, but to negative (positive) amplitude for the case of pressure.

Numerical and experimental results for the hollow pillars either all empty or all filled with water are shown in figure 6.10. The figure presents the band structures for the infinite and periodic strip, the transmissions computed for a 10-pillars long strip, and the transmissions measured with the sample of figure 6.9. Color information was added to the band structures to represent the polarization amount of the z-component of the displacement. Particular frequency ranges where transmission can be switched on and off by filling fluid are highlighted in grey. In order to allow for a fair comparison between numerical and experimental transmission, a 'noise floor' was added to the numerical results in order to limit the minimum of transmission to -86 dB.

Lamb waves in the phononic strip confined in the supporting plate, are periodically loaded with the fluid, and hybridize with internal resonances of the unit cell. Consequently, band structures are composed of both dispersive bands and nearly flat bands. It should be noted that resonances can be either concentrated on the pillar or on the four corners of the supporting plate, as shown in figure 6.10(c_2). Numerical results indicate that flat bands can cause sharp transmission peaks, but these are only faintly present in the

experiment. This discrepancy may be caused by the absence of loss which may lead to damped resonances in the finite element model. Furthermore, the numerical model does not take account of the exact properties of the actual sample. For example, the support of the metastrip during experiments and the inhomogeneity of the excitation source are not considered. The passbands and bandgaps defined by dispersive bands are in contrast clearly observed in the experimental transmissions. They are globally consistent with the numerical transmissions, except for a slight frequency shift that can be attributed a slightly inaccurate modelling of the sample geometry and material properties. In addition, nearly no qualitative change appears in the transmission if a symmetric excitation is applied, as we checked experimentally. As a note, since the structure is not symmetrical with respect to an horizontal plane, bending and torsional modes are always coupled.

The dispersion of passing bands is strongly affected by the presence or absence of water inside the pillars. In general, it is observed that the band structure is compressed, i.e. all bands shift down to lower frequencies when the pillars are filled with water. In order to understand this phenomenon, we consider specifically the in-plane bands a, b, c, d, e and f in figure 6.10. By in-plane bands, we mean that the displacements for the corresponding Bloch waves are mostly in the plane of the supporting strip. The modifications introduced by the addition of water can be tracked by observing modal shapes. Indeed, considering vibration modes at points D_s^2 and D_f^2 of band e, for example, it can be observed that the displacement distributions in the solid part are almost the same, while fluid-solid interaction with the second resonance of the water column brings the frequency down. As a consequence of the frequency downshift, bandgaps become narrower and their central frequencies decrease. Remarkably, the introduction of water enhances the propagation of Lamb waves in the frequency range from 58.5 kHz to 66 kHz where a bandgap was initially present. Concurrently, a bandgap appears in the frequency range from 79.4 kHz to 82.5 kHz where transmission was previously permitted by the presence of the dispersive band labelled f. Observing the modal shapes, it can be concluded that the downshift of band f in the presence of water is indeed the cause of the interchange of bandgaps and passbands. This effect suggests potential applications to the tuning of Lamb wave bandgaps.

Moreover, it can be observed that additional modes are created when water is added. An example is the band supporting the Bloch wave labelled D_f^3. The pressure distribution for the Bloch wave shown in figure 6.10(c_2) reveals that water undergoes vertical vibrations that are similar to that of the first resonance of an isolated water cylinder. This example also implies that different fluid resonances have different coupling strengths with Lamb waves in the solid matrix.

6.3.2/ INFLUENCE OF FLUID-SOLID INTERACTION

We checked that the frequency shift of passbands that we observe cannot be simply attributed to a local-resonance mechanism. Hybridization of a local resonance with a propagating band generally leads to the formation of avoided crossings around the local resonance frequency but not to a shift of the dispersion of the propagating band. In order to verify this point, we replace the fluid by an additional solid mass distributed either only in the base of the pillar (b) or in the base of the pillar as well as in the pillar wall (c) inserted in figure 6.11. The corresponding dispersion curves are shown. For comparison, figures 6.11 (a) and (d) also show the band structures of the hollow pillars without water and filled with water, respectively. In the first case, only avoided crossings appear; in the second case, band shifts are produced as well, similarly to the case of fluid filling. The two situations, distributed solid mass and distributed fluid load, are however not equivalent: even though the added masses are the same, fluid-solid interaction brings in specific features, as we noted above. An important practical difference, furthermore, is that continuously tuning the volume of a fluid is arguably easier than continuously tuning a solid mass.

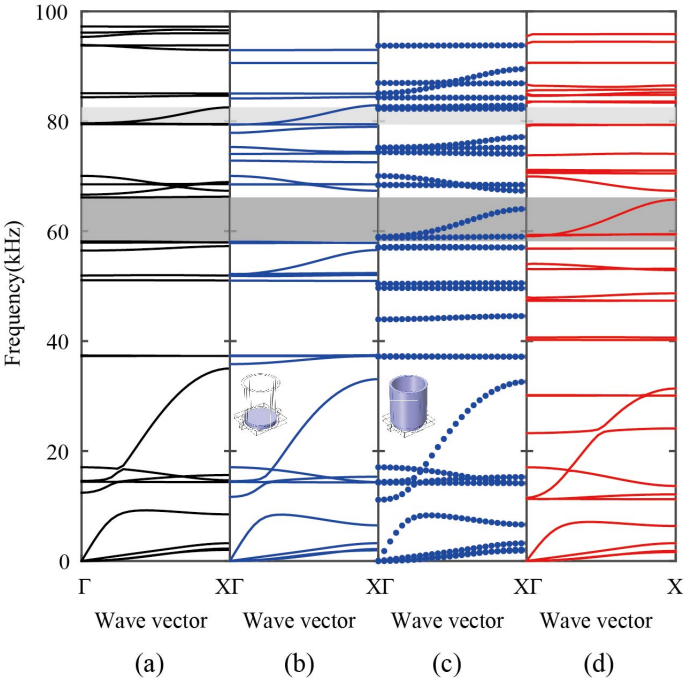

Figure 6.11: Modification of the phononic band structure of the metastrip under different ways of adding the same amount of mass to the pillars. The band structure is shown (a) without added mass, (b) for solid mass distributed in the base of pillar, (c) for solid mass distributed in the base of the pillar as well as in the pillar wall, and (d) for water filling the pillar. The insets in (b) and (c) show the regions where mass is added.

We explain the downshift of the propagating bands as follows. Thanks to the fluid-solid boundary condition inside the hollow pillar, Lamb waves in the solid strip are partly converted to pressure waves in water. The pressure waves in water decompose on the modes available at the particular frequency of excitation, as the volume of water is finite and closed by definite boundary conditions. For most frequencies, however, the conversion is not resonant. Back-conversion to Lamb waves in the solid occurs with a certain delay, causing an apparent slowing down of the propagation of Lamb waves along the strip. As the phase velocity is reduced, the dispersion of propagating bands is effectively shifted downward in frequency for a given wavenumber.

6.3.3/ WAVE PROPAGATION IN A METASTRIP WITH DEFECTS

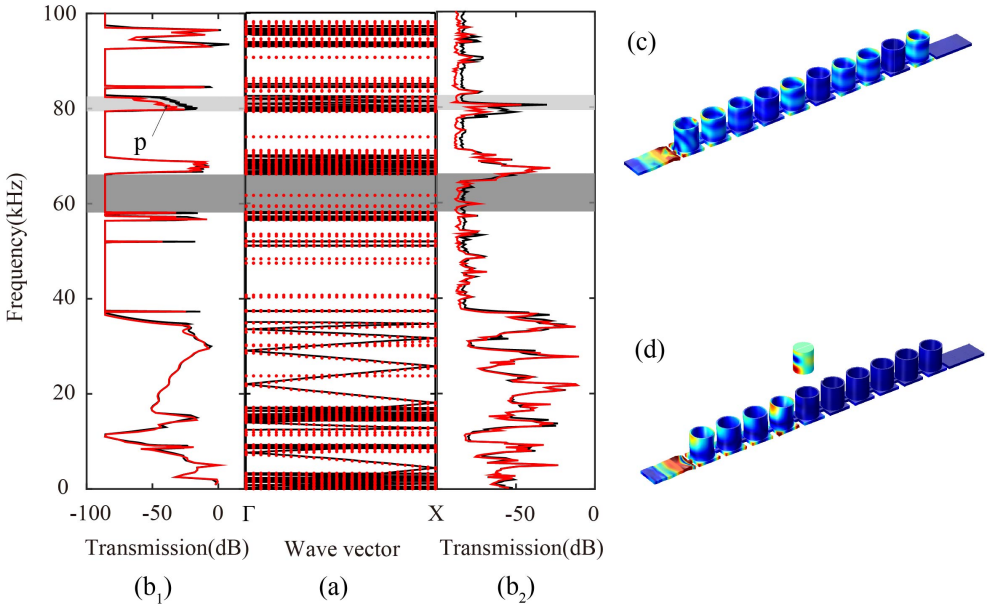

Figure 6.12: Phononic band structure (a), and numerical (b_1) and experimental (b_2) transmission spectra for metastrips either without (black lines) or with the fifth pillar filled with water (red line and red dots). Band structures are obtained from a supercell computation including 10 pillars. The distribution of total displacement at 81 kHz is shown (c) without and (d) with the fifth pillar filled with water. The pressure distribution in water for the fifth pillar is presented as an inset in (d).

Next, we focus on wave propagation in the metastrips with a defect. A point-defect cavity is created by only filling the fifth pillar with water. Figure 6.12 shows the modification of the band structure and of the transmission when water is added. It can be clearly observed that additional bands, corresponding to defect modes, appear inside the complete band gaps of the perfect system. Although there is apparently only a slight change in the spectral transmission upon introducing one defect, transmission properties are quantitatively

affected. For example, the transmission at frequency 81 kHz, labelled P in figure 6.12(b_1), decreases by almost 20 dB when the defect cavity is introduced. This transmission decrease stands for nearly one order of magnitude decrease of the displacement amplitude at the end of the metastrip. Displacement fields in the perfect and defected metastrips are displayed in figure 6.12(c) and figure 6.12(d), respectively. We observe that all hollow pillars vibrate along the perfect metastrip, as expected for a passing band in the dispersion curve. In contrast, wave propagation is quenched by the cavity in the defected metastrip: the hollow pillars to the right of the cavity are almost not vibrating. Reflection of incident Lamb waves occurs near the cavity, as illustrated by the inset of figure 6.12(d).

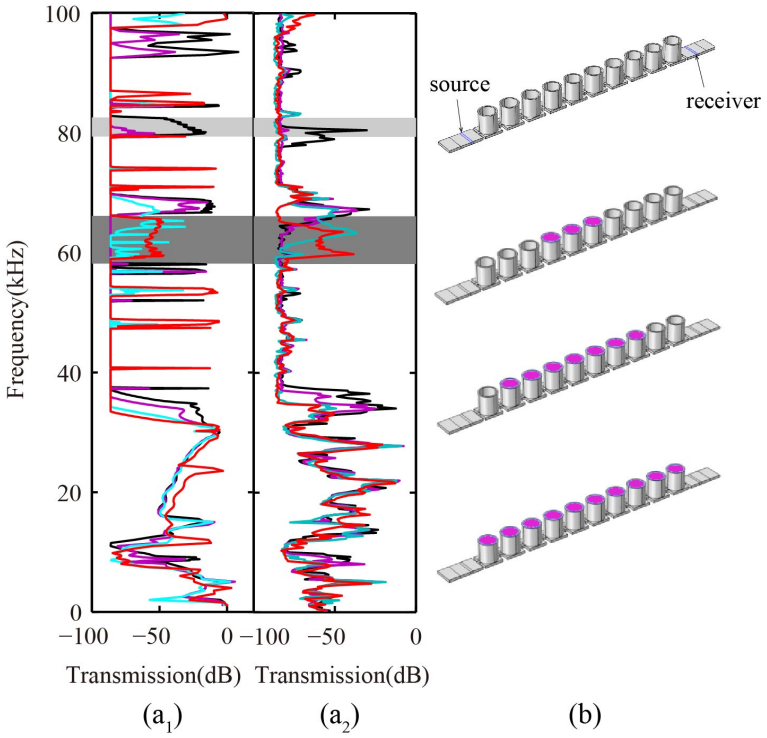

Figure 6.13: Numerical (a_1) and experimental (a_2) transmission spectra for a finite metastrip with 0 (black line), 3 (purple line), 7 (blue line), and 10 (red line) pillars filled with water. The 4 configurations are depicted in panel (b). The pink and gray parts represent for the water and aluminum, respectively.

Finally, we increase the number of filled pillars in the metastrip and observe the changes in the spectral transmission. Figure 6.13 compares the numerical (a_1) and experimental (a_2) transmissions for the metastrips with 0, 3, 7, and 10 filled pillars. With the increase in the number of filled pillars, a transmission band gradually appears in the frequency range [58.5 kHz-66 kHz], from high to low frequencies. As a result, the bandgap switches to a passband gradually. Concurrently, transmission is gradually quenched in the frequency range [79.4 kHz-82.5 kHz] as more pillars are filled. This gives rise to a transition from a passband to a bandgap. Generally, tunability of the metastrip properties by filling water

into the hollow aluminum pillars is observed to be a gradual process.

6.4/ WAVE PROPAGATION IN A TUNABLE FLUID-FILLED PHONONIC METAPLATE

In this section, we extend the concept of the 1D phononic metastrip to a 2D phononic metaplate. We propose a kind of new printing reconfigurable structure by employing the 2D phononic metaplate with fluid filling. Reconfigurable phononic circuits are arbitrarily configured through selectively filling the solid matrix with fluid in a 2D phononic crystal plate based on the fluid-solid interaction. The transmission properties for the waves propagating along them are investigated.

6.4.1/ WAVE PROPAGATION IN A PERFECT METAPLATE

In this subsection, we consider perfect phononic crystals with all hollow pillars with or without water. The unit cell is composed of one hollow pillar grafted onto a perforated plate as depicted in figure 6.14 (a). The manufactured aluminum sample is shown in figure 6.14 (b). The phononic plate with cross holes and all the hollow pillars are combined together by glue. Furthermore, the epoxy sample in figure 6.14 (c) is fabricated by a 3D print technique. Numerical simulations are conducted by using the finite element software COMSOL. Experimental measurements are performed by using the Polytec vibrometer.

For the aluminum metaplate, the material parameters of the isotropic aluminum 6061 are mass density $\rho_s = 2700$ kg/m^3, Poisson's ratio $\upsilon = 0.33$, and Young's modulus $E =$

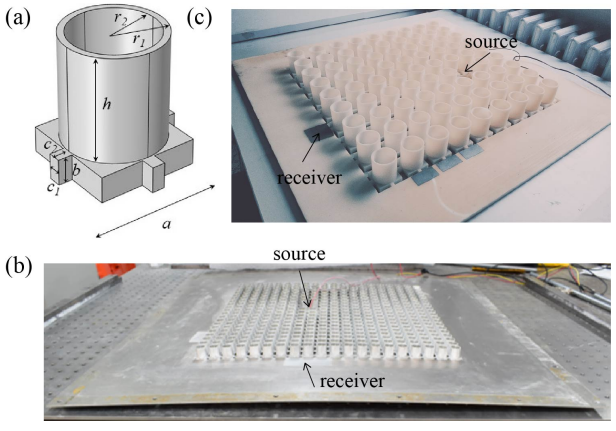

Figure 6.14: Schematic of the PC unit cell (a). A finite 2D phononic plate aluminum sample (b) consisting of 20×20 periodic unit cells and the epoxy sample (c) consisting of 9×8 periodic unit cells removing one for excitation bonded on a plate.

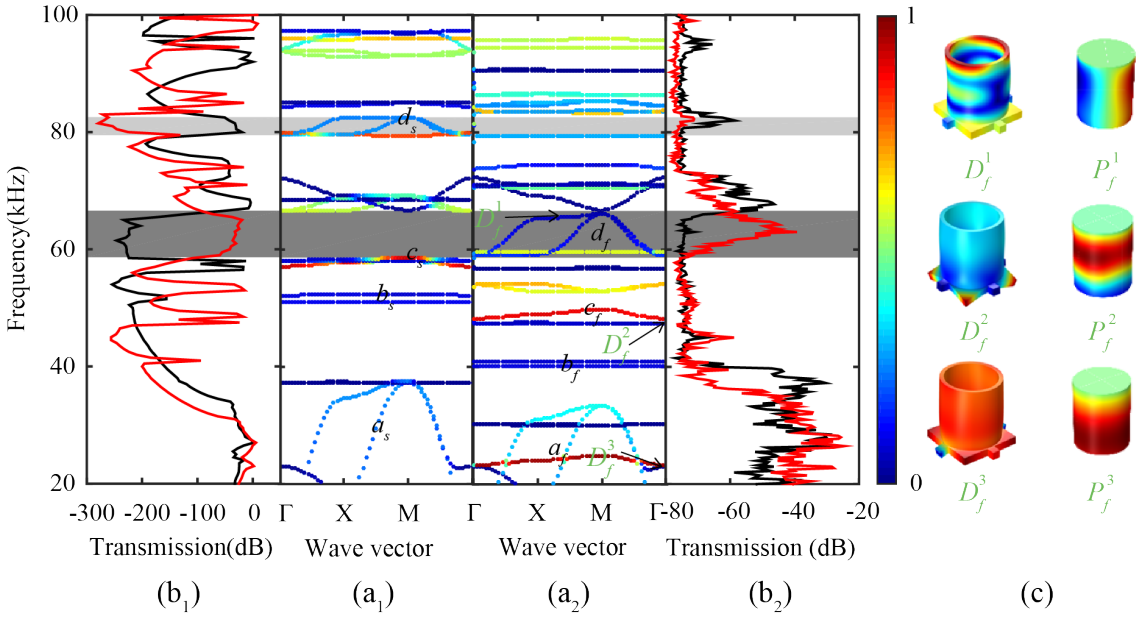

Figure 6.15: Phononic band structure of the perfect aluminum metaplate without (a_1) and with (a_2) water filling all of the hollow pillar. Numerical (b_1) and experimental (b_2) transmission spectra for the finite phononic metaplate with all hollow pillars filled without (black line) or with (red line) water. Eigenmodes at selected points are shown (c) with water filled. The total displacement is shown in both cases and pressure is added in the case of water filling. The gray and light gray frequency ranges highlight particular bandgaps with water and without water discussed in the text. The color scale is for the polarization amount of the z-component of displacement. Blue (red) corresponds to zero (maximum) amplitude for the displacement field.

68.9 GPa. The fluid material is water with mass density ρ_f = 1000 kg/m^3 and sound velocity c = 1490 m/s, respectively. Geometrical parameters of the aluminum unit cell are a=2 cm, h=0.8a, b=0.1a, c_1=0.1a, r_1=0.38a, r_2=0.33a, and c_2=0.11a, respectively. The excitation is introduced at the place where one hollow pillar in the middle of the supercell is removed. This option can effectively improve the wave transmission performance in the 2D phononic plate. Numerical and experimental results of transmission in figure 6.15 are obtained for considering a perfect finite aluminum plate with 11×7 unit cells. The results include the band structures of the infinite and periodic plates by negative printing (a_1) and positive printing (a_2) method together with the numerical (b_1) and experimental (b_2) transmissions. The polarization amount of the z-component of the displacement is represented by the color added to the band structures. Particular frequency ranges where transmission can be switched on and off by fluid filling are highlighted in grey and light grey.

It can indeed be observed from figure 6.15 that many flat bands populate the band structure when fluid-solid interaction is taken into account when fluid is filled into the hollow

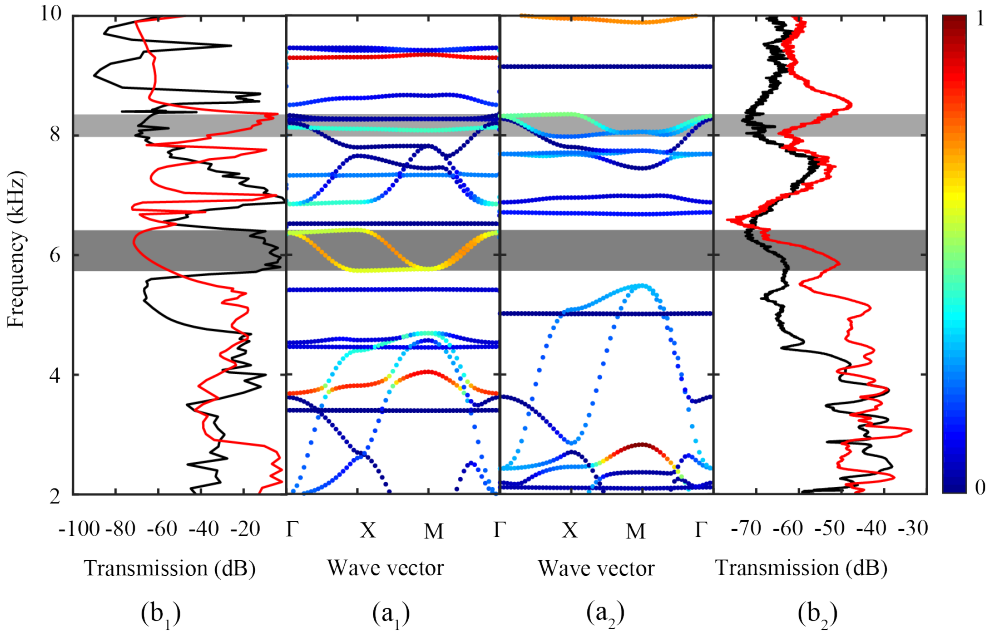

Figure 6.16: Phononic band structure of the perfect epoxy metaplate with (a_1) and without (a_2) water filled the hollow pillars. Numerical (b_1) and experimental (b_2) transmission spectra for the finite phononic metaplates with all hollow pillars filled with (black line) or without (red line) water. The corresponding gray and light gray frequency ranges highlight particular bandgaps discussed in the text. The color scale is for the polarization amount of the z-component of displacement. Blue (red) corresponds to zero (maximum) amplitude for the displacement field.

pillars. The transmission as a function of frequency shows a very clear dip at the flat bands in the transmission that is coincident with the computed band structure. In general, all the bands shift to lower frequencies, which leads to the compression of the band structure after filling water. As an explanation of the shift, the in-plane bands a, b, c, d with the same vibration modes, whether filling water or not, are compared. Band gaps become narrower and their central frequencies decrease. In particular, when filling water inside the hollow pillars, a shifted passing band from 58.7 kHz to 66.6 kHz appears where a bandgap was initially present. On the other hand, the initial passing band (d) from 79.5 kHz to 82.6 kHz shifts to lower frequency leading to the appearance of a band gap. Furthermore, it can be observed that additional modes (D_f^2) are introduced with water. We find that different fluid resonances have different coupling strengths with Lamb waves in the solid matrix, from the vibration modes shown in figure 6.15 (c). We can attribute the downshift of the passing bands not only to the local-resonance mechanism but also to fluid-solid boundary condition that leads to the conversion of Lamb waves to pressure waves in water. The experimental results are globally consistent with the numerical transmissions, except for a slight frequency shift that can be attributed a slightly inaccurate modelling of the sample geometry and material properties. Indeed, the glue between the

hollow pillars and the plate must affect the experimental results.

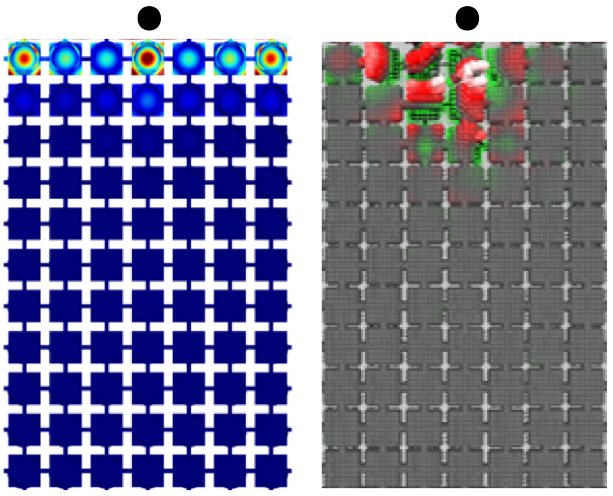

(a) (b)

Figure 6.17: Numerical (a) and experimental (b) distribution of the z-component of the displacement at 60 kHz of the perfect aluminum metaplate without water filling all of the hollow pillars. The wave source position is indicated by the black disk.

As for the epoxy metaplate, the material parameters are mass density ρ_s = 1175 kg/m^3, Poisson's ratio υ = 0.41, and Young's modulus E =3.2 GPa. For epoxy, the lattice constant is enlarged to a=5 cm and the thickness of the epoxy plate b is increased to 0.2a, while other parameters are the same as for aluminum. Numerical and experimental transmissions are then calculated and measured by considering a simplified epoxy metaplate with 9×8 unit cells. Figure 6.16 shows the band structures of the infinite and periodic plates with positive (a_1) and negative (a_2) printing as well as the numerical (b_1) and experimental (b_2) transmissions. As a remark, the transmission curves for positive printing are presented by black lines and that for negative printing are shown by red lines which is opposite to the case of the aluminum metaplate. The gray and light gray frequency ranges highlight particular passing bands of the perfect crystals with and without water, respectively.

It can be inferred from figure 6.16 that the effect of the absence of the water on transmission properties in the epoxy metaplate are almost opposite compared with the results of aluminum metaplate by filling water. In general, all the bands shift to higher frequencies after water is removed from the hollow pillars. As a consequence, bandgaps become wider and their central frequencies increase. A switching between the bandgap and passing bands of the z-polarization modes is clearly observed from 8.0 kHz to 8.35 kHz when water is removed from the hollow pillars. This offers the possibility to realize transmission along different acoustic circuits at these frequencies. There is a bandgap between 4.69

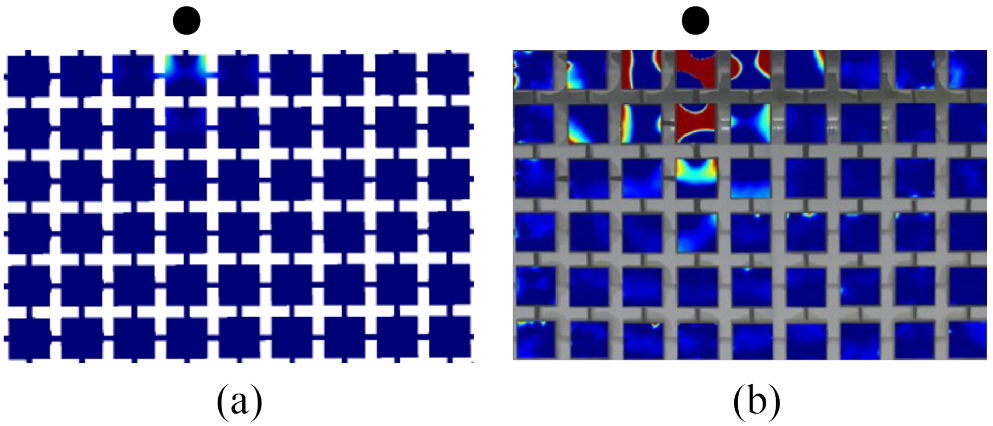

Figure 6.18: The numerical (a) and experimental (b) distribution of z-component of the displacement at 8.35 kHz of the perfect epoxy metaplate with water filling all of the hollow pillars. The wave source position is indicated by the black disk. Blue (red) corresponds to zero (maximum) amplitude for the displacement field.

Hz and 5.73 Hz when the hollow pillars are filled with water. In contrast, the propagation of waves is enhanced particularly from 4.69 kHz to 5.49 kHz after the fluid is removed. After removing the water column, a shifting band gap from 5.73 kHz to 6.41 kHz appears where a passing band was initially present. Furthermore, it can be observed that additional bands around 4.0 kHz disappear when water is removed. The transmission as a function of frequency shows very clear peaks at the flat bands. The experimental results are globally consistent with the numerical transmissions, except for a slight frequency shift.

In general, filling water leads to the compression of the band structure and the frequencies downshift, while removing water brings about the totally opposite phenomenon. As a consequence of the movement of bands, bandgaps and passing bands switch for both positive and negative contrast.

Representatively, distributions of the z-component displacement at 60 kHz for the aluminum metaplate and at 8.35 kHz of epoxy plate are presented in figures 6.17 and 6.18. Vibrations can only propagate within three lattice constants away from the excitation. Numerical and experimental results agree well.

6.4.2/ WAVE PROPAGATION IN A STRAIGHT WAVEGUIDE

In this section, we focus on the design of reconfigurable straight linear waveguides with positive contrast or negative contrast filling method. Positive contrast filling method is introduced by selectively filling fluid into the hollow pillars, while the negative contrast by removing the fluid from the hollow pillars along the circuits.

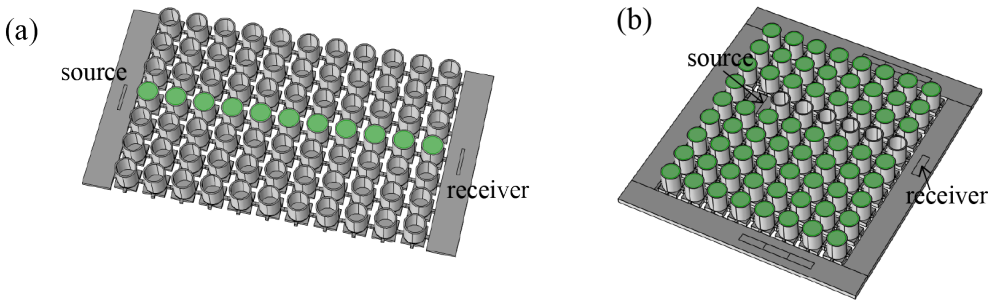

Figure 6.19: Schematic of the aluminum and epoxy metaplate with straight waveguide formed by positive (a) and negative (b) filling methods. The green and gray parts represent for the water and solid materials, respectively.

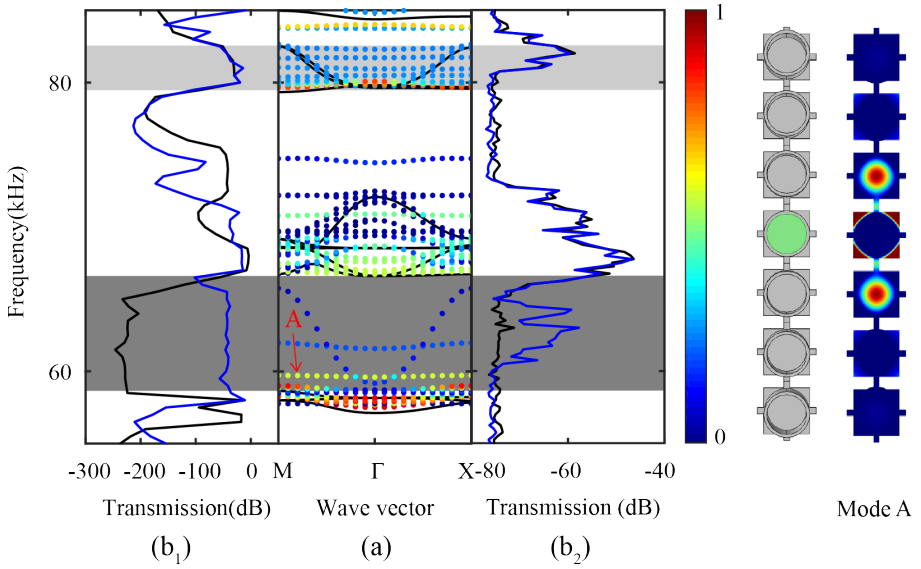

Figure 6.20: Phononic band structure (a) of the perfect (solid line) and with straight waveguide (dotted line) by positive contrast filling aluminum metaplate. The calculation models and the eigenmodes at the marked points are inserted. The corresponding numerical (b_1) and experimental (b_2) transmission spectra with all holow pillars without water (black line) or straight waveguide (blue line). The gray and light gray frequency ranges highlight particular bandgaps discussed in the text.

Figure 6.19 presents two straight waveguides printed by either positive contrast filling in aluminum metaplate or negative contrast filling in the epoxy metaplate. Band structures for the straight waveguides are shown in figures 6.20 and 6.21, together with the numerical and measured transmission properties of a finite structure. For the aluminum metaplate with positive contrast filling method in figure 6.20(a), it can be clearly observed that additional bands appear inside the grey frequency range between 58.7 kHz to 66.6 kHz after fluid is 'printed' into the hollow pillars along the straight waveguide. The defect mode at point A is inserted in figure 6.20. It is a pure bending wave mode that is symmetric with respect to the wave propagation direction. The vibration of the defect unit cell

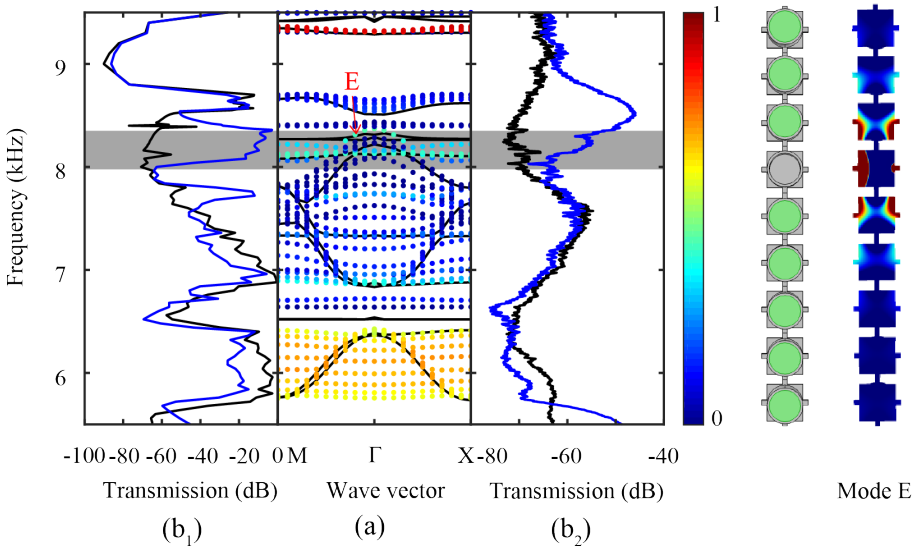

Figure 6.21: Phononic band structure (a) of the perfect (solid line) and with straight waveguide (dotted line) with negative contrast filling epoxy metaplate. The calculation models and the eigenmodes of the marked points are inserted. The corresponding numerical (b_1) and experimental (b_2) transmission spectra with all hollow pillars with water (black line) or straight waveguide (blue line). The gray and light gray frequency ranges highlight particular bandgaps discussed in the text.

is the same as those for the two adjacent unit cells, but with a $\pi/2$ phase difference.

As for the epoxy metaplate with negative contrast filling in figure 6.21(a), the frequency range between 8.0 kHz and 8.35 kHz is initially a bandgap for z-polarized modes that switches to a passing band when removing water from the hollow pillars. In particular, it can be observed from the eigenmode E that the wave vibration of the empty unit cell for negative printing is exactly symmetric with respect to the wave propagation direction at 8.35 kHz. The vibration converts to rotating mode when water is filled into the hollow pillar. The rotation of the water in the hollow pillars adjacent to the empty unit cell is reversed. The wave that ought to be confined in the defect leaks to the nearest cell on both sides because of the fluid-solid interaction. In general, the passbands and bandgaps defined by dispersive bands are clearly observed in the experimental transmissions show in (b_2) of figures 6.20 and 6.21, and are consistent with the numerical results of (b_1) of figures 6.20 and 6.21, respectively.

Figure 6.22 and figure 6.23 present the numerical (a) and experimental (b) distributions of the z-component of the displacement at 60 kHz (same as point A) of the aluminum metaplate with positive contrast filling and 8.35 kHz (same as point E) of the epoxy metaplate with negative contrast filling. The numerical results clearly show that wave propagation is strongly confined in the waveguide in both cases. The experimental results generally

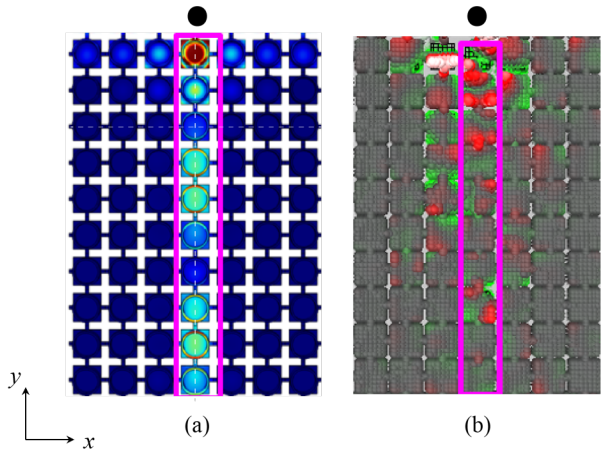

Figure 6.22: The numerical (a) and experimental (b) distribution of z-component of the displacement at 60 kHz of the aluminum metaplate with the straight waveguide by positive contrast filling. The wave source position is indicated by the black disk.

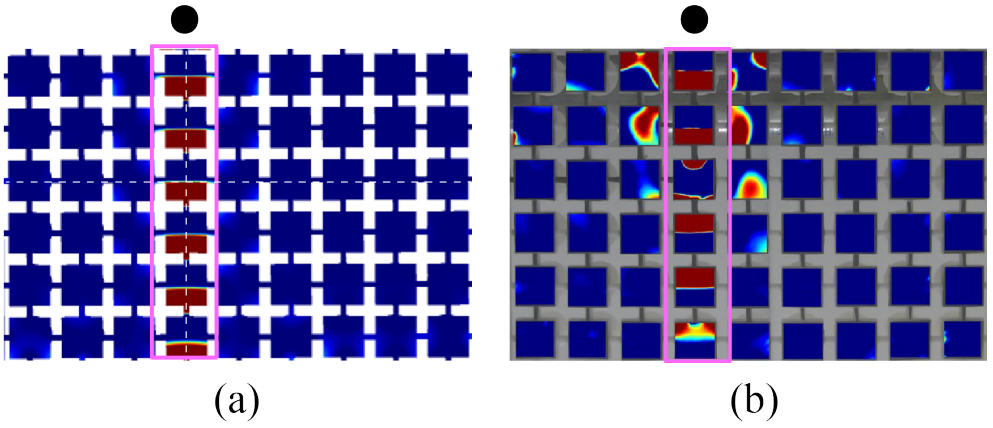

Figure 6.23: The numerical (a) and experimental (b) distribution of z-component of the displacement at 8.35 Hz of the epoxy metaplate with straight waveguide by negative contrast filling. The wave source position is indicated by the black disk. Blue (red) corresponds to zero (maximum) amplitude for the displacement field.

agree with the numerical ones. We could further observe that vibrations decay to zero in just one unit cell far away from the waveguide for the epoxy metaplate with negative contrast filling, and about three unit cells for the aluminum metaplate with positive contrast filling. The waveguide in the epoxy metaplate has a better confinement. The following is a quantitative analysis to prove this point.

To quantitatively compare the confinement of the straight waveguides in the two structures, a concentration degree [167] of the guided wave is defined as

$$C_x = \frac{1}{l_y}\int \frac{1}{l_x}\int \left[\frac{|w|^2}{(|w|^2)_{max}}|x|^2\right]\mathrm{dxdy}, \tag{6.4}$$

where l_x and l_y are the lengths of the finite structure in x- and y- directions along the white dashed lines of the straight waveguide inserted in figure 6.22 (a) and figure 6.23 (a); and x is the distance to the excitation. The concentration degree is obtained as $C_x = 1.5336\mathrm{m}^{-2}$ for the alumimum metaplate by positive contrast filling and is 17 times of magnitude smaller than that of the epoxy metaplate by negative contrast filling with $C_x = 26.062\mathrm{m}^{-2}$. Thus, the wave propagation in the straight waveguide of the epoxy metaplate by negative contrast filling is more concentrated.

6.4.3/ WAVE PROPAGATION IN A BENT WAVEGUIDE

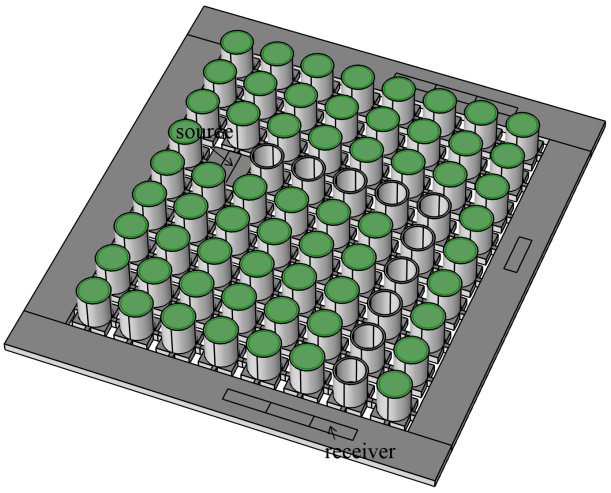

Figure 6.24: Schematic of the epoxy metaplate with bent waveguide formed by negative contrast filling method. The green and gray parts represent for the water and epoxy, respectively.

We now move our attention to a sharp waveguide. A sharp waveguide with one $90°$ bend, as shown in figure 6.24, is designed in the epoxy metaplate with negative contrast filling method. Numerical and experimental transmission spectra for this waveguide are shown in figures 6.25 (a_1) and (a_2), respectively. For comparison, the transmission properties of the fluid-filled perfect PC are added with black lines. It is apparent that a large transmission for the sharp waveguide is obtained around 8.3 kHz, which occupies a big part of the corresponding bandgap for the bare PC. A good consistency is shown between the numerical and experimental results. Since the energy decays very fast in the straight waveguide for the aluminum metaplate by positive contrast filling, we could not observe the waveguiding in the sharp bend, as we have checked experimentally.

Figure 6.26 presents the numerical (a) and experimental (b) distribution of the z-component of the displacement at 8.35 kHz. The vibration is mainly located along the waveguide. It is worthwhile noticing that the vibrations of the empty unit cells along the

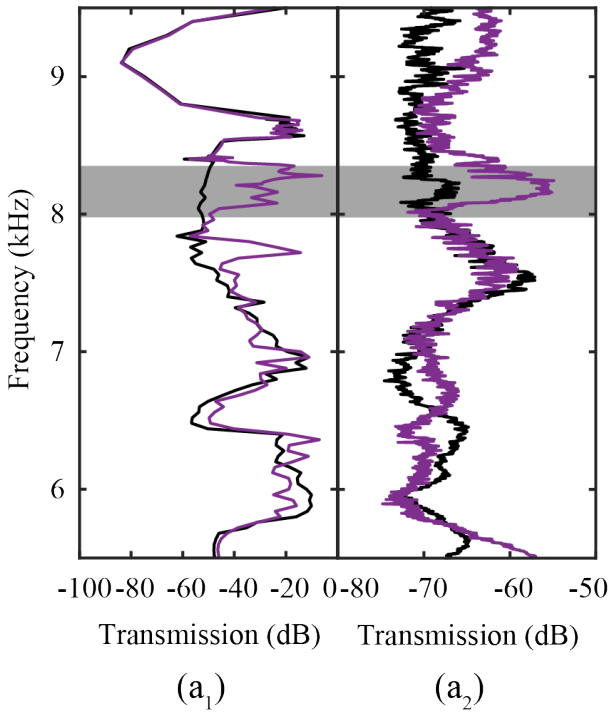

Figure 6.25: Numerical (a_1) and experimental (a_2) transmission spectra for a finite phononic meplate with all hollow pillars filled with water (black line) or bent waveguide (purple line). The light gray frequency ranges presents the passing bands of the metaplate with bent waveguide.

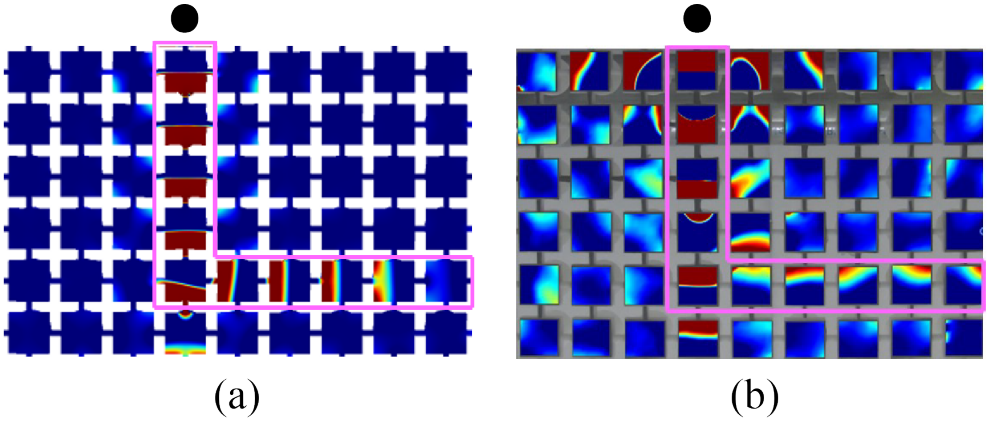

Figure 6.26: The numerical (a) and experimental (b) distribution of z-component of the displacement at 8.35 kHz of the epoxy metaplate with bent waveguide by negative contrast filling. The wave source position is indicated by the black disk. Blue (red) corresponds to zero (maximum) amplitude for the displacement field.

bent waveguide is also symmetric to the wave propagating direction. As a result, the change in the wave propagation direction caused by the sharp bend leads to a change in the direction of the vibration mode, whereas the type of the vibration mode is unchanged. The experimental measurement of the displacement field generally agrees with the numerical one for the waveguide before the bending point. After the bending, the

displacement field tends to rotate as a result of the bending and the energy coupling from the waveguide as we discussed above.

6.5/ CONCLUSIONS

In this chapter, the transmission properties of acoustic and elastic waves in coupled-resonator waveguides are systematically studied. The theoretical model of the channeled spectrum and the approximate theoretical model of the phononic polymer are developed. They predict the field distribution and resonance frequencies as well as their values. The fluid-solid interaction is investigated in fluid-solid phononic crystals. Periodic and aperiodic coupled-resonator waveguides and reconfigurable waveguides are designed. The wave propagation properties along different waveguides are investigated. Corresponding experimental samples are processed and measured. The work is conducted by combining numerical simulation, theoretical model analysis and experimental investigation. Some conclusions are as follows:

(1) Bsed on the water/aluminium phononic crystal, coupled-resonator acoustoelastic waveguides with different numbers of resonators and bends are designed. The influence of the distance between adjacent resonators on the dispersion relationship is discussed. The effect of the polarization of the wave source to the transmission is studied. The transmission characteristics of different types CRAEWs are investigated. The results show that the localized defect modes appearing inside the complete band gap of the perfect PC are the building blocks of a CRAEW. Within a certain distance range, the larger the distance between the neighboring defect cavities is, the smaller the evanescent coupling coefficient between them is, which leads to a decrease of the coupling strength. Different defect states can be generated by selecting the frequency and polarization direction of the excitation source, so as to realize the wave propagation along the different CRAEWs.

(2) Based on the water/aluminium phononic metastrip with hollow pillars, the effects of fluid filling and fluid-solid interaction on the band structure are studied. The influence on transmission of different numbers of fluid filling defects is analyzed. The results show that fluid filling causes the bands to downshift and realizes a conversion between bandgaps and passing bands. Additional modes are generated into both the band gaps and passing bands. By selectively filling fluid into the one-dimensional phononic metastrip and changing the number of filled fluid columns, a

gradual conversion process from a bandgap to a passing band is realized. Numerical simulation and experimental measurements are in good agreement.

(3) Based on the water/solid phononic metaplate with hollow pillars, the positive and negative contrast filling method are proposed. Different reconfigurable waveguides are designed and the transmission properties along them are researched. The energy distribution and energy concentration degree of waves propagating in these two different strictures are discussed. The results show that both positive contrast filling and negative contrast filling of fluid can realize wave propagation along straight waveguides. Compared with the aluminum metaplate with positive contrast filling, the energy localization of waves propagating in the waveguide by negative contrast filling in the epoxy metaplate is better. As a result, wave propagation in a strict 90° bent waveguide with negative contrast filling in the epoxy metaplate is achieved. Experimental results are found to agree satisfactorily with numerical results. Fluid filling can realize the reconfigurability of the waveguide and the reusability of the solid matrix.

The constants of this chapter provides new prospects for reconfigurable and tunable manipulation of acoustoelastic wave propagation. Consideration of more complex phononic circuits than those examined in this chapter is straightforward basing on the CRAEW concept. By using different kinds of fluids or by using a fluid whose properties can be tuned by external means, the phononic circuit could further be made tunable, active, or even smart, and manipulation of elastic waves can be achieved.

III

CONCLUSIONS AND PROSPECTS

7

CONCLUSIONS AND PROSPECTS

7.1/ CONCLUSIONS

In this thesis, the acoustic and elastic waves propagating in both periodic and aperiodic coupled-resonator waveguide are investigated. The fluid-solid interaction in fluid/solid phononic crystals is studied. The work is conducted by combining numerical simulations, theoretical model analysis and experimental investigations. The main contents and conclusions include:

(1) For acoustic wave propagation in a periodic coupled-resonator waveguide, the channeled spectrum model is developed to predict accurately the transmission properties. Different kinds of periodic coupled-resonator acoustic/elastic waveguides are designed and their transmission properties are investigated experimentally. The influence of the material viscosity and of geometric parameters on guided waves is discussed. The results show that the channeled spectrum model can accurately predict the number of oscillations. Channeled spectra depend on the length of the waveguide but are almost independent of the circuit details, including the number of turns. With the increase of the viscous damping, spectral oscillations in the channeled spectrum tend to be washed out. Strong confinement of Lamb waves along different coupled-resonator waveguides is observed. Numerical simulations and experimental results are in good agreement. The slab thickness is found to have little influence on the dispersion of in-plane guided Bloch waves, contrast with the hole length.

(2) For elastic wave propagation in an aperiodic coupled-resonator waveguide, an approximate model of the phononic polymer is proposed to explain the collective resonances of a chain of phononic microresonators. The vibration properties of the aperiodic coupled-resonator waveguide on different resonators and frequencies are

measured. The results show that the approximate model can predict the number of resonance frequencies in the phononic polymer which is the same as the number of resonators in the chain. The collective resonance at the same frequencies of the defect resonators is explained by nearest-neighbor evanescent coupling. The limitation of the periodicity is broken by the aperiodic coupled-resonator waveguide and thus the transmission along the rather arbitrary circuits is realized. Simulations and experiments agree well.

(3) The real band structures, complex-wavevector band structures, complex-eigenfrequency band structures and the resolvent band structures are calculated in one-dimensional locally resonant sonic crystal. The influence of the material viscosity and of the lattice constant is discussed. The influence of the level of water filled in the waveguide on the transmission properties is investigated numerically and experimentally. The results show that the wave attenuation and the resonant band gaps are affected obviously by the lattice constant as well as the material viscosity in the complex-wavevector band structures and complex-eigenfrequency band structures. The continuous tunability of the band gaps is realized by changing the level of water inside the waveguide, effectively changing the cross-section and thereby the dispersion of the evanescent guided waves. The experimental and numerical results are consistent.

(4) The transmission properties of different kinds of coupled-resonator acoustoelastic waveguides are investigated, based on the fluid/solid phononic crystal. The influence of the distance between the nearest resonators and the polarization of the wave source to the wave properties is discussed. The effect of the fluid fillings and the fluid-solid interaction on the band structures is studied. The gradual modification of spectral transmissions as the number of the fluid-filled cavities increases is examined. The transmission properties of the reconfigurable waveguides are researched numerically and experimentally by positive or negative filling method which is realized by filling or removing a fluid into or from the structures. The results show that the coupled acoustoelastic propagation of well-confined waves is achieved. The evanescent coupling strength depends on the separation between the defect cavities. The different defect modes can be independently generated and controlled by selecting excitation frequencies and polarization. The fluid fillings and the fluid-solid interaction contribute to the propagating bands shifting to lower frequencies and the switching between the band gaps and passing bands, as well as the additional propagation modes. Strongly confined energy in the straight waveguide of both aluminum metaplate with positive filling and epoxy metaplate with negative

filling is realized. Furthermore, the transmission of strongly confined Lamb waves along the bent waveguide with strict bend is achieved only in the epoxy metaplate by negative filling due to the higher concentration degree and lower attenuation of energy. Experimental results are found to agree satisfactorily with numerical results.

The channeled spectrum theory and the approximate model of the phononic polymer proposed in the present research provide a theoretical foundation for the research of the wave transmission properties in both periodic and aperiodic coupled-resonator waveguides. The tunable manipulation of the wave characteristics is realized owing to the fluid-solid interaction, which offers more possibilities for designing new acoustic devices.

7.2/ PROSPECTS

The propagation of acoustic/elastic waves in periodic and aperiodic coupled-resonator waveguides, and the propagation of waves in tunable coupled-resonator acoustoelastic waveguides based on fluid-solid interaction have been studied in this thesis. Some achievements have been realized. On the basis of this thesis, there are still many issues that need to be further researched, such as:

(1) Design the experiments of wave propagation along the coupled-resonator acoustoelastic waveguides to realize the propagation of complex acoustic circuits.

(2) Further improve the theoretical model of phononic polymer to realize the prediction of the exact resonant frequency values.

(3) Research the manipulation of the elastic waves in the solid matrix by fluid materials with different characteristics, and further realize the reverse detection of fluid characteristics.

(4) Design tunable phononic crystal structures at the micro-nano scale, realize the active and smart control of the waves along reconfigurable acoustic circuits in simulations and experiments.

(5) Design acoustic devices: Based on fluid-solid interaction and coupling resonance, design acoustic devices with practical applications, such as filters, multiplexers, etc.

BIBLIOGRAPHY

[1] MUKHERJEE, S., AND LEE, E. H. **Dispersion relations and mode shapes for waves in laminated viscoelastic composites by finite difference methods**. *Computers & Structures 5*, 5-6 (1975), 279–285.

[2] MUKHERJEE, S., AND LEE, E. **Dispersion relations and mode shapes for waves in laminated viscoelastic composites by variational methods**. *International Journal of Solids and Structures 14*, 1 (1978), 1–13.

[3] SU, W., SCHRIEFFER, J., AND HEEGER, A. J. **Solitons in polyacetylene**. *Physical Review Letters 42*, 25 (1979), 1698.

[4] TEMKIN, S., AND TEMKIN, S. **Elements of acoustics**, vol. 81. Wiley New York, 1981.

[5] ARMENISE, M., CANALI, C., DE SARIO, M., CARNERA, A., MAZZOLDI, P., AND CELOTTI, G. **Characterization of TiO2, LiNb3O8, and (Ti0. 65Nb0. 35) O2 compound growth observed during Ti:LiNbO3 optical waveguide fabrication**. *Journal of Applied Physics 54*, 11 (1983), 6223–6231.

[6] JOHN, S. **Strong localization of photons in certain disordered dielectric superlattices**. *Physical Review Letters 58*, 23 (1987), 2486.

[7] NOUGAOUI, A., AND ROUHANI, B. D. **Elastic waves in periodically layered infinite and semi-infinite anisotropic media**. *Surface Science 185*, 1-2 (1987), 125–153.

[8] YABLONOVITCH, E. **Inhibited spontaneous emission in solid-state physics and electronics**. *Physical Review Letters 58*, 20 (1987), 2059.

[9] HO, K., CHAN, C. T., AND SOUKOULIS, C. M. **Existence of a photonic gap in periodic dielectric structures**. *Physical Review Letters 65*, 25 (1990), 3152.

[10] AULD, B. A. **Acoustic fields and waves in solids**. Wiley, 1992.

[11] SIGALAS, M. M., AND ECONOMOU, E. N. **Elastic and acoustic wave band structure**. *Journal of Sound and Vibration 158*, 2 (1992), 377–382.

[12] CHARTIER, T., SANCHEZ, F., STÉPHAN, G., LE BOUDEC, P., DELEVAQUE, E., LENERS, R., AND FRANÇOIS, P.-L. **Channeled spectrum of a fiber laser**. *Optics Letters 18*, 5 (1993), 355–357.

[13] KUSHWAHA, M. S., HALEVI, P., DOBRZYNSKI, L., AND DJAFARI-ROUHANI, B. **Acoustic band structure of periodic elastic composites**. *Physical Review Letters 71*, 13 (1993), 2022.

[14] MARTÍNEZ-SALA, R., SANCHO, J., SÁNCHEZ, J. V., GÓMEZ, V., LLINARES, J., AND MESEGUER, F. **Sound attenuation by sculpture**. *Nature 378*, 6554 (1995), 241–241.

[15] KORPEL, A. **Acousto-optics**, vol. 57. CRC Press, 1996.

[16] DOUAK, K., AND MARONI, P. **On d-orthogonal Tchebychev polynomials, I**. *Applied Numerical Mathematics 24*, 1 (1997), 23–53.

[17] SIGALAS, M. **Elastic wave band gaps and defect states in two-dimensional composites**. *The Journal of the Acoustical Society of America 101*, 3 (1997), 1256–1261.

[18] DE ESPINOSA, F. M., JIMENEZ, E., AND TORRES, M. **Ultrasonic band gap in a periodic two-dimensional composite**. *Physical Review Letters 80*, 6 (1998), 1208.

[19] SÁNCHEZ-PÉREZ, J. V., CABALLERO, D., MÁRTINEZ-SALA, R., RUBIO, C., SÁNCHEZ-DEHESA, J., MESEGUER, F., LLINARES, J., AND GÁLVEZ, F. **Sound attenuation by a two-dimensional array of rigid cylinders**. *Physical Review Letters 80*, 24 (1998), 5325.

[20] SIGALAS, M. **Defect states of acoustic waves in a two-dimensional lattice of solid cylinders**. *Journal of Applied Physics 84*, 6 (1998), 3026–3030.

[21] SPRIK, R., AND WEGDAM, G. H. **Acoustic band gaps in composites of solids and viscous liquids**. *Solid State Communications 106*, 2 (1998), 77–81.

[22] GRAVES, R. E., AND ARGROW, B. M. **Bulk viscosity: past to present**. *Journal of Thermophysics and Heat Transfer 13*, 3 (1999), 337–342.

[23] MESEGUER, F., HOLGADO, M., CABALLERO, D., BENACHES, N., SANCHEZ-DEHESA, J., LÓPEZ, C., AND LLINARES, J. **Rayleigh-wave attenuation by a semi-infinite two-dimensional elastic-band-gap crystal**. *Physical Review B 59*, 19 (1999), 12169.

[24] OKA, K., AND KATO, T. **Spectroscopic polarimetry with a channeled spectrum**. *Optics Letters 24*, 21 (1999), 1475–1477.

[25] TORRES, M., DE ESPINOSA, F. M., GARCIA-PABLOS, D., AND GARCIA, N. **Sonic band gaps in finite elastic media: surface states and localization phenomena in linear and point defects**. *Physical Review Letters 82*, 15 (1999), 3054.

[26] YARIV, A., XU, Y., LEE, R. K., AND SCHERER, A. **Coupled-resonator optical waveguide: a proposal and analysis**. *Optics Letters 24*, 11 (1999), 711–713.

[27] KAFESAKI, M., SIGALAS, M., AND GARCIA, N. **Frequency modulation in the transmittivity of wave guides in elastic-wave band-gap materials**. *Physical Review Letters 85*, 19 (2000), 4044.

[28] LIU, Z., CHAN, C. T., SHENG, P., GOERTZEN, A. L., AND PAGE, J. H. **Elastic wave scattering by periodic structures of spherical objects: Theory and experiment**. *Physical Review B 62*, 4 (2000), 2446.

[29] LIU, Z., ZHANG, X., MAO, Y., ZHU, Y., YANG, Z., CHAN, C. T., AND SHENG, P. **Locally resonant sonic materials**. *Science 289*, 5485 (2000), 1734–1736.

[30] PSAROBAS, I., STEFANOU, N., AND MODINOS, A. **Phononic crystals with planar defects**. *Physical Review B 62*, 9 (2000), 5536.

[31] PSAROBAS, I., STEFANOU, N., AND MODINOS, A. **Scattering of elastic waves by periodic arrays of spherical bodies**. *Physical Review B 62*, 1 (2000), 278.

[32] CERVERA, F., SANCHIS, L., SÁNCHEZ-PÉREZ, J., MARTINEZ-SALA, R., RUBIO, C., MESEGUER, F., LÓPEZ, C., CABALLERO, D., AND SÁNCHEZ-DEHESA, J. **Refractive acoustic devices for airborne sound**. *Physical Review Letters 88*, 2 (2001), 023902.

[33] FU-GEN, W., ZHENG-YOU, L., AND YOU-YAN, L. **Stop gaps and single defect states of acoustic waves in two-dimensional lattice of liquid cylinders**. *Chinese Physics Letters 18*, 6 (2001), 785.

[34] KAFESAKI, M., SIGALAS, M., AND GARCIA, N. **Wave guides in two-dimensional elastic wave band-gap materials**. *Physica B: Condensed Matter 296*, 1-3 (2001), 190–194.

[35] KIM, S. W., AND KIM, S. **Fano resonances in translationally invariant nonlinear chains**. *Physical Review B 63*, 21 (2001), 212301.

[36] NOTOMI, M., YAMADA, K., SHINYA, A., TAKAHASHI, J., TAKAHASHI, C., AND YOKOHAMA, I. **Extremely large group-velocity dispersion of line-defect waveguides in photonic crystal slabs**. *Physical Review Letters 87*, 25 (2001), 253902.

[37] WU, F., HOU, Z., LIU, Z., AND LIU, Y. **Point defect states in two-dimensional phononic crystals**. *Physics Letters A 292*, 3 (2001), 198–202.

[38] BENTINI, G., BIANCONI, M., CHIARINI, M., CORRERA, L., SADA, C., MAZZOLDI, P., ARGIOLAS, N., BAZZAN, M., AND GUZZI, R. **Effect of low dose high energy O3+ implantation on refractive index and linear electro-optic properties in X-cut LiNbO3: Planar optical waveguide formation and characterization**. *Journal of Applied Physics 92*, 11 (2002), 6477–6483.

[39] KHELIF, A., DJAFARI-ROUHANI, B., VASSEUR, J., DEYMIER, P. A., LAMBIN, P., AND DOBRZYNSKI, L. **Transmittivity through straight and stublike waveguides in a two-dimensional phononic crystal**. *Physical Review B 65*, 17 (2002), 174308.

[40] AKAHANE, Y., MOCHIZUKI, M., ASANO, T., TANAKA, Y., AND NODA, S. **Design of a channel drop filter by using a donor-type cavity with high-quality factor in a two-dimensional photonic crystal slab**. *Applied Physics Letters 82*, 9 (2003), 1341–1343.

[41] HO, K. M., CHENG, C. K., YANG, Z., ZHANG, X., AND SHENG, P. **Broadband locally resonant sonic shields**. *Applied physics letters 83*, 26 (2003), 5566–5568.

[42] JENSEN, J. S. **Phononic band gaps and vibrations in one-and two-dimensional mass–spring structures**. *Journal of Sound and Vibration 266*, 5 (2003), 1053–1078.

[43] KHELIF, A., CHOUJAA, A., DJAFARI-ROUHANI, B., WILM, M., BALLANDRAS, S., AND LAUDE, V. **Trapping and guiding of acoustic waves by defect modes in a full-band-gap ultrasonic crystal**. *Physical Review B 68*, 21 (2003), 214301.

[44] KHELIF, A., DJAFARI-ROUHANI, B., VASSEUR, J., AND DEYMIER, P. A. **Transmission and dispersion relations of perfect and defect-containing waveguide structures in phononic band gap materials**. *Physical Review B 68*, 2 (2003), 024302.

[45] LAI, Y., AND ZHANG, Z.-Q. **Large band gaps in elastic phononic crystals with air inclusions**. *Applied Physics Letters 83*, 19 (2003), 3900–3902.

[46] SIGMUND, O., AND SØNDERGAARD JENSEN, J. **Systematic design of phononic band–gap materials and structures by topology optimization**. *Philosophical Transactions of the Royal Society of London. Series A: Mathematical, Physical and Engineering Sciences 361*, 1806 (2003), 1001–1019.

[47] ZHANG, X., LIU, Z., MEI, J., AND LIU, Y. **Acoustic band gaps for a two-dimensional periodic array of solid cylinders in viscous liquid**. *Journal of Physics: Condensed Matter 15*, 49 (2003), 8207.

[48] ALIVISATOS, P. **The use of nanocrystals in biological detection**. *Nature Biotechnology 22*, 1 (2004), 47–52.

[49] BELLOUARD, Y., SAID, A., DUGAN, M., AND BADO, P. **Fabrication of high-aspect ratio, micro-fluidic channels and tunnels using femtosecond laser pulses and chemical etching**. *Optics Express 12*, 10 (2004), 2120–2129.

[50] CHANDRA, H., DEYMIER, P. A., AND VASSEUR, J. **Elastic wave propagation along waveguides in three-dimensional phononic crystals**. *Physical Review B 70*, 5 (2004), 054302.

[51] HOU, Z., WU, F., AND LIU, Y. **Phononic crystals containing piezoelectric material**. *Solid State Communications 130*, 11 (2004), 745–749.

[52] KHELIF, A., CHOUJAA, A., BENCHABANE, S., DJAFARI-ROUHANI, B., AND LAUDE, V. **Guiding and bending of acoustic waves in highly confined phononic crystal waveguides**. *Applied Physics Letters 84*, 22 (2004), 4400–4402.

[53] KHELIF, A., WILM, M., LAUDE, V., BALLANDRAS, S., AND DJAFARI-ROUHANI, B. **Guided elastic waves along a rod defect of a two-dimensional phononic crystal**. *Physical Review E 69*, 6 (2004), 067601.

[54] PENNEC, Y., DJAFARI-ROUHANI, B., VASSEUR, J., KHELIF, A., AND DEYMIER, P. A. **Tunable filtering and demultiplexing in phononic crystals with hollow cylinders**. *Physical Review E 69*, 4 (2004), 046608.

[55] QI, M., LIDORIKIS, E., RAKICH, P. T., JOHNSON, S. G., JOANNOPOULOS, J., IPPEN, E. P., AND SMITH, H. I. **A three-dimensional optical photonic crystal with designed point defects**. *Nature 429*, 6991 (2004), 538–542.

[56] STASZEWSKI, W., LEE, B., MALLET, L., AND SCARPA, F. **Structural health monitoring using scanning laser vibrometry: I. Lamb wave sensing**. *Smart Materials and Structures 13*, 2 (2004), 251.

[57] TORRES, M., AND DE ESPINOSA, F. M. **Ultrasonic band gaps and negative refraction**. *Ultrasonics 42*, 1-9 (2004), 787–790.

[58] WU, F., LIU, Z., AND LIU, Y. **Splitting and tuning characteristics of the point defect modes in two-dimensional phononic crystals**. *Physical Review E 69*, 6 (2004), 066609.

[59] ZHANG, X., LIU, Z., LIU, Y., AND WU, F. **Defect states in 2D acoustic band-gap materials with bend-shaped linear defects**. *Solid State Communications 130*, 1-2 (2004), 67–71.

[60] BENCHABANE, S., KHELIF, A., CHOUJAA, A., DJAFARI-ROUHANI, B., AND LAUDE, V. **Interaction of waveguide and localized modes in a phononic crystal**. *EPL (Europhysics Letters) 71*, 4 (2005), 570.

[61] HUANG, Z.-G., AND WU, T.-T. **Temperature effect on the bandgaps of surface and bulk acoustic waves in two-dimensional phononic crystals**. *IEEE Transactions on Ultrasonics, Ferroelectrics, and Frequency Control 52*, 3 (2005), 365–370.

[62] LAUDE, V., WILM, M., BENCHABANE, S., AND KHELIF, A. **Full band gap for surface acoustic waves in a piezoelectric phononic crystal**. *Physical Review E 71*, 3 (2005), 036607.

[63] LEONG, W., STASZEWSKI, W., LEE, B., AND SCARPA, F. **Structural health monitoring using scanning laser vibrometry: III. Lamb waves for fatigue crack detection**. *Smart Materials and Structures 14*, 6 (2005), 1387.

[64] LI, F.-M., AND WANG, Y.-S. **Study on wave localization in disordered periodic layered piezoelectric composite structures**. *International Journal of Solids and Structures 42*, 24-25 (2005), 6457–6474.

[65] PENNEC, Y., DJAFARI-ROUHANI, B., VASSEUR, J. O., LARABI, H., KHELIF, A., CHOUJAA, A., BENCHABANE, S., AND LAUDE, V. **Acoustic channel drop tunneling in a phononic crystal**. *Applied Physics Letters 87*, 26 (2005), 261912.

[66] WU, T.-T., HSU, Z.-C., AND HUANG, Z.-G. **Band gaps and the electromechanical coupling coefficient of a surface acoustic wave in a two-dimensional piezoelectric phononic crystal**. *Physical Review B 71*, 6 (2005), 064303.

[67] WU, T.-T., WU, L.-C., AND HUANG, Z.-G. **Frequency band-gap measurement of two-dimensional air/silicon phononic crystals using layered slanted finger interdigital transducers**. *Journal of Applied Physics 97*, 9 (2005), 094916.

[68] ARCIZET, O., COHADON, P.-F., BRIANT, T., PINARD, M., AND HEIDMANN, A. **Radiation-pressure cooling and optomechanical instability of a micromirror**. *Nature 444*, 7115 (2006), 71–74.

[69] BENCHABANE, S., KHELIF, A., RAUCH, J.-Y., ROBERT, L., AND LAUDE, V. **Evidence for complete surface wave band gap in a piezoelectric phononic crystal**. *Physical Review E 73*, 6 (2006), 065601.

[70] GIGAN, S., BÖHM, H., PATERNOSTRO, M., BLASER, F., LANGER, G., HERTZBERG, J., SCHWAB, K. C., BÄUERLE, D., ASPELMEYER, M., AND ZEILINGER, A. **Self-cooling of a micromirror by radiation pressure**. *Nature 444*, 7115 (2006), 67–70.

[71] MIYASHITA, T. **Acoustic defect-mode waveguides fabricated in sonic crystal: Numerical analyses by elastic finite-difference time-domain method**. *Japanese Journal of Applied Physics 45*, 5S (2006), 4440.

[72] SAINIDOU, R., STEFANOU, N., AND MODINOS, A. **Linear chain of weakly coupled defects in a three-dimensional phononic crystal: A model acoustic waveguide**. *Physical Review B 74*, 17 (2006), 172302.

[73] SUN, J.-H., AND WU, T.-T. **Propagation of surface acoustic waves through sharply bent two-dimensional phononic crystal waveguides using a finite-difference time-domain method**. *Physical Review B 74*, 17 (2006), 174305.

[74] CORBITT, T., CHEN, Y., INNERHOFER, E., MÜLLER-EBHARDT, H., OTTAWAY, D., REHBEIN, H., SIGG, D., WHITCOMB, S., WIPF, C., AND MAVALVALA, N. **An all-optical trap for a gram-scale mirror**. *Physical Review Letters 98*, 15 (2007), 150802.

[75] HU, F., ZHOU, L., SHI, T., AND SUN, C. **Coupled cavity QED for coherent control of photon transmission: Green-function approach for hybrid systems with two-level doping**. *Physical Review A 76*, 1 (2007), 013819.

[76] HUSSEIN, M. I., HULBERT, G. M., AND SCOTT, R. A. **Dispersive elastodynamics of 1D banded materials and structures: design**. *Journal of Sound and Vibration 307*, 3-5 (2007), 865–893.

[77] MOHAMMADI, S., EFTEKHAR, A., KHELIF, A., MOUBCHIR, H., WESTAFER, R., HUNT, W., AND ADIBI, A. **Complete phononic bandgaps and bandgap maps in two-dimensional silicon phononic crystal plates**. *Electronics Letters 43*, 16 (2007), 898–899.

[78] MONAT, C., DOMACHUK, P., AND EGGLETON, B. **Integrated optofluidics: A new river of light**. *Nature Photonics 1*, 2 (2007), 106–114.

[79] XIA, F., SEKARIC, L., AND VLASOV, Y. **Ultracompact optical buffers on a silicon chip**. *Nature Photonics 1*, 1 (2007), 65–71.

[80] BABA, T. **Slow light in photonic crystals**. *Nature Photonics 2*, 8 (2008), 465–473.

[81] MOHAMMADI, S., EFTEKHAR, A. A., KHELIF, A., HUNT, W. D., AND ADIBI, A. **Evidence of large high frequency complete phononic band gaps in silicon phononic crystal plates**. *Applied Physics Letters 92*, 22 (2008), 221905.

[82] NOTOMI, M., KURAMOCHI, E., AND TANABE, T. **Large-scale arrays of ultrahigh-Q coupled nanocavities**. *Nature Photonics 2*, 12 (2008), 741.

[83] OTEY, C. R., POVINELLI, M. L., AND FAN, S. **Completely capturing light pulses in a few dynamically tuned microcavities**. *Journal of Lightwave Technology 26*, 23 (2008), 3784–3793.

[84] PENNEC, Y., DJAFARI-ROUHANI, B., LARABI, H., VASSEUR, J., AND HLADKY-HENNION, A. **Low-frequency gaps in a phononic crystal constituted of cylindrical dots deposited on a thin homogeneous plate**. *Physical Review B 78*, 10 (2008), 104105.

[85] WANG, Y.-Z., LI, F.-M., HUANG, W.-H., JIANG, X., WANG, Y.-S., AND KISHIMOTO, K. **Wave band gaps in two-dimensional piezoelectric/piezomagnetic phononic crystals**. *International Journal of Solids and Structures 45*, 14-15 (2008), 4203–4210.

[86] WU, L.-Y., YANG, W.-P., AND CHEN, L.-W. **The thermal effects on the negative refraction of sonic crystals**. *Physics Letters A 372*, 15 (2008), 2701–2705.

[87] WU, T.-T., HUANG, Z.-G., TSAI, T.-C., AND WU, T.-C. **Evidence of complete band gap and resonances in a plate with periodic stubbed surface**. *Applied Physics Letters 93*, 11 (2008), 111902.

[88] HUSSEIN, M. I. **Reduced Bloch mode expansion for periodic media band structure calculations**. *Proceedings of the Royal Society A: Mathematical, Physical and Engineering Sciences 465*, 2109 (2009), 2825–2848.

[89] LAUDE, V., ACHAOUI, Y., BENCHABANE, S., AND KHELIF, A. **Evanescent Bloch waves and the complex band structure of phononic crystals**. *Physical Review B 80*, 9 (2009), 092301.

[90] LUCKLUM, R., AND LI, J. **Phononic crystals for liquid sensor applications**. *Measurement Science and Technology 20*, 12 (2009), 124014.

[91] MOHAMMADI, S., EFTEKHAR, A. A., HUNT, W. D., AND ADIBI, A. **High-Q micromechanical resonators in a two-dimensional phononic crystal slab**. *Applied Physics Letters 94*, 5 (2009), 051906.

[92] PENNEC, Y., ROUHANI, B. D., LARABI, H., AKJOUJ, A., GILLET, J., VASSEUR, J., AND THABET, G. **Phonon transport and waveguiding in a phononic crystal made up of cylindrical dots on a thin homogeneous plate**. *Physical Review B 80*, 14 (2009), 144302.

[93] ROBILLARD, J.-F., MATAR, O. B., VASSEUR, J., DEYMIER, P. A., STIPPINGER, M., HLADKY-HENNION, A.-C., PENNEC, Y., AND DJAFARI-ROUHANI, B. **Tunable magnetoelastic phononic crystals**. *Applied Physics Letters 95*, 12 (2009), 124104.

[94] WANG, Y.-Z., LI, F.-M., KISHIMOTO, K., WANG, Y.-S., AND HUANG, W.-H. **Elastic wave band gaps in magnetoelectroelastic phononic crystals**. *Wave Motion 46*, 1 (2009), 47–56.

[95] WU, T.-C., WU, T.-T., AND HSU, J.-C. **Waveguiding and frequency selection of Lamb waves in a plate with a periodic stubbed surface**. *Physical Review B 79*, 10 (2009), 104306.

[96] WU, T.-T., WANG, W.-S., SUN, J.-H., HSU, J.-C., AND CHEN, Y.-Y. **Utilization of phononic-crystal reflective gratings in a layered surface acoustic wave device**. *Applied Physics Letters 94*, 10 (2009), 101913.

[97] YU, Z., AND FAN, S. **Complete optical isolation created by indirect interband photonic transitions**. *Nature Photonics 3*, 2 (2009), 91–94.

[98] ZHOU, X.-Z., WANG, Y.-S., AND ZHANG, C. **Effects of material parameters on elastic band gaps of two-dimensional solid phononic crystals**. *Journal of Applied Physics 106*, 1 (2009), 014903.

[99] HSU, F.-C., LEE, C.-I., HSU, J.-C., HUANG, T.-C., WANG, C.-H., AND CHANG, P. **Acoustic band gaps in phononic crystal strip waveguides**. *Applied Physics Letters 96*, 5 (2010), 051902.

[100] HUANG, C.-Y., SUN, J.-H., AND WU, T.-T. **A two-port ZnO/silicon Lamb wave resonator using phononic crystals**. *Applied Physics Letters 97*, 3 (2010), 031913.

[101] HUSSEIN, M. I., AND FRAZIER, M. J. **Band structure of phononic crystals with general damping**. *Journal of Applied Physics 108*, 9 (2010), 093506.

[102] KHELIF, A., HSIAO, F.-L., CHOUJAA, A., BENCHABANE, S., AND LAUDE, V. **Octave omnidirectional band gap in a three-dimensional phononic crystal**. *IEEE Transactions on Ultrasonics, Ferroelectrics, and Frequency Control 57*, 7 (2010), 1621–1625.

[103] OUDICH, M., ASSOUAR, M. B., AND HOU, Z. **Propagation of acoustic waves and waveguiding in a two-dimensional locally resonant phononic crystal plate**. *Applied Physics Letters 97*, 19 (2010), 193503.

[104] PENNEC, Y., VASSEUR, J. O., DJAFARI-ROUHANI, B., DOBRZYŃSKI, L., AND DEYMIER, P. A. **Two-dimensional phononic crystals: Examples and applications**. *Surface Science Reports 65*, 8 (2010), 229–291.

[105] ROMERO-GARCÍA, V., SÁNCHEZ-PÉREZ, J. V., CASTIÑEIRA-IBÁÑEZ, S., AND GARCIA-RAFFI, L. **Evidences of evanescent Bloch waves in phononic crystals**. *Applied Physics Letters 96*, 12 (2010), 124102.

[106] AIROLDI, L., AND RUZZENE, M. **Design of tunable acoustic metamaterials through periodic arrays of resonant shunted piezos**. *New Journal of Physics 13*, 11 (2011), 113010.

[107] BRINGUIER, S., SWINTECK, N., VASSEUR, J., ROBILLARD, J.-F., RUNGE, K., MURALIDHARAN, K., AND DEYMIER, P. **Phase-controlling phononic crystals: Realization of acoustic Boolean logic gates**. *The Journal of the Acoustical Society of America 130*, 4 (2011), 1919–1925.

[108] ELFORD, D. P., CHALMERS, L., KUSMARTSEV, F. V., AND SWALLOWE, G. M. **Matryoshka locally resonant sonic crystal**. *The Journal of the Acoustical Society of America 130*, 5 (2011), 2746–2755.

[109] HWAN OH, J., KYU LEE, I., SIK MA, P., AND YOUNG KIM, Y. **Active wave-guiding of piezoelectric phononic crystals**. *Applied Physics Letters 99*, 8 (2011), 083505.

[110] LIN, S.-C. S., AND HUANG, T. J. **Tunable phononic crystals with anisotropic inclusions**. *Physical Review B 83*, 17 (2011), 174303.

[111] MOHAMMADI, S., KHELIF, A., AND ADIBI, A. **VHF phononic band gap band pass filters using coupled resonator acoustic waveguides (CRAW)**. In *2011 IEEE International Ultrasonics Symposium* (2011), IEEE, pp. 2158–2160.

[112] MOISEYENKO, R. P., AND LAUDE, V. **Material loss influence on the complex band structure and group velocity in phononic crystals**. *Physical Review B 83*, 6 (2011), 064301.

[113] ROMERO-GARCÍA, V., GARCIA-RAFFI, L. M., AND SÁNCHEZ-PÉREZ, J. V. **Evanescent waves and deaf bands in sonic crystals**. *AIP Advances 1*, 4 (2011), 041601.

[114] VASSEUR, J., MATAR, O. B., ROBILLARD, J., HLADKY-HENNION, A.-C., AND DEYMIER, P. A. **Band structures tunability of bulk 2D phononic crystals made of magneto-elastic materials**. *AIP Advances 1*, 4 (2011), 041904.

[115] WANG, Y.-F., WANG, Y.-S., AND SU, X.-X. **Large bandgaps of two-dimensional phononic crystals with cross-like holes**. *Journal of Applied Physics 110*, 11 (2011), 113520.

[116] WU, T.-T., HSU, J.-C., AND SUN, J.-H. **Phononic plate waves**. *IEEE Transactions on Ultrasonics, Ferroelectrics, and Frequency Control 58*, 10 (2011), 2146–2161.

[117] YAO, Y., WU, F., ZHANG, X., AND HOU, Z. **Thermal tuning of Lamb wave band structure in a two-dimensional phononic crystal plate**. *Journal of Applied Physics 110*, 12 (2011), 123503.

[118] ACHENBACH, J. **Wave propagation in elastic solids**. Elsevier, 2012.

[119] BADREDDINE ASSOUAR, M., SENESI, M., OUDICH, M., RUZZENE, M., AND HOU, Z. **Broadband plate-type acoustic metamaterial for low-frequency sound attenuation**. *Applied Physics Letters 101*, 17 (2012), 173505.

[120] BEDOYA, A. C., DOMACHUK, P., GRILLET, C., MONAT, C., MÄGI, E., LI, E., AND EGGLETON, B. J. **Reconfigurable photonic crystal waveguides created by selective liquid infiltration**. *Optics Express 20*, 10 (2012), 11046–11056.

[121] BOU MATAR, O., ROBILLARD, J., VASSEUR, J., HLADKY-HENNION, A.-C., DEYMIER, P. A., PERNOD, P., AND PREOBRAZHENSKY, V. **Band gap tunability of magneto-elastic phononic crystal**. *Journal of Applied Physics 111*, 5 (2012), 054901.

[122] CHAMPION, A., AND BELLOUARD, Y. **Direct volume variation measurements in fused silica specimens exposed to femtosecond laser**. *Optical Materials Express 2*, 6 (2012), 789–798.

[123] FENG, R., AND LIU, K. **Tuning the band-gap of phononic crystals with an initial stress**. *Physica B: Condensed Matter 407*, 12 (2012), 2032–2036.

[124] García-Chocano, V. M., Cabrera, S., and Sánchez-Dehesa, J. **Broadband sound absorption by lattices of microperforated cylindrical shells**. *Applied Physics Letters 101*, 18 (2012), 184101.

[125] Hsu, J.-C. **Switchable frequency gaps in piezoelectric phononic crystal slabs**. *Japanese Journal of Applied Physics 51*, 7S (2012), 07GA04.

[126] Li, B., Cao, Y.-P., Feng, X.-Q., and Gao, H. **Mechanics of morphological instabilities and surface wrinkling in soft materials: a review**. *Soft Matter 8*, 21 (2012), 5728–5745.

[127] Li, J.-B., Wang, Y.-S., and Zhang, C. **Dispersion relations of a periodic array of fluid-filled holes embedded in an elastic solid**. *Journal of Computational Acoustics 20*, 04 (2012), 1250014.

[128] Li, S., and Sun, B. **Advances in soft matter mechanics**. Springer, 2012.

[129] Pichard, H., Richoux, O., and Groby, J.-P. **Experimental demonstrations in audible frequency range of band gap tunability and negative refraction in two-dimensional sonic crystal**. *The Journal of the Acoustical Society of America 132*, 4 (2012), 2816–2822.

[130] Rong-Xin, F., and Kai-Xin, L. **Tuning of band-gap of phononic crystals with initial confining pressure**. *Chinese Physics B 21*, 12 (2012), 126301.

[131] Su, X.-X., Wang, Y.-F., and Wang, Y.-S. **Effects of Poisson's ratio on the band gaps and defect states in two-dimensional vacuum/solid porous phononic crystals**. *Ultrasonics 52*, 2 (2012), 255–265.

[132] Swinteck, N., Vasseur, J., Hladky-Hennion, A., Croënne, C., Bringuier, S., and Deymier, P. A. **Multifunctional solid/solid phononic crystal**. *Journal of Applied Physics 112*, 2 (2012), 024514.

[133] Vrancken, B., Thijs, L., Kruth, J.-P., and Van Humbeeck, J. **Heat treatment of Ti6Al4V produced by Selective Laser Melting: Microstructure and mechanical properties**. *Journal of Alloys and Compounds 541* (2012), 177–185.

[134] Xiao, Y., Wen, J., and Wen, X. **Flexural wave band gaps in locally resonant thin plates with periodically attached spring–mass resonators**. *Journal of Physics D: Applied Physics 45*, 19 (2012), 195401.

[135] ZHEN, N., WANG, Y.-S., AND ZHANG, C. **Surface/interface effect on band structures of nanosized phononic crystals**. *Mechanics Research Communications 46* (2012), 81–89.

[136] BORN, M., AND WOLF, E. **Principles of optics: electromagnetic theory of propagation, interference and diffraction of light**. Elsevier, 2013.

[137] ESCALANTE, J. M., MARTÍNEZ, A., AND LAUDE, V. **Dispersion relation of coupled-resonator acoustic waveguides formed by defect cavities in a phononic crystal**. *Journal of Physics D: Applied Physics 46*, 47 (2013), 475301.

[138] HLADKY-HENNION, A.-C., VASSEUR, J., HAW, G., CROËNNE, C., HAUMESSER, L., AND NORRIS, A. **Negative refraction of acoustic waves using a foam-like metallic structure**. *Applied Physics Letters 102*, 14 (2013), 144103.

[139] HUSSEIN, M. I., AND FRAZIER, M. J. **Metadamping: An emergent phenomenon in dissipative metamaterials**. *Journal of Sound and Vibration 332*, 20 (2013), 4767–4774.

[140] LAUDE, V., ESCALANTE, J. M., AND MARTÍNEZ, A. **Effect of loss on the dispersion relation of photonic and phononic crystals**. *Physical Review B 88*, 22 (2013), 224302.

[141] MANKTELOW, K. L., LEAMY, M. J., AND RUZZENE, M. **Topology design and optimization of nonlinear periodic materials**. *Journal of the Mechanics and Physics of Solids 61*, 12 (2013), 2433–2453.

[142] NGO, D., GRIFFITHS, S., KHATRI, D., AND DARAIO, C. **Highly nonlinear solitary waves in chains of hollow spherical particles**. *Granular Matter 15*, 2 (2013), 149–155.

[143] OTSUKA, P. H., NANRI, K., MATSUDA, O., TOMODA, M., PROFUNSER, D., VERES, I., DANWORAPHONG, S., KHELIF, A., BENCHABANE, S., LAUDE, V., AND OTHERS. **Broadband evolution of phononic-crystal-waveguide eigenstates in real-and k-spaces**. *Scientific Reports 3* (2013), 3351.

[144] WANG, Y.-F., AND WANG, Y.-S. **Complete bandgap in three-dimensional holey phononic crystals with resonators**. *Journal of Vibration and Acoustics 135*, 4 (2013).

[145] WANG, Y.-F., AND WANG, Y.-S. **Complete bandgaps in two-dimensional phononic crystal slabs with resonators**. *Journal of Applied Physics 114*, 4 (2013), 043509.

[146] WANG, Y.-F., AND WANG, Y.-S. **Multiple wide complete bandgaps of two-dimensional phononic crystal slabs with cross-like holes**. *Journal of Sound and Vibration 332*, 8 (2013), 2019–2037.

[147] ZHEN, N., WANG, Y.-S., AND ZHANG, C. **Bandgap calculation of in-plane waves in nanoscale phononic crystals taking account of surface/interface effects**. *Physica E: Low-dimensional Systems and Nanostructures 54* (2013), 125–132.

[148] ZHOU, X., AND CHEN, C. **Tuning the locally resonant phononic band structures of two-dimensional periodic electroactive composites**. *Physica B: Condensed Matter 431* (2013), 23–31.

[149] ADDOUCHE, M., AL-LETHAWE, M. A., ELAYOUCH, A., AND KHELIF, A. **Subwavelength waveguiding of surface phonons in pillars-based phononic crystal**. *AIP Advances 4*, 12 (2014), 124303.

[150] AMOUDACHE, S., PENNEC, Y., DJAFARI ROUHANI, B., KHATER, A., LUCKLUM, R., AND TIGRINE, R. **Simultaneous sensing of light and sound velocities of fluids in a two-dimensional phoxonic crystal with defects**. *Journal of Applied Physics 115*, 13 (2014), 134503.

[151] ASPELMEYER, M., KIPPENBERG, T. J., AND MARQUARDT, F. **Cavity optomechanics**. *Reviews of Modern Physics 86*, 4 (2014), 1391.

[152] BIAN, Z., PENG, W., AND SONG, J. **Thermal tuning of band structures in a one-dimensional phononic crystal**. *Journal of Applied Mechanics 81*, 4 (2014).

[153] CALEAP, M., AND DRINKWATER, B. W. **Acoustically trapped colloidal crystals that are reconfigurable in real time**. *Proceedings of the National Academy of Sciences 111*, 17 (2014), 6226–6230.

[154] CASADEI, F., AND BERTOLDI, K. **Harnessing fluid-structure interactions to design self-regulating acoustic metamaterials**. *Journal of Applied Physics 115*, 3 (2014), 034907.

[155] CLIMENTE, A., TORRENT, D., AND SÁNCHEZ-DEHESA, J. **Gradient index lenses for flexural waves based on thickness variations**. *Applied Physics Letters 105*, 6 (2014), 064101.

[156] HATANAKA, D., MAHBOOB, I., ONOMITSU, K., AND YAMAGUCHI, H. **Phonon waveguides for electromechanical circuits**. *Nature Nanotechnology 9*, 7 (2014), 520.

[157] HU, A., ZHANG, X., WU, F., YAO, Y., CHENG, C., AND HUANG, P. **Temperature effects on the defect states in two-dimensional phononic crystals**. *Physics Letters A 378*, 30-31 (2014), 2239–2244.

[158] HUSSEIN, M. I., LEAMY, M. J., AND RUZZENE, M. **Dynamics of phononic materials and structures: Historical origins, recent progress, and future outlook**. *Applied Mechanics Reviews 66*, 4 (2014).

[159] KAYA, O. A., CICEK, A., SALMAN, A., AND ULUG, B. **Acoustic Mach–Zehnder interferometer utilizing self-collimated beams in a two-dimensional phononic crystal**. *Sensors and Actuators B: Chemical 203* (2014), 197–203.

[160] KIM, E., AND YANG, J. **Wave propagation in single column woodpile phononic crystals: Formation of tunable band gaps**. *Journal of the Mechanics and Physics of Solids 71* (2014), 33–45.

[161] MA, T.-X., ZOU, K., WANG, Y.-S., ZHANG, C., AND SU, X.-X. **Acousto-optical interaction of surface acoustic and optical waves in a two-dimensional phoxonic crystal hetero-structure cavity**. *Optics Express 22*, 23 (2014), 28443–28451.

[162] MORVAN, B., TINEL, A., VASSEUR, J., SAINIDOU, R., REMBERT, P., HLADKY-HENNION, A.-C., SWINTECK, N., AND DEYMIER, P. A. **Ultra-directional source of longitudinal acoustic waves based on a two-dimensional solid/solid phononic crystal**. *Journal of Applied Physics 116*, 21 (2014), 214901.

[163] PENNEC, Y., LAUDE, V., PAPANIKOLAOU, N., DJAFARI-ROUHANI, B., OUDICH, M., EL JALLAL, S., BEUGNOT, J. C., ESCALANTE, J. M., AND MARTÍNEZ, A. **Modeling light-sound interaction in nanoscale cavities and waveguides**. *Nanophotonics 3*, 6 (2014), 413–440.

[164] POPA, B.-I., AND CUMMER, S. A. **Non-reciprocal and highly nonlinear active acoustic metamaterials**. *Nature Communications 5*, 1 (2014), 1–5.

[165] WANG, J., YAO, Z., LEI, T., AND POON, A. W. **Silicon coupled-resonator optical-waveguide-based biosensors using light-scattering pattern recognition with pixelized mode-field-intensity distributions**. *Scientific Reports 4* (2014), 7528.

[166] WANG, Y.-F., LAUDE, V., AND WANG, Y.-S. **Coupling of evanescent and propagating guided modes in locally resonant phononic crystals**. *Journal of Physics D: Applied Physics 47*, 47 (2014), 475502.

[167] WANG, Y.-F., WANG, Y.-S., AND ZHANG, C. **Bandgaps and directional propagation of elastic waves in 2D square zigzag lattice structures**. *Journal of Physics D: Applied Physics 47*, 48 (2014), 485102.

[168] XU, Y., AND NESTERENKO, V. F. **Propagation of short stress pulses in discrete strongly nonlinear tunable metamaterials**. *Philosophical Transactions of the Royal Society A: Mathematical, Physical and Engineering Sciences 372*, 2023 (2014), 20130186.

[169] ZHU, H., AND SEMPERLOTTI, F. **A passively tunable acoustic metamaterial lens for selective ultrasonic excitation**. *Journal of Applied Physics 116*, 9 (2014), 094901.

[170] BAYAT, A., AND GORDANINEJAD, F. **Switching band-gaps of a phononic crystal slab by surface instability**. *Smart Materials and Structures 24*, 7 (2015), 075009.

[171] FRAZIER, M. J., AND HUSSEIN, M. I. **Viscous-to-viscoelastic transition in phononic crystal and metamaterial band structures**. *The Journal of the Acoustical Society of America 138*, 5 (2015), 3169–3180.

[172] LAUDE, V. **Phononic crystals: artificial crystals for sonic, acoustic, and elastic waves**, vol. 26. Walter de Gruyter GmbH & Co KG, 2015.

[173] MINIACI, M., MARZANI, A., TESTONI, N., AND DE MARCHI, L. **Complete band gaps in a polyvinyl chloride (PVC) phononic plate with cross-like holes: numerical design and experimental verification**. *Ultrasonics 56* (2015), 251–259.

[174] MOUSAVI, S. H., KHANIKAEV, A. B., AND WANG, Z. **Topologically protected elastic waves in phononic metamaterials**. *Nature Communications 6*, 1 (2015), 1–7.

[175] SÜSSTRUNK, R., AND HUBER, S. D. **Observation of phononic helical edge states in a mechanical topological insulator**. *Science 349*, 6243 (2015), 47–50.

[176] SWINTECK, N., MATSUO, S., RUNGE, K., VASSEUR, J., LUCAS, P., AND DEYMIER, P. A. **Bulk elastic waves with unidirectional backscattering-immune topological states in a time-dependent superlattice**. *Journal of Applied Physics 118*, 6 (2015), 063103.

[177] WANG, P., LU, L., AND BERTOLDI, K. **Topological phononic crystals with one-way elastic edge waves**. *Physical Review Letters 115*, 10 (2015), 104302.

[178] WANG, Y.-F., WANG, Y.-S., AND LAUDE, V. **Wave propagation in two-dimensional viscoelastic metamaterials**. *Physical Review B 92*, 10 (2015), 104110.

[179] XU, X.-W., LIU, Y.-X., SUN, C.-P., AND LI, Y. **Mechanical PT symmetry in coupled optomechanical systems**. *Physical Review A 92*, 1 (2015), 013852.

[180] BABAEE, S., OVERVELDE, J. T., CHEN, E. R., TOURNAT, V., AND BERTOLDI, K. **Reconfigurable origami-inspired acoustic waveguides**. *Science Advances 2*, 11 (2016), e1601019.

[181] FANG, H., LI, S., JI, H., AND WANG, K. **Uncovering the deformation mechanisms of origami metamaterials by introducing generic degree-four vertices**. *Physical Review E 94*, 4 (2016), 043002.

[182] FANG, K., MATHENY, M. H., LUAN, X., AND PAINTER, O. **Optical transduction and routing of microwave phonons in cavity-optomechanical circuits**. *Nature Photonics 10*, 7 (2016), 489–496.

[183] FENG, W., ZHANG, Y., AND CHE, W. **Tunable dual-band filter and diplexer based on folded open loop ring resonators**. *IEEE Transactions on Circuits and Systems II: Express Briefs 64*, 9 (2016), 1047–1051.

[184] FRAZIER, M. J., AND HUSSEIN, M. I. **Generalized Bloch's theorem for viscous metamaterials: Dispersion and effective properties based on frequencies and wavenumbers that are simultaneously complex**. *Comptes Rendus Physique 17*, 5 (2016), 565–577.

[185] GHASEMI BABOLY, M., RAZA, A., BRADY, J., REINKE, C., LESEMAN, Z. C., AND EL-KADY, I. **Demonstration of acoustic waveguiding and tight bending in phononic crystals**. *Applied Physics Letters 109*, 18 (2016), 183504.

[186] HARNE, R. L., AND LYND, D. T. **Origami acoustics: using principles of folding structural acoustics for simple and large focusing of sound energy**. *Smart Materials and Structures 25*, 8 (2016), 085031.

[187] JIN, Y., PENNEC, Y., PAN, Y., AND DJAFARI-ROUHANI, B. **Phononic crystal plate with hollow pillars actively controlled by fluid filling**. *Crystals 6*, 6 (2016), 64.

[188] JIN, Y., PENNEC, Y., PAN, Y., AND DJAFARI-ROUHANI, B. **Phononic crystal plate with hollow pillars connected by thin bars**. *Journal of Physics D: Applied Physics 50*, 3 (2016), 035301.

[189] TRAINITI, G., AND RUZZENE, M. **Non-reciprocal elastic wave propagation in spatiotemporal periodic structures**. *New Journal of Physics 18*, 8 (2016), 083047.

[190] WANG, Y.-F., WANG, Y.-S., AND ZHANG, C. **Two-dimensional locally resonant elastic metamaterials with chiral comb-like interlayers: Bandgap and simultaneously double negative properties**. *The Journal of the Acoustical Society of America 139*, 6 (2016), 3311–3319.

[191] XIA, B., CHEN, N., XIE, L., QIN, Y., AND YU, D. **Temperature-controlled tunable acoustic metamaterial with active band gap and negative bulk modulus**. *Applied Acoustics 112* (2016), 1–9.

[192] ZHOU, C., SAI, Y., AND CHEN, J. **Tunable Lamb wave band gaps in two-dimensional magnetoelastic phononic crystal slabs by an applied external magnetostatic field**. *Ultrasonics 71* (2016), 69–74.

[193] CHAUNSALI, R., KIM, E., THAKKAR, A., KEVREKIDIS, P. G., AND YANG, J. **Demonstrating an *insitu* topological band transition in cylindrical granular chains**. *Physical Review Letters 119*, 2 (2017), 024301.

[194] COFFY, E., DODANE, G., EUPHRASIE, S., MOSSET, A., VAIRAC, P., MARTIN, N., BAIDA, H., RAMPNOUX, J.-M., AND DILHAIRE, S. **Anisotropic propagation imaging of elastic waves in oriented columnar thin films**. *Journal of Physics D: Applied Physics 50*, 48 (2017), 484005.

[195] OSEEV, A., LUCKLUM, R., ZUBTSOV, M., SCHMIDT, M.-P., MUKHIN, N. V., AND HIRSCH, S. **SAW-based phononic crystal microfluidic sensor—microscale realization of velocimetry approaches for integrated analytical platform applications**. *Sensors 17*, 10 (2017), 2187.

[196] VILA, J., PAL, R. K., AND RUZZENE, M. **Observation of topological valley modes in an elastic hexagonal lattice**. *Physical Review B 96*, 13 (2017), 134307.

[197] WANG, Y.-F., AND LAUDE, V. **Longitudinal near-field coupling between acoustic resonators grafted onto a waveguide**. *Crystals 7*, 11 (2017), 323.

[198] AN, X., FAN, H., AND ZHANG, C. **Elastic wave and vibration bandgaps in two-dimensional acoustic metamaterials with resonators and disorders**. *Wave Motion 80* (2018), 69–81.

[199] CHA, J., AND DARAIO, C. **Electrical tuning of elastic wave propagation in nanomechanical lattices at MHz frequencies**. *Nature Nanotechnology 13*, 11 (2018), 1016–1020.

[200] GHASEMI BABOLY, M., REINKE, C. M., GRIFFIN, B. A., EL-KADY, I., AND LESEMAN, Z. **Acoustic waveguiding in a silicon carbide phononic crystals at microwave frequencies**. *Applied Physics Letters 112*, 10 (2018), 103504.

[201] LAUDE, V., AND KOROTYAEVA, M. E. **Stochastic excitation method for calculating the resolvent band structure of periodic media and waveguides**. *Physical Review B 97*, 22 (2018), 224110.

[202] YUAN, S.-M., MA, T.-X., CHEN, A.-L., AND WANG, Y.-S. **Liquid-assisted tunable metasurface for simultaneous manipulation of surface elastic and acoustic waves**. *AIP Advances 8*, 3 (2018), 035026.

[203] LI, G.-H., WANG, Y.-Z., AND WANG, Y.-S. **Active control on switchable waveguide of elastic wave metamaterials with the 3D printing technology**. *Scientific Reports 9*, 1 (2019), 1–8.

[204] LI, Y., SHEN, Y., CAO, S., ZHANG, X., AND MENG, Y. **Thermally triggered tunable vibration mitigation in Hoberman spherical lattice metamaterials**. *Applied Physics Letters 114*, 19 (2019), 191904.

[205] REYES, D., WALKER, E., ZUBOV, Y., HEO, H., KROKHIN, A., AND NEOGI, A. **All-acoustic signal modulation and logic operation via defect induced cavity effects in phononic crystal coupled-resonator acoustic waveguides**. *New Journal of Physics 21*, 11 (2019), 113012.

[206] ZEGA, V., NASTRO, A., FERRARI, M., ARDITO, R., FERRARI, V., AND CORIGLIANO, A. **Design, fabrication and experimental validation of a MEMS periodic auxetic structure**. *Smart Materials and Structures 28*, 9 (2019), 095011.

[207] ZHANG, Q., CHEN, Y., ZHANG, K., AND HU, G. **Programmable elastic valley Hall insulator with tunable interface propagation routes**. *Extreme Mechanics Letters 28* (2019), 76–80.

LIST OF FIGURES

List of Tables

Document generated with LaTeX and:
the LaTeX style for PhD Thesis created by S. Galland — http://www.multiagent.fr/ThesisStyle
the tex-upmethodology package suite — http://www.arakhne.org/tex-upmethodology/